

STM beyond vacuum tunnelling: Scanning Tunnelling Hydrogen Microscopy as a route to ultra-high resolution

Christian Weiss



STM beyond vacuum tunnelling: Scanning Tunnelling Hydrogen Microscopy as a route to ultra-high resolution

Von der Fakultät für Mathematik, Informatik und Naturwissenschaften der RWTH Aachen University zur Erlangung des akademischen Grades eines Doktors der Naturwissenschaften genehmigte Dissertation

vorgelegt von Diplom-Physiker Christian Weiss aus Essen

Berichter: Universitätsprofessor Dr. F. Stefan Tautz

Universitätsprofessor Dr. Markus Morgenstern

Tag der mündlichen Prüfung: 13.08.2012

Diese Dissertation ist auf den Internetseiten der Hochschulbibliothek online verfügbar.

Forschungszentrum Jülich GmbH Peter Grünberg Institute (PGI) Functional Nanostructures at Surfaces (PGI-3)

STM beyond vacuum tunnelling: Scanning Tunnelling Hydrogen Microscopy as a route to ultra-high resolution

Christian Weiss

Bibliographic information published by the Deutsche Nationalbibliothek. The Deutsche Nationalbibliothek lists this publication in the Deutsche Nationalbibliografie; detailed bibliographic data are available in the Internet at http://dnb.d-nb.de.

Publisher and Forschungszentrum Jülich GmbH

Distributor: Zentralbibliothek

52425 Jülich

Phone +49 (0) 24 61 61-53 68 · Fax +49 (0) 24 61 61-61 03

e-mail: zb-publikation@fz-juelich.de Internet: http://www.fz-juelich.de/zb

Cover Design: Grafische Betriebe, Forschungszentrum Jülich GmbH

Printer: Grafische Betriebe, Forschungszentrum Jülich GmbH

Copyright: Forschungszentrum Jülich 2012

Schriften des Forschungszentrums Jülich

Reihe Schlüsseltechnologien / Key Technologies Band / Volume 47

D 82 (Diss., RWTH Aachen University, 2012)

ISSN 1866-1807

ISBN: 978-3-89336-813-6

The complete volume is freely available on the Internet on the Jülicher Open Access Server (JUWEL) at http://www.fz-juelich.de/zb/juwel

Neither this book nor any part of it may be reproduced or transmitted in any form or by any means, electronic or mechanical, including photocopying, microfilming, and recording, or by any information storage and retrieval system, without permission in writing from the publisher.

Abstract

Direct imaging is a fast and reliable method for the characterization of surfaces. When it comes to small surface structures in the size of the features e.g. in todays computer processors, classical optical imaging methods fail in resolving these structures. With the invention of the scanning tunnelling microscope (STM) for the first time it became possible to image the structure of surfaces with atomic precision. However, the STM fails in resolving complex chemical structures like e.g. organic molecules. The lack of chemical sensitivity in STM images can be overcome by the condensation of molecular hydrogen or deuterium in the STM junction. Images recorded in the so-called scanning tunnelling hydrogen microscopy (STHM) closely resemble the chemical structure of different organic molecules. However, the mechanism behind the contrast formation has not been addressed so far. Here we show that the origin of the STHM contrast is a single hydrogen (H₂) or deuterium (D_2) molecule located directly below the tip apex that acts as a combined sensor and signal transducer. Together with the tip the gas molecule forms a nano-scale force sensor, comparable to sensors in atomic force microscopy (AFM), which probes the total electron density (TED) of the surface trough the Pauli repulsion and converts this signal into variations of the junctions' conductance again via Pauli repulsion. Other than the sensors in conventional scanning force techniques, due to its size, the sensor of the STHM junction is intrinsically insensitive to long-range forces, usually limiting the image resolution. The insensitivity to long-range forces results in a high image resolution, so that even small changes in the TED leave a mark in obtained STHM images. The resolution hereby reaches an unprecedented level as can be seen by the direct imaging of local intermolecular interactions like e.g. hydrogen bonds appear with remarkable clarity in STHM images of organic layers. Thus, besides the identification of chemical species of different adsorbates, the STHM mode allows the study of interactions between adsorbates which e.g. lead to their self organization on the surface. Therefore, the STHM mode may give important insight in the driving mechanisms behind the formation and composition of matter on the atomic level. However, the STHM mode, in which a single H₂ (D₂) molecule probes the TED of the surface, is only one example of a broader class of sensors. It is conceivable, that by an appropriate choice of the molecule in the junction, other surface properties can be imaged which are usually inaccessible by other imaging techniques.

Kurzfassung

Die direkte Abbildung ist eine schnelle und verlässliche Methode zur Charakterisierung von Oberflächen. Allerdings können kleine Strukturen, wie sie zum Beispiel in heutigen Computerprozessoren vorkommen, mit klassischen optischen Methoden nicht aufgelöst werden. Durch die Erfindung des Rastertunnelmikroskops (STM) konnte erstmals die atomare Struktur von Oberflächen direkt sichtbar gemacht werden. Jedoch reicht das Auflösungsvermögen des STMs nicht aus, um komplexe chemische Verbindungen - wie zum Beispiel organische Moleküle - atomar aufzulösen. Durch die Kondensation von molekularem Wasserstoff (H_2) oder Deuterium (D_2) im STM Kontakt kann dieser Nachteil überwunden werden. Bilder verschiedener organischen Moleküle demonstrieren, dass die Auflösung in Aufnahmen mit der sogenannten Rastertunnelwasserstoffmikroskopie (STHM), der chemischen Struktur der Moleküle ähnelt. Allerdings wurde der Mechanismus hinter dem STHM Kontrast noch nicht genauer betrachtet. In dieser Arbeit zeigen wir, ein einzelnes H₂ oder D₂ Molekül direkt unter der Tunnelspitze für die erhöhte Auflösung verantwortlich ist. Dieses Molekül fungiert als kombinierter Sensor und Signalwandler. Zusammen mit dem Molekül bildet die Tunnelspitze einen nanoskopischer Kraftsensor, der durch die Pauli Abstoßung sensitiv auf die totale Elektronendichte (TED) der Probe ist und dieses Signal, ebenfalls durch die Pauli Abstoßung, in Änderungen der Leitfähigkeit des Tunnelkontaktes übersetzt. Im Gegensatz zu konventionellen Kraftsensoren, ist der Sensor bereits durch seine geringe Größe unabhängig von langreichweitigen Kräften, die gewöhnlicher Weise das Auflösungsvermögen von Rasterkraftmikroskopen begrenzen. Die Unempfindlichkeit des Sensors gegenüber langreichweitigen Kräften führt zu einem hohen Auflösungsvermögen, welches ausreicht, um kleinste Änderungen der TED in den Bildern sichtbar zu machen. Die Auflösung erreicht hierbei einen Level, in dem sogar lokale Wechselwirkungen, wie zum Beispiel Wasserstoffbrückenbindungen, in molekularen Schichten direkt und mit erstaunlicher Deutlichkeit in STHM Bildern zu sehen sind. Dies zeigt, dass der STHM Modus neben der chemischen Analyse verschiedener Adsorbate, auch die Untersuchung von lokalen Wechselwirkungen erlaubt, die unter anderem für die selbstständige Anordnung von Adsorbaten auf Oberflächen verantwortlich sind. In diesem Zusammenhang könnte der STHM Modus neue Erkenntnisse über die lokale Zusammensetzung von Festkörpern auf atomarer Ebene liefern. Andererseits kann die Funktionalität des vorgestellten STHM Modus, in dem ein einzelnes H₂ (D₂) Molekül die TED der Oberfläche abtastet, als ein Beispiel für eine große Familie von verschiedenen Sensoren angesehen werden. So ist es vorstellbar, dass durch geeignete Wahl des Moleküls an der Tunnelspitze andere Eigenschaften der Oberfläche direkt abgebildet werden können, die normalerweise mit anderen Techniken nicht zugänglich sind.

Contents

Pı	eface	e	1			
1	Intr	oduction	3			
2	The	Theoretical background and important progressions of the STM				
	2.1	Scanning tunnelling microscopy	7			
		2.1.1 Tunnelling Effect	9			
		2.1.2 Electrode-vacuum-electrode contact	12			
		2.1.3 Theoretical approach	14			
		2.1.4 Tersoff-Hamann-Theory	15			
	2.2	Dynamic force microscopy	19			
		2.2.1 AFM operation modes	19			
		2.2.2 FM-AFM	20			
		2.2.3 qPlus AFM	23			
	2.3	Advancements based on STM/AFM	23			
		2.3.1 Improving the image contrast	24			
		2.3.2 Spectroscopy and secondary signals	26			
3	Pre	paration of STHM experiments	31			
	3.1	Preparation of organic layers	32			
	3.2	Preparation of the tip	32			
	3.3	Adsorption of hydrogen	35			
	3.4	Preparation of the STHM tip	38			
4	Exa	mples of STHM images	41			
	4.1	Image contrast: organic molecules	41			
		4.1.1 PTCDA/Au(111)	41			
		4.1.2 Pentacene/Ag(111)	43			
		4.1.3 Tetracene/Ag(110)	45			
		4.1.4 SnPc/Ag(111)	46			
	4.2	Contrast variation: PTCDA	48			
		4.2.1 Distance dependence	48			
		4.2.2 Tip dependence	52			
	4.3	STHM imaging of intermolecular interactions	59			
		4.3.1 PTCDA/Au(111)	60			

Contents

		4.3.2	Dehydrogenized PTCDA/Au(111)	6
		4.3.3	Metal-molecule bonds in K/PTCDA layer	6
	4.4	Atomi	ic resolution of metal clusters	7
5	For	mation	of the geometric contrast	7
	5.1	Spectr	roscopic characterization of the STHM junction	7
		5.1.1	Evolution during deposition	7
		5.1.2	Switching On/Off STHM contrast	7
		5.1.3	D_2 coverage in the active part of the junction	7
		5.1.4	Structural state of the junction during imaging	8
		5.1.5	Dependence of the conductance on the tip-sample distance $$	8
		5.1.6	STHM resolution at different tip-sample separations	8
	5.2	Ab ini	itio calculations	9
	5.3	Qualit	tative model: sensor/transducer	9
		5.3.1	Visualization at Au dimer	9
		5.3.2	Contrast formation above PTCDA	9
	5.4	Testin	g the model	9
		5.4.1	Atomic resolution of clean metal surface	9
		5.4.2	Expectable corrugation without D_2	10
		5.4.3	Evidence of D_2 in the junction	10
		5.4.4	Influence of D_2 on the junction conductance	10
		5.4.5	Contrast formation	10
	5.5	Attem	apt of quantification: calibration of the force sensor	11
		5.5.1	Force on the tip	11
6	Out	look: F	Forthcoming method development	12
	6.1	Latera	al maps of the interaction potential	12
	6.2	Dynar	mics in the STHM junction	13
		6.2.1	Scattering processes	13
7	Sun	nmary		13
Bi	bliog	raphy		13
Ac	knov	vledger	ments	15
Lis	st of	Acrony	yms	16
Lie	st of	Figure	os	16

Preface

The work presented in this thesis was carried out in the Forschungszentrum Jülich in the Peter Grünberg Institut 3 (PGI-3) headed up by Prof. F. S. Tautz. In particular, the experimental results have been acquired in framework of the research group of Dr. Ruslan Temirov which is focused on complex transport regimes in low temperature scanning tunnelling microscopy. The microscope used for the experiments is a commercially available low-temperature scanning tunnelling microscope. Prior to the writing of this thesis, parts of the results presented in the following have already been published in the following papers:

- C. Weiss, C. Wagner, C. Kleimann, M. Rohlfing, F. S. Tautz, and R. Temirov. Imaging pauli repulsion in scanning tunneling microscopy. *Phys. Rev. Lett.*, 105:086103, 2010.
- C. Weiss, C. Wagner, R. Temirov, and F. S. Tautz. Direct imaging of intermolecular bonds in scanning tunneling microscopy. *Journal of the American Chemical Society*, 132:11864—11865, 2010.
- C. Weiss, C. Wagner, F.S. Tautz, and R. Temirov. Looking inside molecules. *G.I.T. Imaging and Microscopy*, 1:38–40, 2011.

1 Introduction

Interfaces play a major role in our all day life. These interfaces maybe the internal connections in electronic circuits [1–5] which are used e.g. in our cellphones, TVs or computers, the connection between the wheels of our cars and the street [6, 7] or just the connection between a frying pan and a steak to achieve an optimal taste [8–10]. In many cases the properties of the interfaces arise from the structure and the electronic properties of the surfaces which are brought together at the interface. The relation between the properties of the interface and the properties of the surface has led to the development of a whole new field in physics. In the framework of surface science the structure of surfaces, the physical (e.g. friction, electronic transport) and chemical (e.g. catalysis, dissociation and recombination) properties arising from the structure or the adsorption of atoms and molecules from gas phase or liquids are systematically studied.

Scientist's interest in surface properties has hereby induced a fast technical development of new methods for surface characterisation. Many of these techniques address special properties of a surface, thus a comprehensive picture of the surface structure and and its properties can only be drawn by applying different techniques.

The properties of the surface which are investigated range from the structure over the atomic composition to electronic and vibrational characteristics. Vibrational degrees of freedom can be studied for example by the energy transferred into vibrational levels during interaction with electrons in electron energy loss spectroscopy (EELS) [11]. The excited states in EELS experiments are excitations of chemical inter-atomic bonds or molecular vibrations which have a discrete energy. Thus, recorded spectra allow a determination of the composition of the sample whereas the surface structure cannot be determined from the spectra. The electronic properties of the samples can be measured in two ways: on the one hand it is possible to probe occupied states by ultraviolet photo-emission spectroscopy (UPS) [12, 13] on the other hand one can probe unoccupied states by excitation of electrons from occupied into unoccupied states and subsequent photo-emission in two-photon photo-emission (2PPE) [14]. Both techniques allow the investigation of a possible band structure of the surface, but not atomic or molecular structure of the surface.

Another possibility for surface characterisation by inducing photo-emission is the investigation of the samples composition. The composition of the sample surface can be investigated by photo-emission from core levels of the atoms on the surface in x-ray photo-emission spectroscopy (XPS) or Auger electron spectroscopy [15, 16]. Since lower lying

1 Introduction

energy levels in the electronic structure of an atom (core levels) are characteristic for the atoms species, these techniques allow the determination of the composition but not the structure of the sample.

So far, we presented methods which allow the characterisation of any surface, but when it comes to the controlled assembly of surface structures even more information become available. In many cases, the construction of surface structures is realised by adsorption of atoms or molecules from the gas phase or liquids. In this framework, the adsorption energy of the adsorbates, their adsorption height and their orientation with respect to the surface plane can be studied. The adsorption energy can be studied, for example, by the controlled desorption of adsorbate layers due to an increased surface temperature in temperature programmed desorption (TPD) [17]. The height of adsorbate layers on crystalline surfaces is measured in x-ray standing wave (XSW) [18] experiments. In XPS a standing wave pattern in front of the sample is created, where the positions of the maxima of the standing wave can be tuned by scanning through the Bragg condition of the incoming x-ray beam. Whenever a maximum of the standing wave hits the center of an atom, photo-electrons are emitted which allows a precise determination of the height of the atom above the surface. The adsorption geometry of adsorbates with respect to the surface plane can be determined with angular resolved ultra-violet photo-emission spectroscopy (ARUPS) [19] in which maxima in the photo-electron emission with respect to the incoming light wave and the outgoing electron beam denote the orientation of the emitting adsorbates. However, none of these techniques address the structure formed by the adsorbates on the surface.

The surface structure can be reconstructed from obtained diffraction patterns in low energy electron diffraction (LEED) [20, 21], reflection high energy electron diffraction (RHEED) [22, 23], or by direct imaging in scanning electron microscopy (SEM) [24, 25], transmission electron microscopy (TEM) [26, 27], low energy electron microscopy (LEEM) or photo-emission electron microscopy (PEEM) [28–30]. However, except the TEM [31] none of this methods allows a determination of surface structures with atomic precision.

The insensitivity to small structures, which is comparable in all the presented techniques for surface characterisation, limits the applicability of the methods to large well ordered structures in which every scattering center or every emitter is equal since the measured signal is always an average over a large surface areas, thus every dislocation and defect results in an increased noise in the measured signal. The limitation to long range ordered structures has been overcome with the invention of the scanning tunnelling microscope (STM) [32–35].

The popularity of the STM for surface characterisation can be explained by its ability to routinely provide atomic scale resolution [36–41]. However, STM fails in resolving complex chemical structures, because it is only sensitive to electronic states close to the Fermi-level of the sample. These levels are usually quite delocalized since they are strongly involved in chemical interactions, thus they have little relation to the real structure. Therefore it is desirable to go beyond the conventional STM resolution and equip STM with chemical sensitivity to directly observe the underlying structure.

So far different approaches have been presented to achieve chemical sensitivity in STM which can be divided into two families, the first of which is based on spectroscopic analysis of surface properties, while the second one enhances STM resolution in order to directly determine chemical structures from obtained images. Spectroscopic approaches probe either local vibrational or electronic states of the sample. Examples are inelastic electron tunnelling spectroscopy (IETS) [42], tip-enhanced Raman spectroscopy (TERS) [43] or electro luminescence spectroscopy (ELS) [44]. From the obtained spectra it is in principle possible to reconstruct the chemical species of the investigated surface, however in many cases the properties are strongly affected by local interactions with the sample, which limits the applicability of this approaches to a limited number of systems up to now [45–50].

In the case of imaging complex organic molecules, a possibility to enhance the STM resolution can be decoupling from the underlying substrate with a thin insulating film [51]. The achieved resolution of organic molecules adsorbed on the insulating film is then close to gas phase molecular orbitals which can be calculated by density functional theory (DFT) and thus allow the determination of the molecular species. Another approach to enhance the imaging resolution is functionalization of the STM tip by adsorption of a molecule at the tip apex [52–54]. However, the imaging resolution in this case strongly depends on the adsorption geometry of the molecule at the tip, which is not controlled and thus complicates the interpretation of the images [53].

Recently it has been shown that it is possible to directly image the chemical structure of organic molecules with a resolution similar to their drawing in textbooks. This is achieved after the condensation of molecular hydrogen (H_2) or deuterium (D_2) in the junction of a cold STM ($T < 10 \, \text{K}$) [55]. From the resolution in the images it is possible to directly determine molecular species. Images recorded in the so-called scanning tunnelling hydrogen microscopy (STHM) mode closely resemble the chemical structure formulae of different organic molecules on various substrates (cf. fig. 1.1). However, the mechanism which lies behind the contrast formation is not yet understood.

After the invention of the STHM, a similar resolution of organic molecules has been also

1 Introduction

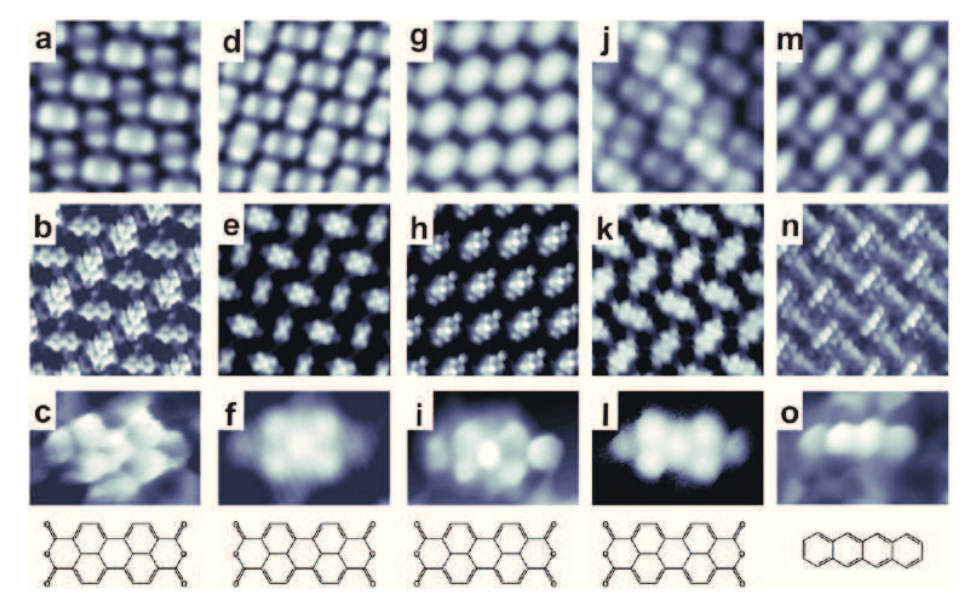


Figure 1.1: Comparison of images recorded in STM and STHM mode for different organic molecules adsorbed on different metallic substrates. The figure is reproduced from reference [55]

demonstrated in atomic force microscopy (AFM) [56–58]. In analogy to STHM, the AFM method allows the direct determination of molecular species from recorded images, but it is much more demanding with respect to the experimental setup.

The aim of this work is to get further insight into the fundamental properties of the STHM junction, e.g. its structure, internal degrees of freedom and the role of H_2 (D_2) in the imaging mechanism which leads to the contrast formation. On the one hand, understanding the contrast formation is indispensable for further applications. On the other hand, the mechanism which lies behind the contrast is of fundamental interest since it provides information about the interactions of H_2 (D_2) in the junction. To elucidate the contrast formation mechanism, we will therefore analyse the imaging capability and the spectroscopic properties of the STHM junction in detail.

2 Theoretical background and important progressions of the STM

In the past three decades after the invention of the scanning tunnelling microscope (STM) by Binnig and Rohrer in 1981 [32, 33, 35, 59] the technique has developed continuously. Today STM became a standard tool in the toolbox of many scientists. The great success of STM originates from its ability to image basically any conducting surface with atomic precision under various experimental conditions, e.g. in solutions [60–62], high pressure atmospheres [63–66] or ultra high vacuum (UHV) [67–69] in a wide temperature range, from high temperatures of several hundred Kelvin [64, 70] to cryogenic temperatures down to the milli-Kelvin regime [71–73]. Although the experimental setup and imaging techniques improved throughout the decades, the working principle which lies behind the operation of the STM did not change. In the following we will discuss the theoretical background behind the working principle and several approaches towards increasing of the resolution and the sensitivity of STM.

2.1 Scanning tunnelling microscopy

Before we turn to the theory behind the working mechanism of the STM, we approach the problem from a technical point of view and discuss what is necessary to construct an STM. An operational scheme of the STM with its essential elements is shown in figure 2.1. The basic setup of the STM consists of a conducting tip in front of a conducting sample. In most cases the tip is made from metal wire which is either cut or etched to obtain a preferably sharp tip. For the positioning of the tip in front of the sample a piezo scanner is used. Nowadays the scanner consists of a single segmented piezo tube to allow a space saving setup like it is illustrated in figure 2.1. The piezo scanner allows a translation of the tip perpendicular (z) and parallel (x, y) to the surface with sub Ångstrom precision by applying appropriate voltage to the segments of the piezo tube.

The tip and the sample are separated by a small gap of ≈ 1 nm so that classically no electrical contact exists between the two. However, the application of a bias voltage

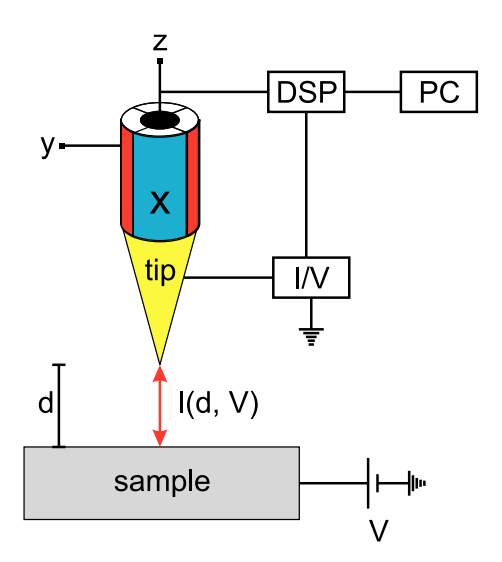


Figure 2.1: Scheme of the STM feedback loop. The scheme shows the essential essential elements of the STM feedback loop. Between tip and sample a bias voltage V is applied which results in a tunnelling current. The tunnelling current is converted into a voltage by the I/V-converter and feed into a DSP-box. The DSP-box compares the voltage with a setpoint voltage. According to the difference between the voltage and the setpoint $\Delta V = V_{tunnel} - V_{set}$ the DSP-box puts out a voltage to the z-piezo to keep the tunnelling current constant. The PC generates grey scale images from the $(x, y, z \propto \Delta V)$ -tuple.

V between tip and sample allows the flow of an electrical current I between the electrodes. The origin of the current is the quantum mechanical tunnelling effect which gives its name to the STM. The tunnelling effect is described in detail in the next section.

In STM experiments the tunnelling current is the measured signal. It is a function of V and the tip-sample separation d. To measure I(V,d) the current signal is converted into a voltage with an I/V converter. The output voltage of the converter is compared to a chosen setpoint by a digital signal processor (DSP-box). If the measured voltage differs from the chosen setpoint, the DSP-box puts a voltage on the z-piezo of the piezo scanner thus changes the tip height until the measured voltage equals the setpoint. By this feedback loop the tip-sample distance (z-direction) is always adjusted to keep the tunnelling current constant even when the tip is displaced laterally.

Applying an appropriate voltage to the (x, y) piezo tubes, the tip can be moved to every position above the sample in a certain area. Usually the tip moves along a line across the sample, is displaced by a step at the end of the line in a direction perpendicular to the line and then moves along a line parallel to the first one 2.2 (a). These operations are repeated until the tip has scanned a whole square while at each position the tip-sample distance is adjusted to the chosen setpoint of the tunnelling current so that at each position a voltage

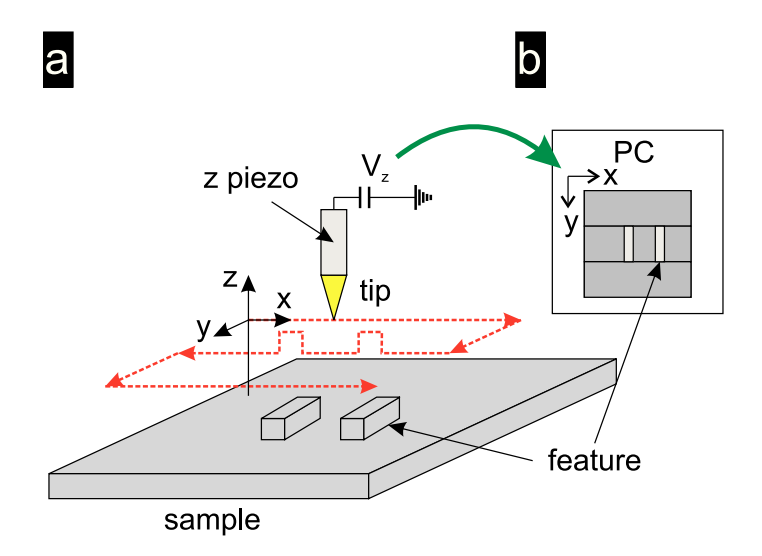


Figure 2.2: Illustration of the image acquiring in constant current mode a) The scanning of the tip above the sample in fast (x) and slow (y) scan direction is illustrated by the red dashed line. As the tip moves across protrusions on the sample surface the tip is retracted from the surface in order to keep the tunnelling current constant. b) Generated grey scale image of the sample surface in which areas with increased tip height appear bright compared to the rest of the surface.

is applied to the z-piezo which in general varies for different tip positions $(V_z(x, y, I_{set}))$. The information of the tip-sample distance encoded in $V_z(x, y, I_{set})$ is then transformed into a grey scale image with a computer connected to the DSP-box as illustrated in figure 2.2 (b).

The above described method of image acquiring is called constant current mode. Its advantage is the possibility to image basically any surface structure independent on it roughness, i.e. height difference between adjacent points of the image. However, the scanning speed of the tip is limited by the speed with which the feedback adjusts the tip height at different positions of the sample so that features in the image tend to smear out if the tip scans to fast across the surface. Another possibility of image acquiring which gets along without feedback is the constant height mode in which the tip scans the surface at a constant distance while the variation of the tunnelling current is measured. However, this imaging mode is limited to rather flat samples since otherwise the tip might crash during the measurement.

2.1.1 Tunnelling Effect

The tunnelling process, which describes the translation of particles across classical forbidden barriers, is the fundamental physical process lying behind the operation of the STM. In the following we will discuss the concept behind the tunnelling through a one dimensional potential barrier.

In classical mechanics the total energy E of a particle is given by the sum of kinetic energy T and its potential energy U

$$E = T + U = \frac{p_z^2}{2m} + U(z), \tag{2.1}$$

where m is the mass of the particle and p_z its momentum in z direction. The translational energy can have only positive values, therefore, according to equation 2.1 the particle can only translate, i.e. $p_z > 0$, in regions where E > U(z) while the particle cannot penetrate into regions where E < U(z).

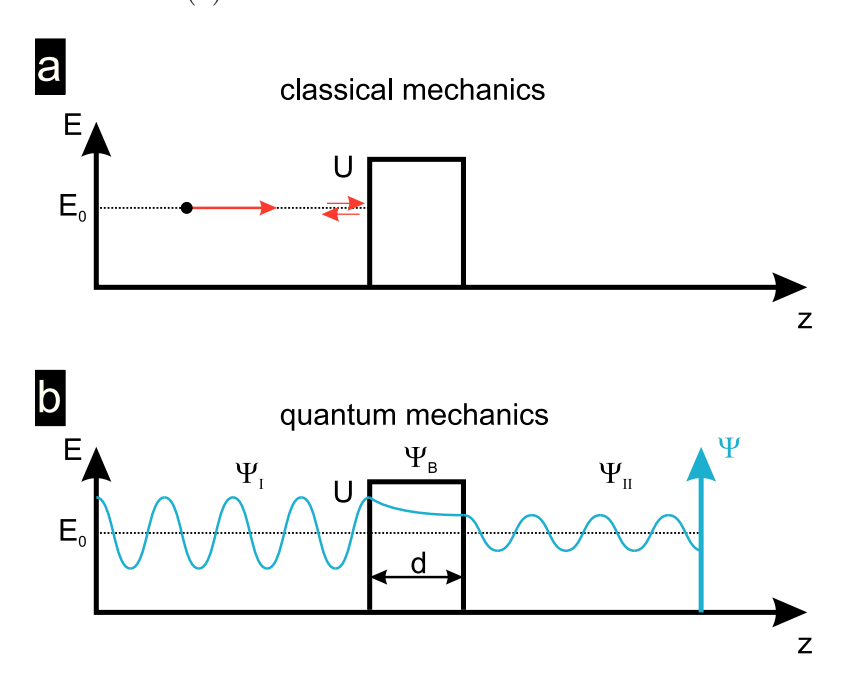


Figure 2.3: Illustration of the difference between the classical- and quantum mechanical description of a particle hitting a potential barrier. a) In classical mechanics a particle with energy E_0 cannot penetrate a barrier with energy $U > E_0$. b) In quantum mechanics a certain probability exists to observe the particle beyond the barrier. In a one dimensional picture the probability depends on the energy difference $U - E_0$ and the thickness of the barrier d.

The classical case is depicted in figure 2.3 (a) for a particle approaching from the left with energy $E_0 > U(z) = 0$. When the particle reaches the position where the potential is larger than the energy of the particle $(U(z) > E_0)$ it is reflected at the potential wall and moves back in negative z direction with the same energy E_0 .

In quantum mechanics the situation is different. In the quantum mechanical picture, a particle is described by a wave function Ψ . The wave function of the particle is given

as a solution of the one dimensional, time independent form of Schrödinger's equation

$$E\Psi = \left(-\frac{\hbar^2}{2m}\frac{\partial^2}{\partial z^2} + U(z)\right)\Psi. \tag{2.2}$$

In a constant potential (U(z)=U<E) a solution of equation 2.2 has the form of a planar wave

$$\Psi(z) = \Psi_0 e^{-i\kappa z},\tag{2.3}$$

where $\kappa = \sqrt{\frac{2m(E-U)}{\hbar^2}}$ and Ψ_0 a initial value of the wave function at position (z=0). In contrast to classical mechanics, Schrödinger's equation has a solution in the classical forbidden region (E < U) for positions of the particle inside the barrier. The penetration of the wave function into the potential barrier indicates that if the barrier is small enough the wave function extends into the space beyond the barrier. In the area beyond the barrier the solution of Schrödinger's equation can again be described by a planar wave like in the regime before the barrier. To obtain a combined solution of equation 2.2 in the whole space, one now has to connect the solutions in the different regimes by solving the connection conditions

$$\Psi_l(z_b) \equiv \Psi_r(z_b) \tag{2.4}$$

$$\frac{\partial \Psi_l}{\partial z}(z_b) \equiv \frac{\partial \Psi_r}{\partial z}(z_b) \tag{2.5}$$

where Ψ_l and Ψ_r are the solutions on the left and right side and z_b the position of the wall of the barrier at each position where two regimes meet each other.

A combined solution of the wave function of a particle with energy E_0 is shown in figure 2.3 (b). The particle is located at the left side of the barrier as indicated by the higher amplitude of $\Psi_{\rm I}$. Insight the barrier the amplitude of the wave function Ψ_B decays exponentially while it is still larger than zero at the other side of the barrier where it is connected to $\Psi_{\rm II}$. On the left side the amplitude of the wave function remains at the lower value compared to the amplitude on the left side of the barrier.

According to Born's probability interpretation of quantum mechanics [74], the wave function of the particle is interpreted as a probability amplitude while the probability P to find the particle at a certain position z_p is given by the absolute square of the wave function

$$P(z_p) = |\Psi(z_p)|^2. \tag{2.6}$$

Born's interpretation results in a certain probability to find the particle which initially is located on the left side of the barrier on the right side. The process of the translation of the particle from one side of the barrier to the other side through the classically forbidden

region is called tunnelling. Inserting 2.3 into 2.6, one obtains the probability of the tunnelling process as

$$|\Psi| = |\Psi_0|^2 e^{-2\kappa d} \tag{2.7}$$

where d is the barrier width.

The exponential decay of the tunnelling probability with increasing barrier width is the key mechanism behind the imaging capability of the STM since it results in a strong dependence of the tunnelling current on the distance between the tip and the sample. The dependence of the tunnelling current on the distance between the electrodes is the origin of the high vertical resolution of the STM. However, the tunnelling effect alone is not sufficient to understand the contrast formation in STM images. Thus we have to expand the picture of the tunnelling junction.

2.1.2 Electrode-vacuum-electrode contact

In STM, electrons tunnel from one electrode to the other. Thus we can model the STM junction by two separated electrodes. Inside the electrodes the electrons can propagate freely while they cannot leave the electrode material. The minimum energy which is necessary to remove electrons from a material is called work function Φ . The smallest energy at which the electron cannot be bound to the material any more is called vacuum energy E_{vac} . With this information we can draw an energy diagram of the one dimensional STM junction (fig. 2.4), where the tip and the sample are represented by the two electrodes separated by a vacuum barrier of width d.

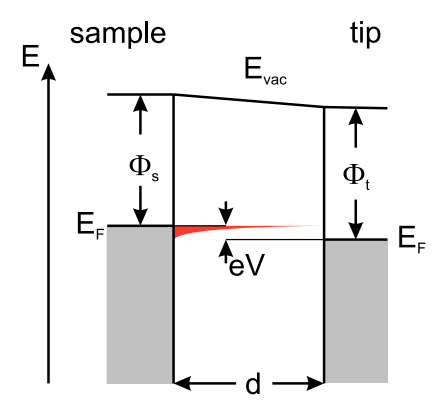


Figure 2.4: Simplified energy diagram of the tunnelling junction.

The energy diagram is shown in figure 2.4. The left electrode represents the sample while the right electrode represents the tip. The grey shaded areas at both electrodes indicate occupied electronic states. In solids the energy of the highest occupied electronic state is called the Fermi energy (E_F) . The difference between the vacuum energy and E_F , i.e. the minimal energy necessary to remove an electron from the bulk, is the work function Φ_s , Φ_t . Equation 2.7 indicated that the tunnelling probability depends on the width of the barrier and its height. Thus the electrons with the highest tunnelling probability are the ones with the highest energy, i.e. the ones at the Fermi energy. The tunnelling probability for these electrons is

$$|\Psi| = |\Psi_0|^2 e^{-2\kappa d} \tag{2.8}$$

where $\kappa = \sqrt{\frac{2m(E-\Phi)}{\hbar^2}}$ is the decay constant which depends on the electron mass m and $\Phi = \frac{\Phi_s + \Phi_t}{2}$ the mean value of the work functions.

So far the situation is not different from the one described in the previous section. Since the tunnelling probability for electrons close to the Fermi level is equal for tunnelling from the tip to the sample and the other way around, this will not lead to a net current between tip and sample.

In the description of the experimental setup we noted that a bias voltage is applied between the tip and the sample which leads to the flow of an electrical current. In the energy diagram the applied voltage leads to a shift of the Fermi levels in the tip and the sample with respect to each other by E = eV. In figure 2.4 the shift is indicated by a shift of the Fermi level of the sample towards higher energies. Now electrons from occupied states in the sample can tunnel into empty states at the tip (red area in fig. 2.4) which results in a net current from the sample to the tip.

The tunnelling current for an applied bias V and a distance d between the electrodes is then given by

$$I \propto \sum_{E_n = E_F - eV}^{E_F} |\Psi_n(0)|^2 e^{-2\kappa d}$$
 (2.9)

where n denotes all states in the energy window $E_F - eV < E < E_F$. If the applied bias is small and the density of electronic states is almost constant in this energy window, we can write 2.9 in terms of the density of states (DOS) of the sample. The DOS ρ_s at a given distance z and energy E is defined by

$$\rho_s(z, E) = \frac{1}{\epsilon} \sum_{E_n = E_F - \epsilon}^{E_F} |\Psi_n(z)|^2.$$
(2.10)

Thus the tunnelling current from equation 2.9 becomes

$$I \propto V \rho_s(0, E_F) e^{-2\kappa d}. \tag{2.11}$$

The simplified model indicates that the tunnelling current between the two electrodes depends on the DOS of the sample in a small energy window at the Fermi energy $(E = E_F)$ of the electrodes. In addition, the tunnelling current depends on the electrode separation d and the height of the tunnelling barrier. The height of the tunnelling barrier is encoded in the decay constant of the tunnelling current and depends on the work functions of the electrode material. For typical electrode materials, like e.g. metals, the work function is in the order of $\Phi \approx 5$ eV [36]. This value for the work function leads to a decay constant of $\kappa \approx 0.5$ Å⁻¹. Thus the tunnelling current changes by one order of magnitude when the distance between the electrodes varies by only 1 Å.

2.1.3 Theoretical approach

Although the energy diagram presented in figure 2.4 gives important insight in the occurrence of the tunnelling current and the dependence of the current on the electrode material, it does not explain the lateral variation of the tunnelling current which leads to the contrast in STM images. To get further insight in the contrast formation in STM we approach the problem from a theoretical side.

In the theoretical approach the transmission of an electron from the tip to the sample can be treated as a transition between quasi stationary states

$$\hat{H} = \hat{H}_{tip} + \hat{H}_{sample} + \hat{H}_t \tag{2.12}$$

where \hat{H}_{tip} , \hat{H}_{sample} are the Hamiltonians of tip and sample and \hat{H}_t denotes the transfer Hamiltonian. If the energy associated with \hat{H}_t is small compared to the energy of \hat{H}_{tip} and \hat{H}_{sample} , it can be treated as small perturbation to the undisturbed Hamiltonian $\hat{H}_0 = \hat{H}_{sample} + \hat{H}_{tip}$ with eigenstates ψ_{μ} in the tip and ψ_{ν} in the sample.

Now one can apply Fermi's golden rule to calculate the transition rate for an electron tunnelling from a state ψ_{μ} to a state ψ_{ν}

$$\Gamma = \frac{2\pi}{\hbar} \left| \left\langle \psi_{\nu} \left| \hat{H}_{t} \right| \psi_{\mu} \right\rangle \right|^{2} \rho(E) \tag{2.13}$$

where $\rho(E)$ is the density of final states. With the transition rate from Fermi's golden rule, the tunnelling current can be calculated by introducing an energy shift due to application of a bias voltage and taking the distribution of the density of states in tip and sample at finite temperature into account. Summing over all states Ψ_{ν} , Ψ_{μ} in the energy window eV, one obtains

$$I = \frac{2\pi e}{\hbar} \sum_{\nu,\mu} \{ f(E_{\nu}) \left[1 - f(E_{\mu} + eV) \right] - f(E_{\mu} + eV) \left[1 - f(E_{\nu}) \right] \}$$

$$\times \delta \left(E_{\nu} - E_{\mu} \right) \left| \left\langle \psi_{\nu} \left| \hat{H}_{t} \right| \psi_{\mu} \right\rangle \right|^{2}. \tag{2.14}$$

The finite temperature in equation 2.14 is represented by the Fermi distribution

$$f(E) = \frac{1}{1 - e^{-\frac{E}{k_B T}}} \tag{2.15}$$

which describes the occupation of the states in the electrodes. The first term in wavy brackets describes the tunnelling from occupied states in the tip to empty states in the sample while the second one describes the opposite situation. In addition, the introduced delta function ensures that the energy of tunnelling electrons is conserved during tunnelling. This conservation of the energy is usually referred to as elastic tunnelling.

According to equation 2.14, the tunnelling current through the junction is proportional to the transition rates from states in the sample to states in the tip. Therefore the transition matrix element can be written as a surface integral over the current operator

$$M = \left\langle \psi_{\nu} \left| \hat{H}_{t} \right| \psi_{\mu} \right\rangle = -\frac{\hbar}{2m} \int d\vec{S} \left(\psi_{\nu}^{*} \nabla \psi_{\mu} - \psi_{\mu}^{*} \nabla \psi_{\nu} \right)$$
[75]
$$. \tag{2.16}$$

The surface integral hereby has to be taken on a separating surface between the two electrodes to sum up all transitions which contribute to the total current.

2.1.4 Tersoff-Hamann-Theory

In 1983 Tersoff and Hamann presented a simplification of equation 2.14 which takes the geometry of the STM into account [76, 77]. In their approach the tip is treated as a single spherical potential well close to a flat sample surface (cf. fig. 2.5). The spherical geometry reminds on an s-orbital therefore Tersoff-Hamann-Theory is often called s-wave model. Additional assumptions to the experimental conditions are low temperatures and small bias. At small bias, the energy window of the tunnelling electrons is small and we

can expand the Fermi distribution

$$f(E_{\mu} + eV) = f(E_{\mu}) + eV \ f'(E_{\mu}). \tag{2.17}$$

In addition, in the low temperature limit, the Fermi distribution can be approximated by a step function while the first derivative becomes a δ -function. Inserting the assumptions into equation 2.14 one obtains

$$I = \frac{2\pi}{\hbar} e^2 V \sum_{\nu,\mu} |M_{\mu\nu}|^2 \delta(E_{\mu} - E_F) \delta(E_{\nu} - E_F).$$
 (2.18)

Now, to calculate the tunnelling current through the junction one still has to calculate the transmission matrix element $M_{\mu\nu}$.

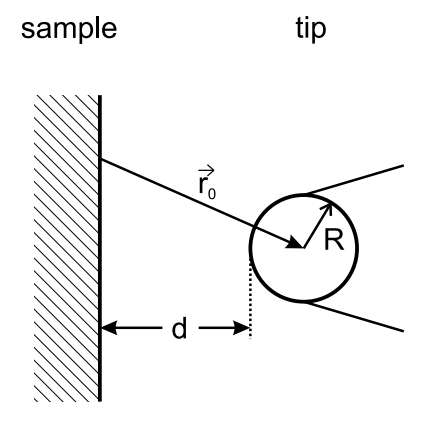


Figure 2.5: Tip-sample geometry in the Tersoff-Hamann approach. The tip is represented by a single s-orbital in front of the sample surface.

To evaluate $M_{\mu\nu}$ the surface wave function and the wave function of the tip are expanded. While for the surface wave function a periodical ansatz with the periodicity of the lattice constant is made, for the tip just the spherical shape of an s wave is used. Inserting the ansatz into equation 2.16 leads to

$$M_{\mu\nu} = \frac{\hbar^2}{2m} 4\pi \kappa^{-1} \Omega^{-1/2} \kappa R e^{\kappa R} \psi_{\nu}(\vec{r_0})$$
 (2.19)

where κ is the decay constant, $\vec{r_0}$ the center of curvature of the tip, R the radius of the sphere, Ω the volume of the probing tip and $\psi_{\nu}(\vec{r_0})$ a sample state at the position of the tip. Inserting now this result into 2.18 yields the famous Tersoff-Hamann-formula

$$I \propto \frac{2e^2}{h} V \rho_t (E_F) e^{2\kappa R} \sum_{\nu} |\psi_{\nu}(\vec{r_0})|^2 \delta(E_{\nu} - E_F)$$
 (2.20)

where $\frac{2e^2}{h} = (14.9 \text{ k}\Omega)^{-1}$ is the quantum of conductance.

For a flat density of states close to the Fermi level the sum in equation 2.20 can be substituted by the LDOS of the sample at the position of the tip

$$\rho_s(E_F, r_0) = \sum_{\nu} |\psi_{\nu}(\vec{r_0})|^2 \, \delta(E_{\nu} - E_F). \tag{2.21}$$

Thus we obtain

$$I \propto \frac{2e^2}{h} V \rho_t \left(E_F \right) \rho_s \left(E_F, r_0 \right) e^{2\kappa R}. \tag{2.22}$$

The Tersoff-Hamann approach has several advantages. First of all it allows an easy interpretation of the resolution in obtained images since for a flat DOS of the tip at the Fermi level the imaged contrast is directly proportional to the density of states of the sample at a certain distance. Therefore, the approach is often used to visualize results from theoretical calculations [53]. A second advantage is the proportionality of the tunnelling current to the applied bias, i.e. the Tersoff-Hamann formula directly reproduces Ohm's law on an atomic level. A third advantage is the fact that the tunnelling current also depends exponentially on the tip-sample distance if we assume that the DOS of the sample decays exponentially into the vacuum $(\psi_{\nu}(z) = \psi_{\nu}(0)e^{-\kappa z})$. In this case the sample DOS can be written as

$$\rho_s(E_F, r_0) = \rho_s(E_F)e^{-\kappa(d+R)} \tag{2.23}$$

where d is the closest distance between the surface and the tip. Inserting the sample DOS into equation 2.18 gives

$$I \propto \frac{2e^2}{h} V \rho_t (E_F) e^{2\kappa R} \rho_s(E_F) e^{-\kappa (d+R)}$$

$$= \frac{2e^2}{h} V \rho_t (E_F) \rho_s(E_F) e^{-\kappa d}. \qquad (2.24)$$

Equation 2.24 is the simplest form of the Tersoff-Hamann formula which shows the proportionality of the tunnelling current on the bias and its exponential decay with increasing tip-sample distance.

Although the formula derived by Tersoff-Hamann has several advantages and is therefore very popular, it also has limitations. For example, the restriction to the LDOS of the sample close to the Fermi level is not valid for weakly interacting adsorbates on the surface like for example some larger molecules. In this case, the discrete molecular electronic states prevail during the adsorption of the molecules on the surface and the LDOS of the sample will depend on the applied bias. To take this dependence into account one needs to generalize the Tersoff-Hamann formula and sum up all contributions from a finite bias

window

$$I \propto \frac{2e^2}{h} \int_{0}^{eV} dE \ \rho_t(-eV + E)\rho_s(E, \vec{r_0})e^{2\kappa_{\text{eff}}(E,V)R}$$
 (2.25)

where $\kappa_{\rm eff}(E,V)=\sqrt{\frac{2m\Phi_{\rm eff}(E,V)}{\hbar^2}}$ and $\Phi_{\rm eff}(E,V)=\frac{\Phi_t+\Phi_s+eV}{2}-E$ is the effective barrier height which depends on the energy of the tunnelling states and the applied bias. Inserting the relation for the sample DOS (eq. 2.23) and introducing the transmission function $T(E,V)=e^{-2\kappa d}$ we obtain

$$I \propto \frac{2e^2}{h} \int_{0}^{eV} dE \rho_t(-eV + E)\rho_s(E)T(E, V). \tag{2.26}$$

Now we can calculate the first derivative of the tunnelling current

$$\frac{dI}{dV}(V) \propto \frac{2e^2}{h} \left(\rho_t(0)\rho_s(eV)T(eV,V) + \int_0^{eV} dE\rho_t(-eV+E)\rho_s(E)\frac{dT(E,V)}{dV} \right). \tag{2.27}$$

According to equation 2.27 the derivative of the tunnelling current is directly proportional to the LDOS of the sample superimposed with a non-liner background originating from the second term. This result has been presented in reference [78] and forms the basis for scanning tunnelling spectroscopy (STS).

Another disadvantage of the Tersoff-Hamann approach is the restriction to spherical shape of the tip apex. The frontier orbitals of typical tip materials like tungsten or platinum and iridium are not s-shaped, thus the assumption of the Tersoff-Hamann formula is not valid for typical experimental images. A solution for this problem has been presented by Chen [36]. Chen introduced a derivative rule to take other than s-shaped orbitals into account and used p_z and d_{z^2} orbitals for his calculations. These orbitals are higher localised than the spherical s-wave and therefore should allow even atomic resolution of metal surface. Recently the validity of the derivative rule has been shown by comparing experimental and theoretical images of molecular orbitals [79]. The images were recorded with a mixture of s and p_z tip and then compared with theoretical obtained images. The authors thereby obtained that the contribution of the p_z orbital was as large as the contribution of the s orbital for their CO-terminated tip. This results emphasises the importance of the tip termination on the contrast formation in STM.

So far we can say that the contrast in STM images depends on the electronic structure of the tip and the sample close to the Fermi level due to the limitation of $V < \Phi_{\text{eff}}$. Although

the resolution in obtained images can be expected to be large (< 1 nm [36]) due to the exponential dependence of the tunnelling current on the tip-sample separation, the limitation to states close to the Fermi level is crucial for the applicability of the STM, because on the one hand it is limited to conducting or semi-conducting samples with a low band gap, on the other hand especially in complex systems, the electronic structure can be quite different from the underlying atomic structure. Thus from STM images alone it may be difficult to draw conclusions of the "real" structure of the surface. Therefore several approaches have been made to overcome the limitations of STM.

2.2 Dynamic force microscopy

One of the most important developments based on the STM is the atomic force microscope (AFM). A striking ability of AFM is the imaging of non-conducting surfaces in contrast to STM. The idea behind the AFM is the measurement of the force or a force related quantity between tip and surface.

In the first design, presented in 1986, a tip was mounted on a flexible cantilever beam [80]. In this geometry, the force acting on the tip results in a deflection of the cantilever. The deflection of the cantilever at different positions of the sample is then measured with an STM mounted on the backside of the cantilever. This technique is demanding since it depends on the precise positioning of two tips on top of each which requires quite a bit of technical effort.

In recent years several improvements have been presented to improve the design of the AFM. On the one hand to improve the handiness of the microscope and on the other hand to improve its resolution.

2.2.1 AFM operation modes

The key element of the AFM is a flexible beam. In many designs, presented up to now, the flexible element is a cantilever beam which is mounted on one side to the body of the microscope while the other end of the cantilever, at which a probing tip is mounted, can move freely. The deflection of the cantilever is measured by optical or electrical methods like interferometry, beam deflection, resistivity or capacitance [81].

Today most AFM's which are commercially available, operate in the so called contact mode where the tip is in direct contact with the investigated sample. By keeping the force on the tip, i.e. the deflection of the cantilever, constant, it is possible to obtain images of the surface structure. Whereas in STM atomic resolution is easily achievable and has been presented quickly after its invention [34], the contact AFM is often considered not to obtain atomic resolution due to the large contact area of the tip [82]. This large contact area leads to images of periodic structures whereas defects in the structures will be averaged out.

The area in which the tip interacts with the surface, compared to the contact mode, is reduced when the tip oscillates in front of the surface while only a comparable slight contact is established during the oscillation cycle. The intermediate contact - or "tapping mode" TM increases the resolution of the AFM and even allows the imaging of more fragile structures like e.g. organic layers. Therefore the tapping mode is often used for roughness analysis of grown films. On the contrary the achieved resolution is still not high enough to allow the imaging of defects in atomically flat surfaces.

Like in the case of the STM the best resolution in AFM should be achieved if only a small part of the tip interacts with the surface. Thus one could imagine a scanning of the surface without contact like in STM and measuring the deflection of the cantilever. However, due to the small spring constant, which is in the order of 10 - 100 N/m for typical cantilevers, the tip-sample force often exceeds the restoring force of the spring. The larger force often causes jumps into contact of the tip towards the surface which prohibits stable imaging.

A solution to overcome the jump-to-contact problem is the excitation of the cantilever in front of the surface. The geometry of the cantilever allows an excitation to a stable oscillation. In this case due to the deflection of the cantilever in the lower turning point of the oscillation cycle the restoring force can be kept always larger than the tip-sample force. On the contrary, it is not possible to measure the tip-sample force directly any more thus another quantity like the amplitude or the frequency of the oscillation has to be used to measure the tip-sample force indirectly.

2.2.2 FM-AFM

In frequency-modulated AFM (FM-AFM) the tip oscillates with a fixed amplitude above the surface while the frequency of cantilever oscillation is used to generate an image of the surface contour [83]. The origin of the frequency change is the tip-sample force which should by definition be smaller than the restoring force of the cantilever. In the following we will elucidate the dependence of the oscillation frequency on the tip-sample force. The motion of the cantilever can be described as a weakly perturbed harmonic oscillator with mass m and spring constant k. The equation of motion for a damped, driven oscillator is then given by

$$m\frac{d^2q}{dt^2} - \gamma \frac{dq}{dt} - kq = F_{ts}(q) + F_0 e^{i\phi t}$$
(2.28)

where q is the deflection of the cantilever out of the equilibrium position, F_{ts} the tip-sample force and F_0 the external driving force. The driving force is chosen such that it excites the cantilever to compensate the internal damping and a harmonic oscillation takes place. With this assumption the equation of motion reduces to

$$m\frac{d^2q}{dt^2} - kq = F_{ts}(q). (2.29)$$

Solving this equation and assuming that the oscillation frequency of the cantilever in the force field of the surface is close to the oscillation frequency of the free cantilever, one obtains

$$\Delta f = -\frac{f_0}{kA^2} \langle F_{ts} q \rangle \tag{2.30}$$

where $\Delta f = f - f_0$ is the frequency shift of the oscillation frequency compared to the resonance frequency $f_0 = \frac{1}{2\pi} \sqrt{\frac{k}{m}}$ of the free cantilever, A the oscillation amplitude and $\langle \rangle$ denotes a time average over one oscillation cycle [84].

Equation 2.30 allows the calculation of the frequency shift for any given force field. However, usually the situation is the other way around and one wants to recover the tipsample force from the measured Δf signal since the tip-sample force contains physical information about the sample. Due to the time average, equation 2.30 cannot be inverted analytically and a closed solution for $F_{ts}(\Delta f)$ cannot be derived. This means that only under certain circumstances and assumptions the tip-sample force can be recovered.

One way to recover the tip-sample force is an integration of the Δf along the tip-sample distance. If the tip-sample force varies slowly on the oscillation path of the tip $(-\frac{\partial F_{ts}}{\partial z} = k_{ts} = const.)$ and Δf is small one obtains the trivial relation

$$\frac{\Delta f}{f_0} = \frac{k_{ts}}{2k}.\tag{2.31}$$

The frequency shift in equation 2.31 is directly proportional to the stiffness of the junction which represents the changed spring constant of the cantilever due to the presence of the force field in front of the sample. According to the picture of a spring with changed

stiffness the tip-sample force becomes

$$F_{ts}(z) = 2 \int_{z}^{\infty} d\tilde{z} \, \frac{k}{f_0} \, \Delta f(\tilde{z}). \tag{2.32}$$

The integration from infinity to the tip-sample distance z at which the force should be recovered in equation 2.32 shows that even in the simplest approximation a determination of the force from the frequency shift is only possible if the evolution of the frequency shift is known for a large distance range between tip and sample. For practical cases it is often enough to measure the frequency shift up to several nanometer away form the surface due to the limited interaction range of the relevant forces [85].

Although equation 2.32 allows the reconstruction of the tip-sample force from the measured frequency shift, it only represents a zero amplitude limit for the force reconstruction. However, the amplitudes used with low stiffness cantilevers are often in the order of several nanometer to avoid the jump into contact. During the oscillation cycle the force substantially changes thus equation 2.32 can only give a rough estimate of the actual force.

A more accurate formula to recover the force from the measured frequency shift which takes the finite amplitude into account has been derived in reference [86]. The obtained equation

$$F_{ts}(z) = 2k \int_{z}^{\infty} d\tilde{z} \left[\left(1 + \frac{A^{1/2}}{8\sqrt{\pi(\tilde{z} - z)}} \right) \Omega(\tilde{z}) - \frac{A^{3/2}}{\sqrt{2(\tilde{z} - z)}} \frac{d\Omega(\tilde{z})}{d\tilde{z}} \right]$$
(2.33)

where $\Omega = \frac{\Delta f}{f_0}$, allows a determination of the force with an accuracy of 5 %.

Regardless of the accuracy with which the force can be determined, the resolution of the Δf measurement is always limited by the large amplitudes. If the amplitude is large compared to the interaction range of the relevant forces, the resulting frequency shift will always be a superposition of the contribution of local forces with non-local forces like e.g. electrostatic forces. Thus, relevant forces which are e.g. responsible for the lateral resolution in AFM images are always measured on an unstructured background. To increase the resolution of the AFM, it is therefore desirable to reduce the oscillation amplitude. A reduction of the amplitude can be realized for example by the use of stiffer cantilevers ($k \gg 10$ nN) to avoid the jump into contact in the lower turning point of the oscillation cycle.

2.2.3 qPlus AFM

The qPlus design of an AFM sensor allows oscillation amplitudes in the sub-Ångstrom regime. This goal is reached by application of commercially available quartz tuning forks as cantilevers [87, 88]. In swiss watches these tuning forks are used as clock due to their frequency stability.

To use a tuning fork as a cantilever in AFM a tip is glued to one prong of the tuning fork while the other one is rigidly fixed to the body of the microscope. The tuning forks have several advantages compared to conventional cantilevers. The stiffness of the fork is much higher $k_{quartz} \approx 1.8 \text{ kN/m}$ than for silicon cantilevers. The tuning fork is self sensing, this means that no external application (e.g. a laser beam) is necessary to measure the deflection of the cantilever. Instead, the deflection of the cantilever is proportional to the voltage between the prongs which is induced when the free side of the tuning fork moves. This feature is especially interesting for low temperature application since it allows a compact design of the AFM. Another advantage of the qPlus design is the possibility to electrically contact the tip and simultaneously record Δf and the tunnelling current through the tip. Besides the simultaneous acquisition of STM and AFM images this allows the determination of the oscillation amplitude by comparing the tunnelling current at different excitations [89].

The described features of the qPlus design illustrate that it combines all advantages of STM and AFM in only one microscope. However it still has the limitations of both techniques concerning the achievable resolution which is in the case of the STM limited by the sensitivity to electronic states and in the case of the AFM limited due to the sensitivity to long range forces.

2.3 Advancements based on STM/AFM

STM and AFM are very successful methods for imaging surface structures of conducting and non-conducting samples with a high lateral resolution. However, the achieved contrast in STM and AFM images is usually far away from resolving atomic structures of the sample surface. Thus the limited resolution prohibits a direct identification of atomic and molecular species from obtained images. Although, atomic resolution in STM and AFM images has been presented, the examples are limited to rather simple systems, e.g. single crystal surfaces [34, 35, 37, 38, 40, 41, 67, 78, 88, 90–97].

The origin of the limited resolution in STM and AFM experiments is the low lateral variation of the measured signal used to generate the images. These signals are the tunnelling current for the STM and the total tip-sample force in the case of AFM. In AFM the total force is a superposition of short range (e.g. chemical forces) and long range (e.g. electrostatic, van der Waals) forces [80, 82, 84, 86, 88, 93, 96, 98–100]. In AFM images, the short range contributions determine the lateral resolution while the long range forces show little variation at different positions above the sample, thus lead to an unstructured background on-top of which the contrast appears. In contrast to AFM, STM senses the electronic structure of the surface.

The electronic states mapped by STM are energetically located close to the Fermi level (cf. equation 2.24). These states are often de-localized in atomic compounds, e.g. molecules [53, 101–108]. The de-localization leads to smearing out of the states across the whole compound, thus complicates the determination of the compound structure and composition from obtained STM images. Up to now, identification is only possible in rather simple systems, e.g for weakly interacting molecular layers adsorbed on a flat single crystal surface [44, 60, 79, 101, 104, 106, 109–129].

Above analysis shows that from a principle point of view the contrast in neither AFM nor STM images allows a doubtless determination of the atomic composition of the surface. To overcome this problem and try to increase the sensitivity of the methods, one can follow two strategies. The imaginable strategies are: increasing of the image contrast to allow a direct determination of atomic species from obtained images and expanding the sensitivity to one or more of the measurement parameters to allow the determination from a spectroscopic characterisation.

2.3.1 Improving the image contrast

The contrast in AFM and STM images depends on the structure and the shape of the tip as well as on the atomic structure of the investigated surface. Due to the correlation between the contrast and the structure of the electrodes, one may try to either change the tip structure in a controlled way or manipulate the structure of the sample to enhance the resolution in obtained images. Up to now it has been shown that both approaches can be realized and lead to promising results. However, the presented realizations also have limitations. In the following we discuss the realizations and their limitations on a few examples. Hereby, we start with the modification of the tip.

The tip is a promising candidate for the contrast enhancement by the choice of an appropriate orbital [36, 92, 95, 104, 121, 130] at the tip apex. Such functionalization

of the tip can be realized e.g. by the adsorption of a molecule at the tip apex [52–54, 56, 104, 111, 131]. In the presented cases, a submolecular contrast of molecular films is achieved by scanning the molecular layer with the frontier orbitals of the molecule at the tip apex. The submolecular resolution allows the determination of molecular species in the film. Nevertheless, the image contrast depends on the electronic structure of molecule adsorbed at the tip, its adsorption geometry and the tip-sample distance. Thus, even in a simple system of molecule at the tip and molecular layer, a whole bunch of different possible contrasts exists which complicates the determination of the surface structure from the contrast in obtained images.

Besides functionalization of the tip it is possible to manipulate the surface structure to enhance the contrast in obtained images. The surface structure for example can be manipulated by decoupling the top most layer from the sample bulk. The decoupling can be realized e.g. by a thin insulating film between the first and the second atomic layer. The decoupling reduces the interaction of the separated layers so that the electronic structure of the first layer is only determined by its atomic configuration. The resulting two dimensional electronic levels can be mapped with STM and than compared to images generated with theoretical methods to determine the atomic configuration of the layer. The working principle of this approach has been demonstrated with large organic molecules adsorbed on a thin insulating film grown on metal surface [51, 56, 58, 79, 132, 133]. The contrast of the molecules in STM images closely resembled the electronic levels obtained from gas phase DFT calculations which left no doubt on the species of the molecule. Although the approach in principle allows the determination of the atomic structure by comparing images and calculations, it only works for atomic films which can be grown subsequent to the insulating film, thus the technique cannot be used in bulk materials.

Another possibility to enhance the contrast in STM images which is not so directly related to changes of the structure of the electrodes is the pulling or pushing of adsorbates across the surface [68, 91, 134–140]. This technique uses the attractive or repulsive interaction between adsorbates and the tip. The adsorbates hereby hops from one adsorption site to the next if the tip-adsorbate distance reaches a certain value during scanning. If the tunnelling current flows through the adsorbate, the hopping actions appear as jumps in an STM image. At the position of the jumps, the current changes from high to low value in the case of pushing or from low to high current if the tip pulls the adsorbate across the surface. Thus, the structure in the image reveals the positions of favoured adsorption sides of the adsorbate in question. If now the moving adsorbate on the surface is as small as a single atom, the image contrast can resemble the atomic structure of the underlying surface [91, 138]. This technique clearly increases the image resolution and even allows

a chemical identification by comparing the binding to different adsorption sites which result in different jumping positions [140]. On the contrary, the moving of adsorbates across the surface can only be realized on rather rigid samples to prevent incorporation of the adsorbate in the investigated sample which occurs e.g. for adatoms in molecular films [101, 141].

2.3.2 Spectroscopy and secondary signals

After presentation of several approaches towards increasing of the image resolution, we now focus on a spectroscopic characterization and contrast enhancements which are not directly accessible, thus require additional technical effort. STM and AFM images represent lateral maps of the tunnelling current I, the frequency shift df at fixed tip-sample distance z_0 or maps of the tip-sample z distance at constant feedback setpoint I_0 and df_0 while in all cases the bias V_0 between the tip and the sample is kept constant. In contrast, in a spectroscopic analysis one varies either the bias V or the tip sample distance z and investigates the effect of the variation on I and df at fixed lateral tip position. The variation of both values lead to important insights in the sample properties and have been used for the further development of the AFM and STM technique. We start the presentation of several spectroscopy related techniques with methods in which the tip-sample distance z is varied.

In STM, the tunnelling current depends on the tip-sample distance. According to the Tersoff-Hamann formalism, the exponential decay in the distance dependence is proportional to the square root of the work function of the surface (cf. equation 2.18). Although, in local molecular orbitals a distance dependence in the obtained contrast in STM images [53, 78, 142] is observed, a systematic investigation of the apparent barrier height, which is associated with the local work function, did not lead to standard procedure in surface characterization yet. However, few promising approaches have been presented [143, 144]. The situation is very different in the case of AFM.

In AFM, the interaction of the tip with the underlying surface is probed. The interaction between the two strongly depends on the species of the interacting atoms [80, 88, 145]. This dependence can be used for a spectroscopic analysis [56, 96, 99, 146]. The results of such analysis allows the direct identification of atomic and molecular species from obtained spectra [56, 79, 96, 146–150]. However, to be sensitive to atomic structures of the sample, one has to get rid of long range contributions to the measured force signal which requires a lot of technical effort. In addition, the best resolution is usually achieved with a rather small tip-sample separation at which chemical reactions may occur between the

tip and the sample, so that the analysis can only be performed if both are chemically inert [56]. In contrast to variations of the tip-sample distance, the variation of the applied bias is much more versatile and has led to developments of various experimental techniques.

The versatility of the bias variation may be explained by the fact that in STM as well as in AFM the bias dependence can by directly interpreted and assigned to a physical property of the sample. The dependence of the bias variation on the measured signal in noncontact AFM is used to extract the so called contact potential difference in Kelvin-Probe experiments [93, 151, 152] while the bias dependence of the tunnelling current or more specific the differential conductance dI/dV is directly proportional to the local density of states of the sample (LDOS) (cf. equation 2.27). The LDOS depends on the local structure of the surface thus allows the determination of the surface structure from obtained spectra [38, 49, 78, 113, 118, 120, 125, 127, 132, 153–155]. However, the identification only works if the sample has discrete states close to the Fermi level in the range accessible with STM. Besides the direct interpretation of the measured signals it is also possible to investigate quantities which are related to the signal.

The structure of the sample can be characterised by the spectrum of its vibrational degrees of freedom. Vibrational states of the sample can be probed by inelastic tunnelling electrons spectroscopy (IETS) [42, 45, 46]. In the obtained d^2I/dV^2 spectra the vibrational states show up as spikes or dips. Although a submolecular lateral resolution in the obtained vibrational spectra is achievable [45], the excited states can in general be active in all three dimensions. Therefore, reconstruction of the surface structure only from IETS results can be quite demanding since in the excited vibrational modes several atoms may be involved while in addition the vibrational mode may depend on the orientation of the excited compound within the surface. Another possibility to directly investigate vibrational modes in surface structure is the excitation with the tip of an AFM.

In frequency modulated AFM (FM-AFM) the frequency shift df of the cantilever is used as measurement signal for a feedback loop. Therefore the cantilever with the AFM tip oscillates in front of the surface while the amplitude of the oscillation is kept constant. The energy conserved in the oscillation is given by

$$E = \frac{1}{2}k_{ts}A^2, (2.34)$$

where k_{ts} is the stiffness of the cantilever and A the oscillation amplitude. During the oscillation the amplitude of the oscillation reduces due to an internal damping of the can-

tilever, thus the cantilever oscillation needs to be constantly excited to keep the amplitude constant [82, 83, 88, 156, 157]. If now the motion of the cantilever couples to vibrational or electronic degrees of freedom of the surface, this would lead to an additional damping of the cantilever [158–161] and therefore to an increase of the excitation E_{ex} . This technique can be used to map the damping of the cantilever above different positions of the sample, thus producing a contrast related to the vibrational spectrum and non-conservative adhesion forces [162] above the sample. The measured damping signal would depend on the structure of the investigated surface, the applied bias and the tip-sample distance. Up to now, it has been demonstrated that the damping signal allows the identification of large organic molecules [163, 164]. However, the resolution in the images strongly depends on the shape of the tip and on the internal damping of the cantilever which results in a large background on top of which the damping signal from the tip-sample interaction has to be measured.

Finally, we note a family of approaches which may indirectly lead to a chemical sensitivity in AFM and STM experiments. These approaches address lower lying or electroluminescent active electronic states in the sample surface but require additional technical effort. On the one hand, it is possible to excite lower lying electronic states with laser light from an external source and probe the excited states with STM [43, 47, 48]. On the other hand, it is possible to excite states in the sample which emit light during relaxation. The emitted light can then be detected by e.g. an external photomultiplier tube [44, 49, 50]. Both techniques can be used for the chemical identification of molecules at the surface, however, they both require discrete electronic states in the sample which limits their applicability.

Although all presented approaches in principle equip STM and AFM with chemical sensitivity down to the atomic scale, they all have their special limitations. In many cases, the limitations originate from the probed surface property directly, thus the techniques cannot be improved by further technical development. Therefore we look for a new method which differs from the ones presented before. A promising candidate is scanning tunnelling hydrogen microscopy (STHM) [55]. The contrast of organic molecule imaged in STHM is close to their chemical structure, thus it allows a chemical identification, whereas the STHM approach systematically differs from all other methods, since here a gas atmosphere is created which leads to an increased resolution in obtained images. A comparable resolution is only achieved in the combined AFM-tip functionalization approach presented in reference [56–58, 148]. Although the resolutions in both cases are comparable, the technical effort to drive the AFM approach to its limits is much larger compared to STHM. The less effort to achieve a similar resolution and the systematic difference of the STHM approach with respect to all other techniques presented in this

section suggest that it is worth to further investigate STHM, as we demonstrate in the following.

3 Preparation of STHM experiments

In order to get further insight into the properties of the STHM imaging mode we need a test system for our investigations. This test system has to fulfil several prerequisites which will be discussed in the following.

The STHM method was discovered by imaging of organic molecules on various metallic substrates (cf. fig. 1.1). Therefore it seems to be natural to choose one of these systems, since this allows the direct characterisation of the contrast by comparing the resolution of the molecule in STHM images with its chemical structure. The molecule which is chosen has to fulfil several additional requirements which originate from the scanning process in STHM mode.

The best resolution in STHM images is obtained when scanning in constant height mode, with a small tip-sample separation (z < 1 nm) and at low bias (|V| < 10 mV). This means that the molecule should be rather flat, adsorb planar on the metal substrate to avoid a large surface corrugation, be stably bound so that it cannot be moved by the tip, and in the best case it should have a flat DOS at the Fermi level to avoid an influence of the electronic characteristics of the particular molecule on the STHM contrast. All these conditions can be fulfilled, for example, by large aromatic molecules which in many cases adsorb flat on metals [102, 110, 112, 119, 124, 125, 128, 129, 165], self organize into long range ordered films [102, 110, 112, 119, 165] and physisorb on noble metal substrates [18, 46, 102, 128]. Many of these molecules in addition tend to form islands when deposited in the submonolayer regime, whereas large areas of the surface remain uncovered. For our test system this is a desired behaviour, since the bare substrate can be used to reproducibly prepare clean metallic tips.

A combination of aromatic molecule and metal surface which fulfils all of the above requirements is 3,4,9,10 perylene-tetracarboxylic-dianhydride (PTCDA) on Au (111), since PTCDA physisorbs in a planar geometry on Au(111) [114, 166] and forms large ordered islands at submonolayer coverage [114, 154].

3.1 Preparation of organic layers

The Au(111) single crystal surface is cleaned by repeated sputtering and annealing cycles. First adsorbates are removed by sputtering the surface with 0.8 kV Ar⁺ ions. Then the sample is annealed to ≈ 420 °C for 15 min in order to cure defects from ion bombardment. This procedure results in adsorbate free large terraces (width > 100 nm) separated by monoatomic steps. Subsequent to the annealing step, the crystal is kept at ≈ 180 °C for 1 h. The subsequent heating of the crystal supports the relaxation of the sample surface, thus results in the well known $22 \times \sqrt{3}$ herringbone reconstruction of Au(111) [167]. Usually after two or three preparation cycles PTCDA is deposited on the Au substrate.

PTCDA is deposited on the cleaned surface from a homebuilt Knudsen cell. The material is kept close to the evaporation temperature of $T_{dep}=300\,^{\circ}\mathrm{C}$ for 12 h to remove possible contaminants, before deposition. After the cleaning procedure PTCDA is evaporated with a flux of $\approx 0.1\,\mathrm{ML/min}$ for 30 s while the sample is kept at room temperature during deposition. Subsequently, the organic layer is heated to 100 °C for 2 min before putting the sample into the cold STM ($T<10\,\mathrm{K}$). The heating increases the mobility of PTCDA on the surface, thus supports the formation of large islands. In the literature different phases of PTCDA/Au(111) are reported [168]. The most prominent one, resulting from the preparation method described above, is the so called herringbone phase [168, 169].

3.2 Preparation of the tip

The PTCDA islands in the herringbone phase are used to control the tip quality by looking at the resolution of the molecular layer in conventional STM images. The quality of the tip is important since, according to our experience, only a tip which shows good resolution in STM mode is capable to show good resolution in STHM mode. In this context, "good" resolution in STM mode means resolving single, featureless molecules in the layer while no additional features like asymmetry, doubling of the contrast or abrupt jumps in the tunnelling current appear in the images. An example for "good" resolution in conventional constant current STM images is shown in figure 3.1 (a). The PTCDA molecules appear as oval homogeneously bright protrusions on a dark background.

To reproducibly achieve this kind of resolution we prepare the tip by controlled indentation into the clean, i.e. uncovered, metal substrate. To this purpose the tip is approached to the Au surface by 8-15 Å from its stabilization point above the surface. This distance is only slightly larger than the expected tip-sample separation under tunnelling conditions (e.g. I=0.1 nA, V=-340 mV), ensuring that only the very apex contacts the substrate during the preparation cycle. After the contact has been established, a cluster of Au atoms can remain at the tip apex when it is retracted [137]. In the best case, a single atom sticks out of the attached cluster after retraction. The major part of the tunnelling current will go through the outermost atom of the tip, resulting in a sharp contrast of the organic layer in STM images.

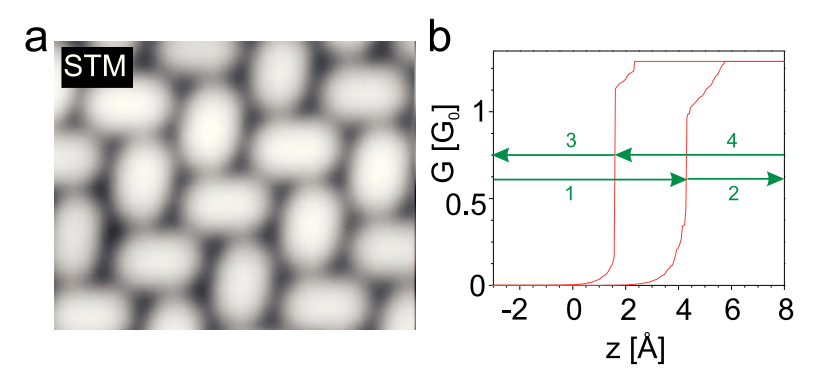


Figure 3.1: Tip preparation above a clean Au(111) surface to adsorb substrate material at the tip apex. Therefore direct contact between tip and sample surface is established. After each preparation the quality of the tip is checked by scanning a PTCDA island. a) Molecular resolution of PTCDA/Au(111) with a clean metal tip after successful tip preparation. b) Evolution of the junctions conductance during the preparation procedure. The tip approaches the surface until contact is established at z=4.3 Å. During retraction the contact is broken at z=1.6 Å. The later breaking of the contact indicates an elongation of the tip most properly due to adsorbed substrate material. The tip movement direction in the four parts of the preparation cycle are indicated with arrows and numbers. $G_0 = \frac{2e^2}{h}$ is the quantum of conductance. Image parameters: 50×40 Å², const. height, V = -5 mV

During the preparation procedure the conductance of the junction is monitored, which gives first hints about the quality of the prepared tip. The establishment and the breaking of the contact appear as sudden jumps in the conductance at a specific tip-sample separation. The distances at which the jumps occur mark the transitions between tunnelling and direct current regime.

An example of the conductance evolution during the preparation procedure is shown in figure 3.1 (b). The conductance evolution shows an approach and retraction cycle where the tip approaches by 8 Å from the stabilization point above the surface (zero on the z-axis). The tip-sample contact is established at z = 4.3 Å while it breaks at z = 1.6 Å.

3 Preparation of STHM experiments

The elongation of the tip by ≈ 2.7 Å indicates that a cluster of atoms has been picked up from the substrate.

Although the length of the tip is increased after the indentation into the metal, the size and shape of the cluster cannot be deduced from the conductance evolution. Controlling the shape of the cluster would help to reproducibly establish experimental conditions. But when the tip is brought into close vicinity of the surface one can expect deformations of the junction [170]. The deformations will influence the tip-sample distance and therefore the conductance of the junction. The origin of the deformations are tip-sample interactions whose strength drastically increases with decreasing separation. In addition the strength of the interaction depends on the shape of the tip apex which is unknown.

The conductance trace in figure 3.1 (b) can be divided into four parts [69]. In the first part, the conductance of the junction exponentially increases with decreasing tip-sample separation as expected in the tunnelling regime. At the position of the jump the conductance suddenly increases, indicating the establishment of the contact. In part two, the conductance of the junction is close to or larger than the quantum of conductance while the tip still approaches the surface. In this regime, the conductance of the junction further increases with decreasing tip-sample separation while additional steps in the conductance trace indicate the establishment of additional conductance channels between tip and sample. In the third part of the preparation cycle, the tip retracts from the surface while the tip-sample contact first remains unbroken. During the retraction again several steps in the conductance may occur before the contact finally breaks. At the final jump, the conductance value drops into the tunnelling regime ($G \ll G_0$) in part four of the preparation cycle.

The breaking and the further retraction of the tip in part four is often accomplished by the appearance of additional jumps or steps in the conductance trace. The non-exponential conductance behaviour after re-entry in the tunnelling regime indicates structural relaxation of the junction. According to our experience, tips which are not stable after braking of the contact are usually not good for imaging in STHM mode. Such tips often break or show instabilities under STHM imaging conditions. Thus, the relaxations in the junction conductance during tip preparation indicates an undesired tip shape. But disregarding the origin of the behaviour, in most cases after 5 to 10 additional preparation cycles a tip can be prepared which reveals a stable and continuous conductance behaviour.

3.3 Adsorption of hydrogen

Once a tip is prepared which shows "good" resolution of PTCDA molecules in STM mode, we can continue the preparation for STHM imaging. The STHM imaging contrast is only observed after condensation of H_2 or D_2 on the sample surface. This indicates that H_2 (D_2) is necessary for operation in STHM mode. However, according to our experience the situation seems to be more complicated, because the achieved resolution in STHM images depends on the coverage of H_2 (D_2) on the substrate. If the coverage is to small, stable imaging in STHM mode is not possible, while at too large coverages the contrast changes, i.e. a resolution comparable to the one presented in figure 1.1 is not achievable. The best resolution of organic layers in STHM images is achieved at an intermediate coverage after stable imaging became possible but before the contrast changes. Therefore, we have to control the coverage of H_2 (D_2) on the substrate to prepare reproducible experimental conditions.

In conventional STM images H_2 (D_2) is usually invisible, therefore the coverage cannot be directly deduced from obtained images. But, as discussed in the previous paragraph it is possible to characterize the coverage from the imaging conditions in the STHM mode itself. In the following we will elucidate the preparation procedure by discussing the example of $D_2/PTCDA/Au(111)$.

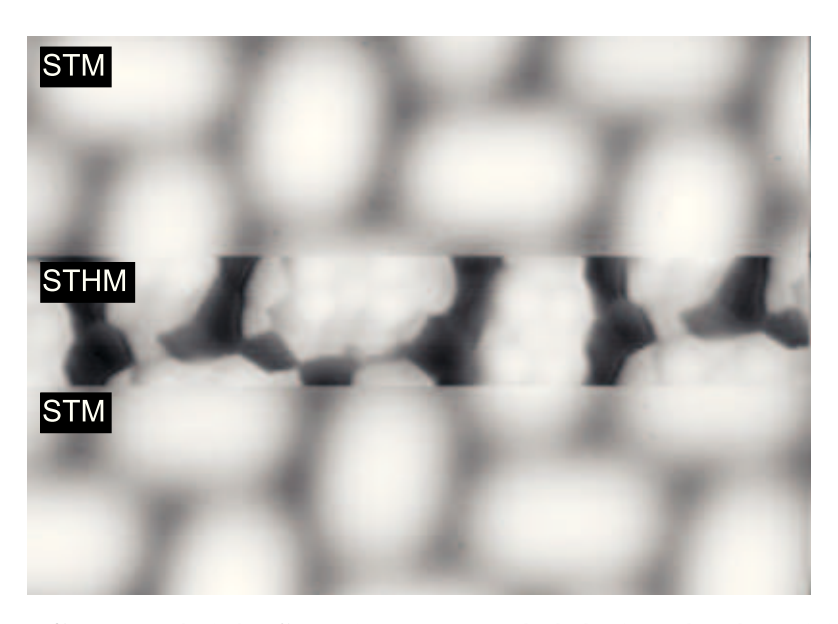


Figure 3.2: Constant height STM image recorded during the deposition of D_2 on PTCDA/Au(111). At the upper and lower part conventional STM contrast is visible while a small stripe in the center of the image reveals STHM contrast. Image parameters: $50 \times 35 \text{ Å}^2$, const. height, V = -5 mV

3 Preparation of STHM experiments

To monitor the coverage during D₂ exposure, we image a PTCDA island under STHM conditions, i.e. in constant height mode at low bias (V < 10 mV). Before D_2 exposure, PTCDA molecules are imaged as featureless protrusions as in conventional constant current STM images [169] (cf. upper and lower part of fig. 3.2). A dosing valve directly attached to the STM chamber is used to increase the pressure of D₂ inside the cryostat to $p_{D_2} \approx 2 \cdot 10^{-8}$ mbar, while the tip constantly scans the surface. During deposition the temperature inside the STM is kept at a temperature of ≈ 5 K to allow condensation of D₂ in the STM junction [171]. After a certain exposure time which varies between $\tau = 15$ min and several hours, first signs of the presence of D_2 in the junction appear by spontaneous switching between STM and STHM imaging contrast (cf. fig. 3.2). With increasing coverage the number of switching events increases until no restoring of the STM imaging contrast is observed any more. At this coverage stable operation in STHM mode becomes possible even after rough tip preparations and the deposition of D₂ is stopped by closing the valve. Rough tip preparations means indenting the tip by more than 1 nm into the substrate or applying high bias voltage (V > 5 V) to cause changes of the tip shape. The now established experimental conditions, i.e. the produced D_2 coverage, can persist on a time scale of weeks without changing.

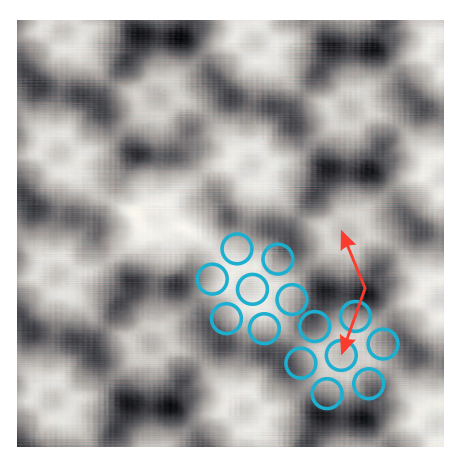


Figure 3.3: STHM imaging contrast of PTCDA/Ag(111) recorded with H_2 after too long exposure. In the center of each molecule a dark spot appears (red arrow), surrounded by other dark spots. The blue rings indicate the positions of H_2 in a possible overlayer. Image parameters: $45 \times 45 \text{ Å}^2$, const. height, V = -154 mV.

If D_2 exposure continues after stable imaging became possible, the coverage exceeds the window in which the STHM resolution is achieved and the contrast changes. An example of a typical changed imaging contrast at a too large coverage for $H_2/PTCDA/Ag(111)$ is shown in figure 3.3. However, we observe a similar contrast also on $D_2/PTCDA/Au(111)$. The similar contrast suggests that the resolution in figure 3.3 is a property of the H_2 (D_2) coverage, while the influence of the substrate or the used gas is small.

Although the contrast in figure 3.3 differs from the one in conventional STM or STHM images of PTCDA, the single PTCDA molecules are clearly distinguishable. Additionally, figure 3.3 reveals a submolecular resolution: in the center of each molecule a dark spot is visible. The spot is surrounded by a bright ring; from the ring six lines pointing radially outwards. The now resembled submolecular resolution is not related to the structure of the underlying PTCDA molecule.

So far we can conclude that the contrast in figure 3.3 is not related to the substrate nor directly related to the structure of PTCDA. Together with the fact that we observe this contrast only at elevated H_2 (D_2) coverage, beyond the one which is necessary to allow stable imaging in STHM mode, may indicate that the contrast originates from a H_2 (D_2) layer which condenses on top of the PTCDA island. Although in conventional STM images $H_2(D_2)$ is usually invisible, in reference [172] it has been shown, that it is possible to image a condensed monolayer of H_2 on Cu surface.

According to the picture of condensed H_2 one could explain the contrast in figure 3.3 by one H_2 molecule in the center of each PTCDA molecule surround by six H_2 forming a hexagonal structure (blue circles in figure 3.3). The distance between adjacent H_2 molecules in the hexagonal structure is ≈ 4.1 Å which is close to the value given in reference [172] (3.8 Å) where the molecules are condensed in a hexagonal arrangement. A similar intermolecular distance has been also found for solid H_2 and D_2 [173–175] which supports the picture of the condensed layer. On the contrary, expanding the hexagonal structure drawn above one molecule across the whole image is impossible. This means that although the supposed H_2 molecules form a short range hexagonal order above each single PTCDA molecule, the H_2 layer is not long range ordered as observed for the monolayer on top of a clean metal surface [172].

At coverages where the changed contrast appears, we never observed condensation of H₂ (D₂) on the bare metal substrate like in reference [172]. Thus, to favour the clustering of H₂ on top of PTCDA the H₂-PTCDA interaction needs to be stronger than the interaction between H₂ and the Au substrate. In addition, the molecule-molecule interaction between different H₂ molecules on top of PTCDA should result in a relaxed layer, thus to force H₂ into the observed short range order, the H₂-PTCDA interaction needs to be stronger than the H₂-H₂ interaction. Although, the appearance of the contrast at higher H₂ coverage strongly indicates a correspondence of the contrast in figure 3.3 to a layer of condensed H₂, one would need to further investigate the interactions between the different adsorbates and the substrate to determine this correspondence. However, the image contrast has another interesting property, namely its resistance against the application of high bias.

The STHM contrast usually appears close to zero bias (|V| < 10 mV), while at elevated bias the conventional STM contrast restores. Once the coverage has reached a value which allows the condensation of H₂ on top of PTCDA, the changed contrast appears in a wide range of bias without changing. In the case of figure 3.3 the contrast appears while scanning at V = -154 mV. In some cases we observe a similar contrast while scanning at $V = \pm 1 \text{ V}$. The voltage at which the contrast still appears varies between different preparations. The observation of the contrast in different bias windows may indicate a dependence of the stability of the H₂ layer on the total coverage.

3.4 Preparation of the STHM tip

Imaging organic layers in STHM mode after preparing the right coverage, one observes a dependence of the image contrast on the tip state. Although all prepared tips resolve single molecules in STM mode and show similar STHM contrast, distortions are visible in the images. The distortions appear as asymmetries of the molecular resolution, e.g. in some cases the resolution depends on the orientation of a molecule (cf. fig. 3.4 (a)). But the observed distortions can be removed by additional preparation of the tip to optimize the STHM contrast, which indicates that they only depend on the tip shape.

The preparation of the STHM tip is done in a similar manner as for the STM tip (cf. section 3.2) by careful indentation of the tip into the bare substrate. But in contrast to the STM tip-preparation procedure, we have to modify the manipulation parameters. While in the case of the Au-Au junction the contact between tip and sample usually rips off after retracting the tip by a few Ångstrom (cf. fig. 3.1), the presence of H_2 (D_2) changes the properties of the tip-sample contact. The condensed H_2 (D_2) increases the plasticity of the junction which leads to the formation of chains, thus the contact rips off at larger vertical distances of the tip compared to the empty junction [176]. The length of the pulled chains is of the order of a few nanometres. Clearly, for the STHM tip preparation it is desirable to retract the tip further, e.g. at least 5-10 nm, so that the contact breaks off while the tip moves perpendicular to the surface, to prevent distortions of the tip apex due to bending of the chain.

As in the case of the STM tip-preparation, the conductance of the junction is monitored during the preparation process. To ensure that the pulled wire breaks while the tip moves away from the surface we increased the tip-sample separation by applying an offset voltage of 30 V to the z-piezo before starting the preparation process. The increasing of the tip-sample distance is necessary, since due to the experimental setup the tip returns to the

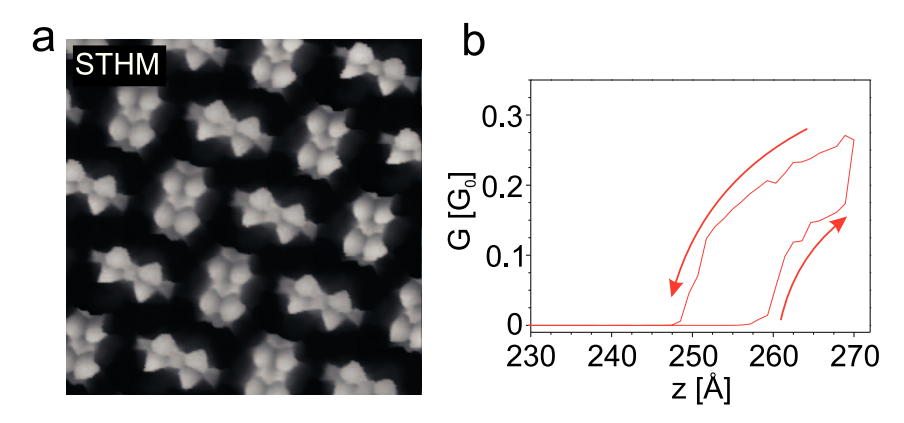


Figure 3.4: Preparation of the tip after condensation of D_2 on the surface. a) Not optimized resolution of PTCDA/Au(111) in STHM mode. The resolution of two molecules in the unit cell differ from each other. b) Evolution of the conductance of the junction during tip preparation after D_2 exposure on clean Au(111). Before the tip is brought into contact with the Au surface it is retracted by 228 Å to monitor the conductance during retraction. Tip-sample contact is established at z=257 Å indicated by the increase of the current through the junction. Then the tip is moved further towards the sample by 13 Å. During retraction the contact brakes at z=248 Å. The direction of tip movement is indicated by red arrows. Image parameters: $4.5 \times 4.5 \text{ nm}^2$, const. height, V=-5 mV

stabilization point ($z \approx 1$ nm) at the end of the preparation procedure and before the feedback is switched on again. Applying 30 V to the z-piezo leads to an increase of the tip-sample distance by ≈ 228 Å, which is much larger than the typical length of the pulled wires.

An example for the conductance evolution is shown in figure 3.4 (b), where approach and retraction traces are indicated by red arrows. After the tip approached by z=257 Å the contact between tip and sample is established, indicated by a sudden jump of the conductance. Approaching the tip further, several steps appear in the conductance while the total value stays below 1 G_0 which is expected to be the conductance of a single Au-Au contact [176]. The remarkably lower conductance in the contact regime may be explained by the presence of D_2 which is incorporated in the junction and thus decreases the conductance [176]. During retraction the conductance also shows a step like behaviour while it drops until the contact breaks at z=246 Å. The difference between the contact formation and breaking distance is 9 Å, which is about twice larger than in the example in figure 3.1. The larger distance, together with the low conductance (< 1 G_0), indicates the formation of a chain between tip and sample.

The final assessment of STHM tip quality is only possible by looking at STHM images themselves. It turns out that the image contrast in STHM mode is much more sensitive to the shape of the tip as the image contrast in STM mode. In the case of STM almost

3 Preparation of STHM experiments

every second tip shows the above discussed desired resolution. The STHM tips prepared according to the method presented above show more variability in the achieved contrast, whereas we obtain a success rate of $\approx 10~\%$ to prepare a tip which reveals a symmetric STHM contrast.

In the beginning we will start to summarize the main features of the STHM resolution. This motivates our further analysis of the STHM mode in order to characterize its abilities and investigate the imaging mechanism.

4.1 Image contrast: organic molecules

The most striking feature of STHM mode is its ability to directly resolve the inner structure of complex organic molecules. This will be demonstrated in the following by looking at different examples of STHM images. The palette of imaged molecules, hereby, goes from one dimensional aromatic hydrocarbons like tetracene and pentacene over small graphene fragments with functional groups like PTCDA to two dimensional molecules like tin-II-phthalocyanine (SnPc).

4.1.1 PTCDA/Au(111)

In the case of PTCDA/Au(111) the resolution in STHM images reaches an unprecedented level getting very close to the chemical structure formula of PTCDA. However, the correspondence between the chemical structure and the contrast in STHM images is not clear from the beginning. In fact, the images show some variability of the contrast between different tips, but also between different sets of imaging parameters. But before we have a closer look at the variability of the contrast, we directly compare the STHM resolution with the chemical structure to elucidate their close relation.

Typical images acquired in STM and STHM mode of a single PTCDA/Au(111) are shown in figure 4.1 together with the chemical structure formula of PTCDA. In STM the molecule appears as a bright featureless protrusion while the STHM image contains much more information.

In STHM mode (fig. 4.1 middle panel) the molecule appears bright like in the case of STM. But in contrast to the former case a sharp submolecular contrast is visible. The image of the molecule consists of seven well separated rings. The order of the rings is symmetric along the long axis of the molecule. Although the borders between the rings appear sharp and edged, the shape of the rings shows differences depending on their position above the molecule. The central ring has a hexagonal shape, the four rings attached to it appear

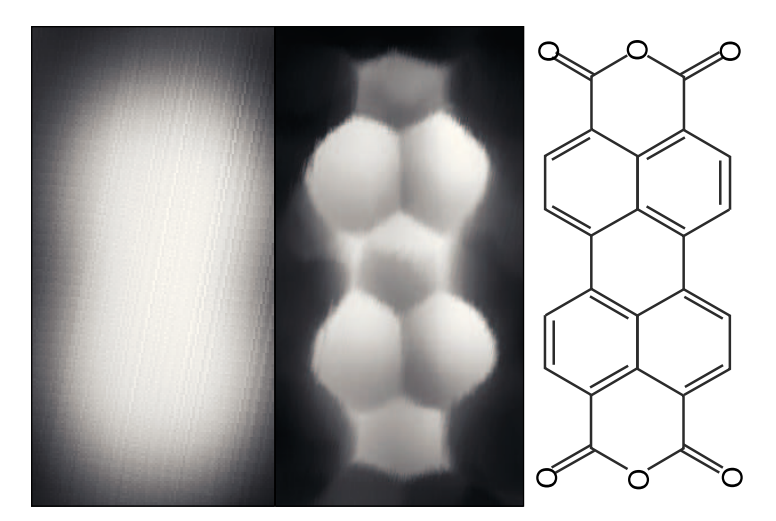


Figure 4.1: Chemical structure of 3,4,9,10 perylenetetracarboxylic-acid-dianhydride (PTCDA) adsorbed on a Au(111) surface imaged with D₂ (middle panel). For a direct comparison the conventional LDOS contrast of the STM (left panel) and the chemical structure formula (right panel) is shown. Image parameters: $1.3 \times 0.7 \text{ nm}^2$, left panel: const. height, I = 0.1 nA, V = 316 mV, center: const. height, V = -5 mV.

rounded at the outer part of the molecule and the rings at the ends of the long axis show three extensions pointing away from the molecule. If we now compare the contrast in the image with the chemical structure of the molecule, the close relation between the two becomes clear.

All rings in the STHM image can be identified in the chemical structure formula of PTCDA (cf. fig. 4.1 right panel). The central and the four adjacent rings correspond to the perylene backbone, consisting of five connected C_6 rings. The outer rings, at the top and the bottom of the molecule in figure 4.1 correspond to the oxygen terminated C_5O heterorings at the ends of the molecule. The extensions at the heterorings which point away from the molecule may indicate the positions of the oxygen atoms, which are not directly imaged. In contrast to the C_5O rings, the rings at the hydrogen terminated sides of the molecule appear rounded.

The STHM contrast in figure 4.1 is very close to the chemical structure formula, however, the correspondence is not perfect. The ring like structure of the molecular backbone is reproduced in the STHM image, while the shape of the rings is not. The hydrogen terminated sides of the molecule are imaged rounded, whereas the C_6 rings in the chemical structure have hexagonal shape. The molecule is expected to be symmetric with respect to the short axis of the molecule, but the upper C_5O ring appears darker than the rest of the molecule. Finally, in the STHM image a complex internal structure appears inside the rings, giving rise to a three dimensional impression, where one side of each ring appears

higher than the other. The internal structure does not correspond to the molecular structure which is expected to be flat while it also varies between images recorded with different tips.

The observed differences between the contrast in STHM images and the structure formula indicates a complex mechanism which lies behind the contrast formation. However, the direct connection between the two becomes clear when considering other examples of STHM images.

4.1.2 Pentacene/Ag(111)

The relation between the STHM contrast and the chemical structure in the case of PTCDA is only one example. The STHM mode has been successfully applied to other organic molecules adsorbed on metal surface with comparable high resolution. A second example where the STHM contrast closely resembles the chemical structure of the imaged molecule is pentacene adsorbed on a Ag(111) surface.

Pentacene is an aromatic hydrocarbon consisting of five connected C₆ rings. So far, the structure is similar to PTCDA, but in contrast to the perylene backbone of PTCDA, the aromatic rings of the pentacene molecule form a straight line. Although the conformation of the carbon atoms is different compared to PTCDA, both molecules appear very similar in conventional STM images (cf. 4.2 (a)). The contrast of pentacene in conventional STM images is blurred and shows no submolecular features like the STM contrast of PTCDA on Au(111) (cf. fig 4.1). This is different in STHM images.

An image of pentacene/Ag(111) recorded in STHM mode is shown in figure 4.2 (b). Like for PTCDA, the contrast in STHM mode is much sharper compared to the STM contrast. Although the length of the molecule in both imaging modes is comparable, the width of the molecule in STHM mode (≈ 3 Å) is 2.5 times smaller than in the STM image (7.5 Å). In addition to the thinner appearance of the molecule a submolecular contrast appears in the image.

The submolecular resolution in the STHM image consists of five separated rings. The rings are separated by lines where the conductance is lower than inside the rings. The center of the rings form a line along the long axis of the molecule. The rings at the ends of the molecule and the central ring appear slightly larger than the ones in between. Numbering the rings from top to bottom, the first and third ring have a diameter of 3 Å, ring number two has a diameter of 2.1 Å, the forth ring has a diameter of 2.3 Å and ring five a diameter of 2.7 Å.

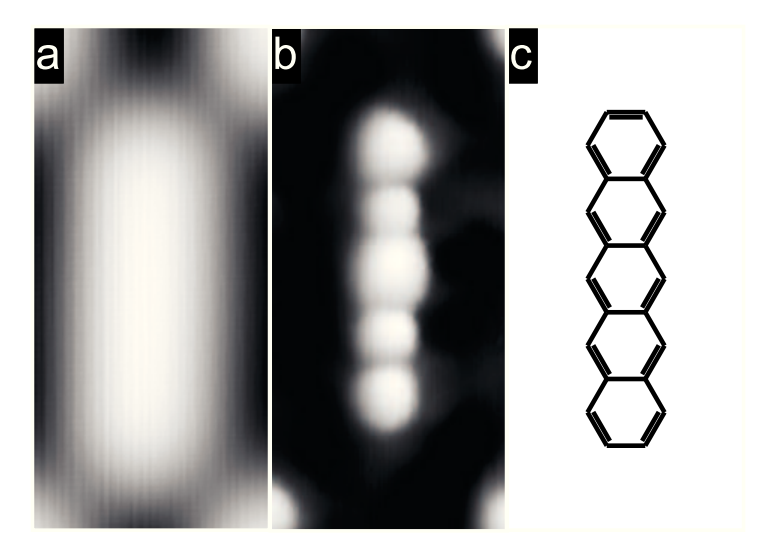


Figure 4.2: STHM contrast of a one dimensional aromatic hydrocarbon adsorbed on a silver surface. a) STM contrast of a single pentacene. b) Corresponding STHM image. c) Chemical structure of pentacene. Image parameters: $D_2/pentacene/Ag(111)$, a) $1.9 \times 0.9 \text{ nm}^2$, V = -340 mV, I = 1.2 nA, b) $1.9 \times 0.9 \text{ nm}^2$, V = -2 mV, const. height dI/dV.

Comparing the STHM image with the structure formula of pentacene (fig. 4.2 (c)) reveals the connection between the two. Each of the rings in the image corresponds to one of the C₆ rings of the structure. But whereas the rings in the image have various diameters the C₆ rings in the structure formula are all the same. The diameter of a benzene ring is 2.54 Å [177]. This means that the larger rings in the image are larger than a single C₆ ring, whereas the rings with smaller diameter have a smaller diameter. In addition, neither the carbon atoms nor the hydrogen atoms, which terminate the bonds of the aromatic rings are directly visible. The absence of the atoms is the same as in the previous example of PTCDA, where none of the atoms directly appears in the STHM image. Although the contrast in the STHM image is again similar to structure formula additional features appear in the image which cannot be understood from the chemical structure.

The appearance of rings with alternating diameter is not directly related to the structure formula of pentacene. In accordance to the STHM image of PTCDA the hydrogen terminated sides of the molecule appear rounded. The direct connection of the rounded sides by the dark lines may hereby lead to the circular appearance of the C₆ rings in the STHM image. In contrast to the image of PTCDA, an internal structure inside the rings, which leads to a three dimensional impression like in the STHM image of PTCDA does not appear in the STHM image of pentacene.

4.1.3 Tetracene/Ag(110)

As a third example for the STHM contrast, we discuss another aromatic hydrocarbon adsorbed on metal surface, i.e. tetracene on Ag(111). The structure of tetracene is very similar to the structure pentacene, except tetracene consist out of four aromatic C_6 rings instead of five. Due to the similar structure of both molecules one may expect that they also appear similar when imaged in STM and STHM mode.

The electronic structure represented by the STM image is indeed close to the contrast of pentacene and PTCDA. Tetracene appears as a featureless elongated protrusion (cf. fig. 4.3 (a)). The molecule is elongated along the long axis of the molecule while no submolecular resolution is visible.

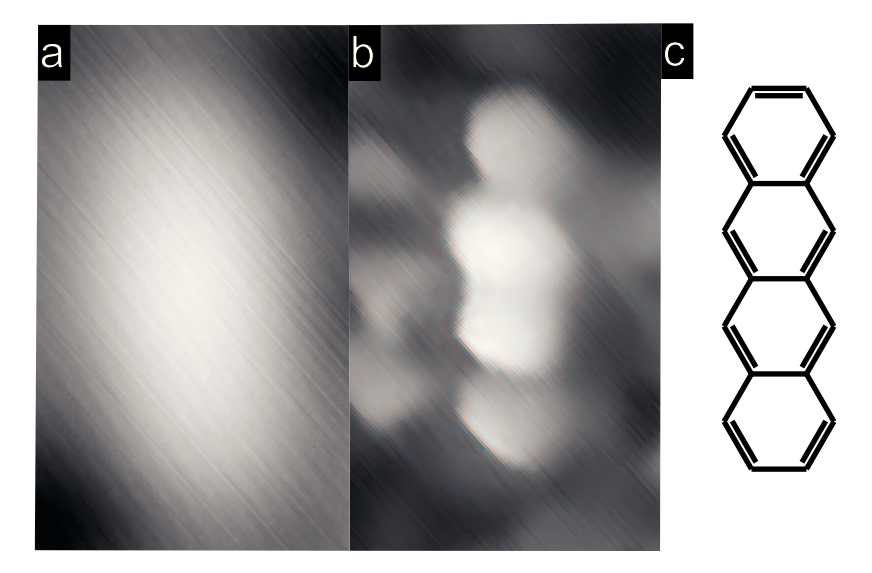


Figure 4.3: Comparison between STM and STHM contrast for tetracene/Ag(111). a) Typical STM contrast shows now submolecular resolution. b) In STHM mode the structure of the molecule is reproduced by the contrast. The image of the molecule contains four rings. The rings differ from one another in shape and brightness. c) Chemical structure of tetracene. Image parameters: a) $1.5 \times 0.9 \text{ nm}^2$, const. height, V = -340 mV. b) $1.5 \times 0.9 \text{ nm}^2$, const. height, V = -10 mV. Images of the STM and STHM contrast reproduced from reference [55]

Imaging tetracene in STHM mode a submolecular structure appears. The submolecular structure in the STHM contrast consists of four rings along the long axis of the molecule. The outer rings are well separated while between the inner two rings only a faint line is visible separating both rings from each other. In addition the central two of these rings appear brighter than the outer ones.

The contrast in the STHM image reproduces the structure formula of tetracene (cf. fig 4.3 (c)). Both, the structure formula and the contrast in the STHM image, consists of

four rings. So far typical for the STHM contrast, the atoms are not directly visible in the image. However, the situation in figure 4.3 (b) is more complicated than in the examples in the previous sections.

In the previous examples of STHM images the conductance above the molecules has been almost homogeneous while in figure 4.3 (b) it is not. At both ends of the molecule the conductance drops. The drop of the conductance leads to the impression that the molecule is bend down towards the surface, while it is expected to be flat lying [125, 165]. In addition to the different brightness of the rings, their shape is distorted. The rings neither appear rounded like in the pentacene image nor hexagonal like in the structure formula.

Although the chemical structure of pentacene is very similar to the structure of tetracene, both molecules appear different in STHM images. In both cases the STHM contrast reproduces the basic characteristics, i.e. shape of the structure and number of rings, however, the image contains more information. This information is encoded in the shape and brightness of the rings. The origin of the contrast variation may be related to the shape of the tip and the used substrate which is not the same in both cases. Before we turn to a discussion about the variability of the STHM contrast we will present one last example of the STHM contrast.

4.1.4 SnPc/Ag(111)

The final example of STHM images of organic molecules is tin-II-phthalocyanine (SnPc) on Ag(111). SnPc stands for a new class of molecules to which the STHM mode is applied. On the one hand, SnPc is a two dimensional molecule the length and width of which are equal. On the other hand, the chemical structure of SnPc is more complex compared to the formerly imaged molecules. Besides aromatic C₆ rings, SnPc contains C₄N rings and a complex structure of C,N and Sn atoms in the center of the molecule.

In addition, SnPc is a non-planar molecule. The Sn atom in the center of the molecule sticks out of the molecular plane formed by the other atoms. SnPc adsorbs in two different configurations on Ag(111): with the tin atom pointing towards the vacuum (tin up) and with the tin atom pointing towards the silver surface (tin down) [127, 178].

A conventional STM image of SnPc/Ag(111) in tin down configuration is shown in figure 4.4 (a). The image shows the LUMO of the molecule which has a two fold symmetry

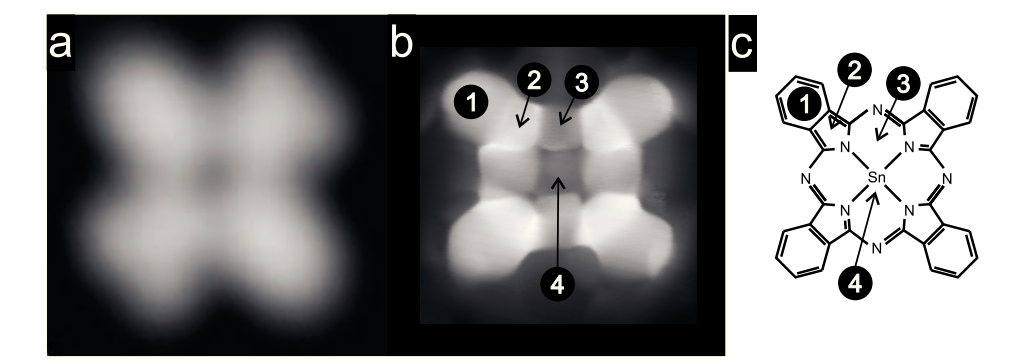


Figure 4.4: Enhanced contrast of tin-II-phtalocyanine (SnPc) adsorbed on a Ag(111) single crystal surface imaged with H₂ (b). For a direct comparison the conventional LDOS contrast of the STM (a) and the chemical structure formula (c) is shown. Numbers in the right and middle panel mark corresponding rings. Image parameters: a) $2 \times 2 \text{ nm}^2$, const. current, I = 1 nA, V = -190 mV, b) $1.5 \times 1.5 \text{ nm}^2$, const. height, V = -5 mV.

because of a degeneracy of the molecular orbital arising from the different rotational symmetries of the molecule and the substrate [178]. Unlike the electronic molecular states, the STHM contrast of the molecule is not degenerated.

In contrast to the STM contrast, the STHM contrast of SnPc/Ag(111) reproduces the four fold symmetry of the molecular structure (cf. fig. 4.4 (b)). The image contrast consists of sharp tiles of different brightness arranged in a clover-leaf structure. In the center of the molecule a dark square is visible which is surrounded by the brighter wings of the molecule. The wings of the molecule consists of two parts a bright one close to the center of the molecule and one with lower brightness on the outer part.

The STHM contrast reproduces all elements of the molecular structure (cf. fig 4.4 (c)), but the shape of the elements is distorted and the Sn atom in the center of the molecule is not visible. The C_6 rings at the ends of the wings (1 in figure 4.4 (b,c)) are imaged rounded while the adjacent C_4N rings (2) are imaged with the same diameter but edged towards the center of the molecule. Up to this point, the imaged structures are similar to the C_6 , C_5O rings in the PTCDA image, this is different for the remaining structure in the center of the molecule.

In the center of the molecule additional rings are formed by the atoms, which appear as tiles in the STHM image. First there is a ring-like structure formed by two carbon and three nitrogen atoms between the wings of the molecule (3). This ring appears as a square in the STHM image. Finally there is a ring formed by the four nitrogen atoms in the center of the molecule which bind the tin atom. This place, where the tin atom is expected also appears as a square in the image while the square in the center is darker

than the rest of the molecule.

The STHM contrast of SnPc/Ag(111) shows some of the characteristics which have been identified in the previous examples for the STHM contrast. Each ring-like structure of the molecule appears as a tile in the STHM image. At the positions, where these tiles meet they are separated from each other by sharp lines. Hydrogen terminated sides of the molecule like the C_6 rings at the end of the wings are imaged rounded. Besides the similarities, the image also reveals features which have not been identified so far.

In the image the four C₄N rings appear brightest. In comparison with the other rings out of which the molecule consists these rings are the smallest in diameter. This finding may indicate a dependence of the brightness on the ring diameter. However, the STHM image of tetracene revealed different brightnesses for rings with equal diameter. Secondly inside the rings an internal structure is visible. Unlike the STHM image of PTCDA (fig. 4.1), the internal structure is not the same in all the rings, thus it does not lead to a similar three dimensional impression of the molecule.

4.2 Contrast variation: PTCDA

Having shown that STHM can resolve the chemical structure of different aromatic organic molecules, we will turn to a discussion of the variability of the achieved contrast on the experimental conditions. The dependence of the STHM contrast on the coverage of H_2 (D_2) on the surface has been discussed already in section 3.3, but besides the coverage two additional parameters turn out to be important. These parameters are the tip sample distance at which STHM images are recorded and the state of the used tip. The analysis of the variability of the image contrast in both, the distance and the tip state, in the following section is a first step towards the understanding of the mechanism which lies behind the contrast formation.

4.2.1 Distance dependence

We start the analysis with the dependence of the image contrast on the tip sample distance. As a reminder: STHM imaging are usually recorded in constant height mode at low bias (|V| < 10 mV). This means that during scanning the bias and the tip-sample

distance stay constant, however, the absolute distance at which the tip scans the surface remains as a free parameter. In fact, it is found that the tip-sample distance has considerable influence on the obtained contrast in the image.

A method to adjust the tip-sample distance for the STHM images is: stabilization of the tip in the center of PTCDA under tunnelling conditions ($I_t = 0.1 \text{ nA}$, V = -340 mV) and approach with the tip by $\approx 2-3 \text{ Å}$ towards the surface before starting scanning. At a tip-sample distance adjusted with this procedure STHM contrast usually appears, whereas the contrast is different when the chosen distance is significantly larger or smaller.

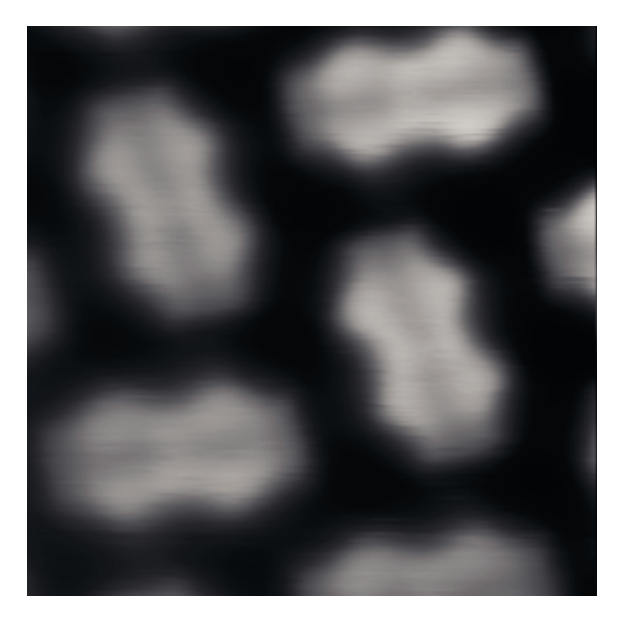


Figure 4.5: Differential conductance STHM image contrast at increased tip-sample separation. In the center of the molecule a dark node appears, but the shape of the molecule is reproduced in the image. Image parameters: $H_2/PTCDA/Au(111)$, $2.5 \times 2.5 \text{ nm}^2$, const. height, V = -1 mV

Scanning a PTCDA island at increased tip-sample distance, compared to the one at which the STHM contrast appears, the molecular resolution in the image differs from both, STHM and STM contrast. A typical image recorded at increased tip-sample separation is shown in figure 4.5. The contrast in figure 4.5 reproduces the outer shape of the molecules like they appear in STHM images, whereas the submolecular contrast is different from the one obtained in STHM mode.

The outer shape of the molecule, which is very similar to the image contrast in STHM images, indicates, that the contrast in figure 4.5 is increased with respect to the conventional STM contrast. But in contrast to the STHM resolution with its ring structure, a dark node appears along the long axis of the molecule. Such a nodal plane in the center

of the molecule can be found in some of the gas phase molecular orbitals [53], whereas the molecular structure does not have a node in the center. Up to now the origin of the contrast in figure 4.5 has not been understood. Nevertheless, according to our experience, the observation of a contrast like in figure 4.5 always indicates a too large tip-sample distance during scanning, so that the resolution can be drastically increased by reducing the tip height.

Reducing the tip-sample separation during scanning, the image contrast usually converts into STHM resolution. This finding emphasises that the contrast appearing at imaging conditions like in figure 4.5 is a precursor of the STHM contrast. According to this picture, at larger tip-sample separation the image contrast is strongly affected by electronic states close to the Fermi-level, which shows a nodal plane, whereas at smaller tip-sample distance the contrast becomes affected by energetically lower lying states, which are drawn in the structure formula. At the same time, the tip height must not be too small.

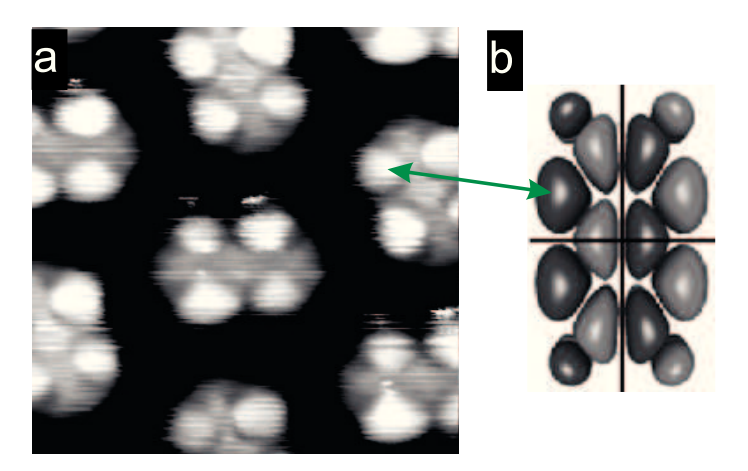


Figure 4.6: At to small tip-sample distance the molecular contrast resembles the shape of the gas phase LUMO. a) Differential conductance image of PTCDA scanned with small tip-sample separation. The contrast of the molecules looks similar to the calculated LUMO of gas phase molecules presented in b). The corresponding lobes are indicated with the green arrow. b) Calculated LUMO of PTCDA in the gas phase reproduced from reference [169]. Image parameters: $\rm H_2/PTCDA/Au(111), 2.5 \times 2.5 \ nm^2,$ const. height, $V=5 \ mV$

If the chosen tip-sample distance is too small, the contrast also differs from the one in STHM mode. An example for the obtained contrast when the tip scans the surface at distances closer than the one at which the STHM contrast appears is shown in figure 4.6 (a). The molecules in the image appear as oval protrusions with four bright lobes. Two of the lobes appear on each side of the molecule. The lobes are extended to the center of the molecule such that a zigzag structure forms along the long axis of the

molecule.

At the first glance the contrast is reminiscent of the STHM contrast where the four bright lobes with their center would correspond to the five C_6 rings of the perylene backbone and the darker areas at the end of the molecule correspond the C_5O heterorings. However, the molecule in the image appears broadened compared to the usual appearance in STHM images. In addition to the increased width, the zigzag structure appears in the center of the molecule while in STHM images the rings of the molecular structure usually appear rounded or edged. To determine if the contrast in figure 4.6 is a kind of STHM resolution we have to look at another example of STM images.

A similar contrast to the one in figure 4.6 (a) has been found for PTCDA/Ag(111). The contrast of PTCDA in reference [142] also shows four bright lobes and a zigzag structure in the center of the molecule. The resolution of the molecule is identified with the LUMO of PTCDA/Ag(111) which is located close to the Fermi level due to the strong interaction between PTCDA and Ag. A direct comparison between the gas phase LUMO (4.6 (b)) and the contrast in figure 4.6 (a) suggests a correspondence between the two. In contrast to PTCDA/Ag(111), the interaction with Au is weaker which does not lead to a charge transfer upon adsorption. Thus the LUMO of PTCDA is not shifted on Au.

In fact STM images of the LUMO of PTCDA on Au(111) have been presented in reference [154]. The LUMO contrast is very similar to the contrast in reference [142], but the images were recorded at V = +1 V and not at zero bias where STHM images are recorded. The location of the LUMO 1 V away from the Fermi level means that it should not be possible to tunnel into this state if no bias is applied to the junction.

It is conceivable, that at close tip-sample distance the electronic states of the tip hybridize with molecular states, thus lead to a local redistribution of the molecular states and so result in the observed contrast. Clearly, most favourable states for the hybridisation are the ones closest to the Fermi level which may explain the observation of a LUMO like contrast. Such effect has been reported earlier for $C_{60}/Cu(111)$ [179–181]. For $C_{60}/Cu(111)$ the hybridisation is observed at conductance values of $> 5 \times 10^{-2}$ G₀. In the present case the conductance reaches a maximum above the lobes of only 2×10^{-2} G₀. However, the shift in conductance values may originate from the coupling between molecule and substrate which can be expected to be weaker for PTCDA/Au(111).

Thus, we conclude that the contrast observed at close tip sample separation represents the LUMO of PTCDA which becomes accessible due to a hybridisation with states in the tip.

4.2.2 Tip dependence

Scanning the surface at a tip-sample distance at which the STHM contrast appears, the obtained contrast still shows some variability. The origin of this variability is the specific shape of the tip, since the obtained contrast can be affected by preparation of the tip (cf. section 3.4). Analysing different frequently observed contrasts gives first impressions about the properties of the imaging mechanism.

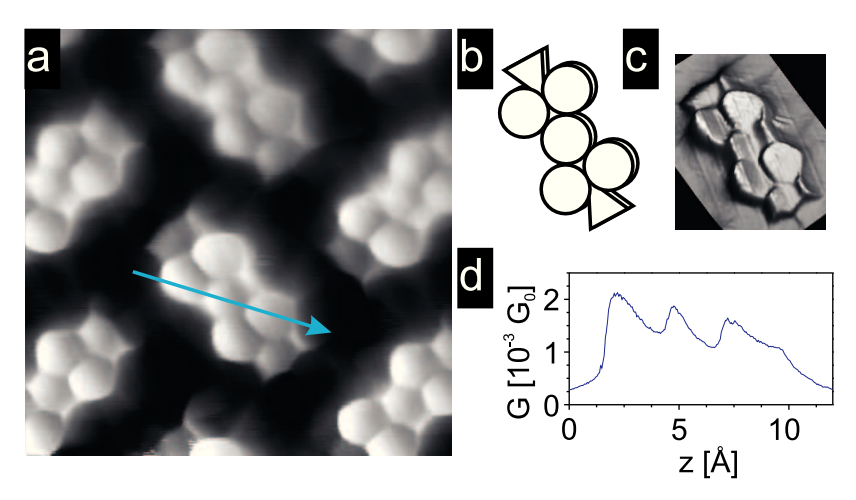


Figure 4.7: Doubling of the STHM contrast. a) STHM image with right edge of each molecule appearing broadened compared to the left edge. The contrast broadening is independent of the orientation of the molecule always on the right side. b) Sketch of the molecular resolution with the doubled contrast on the right part. c) Three dimensional illustration of the topographic map of a single molecule. The shading of the image is interpreted as height information to generate a tree dimensional impression. Thus the brighter part of the molecule appear higher than the darker ones. d) Linescan along the arrow marked in a). Image parameters: $H_2/PTCDA/Au(111)$, a) $2.5 \times 2.5 \text{ nm}^2$, const. height, V=10 mV

In the beginning we will start with a closer look at the contrast variations of PTCDA on Au(111) and the distortions in the molecular contrast. One example of the achieved contrast is shown in figure 4.7 (a). The resolution in figure 4.7 is comparable to the previous examples of STHM images of PTCDA. The contrast of a PTCDA molecule in figure 4.7 consists of seven well separated rings which show an internal shading like in figure 4.1. As before, the seven rings of the STHM contrast can be identified with the rings (C_6 , C_5O) in the structure formula, while the lines separating the rings from each other form angles of 120° like expected for the C_6 rings. But unlike the contrast of figure 4.1, at the right side of each molecule a bright line is visible. This line follows the shape of the molecule and leads to the impression of a doubling of the contrast. A sketch to illustrate the doubling is shown in figure 4.7 (b).

At this stage we will use the opportunity to analyse the appearance of the shading inside the rings. The brightness variation in each ring has the same shape. The left part of each ring appears brighter than the right part. In the conventional colour code used to display topographic STM images of surfaces, brighter colours correspond to a smaller tip-sample separation and therefore to higher features on the sample. This means, that the left part of each ring appears higher than the right part (cf. fig. 4.7 (c)). While the molecule is expected to be flat lying, it is conceivable that the effect of the hight variation originates from the scanning process, such that the conductance is always increased when the tip moves in a certain direction above the surface. Looking at a linescan across the molecule (fig. 4.7 (d)) we observe that every time the tip scans across the bond on the left side of the ring structure the conductance suddenly increases while the conductance constantly drops when the tip moves away from this bond. However, the shading inside the rings also depends on the shape of the tip since it also changes with tip preparation.

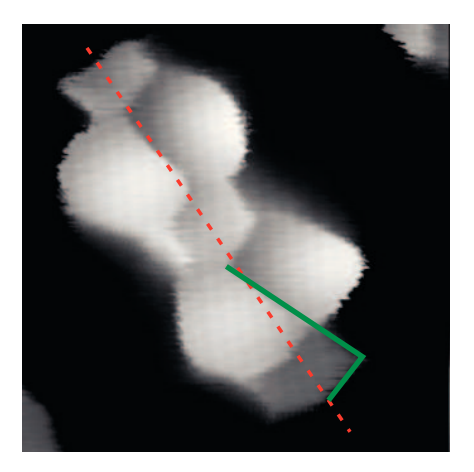


Figure 4.8: Distorted molecular contrast in STHM mode. Parts of the molecular appear rotated around the center, therefore the rings are not aligned to the molecular axis. The rotation is indicated by the green line. The orientation of the molecule, i.e. the molecular axis (red dashed line) has been extracted form another image. Image parameters: $H_2/PTCDA/Au(111)$, $1.1 \times 1.1 \text{ nm}^2$, const. height, V = -1 mV

Besides the variability of the internal conductance variation, we often observe distortions of the molecular plane in the STHM contrast. An example for such distortion is shown in figure 4.8. In the image all rings are visible with an internal shading like in figure 4.7 (a). But in contrast to the previous examples, the four rings around the central one appear rotated with respect to the molecular axis. The border between the rings is rotated out of the molecular axis as indicated by the green line. The rotation leads to a breaking of the 120° symmetry at the connections of the rings and gives the contrast a two fold rotational symmetry with respect to the center of the molecule.

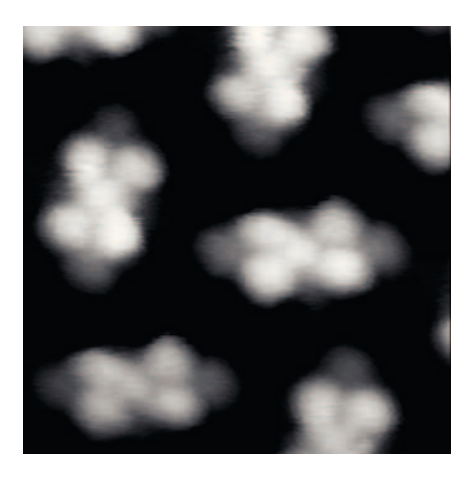


Figure 4.9: Differential conductance STHM contrast with highlighted perylene backbone. a) STHM image of PTCDA where the perylene backbone appears brighter than the rest of the molecule. The backbone is imaged as five equally sized circles. b) Magnification of one molecule from the image in a). The position and size of the circles of the molecular backbone are indicated by the rings. Image parameters: $H_2/PTCDA/Au(111)$, a) $2.5 \times 2.5 \text{ nm}^2$, const. height, V = -1 mV, b) $1.3 \times 0.8 \text{ nm}^2$, const. height, V = -1 mV

The structure of the molecule in figure 4.8 is still well visible but even this is not always the case. Sometimes the borders between the rings are not so well resolved and the single rings appear rounded as in the STHM images of tetracene (fig. 4.3) and pentacene (fig. 4.2).

An example for this kind of resolution is shown in figure 4.9. In the image all the rings of the structure are again visible. The five rings corresponding to the perylene core are imaged brighter than the C_5O rings at the ends of the molecule. The rings in the image are separated by dark lines. At the positions where the lines meet each other, the contrast is blurred and dark spots appear which leads to the rounded impression of the central ring. Due to the rounded appearance of the rings, the symmetry between the lines (120° angle) is not so clear as in figure 4.7 (a).

Another similarity between the contrast in figure 4.9 and the STHM contrasts of tetracene and pentacene is the absence of an internal conductance variation inside the rings. The brightness of each of the rings in figure 4.9 is homogeneous across the ring. The absence of the shading is usually not observed for PTCDA on Au(111) but more often we observe a contrast comparable to figure 4.9 if we image PTCDA adsorbed on a silver surface, where also the tetracene and penatacene images have been recorded.

The STHM contrast of PTCDA/Ag(111) is shown in figure 4.10. The contrast in the image is similar to the one in figure 4.9: The rings appear rounded and no brightness variation appears inside the rings. But in contrast to the images on Au(111) the space

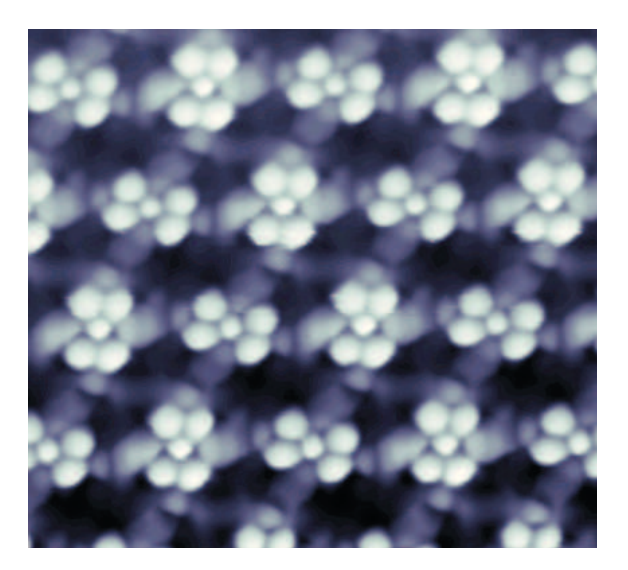


Figure 4.10: Typical STHM contrast of PTCDA/Ag(111). The C_6 rings of the perylene core of PTCDA are very pronounced and appear rounded in the image. C_5O rings at the end of the molecule are there but they appear distorted. Besides the molecular contrast a pattern between the molecules appears which connects the long sides of the molecule with the short side of the adjacent molecule in the unit cell. The pattern is not directly related to the underlying molecular structure. The intensity of the pattern at the long sides of the molecule is even higher than the intensity of the C_5O rings. Image parameter: PTCDA/Ag(111), $50 \times 50 \text{ nm}^2$, const. height dI/dV, V = -1 mV

between the molecules is not empty. Between the molecules, bright areas are visible which connect the long sides of one molecule with the short side of the adjacent molecule. Compared to the contrast of the molecules these areas are almost as bright as the C_5O rings of the molecule. In contrast to the contrast above the molecule the bright areas do not directly correspond to the structure of the molecules.

The features between the molecule frequently appear in STHM images of PTCDA on Ag(111) and therefore seem to be a generic feature of the contrast. In addition, one important thing about the contrast between the molecules is: for the first time a feature in the STHM image cannot be associated with an underlying ring structure. It may be possible that the contrast between the molecules originates from a doubling of the contrast but due to the frequent observation of such features this explanation is unlikely.

The contrast in figure 4.10 is not the only type which we obtain when scanning PTCDA on Ag(111) in STHM mode. Often the PTCDA layer is imaged as shown in figure 4.11. The contrast in figure 4.11 is not as sharp as in figure 4.10. Although all rings of the molecular structure can be found in the image, the central ring appears smaller than the outer rings. In total the outer rings of the molecule appear broader and distorted with respect to the

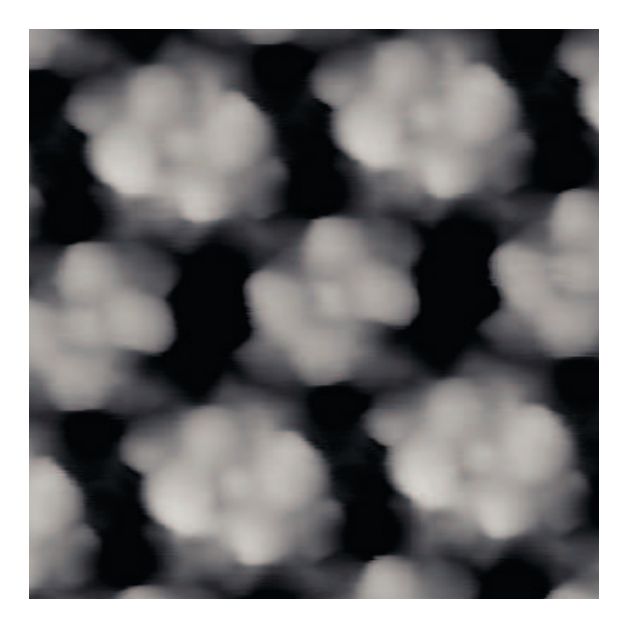


Figure 4.11: STHM contrast where the four outer rings of the perylene core are imaged more pronounced with respect to the central ring. The center of the four rings appear symmetric, but the diameter of the rings is different. Rings on a diagonal have almost the same diameter. Image parameters: $D_2/PTCDA/Ag(111)$, $3 \times 3 \text{ nm}^2$, const. height, V = 100 mV

ideal hexagonal or rounded shape. Inside of the distorted rings a contrast variation is visible but in contrast to figure 4.7, the different brightness does not always occur on one side of the rings but is more randomly distributed.

In figure 4.11 a contrast between the molecules is visible although it is not as pronounced as in figure 4.10. This time the bright areas are directly connected to the long sides of the molecule and are elongated towards the short sides of the adjacent molecules. The bright areas are narrowed at the sides close to the adjacent molecule but they are not directly connected to the C_5O rings. Between the rings and the areas always a dark line appears separating the molecules from each other.

In figure 4.11 the rings of the molecules appeared slightly distorted but sometimes the distortion of the contrast becomes extreme. An example for a strongly distorted contrast is shown in figure 4.12. The molecule again appears broadened as in the LUMO contrast (fig. 4.6) and the C₅O rings only vaguely appear. The four outer rings appear brighter at the outer part, but this brightness variation is different from the one in figure 4.7 since it only appears at the outside of the molecule.

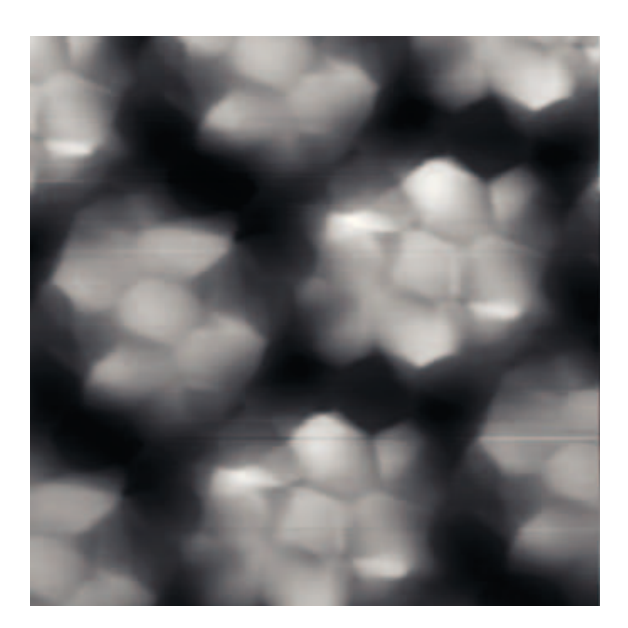


Figure 4.12: Faceted STHM contrast. The molecules structure of the molecules vagually appears in the image while the overall contrast looks refracted. The inner structure in the center of the molecule is well visible while some rings reveal additional edges at the outer part of the molecule. Image parameters: $\rm H_2/PTCDA/Ag(111),\ 2.5\times2.5\ nm^2,$ const. height, $V=-5\ mV$

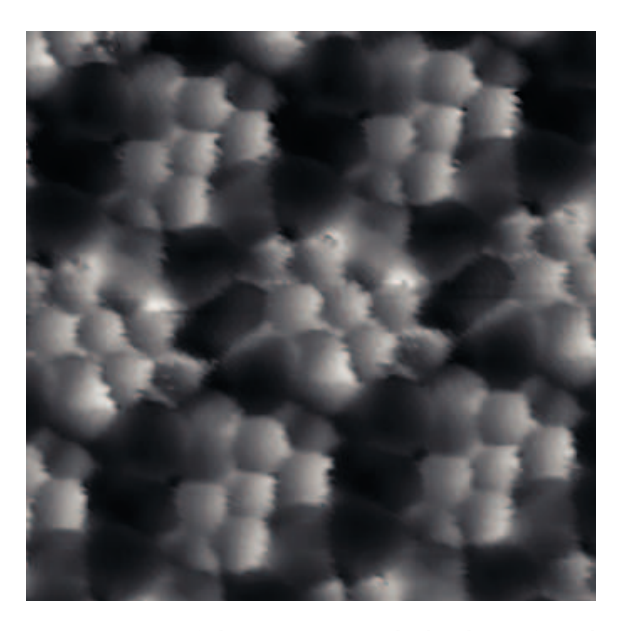


Figure 4.13: STHM contrast with pronounced shadows inside of the rings. The difference between the conductance at the corner of the ring and the value inside the ring lets the contrast appear plastic. In addition to the contrast above the molecules, between the molecules a pattern is visible. Image parameters: $\rm H_2/PTCDA/Ag(111),\ 3\times3\ nm^2,$ const. height, $V=-2\ mV$

On the contrary, although the outer part of the molecule is strongly distorted, the contrast at the central ring is sharp. The central ring is imaged as large as the four outer rings and separated from them by sharp lines. These lines form angles of 120° at the positions where they meet like in figure 4.7.

The previous image has shown that also for PTCDA/Ag(111) it is possible to obtain a sharp hexagonal structure inside the molecule in STHM mode. A contrast which is very close to the one in figure 4.7 but for PTCDA on Ag(111) is shown in figure 4.13. The image shows a good resolution of the molecular structure: all rings are visible, the lines separating the rings show the angle of 120° and a 3D shading appears inside of each ring where the lower right part of each ring is imaged brighter than the rest of the molecule. But in addition to the good resolution, we obtain a strong contrast between the molecules. Also in this example the long sides of the molecules appear bright showing extensions towards the adjacent molecules. In contrast to the previous images some of these extensions become so sharp that they appear as bright lines between the molecules. Although these lines are not directly related to the molecular structure, they appear at the positions where one would expect hydrogen bonds between the molecules which will be demonstrated in the next section.

From the observations related to the contrast variations in STHM mode we can draw the following conclusions:

- 1. The tip-sample distance during imaging is a crucial parameter for the STHM contrast. The height must neither be to high nor to low to obtain the best resolution in STHM images. This behaviour makes the tip-sample distance a parameter to determine the mechanism behind the contrast formation and therefore it will be further analysed in chapter 5.
- 2. The STHM contrast has been investigated for PTCDA adsorbed on two different substrates, Au and Ag. Although PTCDA bounds differently on the surfaces [166], it is possible to obtain STHM contrast in both cases. However, the obtained contrast in STHM images showed some systematic differences. The characteristic features of a typical image on Au (fig 4.7 (a)) exhibits a shading inside the ring which leads to a three dimensional impression and a weaker contrast between the molecules. In total the contrast is much sharper on Au than on Ag. The typical contrast on Ag (fig. 4.10) reveals a rounded appearance of the rings without the internal shading and a stronger contrast between the molecules. The reason for the different contrast may originate from the different tip materials in both cases. Up to now the substrate material in all cases equals the tip material due to the tip preparation procedure (cf. section 3.4). However, in some cases we obtained the other contrast on both

substrates which indicates that the situation is more complicated (cf. figures 4.9 and 4.13). The possibility to prepare tips which show one or the other type of resolution on both substrates suggests that additional parameters like e.g. the tip shape play a role in the contrast formation, whereas the probability to prepare a certain type of tip depends on the substrate.

3. Besides the material of the tip some of the images showed additional influence of the tip onto the obtained contrast. This influence showed up as distortions in the molecular resolution or doubling of the contrast. We obtained such asymmetries in the STHM contrast on both substrates on Au and on Ag, thus it does not depend on the tip material itself. Furthermore, it may be the integrity of the tip which influences the image contrast. A possible origin for the asymmetries may be a structural flexibility of the tip similar to the situation presented in reference [146]. Following this idea, during scanning the tip apex would be displaced from its equilibrium position and than relax when the tip moves further. The interplay between displacement and relaxation than leads to distortions in the molecular contrast. Clearly the flexibility of the tip will depend on its atomic structure and will be strongly anisotropic. Therefore, a plastic tip can produce a wide range of different contrasts.

4.3 STHM imaging of intermolecular interactions

The analysis of the different contrasts achieved in STHM mode of PTCDA has shown that besides the STHM contrast of the molecules something else appears in the images. In basically all of the images of molecular islands a contrast also appears between the molecules. Compared to the brightness of the molecules, the strength of the contrast varies between different images. So far we observed that the strength of the contrast is tendentially higher on Ag than on Au.

The origin of the contrast between the molecules is not obvious. Regarding the molecular structure of the organic film, the spaces between the molecules can be expected to be empty, i.e. no adatoms or other molecules are bound in the cavities created by the PTCDA molecules, neither on Ag nor on Au.

In the following we will focus on the contrast pattern between the molecules at the example of PTCDA/Au(111). The key task in this context is the determination of the origin of the contrast.

4.3.1 PTCDA/Au(111)

We start with a closer look at STHM images of the herringbone phase of PTCDA on Au(111). The herringbone phase is the most prominent phase, if the sample is prepared according to the recipe described in section 3.1. The herringbone phase has been used to elucidate the contrast variation in STHM mode in the previous section. Therefore, we know that STHM images of the herringbone phase show the enhanced conductance between the molecules. However, the strength of the contrast varies between the different examples of STHM images. Although we observed a tendency that the contrast between the molecules is always stronger for the herringbone phase of PTCDA on Ag compared to the one Au substrate, the contrast is present in every image.

An STHM image of the herringbone phase is shown in figure 4.14 (a). A two colour palette is used to highlight the contrast between the molecules. Since the conductance atop of the molecules is about 5 times larger than above areas between the molecules, this method allows an enhancement of the contrast between the molecules.

The PTCDA molecules in the image (grey) exhibit a usual STHM contrast of PTCDA on Au(111) (cf. fig. 4.1). The conventional STHM contrast is characterized by the hexagonal appearance of the central ring and the shading inside the rings. In addition, slight distortions are visible in the molecular structure. The vertical molecules are imaged broader than the horizontal molecules and the C_5O rings appear darker than the rest of the molecule and distorted at the outer part.

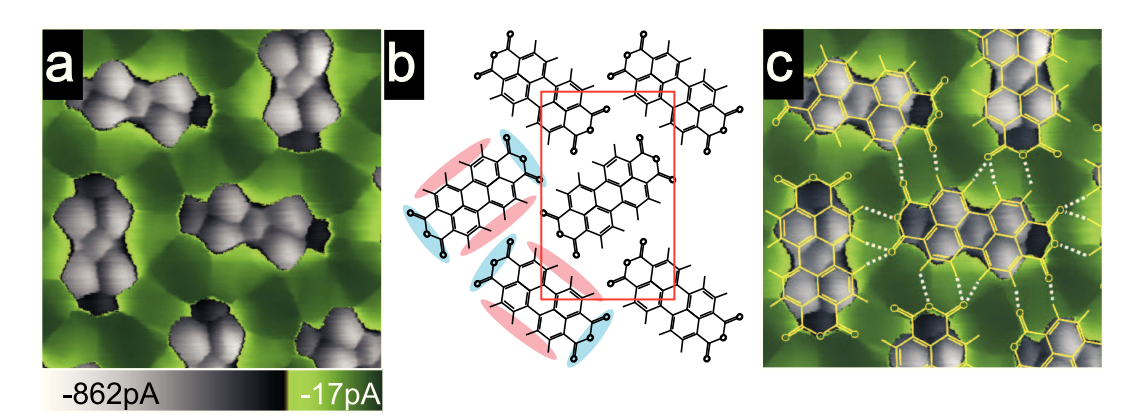


Figure 4.14: Herringbone phase of PTCDA molecules on Au(111). (a) STHM image shown on a two colour palatte to highlight the contrast between the molecules. (b) Structure model, lattice constants $(12.3 \times 19.2 \text{ Å}^2)$ taken from ref. [168], molecular orientation and structure in analogy to bulk β-PTCDA [182]. The molecular quadrupole moment and the unit cell are indicated. (c) Superposition of the image from (a) with the structure of the herringbone phase in (b). White lines mark the possible hydrogen bonds. Image parameters: (a and c) $25 \times 25 \text{ Å}^2$, const. height, V = -2 mV.

Together with the contrast of the molecules a clear tile pattern (green) appears in the area between the molecules. Two types of tiles are visible in the image: one with triangular and one with rectangular shape. The triangles connect the C_5O rings of one molecule with the hydrogen terminated side of an adjacent molecule. The rectangles connect one edge of the C_5O ring with the edge of the closest hydrogen terminated ring of the adjacent molecule. Inside the tiles an internal structure is visible, the conductance is always increased at the sides where the tiles touch the hydrogen terminated sides of the molecules. In order to identify the origin of the tiles we compare the STHM contrast with the film structure.

A model of the herringbone phase is shown in figure 4.14 (b). The molecules in the model are represented by their chemical structure. The unit cell of the herringbone phase (red rectangle) is known from electron diffraction [168]. The orientation of the molecules within the unit cell is taken from transmission electron microscopy (TEM) data in the bulk [182]. The parameters determined for the bulk structure are used since the herringbone phase is found to be very close to the molecular arrangement in the (102) plane of β -PTCDA [182]. Once we determined the molecular ordering in the herringbone phase, we can compare the structure with the contrast in the STHM image.

For the comparison between the two, we overlay the structure of the herringbone phase with the STHM image (fig. 4.14). Doing so, we obtain a good agreement between the molecules in the structure and the molecules in the STHM image. The close reproduction of the molecular structure allows us to determine the positions of the tiles in the image with high precision.

The overlaid image in figure 4.14 shows that the tiles are visible between oxygen and hydrogen atoms of adjacent molecules. The borders of the tiles always appear at a connection between two opposing atoms (white lines in fig. 4.14). At such positions, between oxygen and hydrogen atoms, hydrogen bonds may establish which would lead to a stabilization of the film.

Compared to other metal substrates (e.g. copper) the interaction between PTCDA and Au is comparably weak since PTCDA physisorbs on Au (111) [166]. Due to its weakness, the molecule-substrate interaction is expected to have little influence in the formation of the long range ordered structures [183]. Thus, the driving force for the structure formation should be the intermolecular interaction. One of these intermolecular interactions is the electrostatic interaction between global quadrupol moments of adjacent PTCDA molecules [184], which favours the arrangement in the herringbone phase (cf. fig. 4.14). However, due to the small distance between hydrogen and oxygen atoms of adjacent molecules hydrogen bonds are expected to contribute to the structural organisation

4 Examples of STHM images

[185]. In addition, the presence of intermolecular interactions in the herringbone phase has been concluded from their effect on the adsorption distance for PTCDA on Ag(111) [183].

In reference [186] different ordered phases of PTCDA have been investigated in order to determine favoured adsorption geometries. In this work the authors found hydrogen bonds between adjacent molecules in a structure constructed of molecular dimers. The position and orientation of the molecules in the constructed monolayer structure is similar to the herringbone phase. Remarkably, considering possible H - O connections above the tiles as hydrogen bonds, their number and locations coincide with the ones found in reference [186]. The coincidence is found for all possible H-bonds in this work except the one involving the anhydride oxygen atoms. Whereas in the STHM image the tiles also appear between the anhydride oxygen atom and the hydrogen atoms of an adjacent molecules, this bond is not observed in the theoretical work.

To test if the contrast between the molecules can be assigned to hydrogen bonds, we imaged another self organized structure of PTCDA molecules on the Au(111) surface. The square phase [114, 122, 185] coexists with the herringbone phase and usually appears in small patches in between herringbone islands on our samples. The scarcity at which the square phase is observed suggests less stability of the phase at the given preparation parameters (cf. section 3.1). The lower stability in turn indicates a weaker intermolecular interaction which would stabilize the phase. The different intermolecular interaction with respect to the herringbone phase should lead to a different intermolecular contrast in STHM images of the square phase.

A model of the square phase is shown in figure 4.15 (a). In contrast to the herringbone phase, the square phase has a quadratic unit cell. Like the unit cell of the herringbone phase, the unit cell of the square phase also contains two molecules. The angle between the molecules in the unit cell is close to 90°. But the angle between the unit cell vectors and the molecular axis is not precisely 45° which would lead to a symmetric ordering of the molecules within the unit cell. Thus the molecular axes do not point to the center of the next molecule in the unit cell but are shifted by ≈ 0.3 Å. This shift of the molecular axes leads to the formation of two differently sized cavities between the molecules labelled 1 and 2 in fig. 4.15 (a).

On the one hand, the same argument for the formation of the herringbone phase holds for the molecular arrangement in the square phase. The comparably weak molecule substrate interaction suggests that the molecular organization is governed by interactions between the molecules. The positions where the interaction occur slightly changed with respect to the herringbone phase, but like in the previous case hydrogen bonds

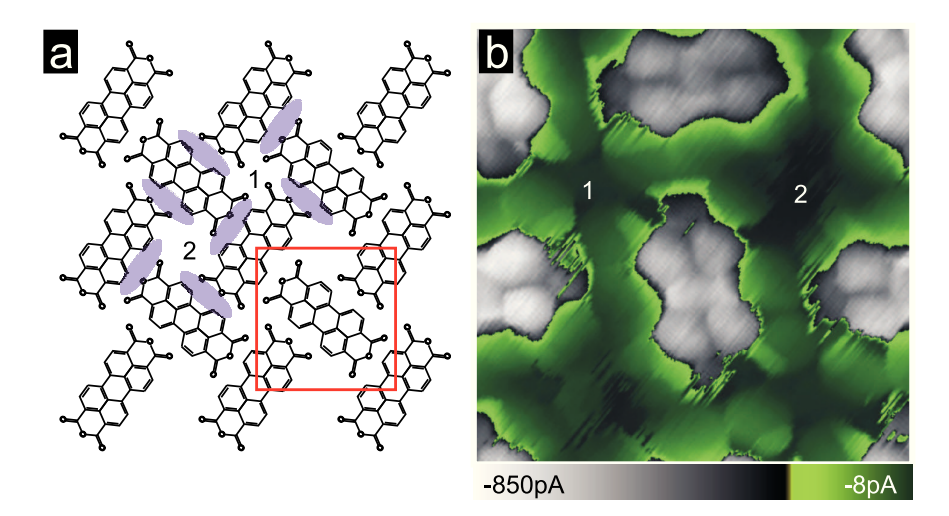


Figure 4.15: Square phase of PTCDA on Au(111). (a) Structure model of the square phase. Unit cell parameters $16.1 \times 15.5 \text{ Å}^2$ taken from reference [122]. The orientation of the molecules in the unit cell approximated from the STHM image in (b). Violet ovals indicate possible areas of hydrogen bonds. (b) STHM image pf the square phase. A similar two-color palette is used to enhance the contrast between the molecules as in figure 4.14. In (a) and (b) 1 & 2 mark the corresponding small and large cavities arising from the molecular ordering. Image parameters: (b) $24 \times 24 \text{ Å}^2$, const. height, V = -2 mV.

may be established where short and long axes of adjacent molecules come close to each other.

On the other hand, the rectangular orientation of the molecules in the unit cell may indicate an organization of the molecules which is strongly influenced by the electrostatic quadrupol moment of the molecules. However, if the driving force for the structural organization is the electrostatic interaction, the organization should be symmetric so that the positive charge of one molecule is located next to the center of the negative charge of the adjacent one (cf. structure D1 in reference [186]).

The observed shifts of the molecular axes, thus indicates the involvement of an interaction which favours the asymmetric ordering. This interaction may be hydrogen bonds between oxygen and hydrogen atoms which are stronger if the molecules are slightly shifted. If we assume the participation of hydrogen bonds in the structure formation, these bonds should occur in the purple shaded areas in figure 4.15 (a).

The STHM image of the square phase (fig. 4.15 (b)) reveals a contrast between the molecules. In contrast to the STHM image of the herringbone phase (fig. 4.14), the pattern is not as well resolved. Sharp tiles connecting adjacent molecules are absent in the image, however, brighter areas are visible between the molecules. These areas are brighter at the hydrogen terminated sides of the molecules and become darker towards

4 Examples of STHM images

the oxygens of the adjacent molecule. Now we can compare the contrast with the structure model.

To compare the model with the STHM contrast we will first focus on the cavities in the structure. Looking at the image one observes that the brightness is minimal in the center of both cavities while the area between the molecules appears bright. This means, areas where hydrogen bonds may establish, i.e. between hydrogen and oxygen terminated sides of adjacent molecules, appear brighter than areas in between. This is in agreement with the findings for the herringbone structure. But the contrast inside the cavities contains more information. In the smaller cavities (1 in fig. 4.15) four dark lines pointing from the molecules to the center of the hollow are visible. These dark lines appear where bright areas at the oxygen- and the hydrogen terminated sides of the molecules meet and no intermolecular interactions are expected. In contrast to the smaller cavities, the larger ones (2 in fig. 4.15) do not show these lines due to the larger distance between the bright areas.

Besides the structure of the cavities, a complex internal structure is visible inside the bright areas. The most prominent feature is a line pointing from the anhydride oxygen atoms of the molecules to an opposing C₆ ring. In some cases these lines appear brighter while in some cases the lines appear darker than the surrounding area. These prominent lines may indicate a special character of the bonds involving the anhydride oxygen atoms.

Having discussed the contrast between the molecules, we want to look at the contrast of the molecules. The perylene core of the molecules resembles a usual STHM contrast. However, an increased noise appears above the C₅O rings and the hydrogen terminated sides of the molecules. The appearing noise may be interpreted as instabilities of the molecule while the tip scans across its borders.

To investigate the differences between the STHM contrast of the herringbone and the square phase, we imaged both phases simultaneously. Figure 4.16 shows an STHM image of an island with both phases. The upper left corner of the image shows the herringbone phase while the lower right part shows the square phase.

The STHM contrast of herringbone phase is stable and reveals the same intermolecular contrast as shown in figure 4.14. In contrast to the herringbone phase, the STHM contrast of the square phase shows a similar noise as in figure 4.15 (b). The intermolecular contrast appears as structured rectangles around the molecules. At the positions where the bright rectangles of adjacent molecules meet a dark line appears which separates the molecules from each other.

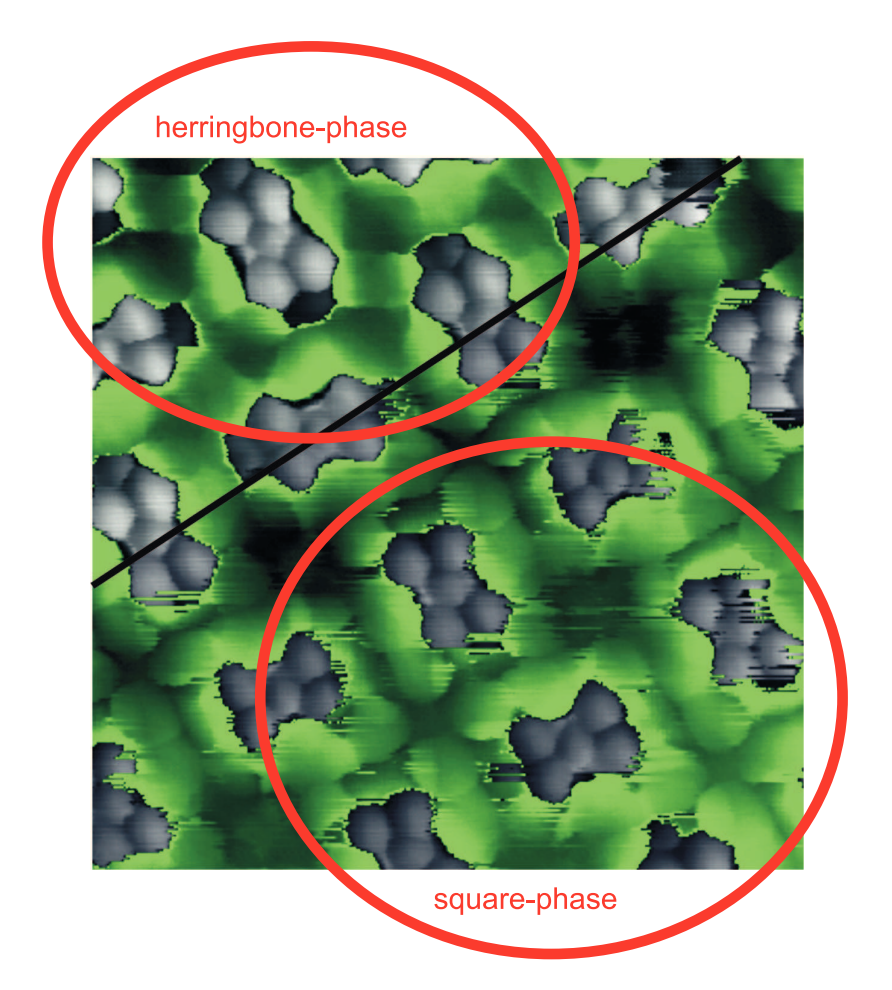


Figure 4.16: STHM image of PTCDA in herringbone and square phase. In the upper right corner of the image the herringbone phase is visible while in the lower left part of the image the square phase is imaged. From the image the differences in the intermolecular contrast can be seen directly, whereas sharp tiles appear between the molecules in the herringbone phase, more structures and increased noise appears in the square phase. The increased noise may indicate a lower stability of the square phase compared to the herringbone phase. To increase the contrast between the molecules two slightly different colour palettes have been used to illustrate the two phases. The cut of the images is indicated by the black line separating the square and the herringbone phase. Image parameters: $4 \times 4 \text{ nm}^2$, const. height, V = -2 mV.

The direct comparison between the two phases in figure 4.16 suggests that the increased noise observed in STHM images of the square phase is an intrinsic property of the molecular arrangement. Previously the higher stability of the herringbone phase in comparison with the square phase has been concluded from their different appearance on the samples. The contrast in figure 4.16 now supports this conclusion. Whereas the herringbone phase is stably imaged in STHM mode, an increased noise only appears in the square phase. Thus, the noise in the image directly indicates a lower stability of the square phase. The noise itself hereby may be generated from the molecules moving below the tip while scan-

4 Examples of STHM images

ning due to a lower internal fixation inside the layer. A third indication for the lower stability of the square phase, besides its appearance and the noise, is the STHM contrast between the molecules. The tiles between the molecules in the herringbone phase clearly connect adjacent molecules, but the intermolecular contrast between molecules in the square phase appears separated due to the dark lines between bright rectangles. The dark lines which interrupt the connections between adjacent molecules may therefore suggest a weaker interaction between the molecules which results a weaker binding of the molecules in the layer.

The comparison of the STHM contrasts of two self organized phases of PTCDA supports the finding that STHM directly images intermolecular interactions as can be seen by the different contrasts between the molecules. Secondly, the appearance of the organic layers in STHM images allows to draw conclusions about the stability of the phases and the fixation of the molecules within the layers due to different noise levels in obtained images.

4.3.2 Dehydrogenized PTCDA/Au(111)

So far, the STHM mode has shown to be sensitive to the structure of the sample. STHM images closely resemble the structure of the molecules. STHM images of molecular films suggest that besides the structure of the molecules even intermolecular interactions leave a mark. Now we would like to change the structure of the molecular film and test whether the changes can be observed in the images. Fortunately, the STM tip can be used to induce local chemical reactions, i.e. formation and breaking of intermolecular bonds [136]. In particular it is possible to controllably break C-H bonds [46, 187].

In the present context, we have strong indications that we are able to image hydrogen bonds in STHM. Thus, we would expect that the contrast between the molecules disappears if hydrogen atoms are removed from the molecules.

Scanning a PTCDA island at elevated bias (e.g. $V=4.5~\rm V$) induces chemical reactions within the layer. For the investigations we choose an island in herringbone phase since for the herringbone phase we observed the strongest indications of hydrogen bonds. A typical STM image after scanning is shown in figure 4.17 (a). The major part of the layer remains unaffected, while the molecule in the center of the yellow square (molecule A) exhibits changes in the molecular contrast. In contrast to other molecules, molecule A is not imaged oval but shows deformations in its lower right corner. Although the STM image vaguely indicates which part of the molecule is distorted, detailed information of

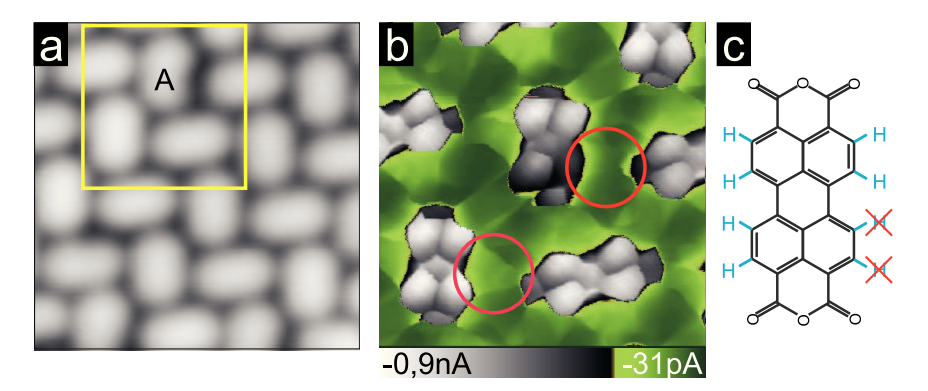


Figure 4.17: Chemical modified film structure. (a) STM image of the herringbone phase of PTCDA on Au(111) after applying $V=4~\rm V$ to the sample. The yellow square marks an area where a chemical reaction took place. (b) STHM image of the yellow square in (a). For a comparison identical positions are marked with red circles. In the lower circle the STHM contrast between the molecules is intact (cf. fig. 4.14). In the upper circle the contrast originating from the hydrogen bond is missing. (c) Chemical structure of a PTCDA molecule. The possibly removed hydrogen atoms are marked by a cross. Image parameters: (a) $50 \times 50~\rm \AA^2$, $I=0.1~\rm nA$, $V=316~\rm mV$, (b) $25 \times 25~\rm \AA^2$, const. height, $V=1~\rm mV$.

the nature of the distortions is not contained in the image. This is different in STHM (cf. fig. 4.17 (b)).

The molecules surrounding molecule A show the usual STHM contrast. But the contrast of molecule A is different. The upper part of the molecule exhibits no changes, but the lower part of molecule A appears slightly darker compared to other molecules. In addition, the lower left ring of the perylene core is still visible while the right ring appears faint. Moreover, looking at the pattern between the molecules, one observes that the pattern between the molecules is also missing next to the missing ring.

The STHM contrast of molecule A indicates where the molecular structure has changed. The faint appearance leads to the conclusion that one or both H-atoms may have been removed from the lower right C₆ ring (cf. fig 4.17 right panel). The missing termination of the ring may cause binding to the substrate and therefore a bending down of the lower part of the molecule, similar to the situation described in references [46, 187–189]. A bending of the molecule would explain the lower conductance above the lower part of the molecule due to an increased tip-sample distance.

In addition, if the hydrogen atoms are not present also hydrogen bonds must be absent. This is indeed observed in the image, where the pattern between the lower right ring and the adjacent molecule is missing, while the rest of the pattern reproduces the tile structure of the undisturbed herringbone phase (cf. fig. 4.14). Therefore, this confirms

4 Examples of STHM images

the interpretation of the interstitial contrast as being due to the presence of hydrogen bonds.

Summarizing the findings above, we used the STM-tip to cause chemical reactions in an organic layer. In particular, we removed hydrogen atoms from one of the molecules to break the intermolecular interaction which causes the structural organization of the layer. In contrast to conventional STM, the contrast in STHM mode leaves no ambiguities which part of the molecule changes due to the reaction. Additionally, the STHM contrast reveals the nature of the chemical reaction. In the area where the molecular structure changes the tile pattern between the molecules is absent. Before we associated the pattern with the hydrogen bonds, thus its absence suggests that due to the reaction H-atoms have been removed form the molecule. This finding is a strong indication for the ability of STHM to directly visualize intermolecular interactions.

4.3.3 Metal-molecule bonds in K/PTCDA layer

Up to now we used the STHM mode only to image hydrogen bonds between organic molecules. It would be interesting now to find out if it also works for other interactions. To this purpose we study a self organized structure of K/PTCDA/Au(111). The presence of metal atoms in the organic film change its electronic structure [190]. We will see below that the effect on the STM contrast of the molecular layer is not big at low concentration of metal atoms on the surface. But at higher dopant concentration, their interaction with the molecules leads to a reorganisation of the organic layer [101]. Thus, in the reorganized layer we can expect bonds between the molecules and metal atoms. In the following we want to see whether these bonds also directly appear in STHM images.

An STM image of a partially reordered island is shown in figure 4.18. In the upper left part of the image a gold step is visible at which PTCDA molecules are attached. In the center of the image the unchanged herringbone arrangement is still visible while in the lower part of the image reconstructed domains appear due to the incorporation of K into the molecular film.

The incomplete reordering of the molecular layers indicate that the amount of K is not sufficient to induce a complete restructuring. The most prominent structure of the K/PTCDA layers is the one in the lower right corner of figure 4.18. At first glance, this structure resembles the square phase of PTCDA on Au(111). However, the square phase is usually found only in small patches between larger domains in herringbone arrangement [122].

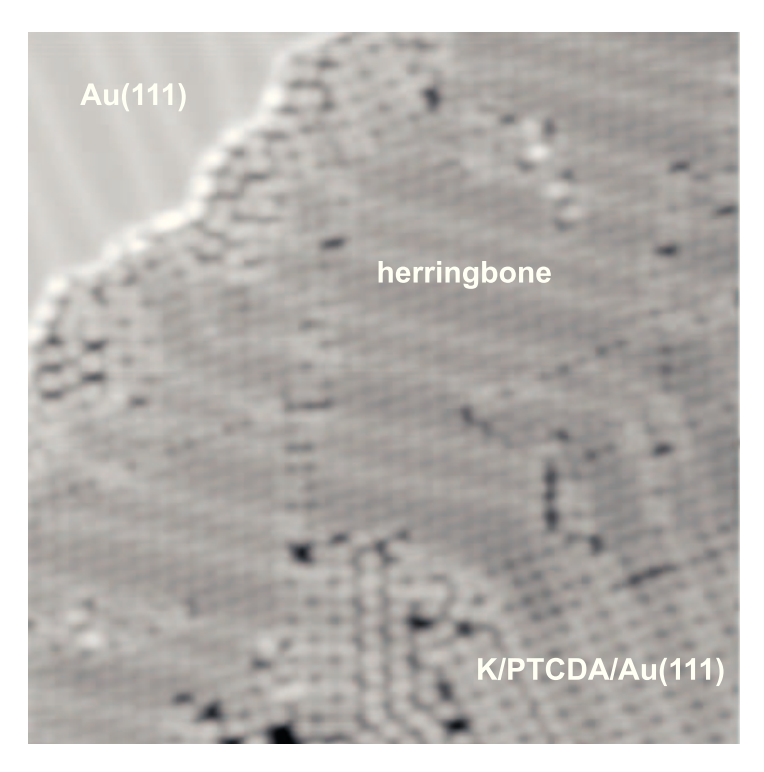


Figure 4.18: STM image of the restructured PTCDA/Au(111) after the deposition of K. Image parameters: $39 \times 39 \text{ nm}^2$, I = 75 pA, V = 1.5 V.

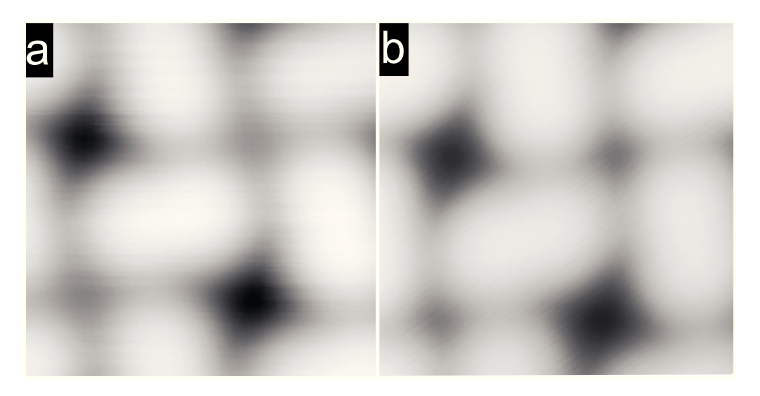


Figure 4.19: Comparison of STM contrast between K/PTCDA/Au(111) and the square phase of PTCDA/Au(111). (a) STM image of the reorganized part of an herringbone island. (b) STM image of the square phase recorded in the absence of K on the surface. Image parameters: (a) $2.4 \times 2.4 \text{ nm}^2$, I = 0.1 nA, V = 340 mV, (b) $2.4 \times 2.4 \text{ nm}^2$, I = 0.1 nA, V = 314 mV

Figure 4.19 (a) shows a magnified STM image of the K-induced square phase on a sample with a 1:1 ratio of square and herringbone phase. The size of the unit cell $(1.6 \times 1.6 \text{ nm}^2)$ and the orientation of the PTCDA molecules are very similar to the square phase (Unit cell: $16.1 \times 16.5 \text{ nm}^2$ taken from ref. [122]) of clean PTCDA/Au(111) (fig. 4.19 (b)). Since the STM image contains no direct evidence for the presence of K atoms in the

4 Examples of STHM images

structure, both phases appear virtually identical. The situation is very different if STHM images are considered.

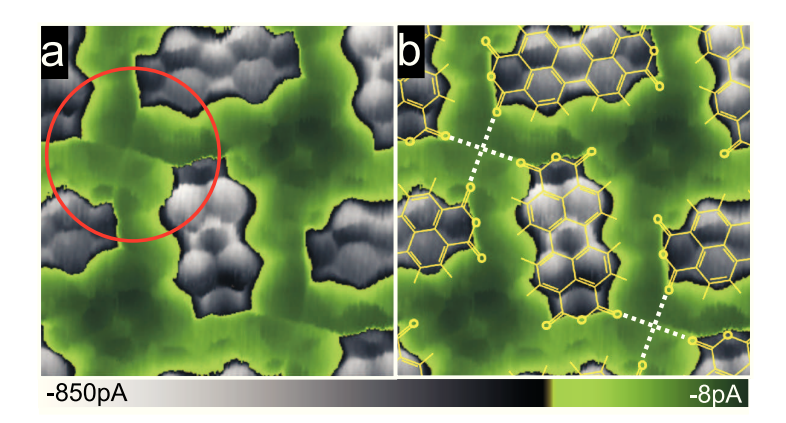


Figure 4.20: Imaging molecule-metal bonds in STHM. (a) STHM image of the area in figure 4.19 (a). The area in which the K ion is coordinated by the surrounding PTCDA molecules is indicated with a red circle. (b) The same image as in (a) but with the structure of PTCDA superimposed. Unit cell vectors: $b_1 = b_2 = 1.6 \pm 0.2$ nm. Additionally the bonds to the K-ion are indicated by the dashed white lines. Image parameters: (a) 2.4×2.4 nm², const. height, V = -2 mV.

In both imaging modes (STM and STHM) the potassium atoms are not directly visible. However, we will see in the following that in STHM the atoms leave a mark in the images. The feature indicating the presence of K will allow us to indirectly determine the positions of the metal atoms in the film. But before turning to the potassium related features in the STHM image, we want to compare the STHM contrast of the K-doped phase with the one of the pure square phase.

The STHM contrast of the K-doped phase (figure 4.20 (a)) reveals a sharp contrast of the molecules. Usually STHM images of the square phase of pure PTCDA exhibit an increased noise at the borders of the molecules, whereas the contrast in figure 4.20 (a) is as sharp as in STHM images of the herringbone phase (fig. 4.1). The noise at the borders of the molecules has been identified as an indication for a weaker binding of the molecules in the structure which in turn leads to a moving of the molecules in close vicinity of the scanning tip. Thus, the sharpness of the contrast suggest a stabilization of the molecules in the K-doped phase compared to the pure square phase. The stabilization in this case reaches a level which favours the square phase even with respect to the herringbone phase. But the reduced noise is not the only difference between the K-doped phase and the pure square phase.

The STHM image of the K-doped phase shows a remarkable feature in the small hollows between the molecules (upper right and lower left part of figure 4.20 (a)). Four thin sharp

lines extended from the corners of the adjacent molecules to the center of the hollow, forming a clover-leaf-like structure, whereas in the larger hollows (upper left and lower right part of figure 4.20 (a)) no such feature is observed.

In the square phase of pure PTCDA (fig. 4.15) a similar structure inside the small hollows is not observed. The sharp borders of the structure are reminiscent of the tiles between the molecules in the herringbone phase. In the herringbone phase the tiles represent the hydrogen bonds between adjacent molecules which lead the molecular organization in the layer. The comparable contrast between the lines may indicate a relation between the lines and the stabilization in the square phase.

A superposition of the molecular structure and the STHM contrast (fig. 4.20 (b)) clearly shows that the lines in the small hollows originate precisely from the carboxylic oxygen atoms of the four surrounding molecules. The molecules around the hollow form a clover leaf structure in which the cross in the center represents a stabilizing element. The stabilizing element in the structure can only be potassium which is located at the positions where the lines meet - in the center of the hollow.

In reference [191] potassium is found in an positive ionic state on Au surface at low coverages. With this the following picture emerges: at the position in the center of the small hollow a positively charged potassium ion interacts with the negatively charged oxygen atoms of the surrounding PTCDA molecules. The result is a 1:2 K/PTCDA structure of the mixed phase on the Au surface. Notably, the same structure has been suggested for the stabilization of PTCDA films with another metal dopant [101].

The present example indicates that besides hydrogen bonds also other interactions are directly visualized in STHM images. In this case, the electrostatic interaction between positive and negatively charged atoms appears as lines in the STHM image. These lines indicate the positions of potassium ions coordinated by the oxygen atoms of adjacent molecules which stabilize the film structure.

So far we can conclude that intermolecular interactions like hydrogen bonds and electrostatic interactions appear with remarkable clarity in STHM images. Both interactions have a rather polar character since they originate from the local charge distribution [192, 193]. Thus the appearance of the STHM contrast suggests that STHM may be sensitive to local electric fields in the sample plane.

4.4 Atomic resolution of metal clusters

We have successfully imaged the chemical structure of organic molecules and their interactions in STHM. In all the presented examples the contrast reproduced the bonding structure between the atoms on the surface. Now we want to apply the STHM imaging mode to other nano sized objects and see whether their structure is reproduced in the images.

Clusters of metal atoms develop interesting physical and chemical properties, e.g. as reactive surfaces for catalysis [194]. If we could image these surfaces atom by atom it would have many advantages, e.g.: precise determination of the cluster size, identification of reactive sites or engineering clusters atom by atom.

From STM images the size of small metal clusters is difficult to obtain due to an overlap of the wave functions of adjacent atoms [195, 196]. Up to now different approaches have been presented to determine the cluster size, e.g. by investigation of standing wave patterns [105]. However, determining the atomic structure of a cluster from a standing wave pattern may be quite demanding when it comes to more complex 2D arrangements. In the following we will demonstrate that in STHM images atomic resolution of the cluster can be achieved. This allows the determination of the cluster size by simply counting the atoms.

To build small clusters of adatoms on surfaces two different approaches are commonly used in STM. On the one hand single atom manipulation [135, 139, 140] and on the other hand indentation of the tip into the surface [137]. Here we choose the second method to produce small clusters of Au adatoms on the Au(111) surface.

Figure 4.21 (a) shows an STHM image of the adatom cluster. The cluster consists of 44 rounded, bright protrusions. The distance between the protrusions is 3 Å. The protrusions at the border of the cluster show a slightly different contrast than the protrusions in the center which may indicate a superposition of STM and STHM contrast, since in STM images of a single adatom on metallic surface often show unphysical heights due to a large density of states at the position of the adatom.

The distance between the protrusions in the image is close to the lattice constant of Au(111) (2.82 Å [168]). This finding suggests that each protrusion in the image corresponds to one Au adatom, however, this correspondence is not clear from the beginning.

The STHM images presented so far are closely related to the bonding structure of the surface. This is different in figure 4.21 (a). To elucidate the difference between the

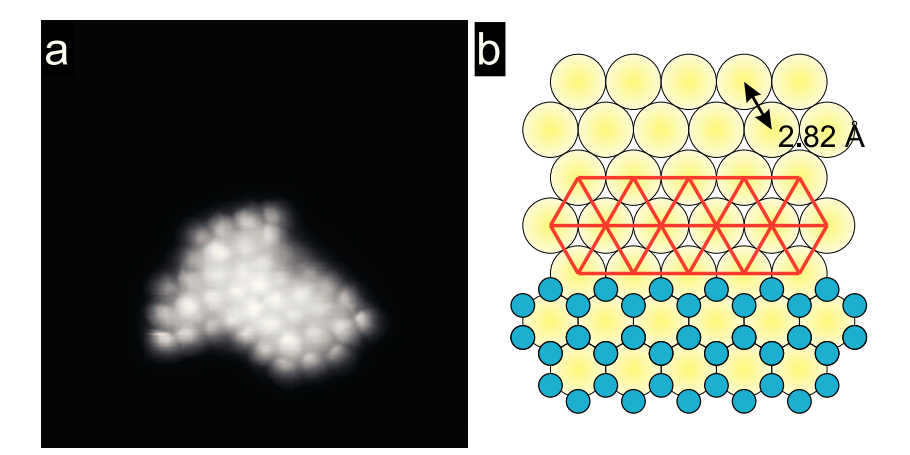


Figure 4.21: STHM contrast of metal clusters. (a) Image of a cluster of 44 Auadatoms on Au(111). (b) Sketch of different structures resulting from the closed packed
atom arrangement. top: structure of the Au (111) plane. Each of the yellow balls represents one of the Au atoms. middle: structure of the metallic interatomic bonds superimposed to the atomic structure. bottom: inverted contrast of the structure. Blue dots
imply a contrast in which the hollow sites between the atoms appear brighter than the
atop positions. Image parameters: (a) 5×5 nm², const. height, V = 2 mV.

bonding structure and the contrast, we have a look at a sketch of the structure of the Au lattice.

The atomic structure of the Au lattice is shown in figure 4.21 (b) top part. The red lines in the central part of figure 4.21 (b) indicate the positions of interatomic bonds. If the STHM mode would be sensitive to the bonds between the metal atoms one would expect that the areas between the bonds appear brighter or darker than the bonds themselves. The resulting structure would reproduce the hollow sites as dark or bright spots in the STHM image (bottom part of fig. 4.21 (b)). The resulting structure is thus reminiscent of a hexagonal or honeycomb lattice instead of the closed packed arrangement formed by the centers of the atoms. In addition, a contrast related to the hollow sites of the structure would lead to a smaller distance (1.62 Å) between the protrusions. The hexagonal arrangement and the resembling of Au lattice constant lead to the conclusion that each of the bright protrusions corresponds to one of the Au atoms of the cluster.

From the atomic resolution of the cluster we can draw the following conclusions for the STHM mode. Whereas in the STHM images of the organic molecules, the positions at which one would expect interatomic C–C and C–O bonds showed up as lines between brighter areas, the situation is different in the STHM image of the cluster of atoms. In the STHM image of the cluster, the positions of the atoms appear bright while at the positions at which one would expect interatomic Au–Au bonds the STHM contrast of the cluster shows no features. This finding shows that the STHM mode is not sensitive to

Examples of STHM images

every kind of interatomic bond. The insensitivity to the metallic Au–Au bonds leads to the question what is the similar quantity between the C–C, H–O, K–O bonds and the Au atoms that is sensed by the STHM mode?

5 Formation of the geometric contrast

The previous chapter dealt with different examples of STHM images. They demonstrated the power of the STHM mode by imaging the chemical structure of organic molecules, achieving atomic resolution of metal clusters and even directly visualize interactions between different adsorbates on metallic surface. However, the mechanism which lies behind the contrast formation has not been addressed so far.

Based on a detailed spectroscopic characterisation of the STHM junction, in the following we will analyse the properties of the imaging mechanism which leads to the geometric resolution in STHM mode and propose a model to explain the contrast formation.

5.1 Spectroscopic characterization of the STHM junction

The appearance of STHM contrast after condensation of H_2 (D_2) in the STM junction coincides with the emergence of non-linear differential conductance spectra ($G(V) \equiv dI/dV(V)$) [55]. The nature of the non-linear behaviour has been investigated in detail in nanojunctions containing H_2 [55, 172, 197–199]. The non-linear behaviour shows up as spikes and dips in the conductance evolution. In the literature, the spikes and dips have been assigned to transitions between structural different states of the junction. The transition occurs due to inelastic scattering electrons which dissipate part of their energy into the junction. However, the precise nature of the associated two level system is still debated [172, 197, 198].

Disregarding the physical processes which originate in the specific shape of the spectra, the coincidence in appearance of the image contrast and the non-linear spectra suggests a relation between the two. Therefore, we will investigate the spectroscopic properties of the junction to characterize the state which leads to STHM image contrast. Without loss of generality, we will restrict the following discussion to D_2 since we never observed any systematic difference between the STHM images recorded with H_2 and D_2 .

5.1.1 Evolution during deposition

We start our investigations by looking at the evolution of conductance spectra during deposition of D_2 on the surface. Whereas we usually control the coverage of D_2 from the STHM contrast in obtained images (cf. section 3.3), the presence of D_2 also shows up in recorded spectra.

The spectra in figure 5.1 show the evolution of the conductance behaviour with respect to the exposure time. Before deposition I shows a linear dependence on the applied bias while the dI/dV spectrum is constant (black in fig. 5.1). After a certain, exposure time an increased noise appears in the regime close to zero bias (|V| < 25 mV). In this case, the deposition is stopped, subsequent to the observation of the noise. With increasing residence time (sequence blue to magenta), the noise first increases before the conductance around zero bias stabilizes. Usually, shortly after stable spectra are obtained, the junction reaches its final state, which is characterised such, that no further evolution of the spectra occurs. At this point, subsequently recorded spectra show no difference between each other.

The evolution of the conductance spectra in figure 5.1 reveals the influence of D_2 on the conductance of the spectra. At low coverages the presence of D_2 shows up as increased noise close to zero bias while the conductance at higher bias remains unaffected. Images recorded at this coverage show spontaneous switching events between the conventional STM and the STHM contrast (cf. section 3.3), whereas with increasing coverage the number of switching events increases until stable imaging in STHM mode becomes possible. The evolution of the spectra with residence time shows a similar behaviour: first the noise around zero bias increases before the conductance stabilizes. Only after stabilization of the spectra we obtain stable STHM images. This finding suggests a relation between the STHM contrast and the final shape of the conductance spectrum.

The final shape (magenta in fig. 5.1) is characterised by two sharp spikes ($V \approx -40 \text{ mV}$) and $V \approx +40 \text{ mV}$) and a zero bias anomaly (ZBA) appearing as a dip in dI/dV. Although the distinct shape of the spectra recorded after different sample preparations show some variability, we can identify a characteristic behaviour.

The recorded spectra always appear symmetric around zero bias, i.e. the position of features in the spectra occur always for positive and negative bias at the same value. These features are the ZBA and the spikes. Whereas the ZBA sometimes appears as a dip, a protrusion or is absent at all, we always observe spikes in the spectra.

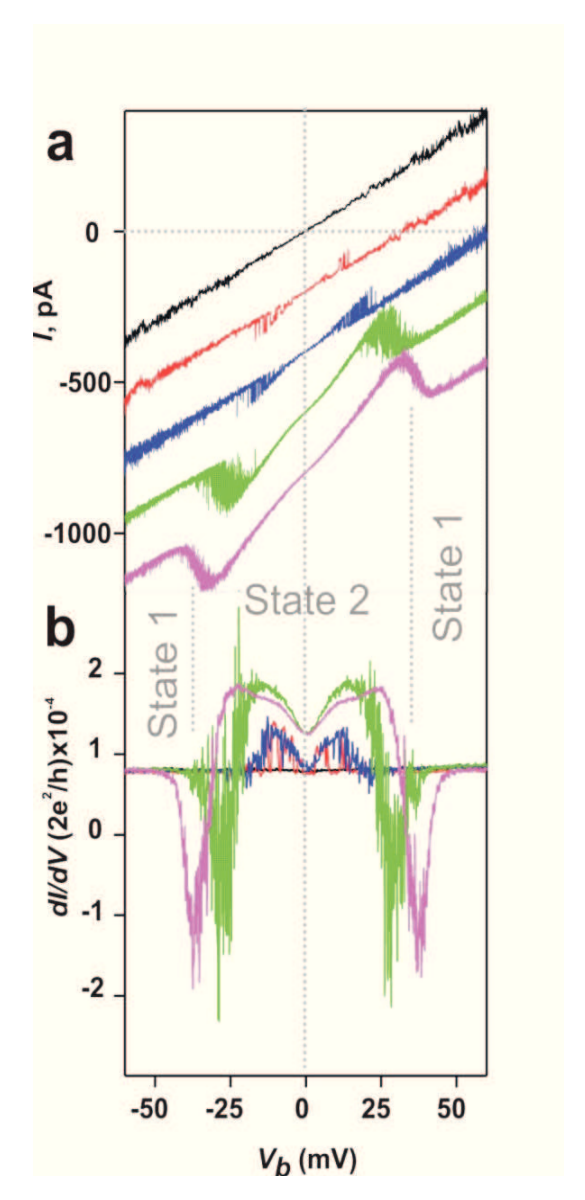


Figure 5.1: Spectroscopic characterisation of the junction after deposition of H_2 . Reproduced from reference [55] (a) I/V curves measured after different delay times. The topmost spectrum has been measured before H_2 deposition and reveals a linear current behaviour as expected for a clean junction. With increasing time (top to bottom) the behaviour of the junction changes and a second state evolves close to zero bias. First, the second state appears as noise in the spectrum at $|V| \approx 20$ mV. After some time the noise disappears and the second state stabilizes. (b) Differential conductance measured simultaneously with the current in (a). In the dI/dV curves the transition between the different conductance states of the junction shows up as spikes in the spectra. With increasing time this spikes shift to higher voltages. In addition a zero bias anomaly (ZBA) appears in the spectra. Colour code: black: without H_2 , red: at t=0 s when deposition of H_2 is stopped, blue: t=22 min, green: t=80 min, magenta: t=14 h; stabilization point for all spectra I=0.1 nA, V=340 mV

5 Formation of the geometric contrast

The spikes frame the bias range close to zero bias in which the noise appeared before. Clearly the increased noise arises from the presence of D_2 in the junction. Thus, the spikes mark the transition between two different states of the junction, one without D_2 (state 1) and one with D_2 (state 2). This interpretation of the spikes is in agreement with the findings in literature [172, 197, 198], where the spikes are identified with inelastic transitions between structural different states of the junction.

5.1.2 Switching On/Off STHM contrast

According to the findings in the previous section, the following picture emerges, which is schematically sketched in figure 5.2. At bias values $|V| < |V_{inel}|$ (grey shaded area in fig. 5.2) D_2 is present in the junction, whereas at bias $|V| > |V_{inel}|$ the junction is empty. Consequently, the spikes at $|V| = |V_{inel}|$ mark the transitions between the two states. At this bias ($|V| = |V_{inel}|$) D_2 is expelled from the junction, thus one would expect the STHM contrast to disappear once a high bias ($|V| > |V_{inel}|$) is applied.

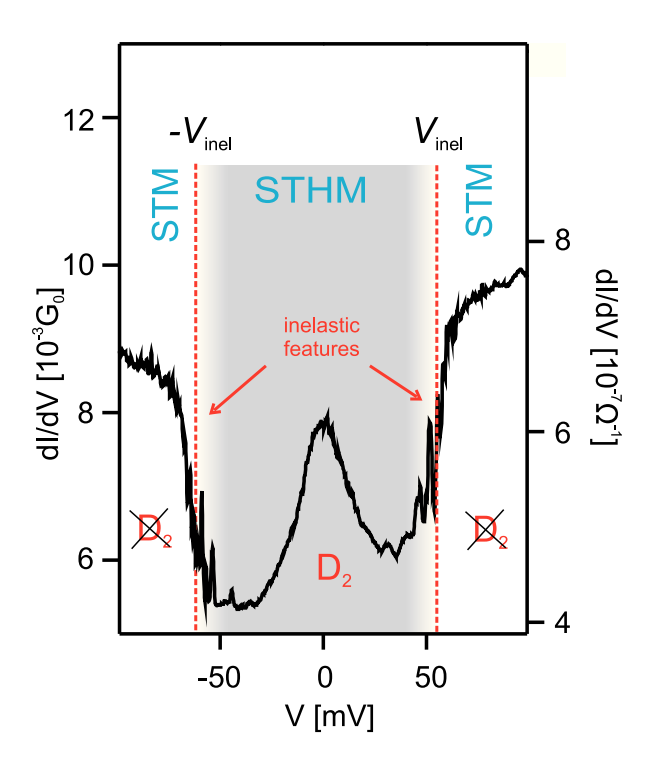


Figure 5.2: dI/dV spectrum measured in the center of PTCDA/Au(111). The spectrum is recorded with lock-in detection (10 mV modulation, frequency 1.3 kHz). $G_0 = \frac{2e^2}{h} = (12.9 \text{ k}\Omega)^{-1}$

Looking at images recorded at a bias assigned to the different states confirms this assumption. Images recorded in state 1 ($|V| > |V_{inel}|$) show no difference to the conventional STM contrast (cf. fig. 4.1 left), whereas Images recorded in the state 2 ($|V| \approx 0$ mV) show STHM resolution (cf. fig. 4.1 center). In addition, the identity of subsequently recorded spectra indicates that it should be possible to reproducibly switch between the STM and the STHM contrast by choosing an appropriate bias.

The reproducible switching between STM and STHM contrast enables us to directly compare both structural states of the junction. But before continuing the spectroscopic analysis, we will shortly turn to the amount of D_2 which is accommodated in the junction during the STHM contrast formation.

5.1.3 D_2 coverage in the active part of the junction

The observation that the STHM contrast only appears in state 2 indicates, that we need to understand the structure of the STHM junction in this state to identify the imaging mechanism. To this end, we will start by analysing the amount of D_2 present in the junction during scanning in STHM mode.

The conductance values in our experiments are usually in the range of $G > 5 \times 10^{-5}$ G₀. At this conductance the tip-sample separation should be smaller than 1 nm as the following estimation shows: At direct contact, which corresponds to a tip-sample separation of $d \approx 3$ Å (atomic Au-Au distance [168, 200]), the conductance is typically in the order of the conductance quantum ($G_0 = 2e^2/h$). For a pure metallic junction the current decays by a factor of 7.4 Å⁻¹ [36]. Inserting all values into the first derivative of equation 2.11 yields a maximum distance of $d_{max} \approx 8$ Å.

Given a typical adsorption height of H_2 $d_{alt} \approx 3.2$ Å [201] and the typical H_2 - H_2 distance (in the condensed bulk) of $d_{H_2H_2} \approx 3.3$ Å [173], two monolayers would require a tip sample distance of $d_{double} \geq 2d_{alt} + d_{H_2H_2} \approx 1$ nm [202]. Comparing now this distance with the estimated tip-sample separation (d_{max}) leads to the conclusion that under STHM imaging conditions at most a single monolayer of D_2 can accommodate in the junction. Having estimated the height of the D_2 cluster below the tip, we can also estimate its lateral dimensions.

Clearly, the STHM imaging mode requires the presence of D_2 just below the STM-tip apex in the region of the tunnelling electrons. The high lateral resolution achieved in STHM images, which in fig. 4.1 is in the order of 50 pm compared with the size of a single D_2 molecule ($d_{D_2} \approx 3 \text{ Å } [173]$) suggests that only a single D_2 molecule is located in the

active part of the junction during the contrast formation. Thus, we can model the STHM junction by a single D_2 molecule just below the tip apex.

5.1.4 Structural state of the junction during imaging

So far we can conclude that the condensation of a single D_2 monolayer induces a new conductance state close to zero bias. Scanning the surface at low bias (|V| < 10 mV), we obtain STHM resolution. This means that during the image acquisition the junction is all the time kept in the new conductance state.

The STHM images themselves represent lateral maps of the junction conductance in the D_2 induced state $(dI/dV(x,y,z_0,V\approx 0 \text{ mV}))$, where $z_0=const.)$. Thus, one may ask if the contrast originates from the lateral variation of the junction's shape, which yields different conductance values at zero bias, or if the scanning of the tip plays an additional role in the contrast formation, e.g. by dragging a D_2 cluster across the surface.

Now we address the issue of lateral variations of the D_2 induced state. To this end, we recorded a full dI/dV spectrum at each point of an image. The recorded datacube on the one hand allows the comparison of spectra recorded above different positions of the sample, on the other hand it allows the reconstruction of images at any bias.

Fig. 5.3 shows images and spectra extracted from a dI/dV(x,y,z=const,V) datacube consisting of 64×64 spectra recorded while the tip constantly scanned a single PTCDA molecule. Figure 5.3 (a-d) shows four images reconstructed from the datacube at different bias values. Figure 5.3 (e) shows two examples of spectra taken from positions indicated in 5.3 (a). The right part of the figure corresponds to the spectrum at the specific position of the dot. The left part shows an average over adjacent spectra with a diameter of 0.6 Å (indicated by the diameter of the spots in (a)).

Comparing the image reconstructed at zero bias (fig. 5.3(a)) with the one recorded with a scanning tip (fig. 4.1), one observes that they are identical. The fact that the observed STHM contrast in both images is the same proves that the STHM contrast is independent of the scanning process. This indicates that the junction is always in an equilibrium state during scanning and that all relevant time scales for the contrast formation process are fast compared to the time scale of the measurement.

Note, however, that D_2 can be expected to freely diffuse on the surface due to its comparatively small binding energy ($\approx 20 \text{ meV} [200]$) compared to e.g. CO ($E_b = 550 \text{ meV}$

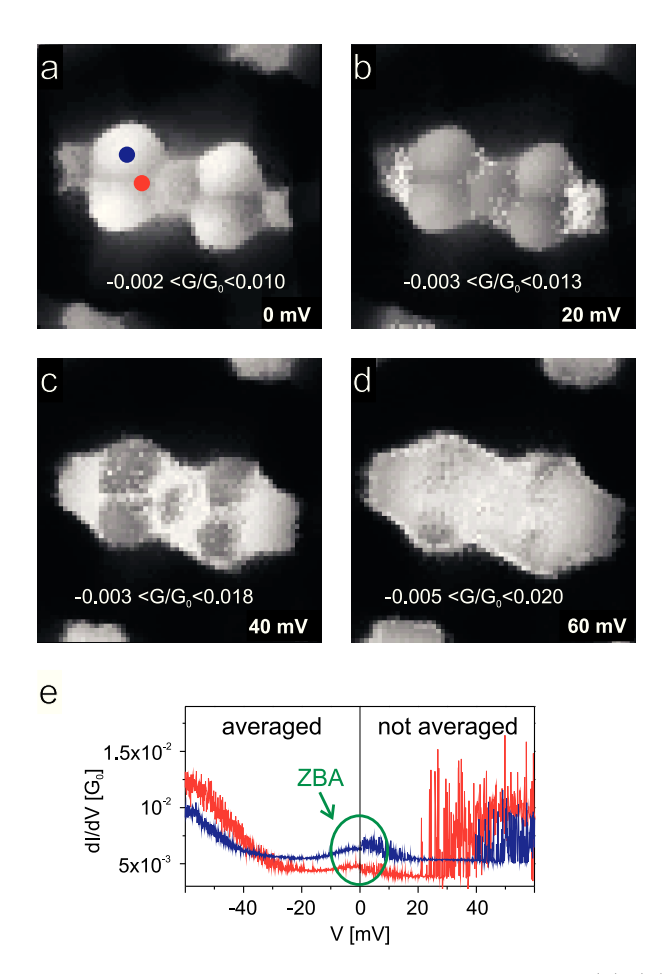


Figure 5.3: Results from a spectroscopic datacube. (a)-(d) 64×64 pixel, 1.3×1.3 nm² dI/dV constant height STHM images extracted from the spectroscopic data acquired above PTCDA/Au(111) with D₂. At each pixel of the image one dI/dV spectrum was recorded, using lock-in detection (modulation amplitude 4 mV, frequency 4.8 kHz, spectrum acquisition time 1 s). Minimum (black) and maximum (white) differential conductances are given in the images, in units of the quantum conductance $G_0 = \frac{2e^2}{h}$. Negative conductance values are caused by sharp conductance spikes (cf. text). (e) dI/dV spectra measured at the marked locations in (a). Right panel: spectra as measured. Left panel: spectra averaged over red and blue circles (diameter 3 pixels ≈ 1 Å) in (a). Sharp noise features beyond 20 mV bias are conductance spikes associated with the D₂ molecule out of the junction (cf. text).

[203]) which statically binds on Au(111) at temperatures used in our experiments. The independence of the contrast on any experimental time scales suggests that for a simple model of the STHM junction we can disregard dynamics in the junction. Thus, it is sufficient to model the STHM junction with a single D_2 molecule statically bound to the tip.

Once we determined that the information leading to the STHM contrast in scanned images is also contained in the recorded datacube, we can continue the analysis. First we

5 Formation of the geometric contrast

start with the behaviour of the STHM contrast at finite bias. The images reconstructed at different bias show how the contrast disappears at increased bias (cf. fig. 5.3 (a-d)).

With rising bias, the conductance above more and more points atop of the molecule switches to a higher value which is the same for all positions ($G_{vac} \approx 1.5 \times 10^{-2} \,\mathrm{G_0}$). This evolution continues until the conductance is homogeneous above the entire molecule as expected for conventional STM. The first positions where the conductance changes are the C₅O rings at the ends of the molecule which appear bright already at $V = 20 \,\mathrm{mV}$ (cf. fig 5.3 (b)). Increasing the bias further, the contrast disappears above positions where C-C bonds are expected leading to the impression of an inverted contrast in the image reconstructed at $V = 40 \,\mathrm{mV}$ (cf. fig 5.3 (c)). Finally, the conductance values increase in the center of the C₆ rings, so that at $V = 60 \,\mathrm{mV}$ the conductance above the molecule is almost homogeneous (cf. fig 5.3 (d)). In figure 5.3 (d) the contrast, except the outline of the molecule, is already very close to the one in conventional STM images (cf. fig. 4.1).

The evolution of the reconstructed images in figure 5.3 (a-d) suggest that the image contrast does not suddenly switch between STM and STHM contrast when the bias crosses the position of the spikes in the dI/dV spectra (cf. fig. 5.2). The stepwise vanishing rather indicates that the bias at which D_2 is excited out of the junction depends on the position of the tip above the molecule. To determine if the bias, at which the spikes in the spectra appear, changes between different tip positions we have to have a closer look at the obtained spectra.

All spectra contained in the datacube show the same characteristic features, a dip at zero bias (ZBA) and increased noise at elevated bias (cf. figure 5.2). However, the distinct shape of the spectra changes from point to point. The observed differences are the conductance around zero bias and the bias at which the increased noise appears. This is shown for two points in figure 5.3 (e).

The noise in the spectrum recorded above a carbon atom (red spectrum in fig. 5.3(e)) appears at smaller bias than the noise in the spectrum recorded above the center of a C_6 ring. Since in the bias region where the noise appears, the conductance is increased with respect to the conductance around zero bias, the higher bias at which the noise appears leads to the observed inversion of the contrast in figure 5.3 (c).

Assigning the noise to the excitation of D_2 in the junction, the different behaviour in figure 5.3 (e) can be easily understood. The center of a C_6 ring can be expected to be a preferred binding site for D_2 [201]. Thus the binding of D_2 in the junction should be stronger when

the tip is located above this position than e.g. above a carbon atom. Consequently a higher energy (E = eV) is necessary to excite D_2 away from the stronger bound position above the center of a C_6 ring (blue spectrum in fig. 5.3(e)) than above a carbon atom (red spectrum in fig. 5.3(e)).

The different binding of D_2 , depending on the position above the sample, explains the evolution of the contrast with increasing bias, although, the mechanism behind the contrast formation cannot be determined from the presented data. However, up to now we only varied two free parameters, bias (V) and lateral tip-position (x, y). Thus, to get further insight into the STHM mechanism, we should vary the last free parameter, namely the tip-sample distance (z).

5.1.5 Dependence of the conductance on the tip-sample distance

In section 4.2.1 we saw that the tip-sample distance during scanning affects the obtained contrast. The distance dependence of the contrast may indicate that the tip-sample separation has substantial influence on the junction conductance in the D_2 induced conductance state. To test the influence of the tip distance to the molecule on the conductance of the junction, we recorded differential conductance spectra at various distances.

A series of dI/dV(V) spectra recorded above the center of PTCDA with subsequent decreasing of the tip-sample distance in steps of only 0.1 Å is shown in fig. 5.4. The acquired spectra cover a total range of 3.4 Å, starting from the stabilization point of the tip above the molecule ($z_{displacement} = 0$ Å).

The dI/dV-spectra presented in figure 5.4 clearly show a dependence of the shape of the spectrum on the tip height. Depending on the tip sample distance the spectra contain spikes at two different positions ($V_{outer} \approx 75 \text{ mV}$ and $V_{inner} \approx 25 \text{mV}$) and a ZBA which appears as a dip at the stabilization point then converts into a peak before it disappears completely.

Although the spectra show a complex, continuous evolution with decreasing tip-sample distance, we can identify three different kinds of spectra which are characterised by the position of the spikes and the appearance of the ZBA. The first kind of spectrum is the one obtained at the largest tip-sample separation covered by the experimental data $(z_{displacement} < 0.3 \text{ Å})$: the spikes appear at $\pm V_{outer}$ and the ZBA appears as a dip. The second kind of spectra appear at intermediate distance $(0.4 \text{ Å} < z_{displacement} < 1.8 \text{ Å})$. The second kind has spikes at $\pm V_{inner}$ while the ZBA appears as a peak. Finally, the

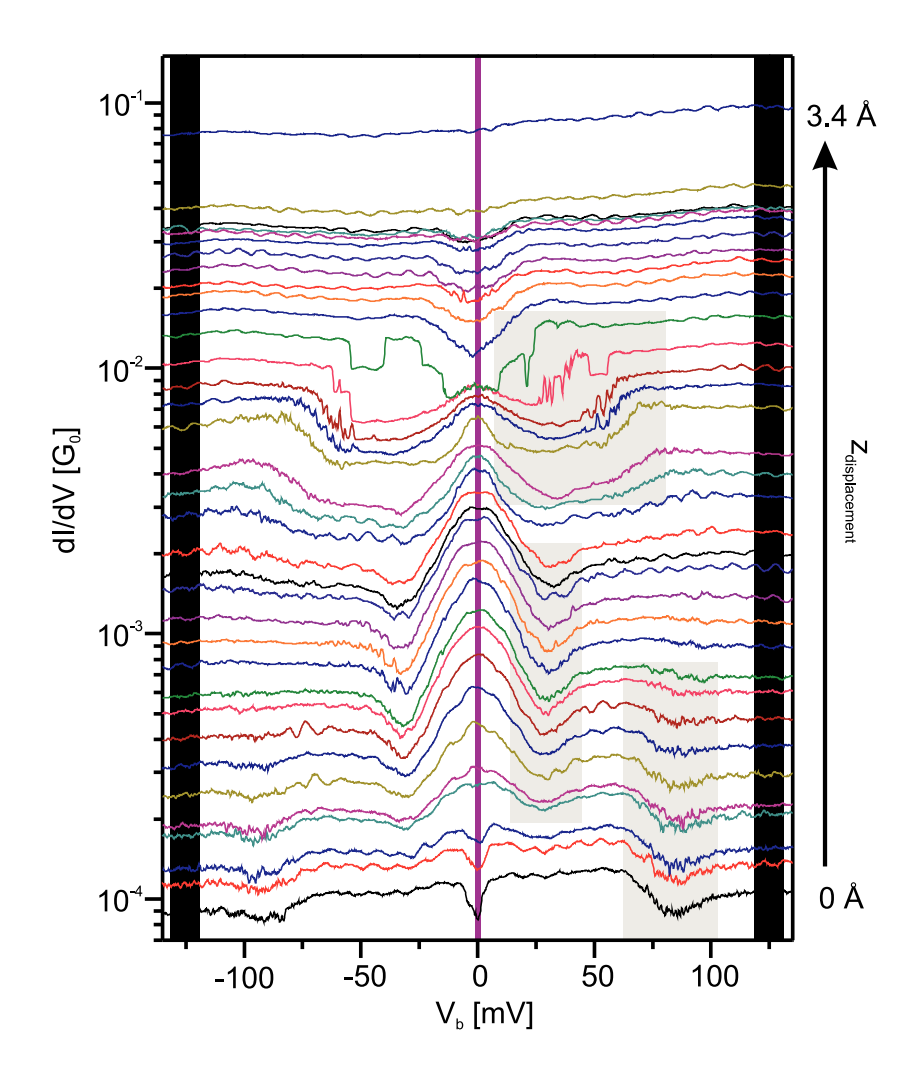


Figure 5.4: dI/dV spectra measured in the center of PTCDA/Au(111) with D₂ at different tip-surface distances (step = 0.1 Å. The spectra are recorded with lock-in detection (modulation amplitude 10 mV, frequency 2.3 kHz)). Regions shaded in light grey indicate the regions of the conductance spikes (cf.text).

third kind of spectra appear at close tip-sample distance ($z_{displacemenet} < 2.3 \text{ Å}$). In these spectra no spikes appear, however, they exhibit a small dip at zero bias which fades away while the tip height is further reduced.

The transitions between different kinds of spectra appear smoothly so that at each distance we obtain a reproducible shape of the spectrum. Although the spectra recorded with

different tips and at different D_2 coverages show some variability, the unique shape of the spectra at a certain tip height indicates, a special dependence of the interaction of D_2 in the junction on the tip-sample separation. The property which leads to the dependence of the shape of the spectrum on the tip height may be the same as the one which leads to the contrast in STHM images, therefore, we need to further analyse the relation between the two.

The spectra presented so far (cf. figures 5.1, 5.2, 5.3) have a similar shape as the second kind of spectra, i.e. spikes at low bias and the ZBA appearing as a peak, therefore we will start the further discussion with these spectra. The spectra of the second kind appear at an intermediate distance (0.4 Å $< z_{displacement} < 1.8$ Å). According to the results obtained in the previous paragraphs, at these distances we would expect that at low bias ($|V| < V_{inner}$) a single D₂ monolayer is present between the tip and the sample which is excited out of the junction at a bias higher than the spikes ($|V| > V_{inner}$).

In figure 5.4, at increased tip-sample separation ($z_{displacement} < 0.4 \text{ Å}$) a second set of spikes appears (at $|V| = V_{outer}$) whereas the spikes at $|V| = V_{inner}$ are not present. The second set of spikes may be interpreted as different structure of D_2 in the junction [172]. The different structure may either indicate a different geometry of D_2 in the junction or the presence of a D_2 cluster containing several molecules which fits below the tip at higher tip-sample separation. Although the origin of the different shape of the spectra is unknown, it shows that the interaction of D_2 in the junction changes at elevated tip-sample distance. Together with the observation that images recorded at larger tip height do not show STHM contrast (cf. fig. 4.5), this suggests that the mechanism which lies behind the contrast formation in STHM images involves a particular state of the junction which only forms at close tip-sample separation.

If the tip-sample distance is further reduced from the distance at which the spectra of the second kind are obtained, the spikes smear out and after a noisy transition, the spectra convert into the third kind. The spectra of the third kind appear flat in a wide range of bias, except close to zero. A flat conductance is also expected for an empty junction without D_2 . The similarity to the behaviour of the empty junction suggests that with decreasing tip-sample distance the influence of D_2 on the conductance is getting smaller or even disappears completely. This picture is supported by the images recorded at small tip height which show a LUMO-like contrast (cf. section 4.2.1).

The analysis of spikes leads to suggestions how D_2 interacts with the junction at different distances, although, information about the junction's state which leads to the STHM contrast cannot be directly extracted. Since the STHM contrast only appears close to zero bias (cf. fig. 5.3), the information about the relation between the distance and

5 Formation of the geometric contrast

the contrast should be encoded in the evolution of the conductance close to zero bias. To elucidate the dependence of the conductance at zero bias, we extract its values from figure 5.4 and plot them against the z displacement. In addition, the fact that at high bias ($|V| = V_{outer}$) the junction is expected to be empty allows us to directly compare the conductance of the empty junction with the state which leads to the STHM contrast.

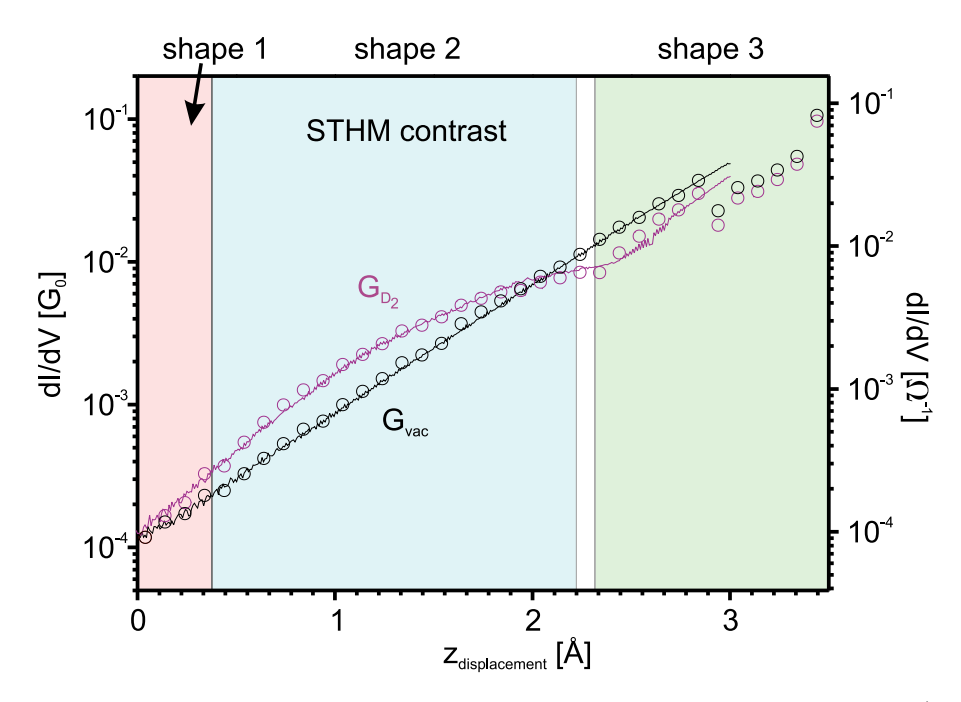


Figure 5.5: Differential conductance with an approaching tip at -5 mV (purple line) and 120 mV to 130 mV (black line). The black line was averaged over four different spectra as $(\frac{dI}{dV}(-130 \text{ mV} + \frac{dI}{dV}(-120 \text{ mV} + \frac{dI}{dV}(120 \text{ mV} + \frac{dI}{dV}(130 \text{ mV})/4$. Data points (purple and black open circles) have been extracted from the shaded regions in figure 5.4. In addition, the areas in which the different shapes of the spectra are obtained are indicated.

Averaging dI/dV-data over the two shaded areas in figure 5.4, one obtains one spectrum for the evolution of the conductance at zero bias (G_{D_2}) and one at elevated bias (G_{vac}) . The resulting data points are plotted against the tip displacement in figure 5.5 (open circles in the corresponding colour to the shading). In addition dI/dV-spectra recorded at fixed bias while the tip approaches the surface (lines in figure 5.5) are shown.

Before turning to the discussion of the conductance evolution, we focus on the resistivity of the junction's state against tip manipulation. Figure 5.5 shows that the spectra recorded with approaching tip and reconstructed from the series of spectra in figure 5.4 are identical. This indicates, that the STHM junction is not only in an equilibrium state

during lateral movement (cf. fig. 5.3), but also when the tip moves perpendicular to the surface.

Now we turn to the dependence of the conductance in the two states (with and without D_2). The conductance at high bias, when the junction is empty, shows a simple exponential increase with decreasing tip-sample distance as expected for pure tunnelling. The evolution of the conductance at zero bias, where STHM images are recorded (light blue area in fig. 5.5), is more complex and deviates from the exponential increase of G_{vac} . The deviations show up as two regimes in the conductance evolution. For larger tip sample separation ($z_{displacement} < 1.2 \text{ Å}$), the conductance of G_{D_2} increases faster than G_{vac} , while for shorter distances (1.2 Å $< z_{displacement} < 3 \text{ Å}$) the conductance increases more slowly than the one of the empty junction.

In addition, figure 5.4 has shown that at closest distances ($z_{displacement} > 3 \text{ Å}$) we obtain a different shape of the spectra without spikes (third kind). At this distance range both spectra (G_{D_2} and G_{vac}) in figure 5.5 reveal deviations from the exponential behaviour. This leads to the conclusion that the deviations from the exponential behaviour in both spectra for close tip-sample distance most likely indicate structural changes in the junction.

So far we can conclude that in the presence of D_2 the dependence of the junction conductance on the tip-sample separation is more complicated than for pure tunnelling. However, the question whether the distance dependence is related to the STHM contrast cannot be deduced from considering a single spectrum. Rather, we need to compare the evolution of the conductance with tip-sample separation at different points of the STHM image.

5.1.6 STHM resolution at different tip-sample separations

The evaluation of figure 5.5 has shown that spectra recorded with approaching tip (G(V = const., z)) are identical to the ones extracted from dI/dV(V, z = const.) data. Therefore, to compare the conductance behaviour above different points it is sufficient to record G(V = const., z) above positions at which we observe a difference in STHM images, these positions are e.g. the center of a C₆-ring and the carbon atoms.

To quantify the effect of D_2 on the junction conductance and to simplify the comparison of the spectra we define the conductance ratio $R_G(\vec{r}) = G_{D_2}/G_{vac}$, where \vec{r} denotes the lateral tip position. The normalization of G_{D_2} to the conductance evolution without D_2 (G_{vac}) in this context makes sense since in STM images no submolecular resolution is

observed (cf. fig. 4.1), thus no variation in G_{vac} spectra is expected for different positions of the sample (cf. green curve in fig. 5.6 (b)).

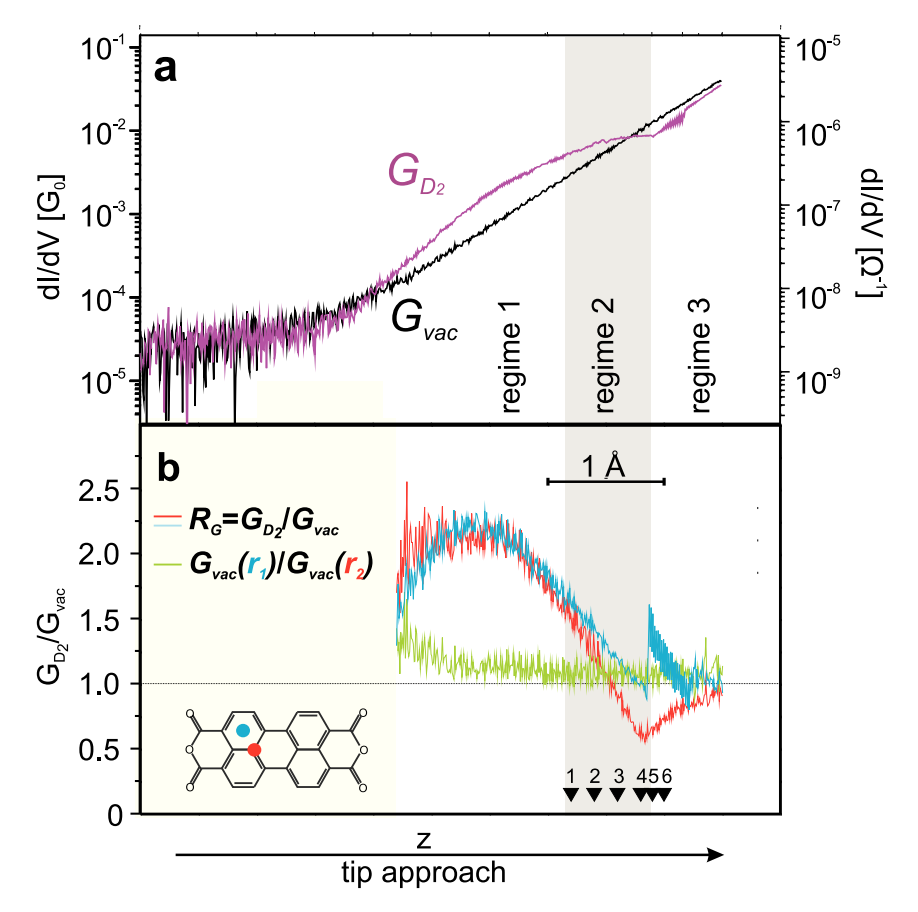


Figure 5.6: Direct comparison of the evolution of the conductance with decreasing tip sample distance above different positions of PTCDA. (a) $\frac{dI}{dV}(z)$ spectra recorded at fixed bias, measured with D₂ on PTCDA/Au(111) (z-axis scale given by scale bar). $G_0 = \frac{2e^2}{h}$ is the quantum conductance. G_{D_2} (magenta): V = -5 mV. G_{vac} (black): V = -130 mV. All spectrarecorded from the same stabilization point. (b) $R_G(z)$ curves (cf. text) measured at positions \vec{r}_1 (blue) and \vec{r}_2 (red) marked in the lower inset. The ratio $G_{vac}(\vec{r}_1)/G_{vac}(\vec{r}_2)$ is shown in green.

For a direct comparison between the conductance ratios and the single spectra (cf. fig. 5.5), the originally recorded spectra above the center of a C₆-ring which result in $R_G(\vec{r_1})$ are shown in figure 5.6 (a). Conductance ratios for different points above PTCDA are shown in figure 5.6 (b) (red and blue spectrum). The positions above the molecule where the spectra have been recorded are shown in the inset of figure 5.6 (b).

The evolution of R_G curves measured above different points of the PTCDA molecule in figure 5.6 (b) show the same qualitative behaviour: first conductance ratios increase until they reach a maximum while beyond the maximum both ratios quickly drop. Until the maximum is reached both curves coincide but after they have reached their maximum,

they start to deviate from each other. The one recorded above the carbon atom (red curve) drops faster than the one recorded above the center of the C₆-ring (blue curve). Hereby, the curves show the maximal difference between each other just before abrupt changes appear in the spectra.

In accordance to the findings in the previous section, the abrupt changes of the ratios most likely originates from structural changes of the junction. In addition, since we observe a difference between the inner part of the ring and the position of the carbon atom, the STHM contrast can only appear where $R_G(\vec{r_1}) > R_G(\vec{r_2})$ and the junction is still stable (grey shaded area in figure 5.6). STHM images recorded at different tip-sample distance in the distance regime in which the STHM contrast can be expected confirm this assumption while the images reveal even more.

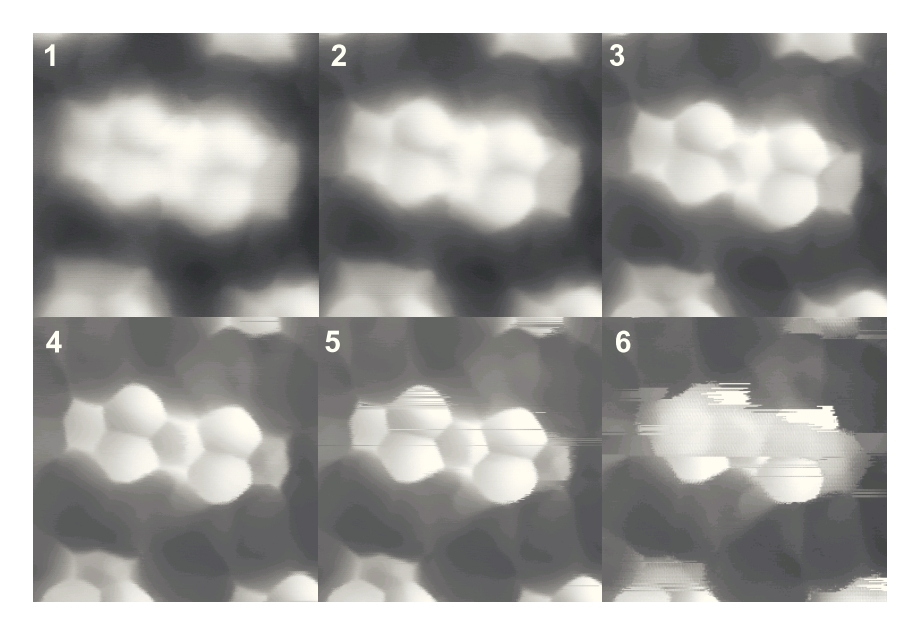


Figure 5.7: STHM images of PTCDA/Au(111) measured with D_2 at different tip-sample distance. The distance at which images are recorded is indicated by the black triangles in figure 5.6 (b)). Image parameters: $1.3 \times 1.3 \text{ nm}^2$, constant height, V = -5 mV

Fig. 5.6 (c) shows six STHM images recorded at different tip-sample distances in the regime where we expect the STHM contrast. The corresponding tip-sample distance is indicated in fig. 5.6 (b) (black triangles). The images show a trend that with decreasing tip height the resolution of the images constantly increases.

While the molecule appears blurred in images 1-3, images 4 and 5 show a sharp contrast where the molecule and its internal structure is well visible. Besides the STHM contrast of the molecule, in image 5 sharp lines across one of the C_6 rings in the upper left corner of the molecule appear. The number of lines increases when the tip-sample distance is

further reduced. At the distance at which image 6 has been recorded the contrast has almost vanished above the entire molecule.

Comparing the images with the spectra in figure 5.6, one observes that image 6 has been recorded close to the distance at which structural changes of the junction appear when the tip approaches the surface. Thus this distance can be seen as a borderline: up to that point the distance, the bias and the contrast can be switched reversibly between STHM and STM mode. Beyond the borderline irreversible structural changes of the junction likely occur which appear as abrupt changes in the junctions conductance and a sudden loss of the contrast.

This finding allows the definition of three different regimes as indicated in figure 5.6. In regime 1 the conductance above both positions above the molecule evolves equally. In regime 2 the conductance evolution of G_{vac} and G_{D_2} deviates from each other. Finally in regime 3 the STHM contrast gets lost.

The sudden loss of the STHM contrast in regime 3, together with the observation that in this regime often structural changes of the junction are observed, suggests that the tip-sample separation is comparably small. This leads to the conclusion that due to the small tip-sample separation D_2 is mechanically squeezed out of the junction. Therefore the preceding regime 2, in which the STHM resolution evolves, is identified with a gradual compression of D_2 in the junction. This compression then leads to a decreasing of the junctions conductance when the tip-sample distance is reduced (cf. fig. 5.5). However, the mechanism which lies behind the reduction of the junction conductance is not yet clear.

5.2 Ab initio calculations

To investigate the influence of D_2 on the conductance of the junction in regime 2, density functional theory (DFT) calculations were carried out by our collaborators from Osnabrück [204]. Before turning to the results of the calculations, we summarize the findings from the previous sections to motivate the model used for the calculations.

With the information from the previous sections, we can draw the following picture of the STHM junction: in the junction, i.e. between the tip and PTCDA, a single D_2 molecule is statically bound. According to this picture, the junction can be modelled by a D_2 molecule bound between two electrodes. In addition, the molecule in the junction influences the conductance evolution at zero bias depending on the tip-sample separation. This means that the distance between the electrodes have to be varied. In a simple model the molecule

is bound between identical electrodes. In this case, variations of the electrode separation will change the equilibrium distance of D_2 in the junction. However, the effect on identical electrodes will be the same on both sides of the junction. Thus, it is sufficient to model the STHM junction only by one electrode in front of which a single D_2 molecule is located and systematically vary the distance (z') between the two.

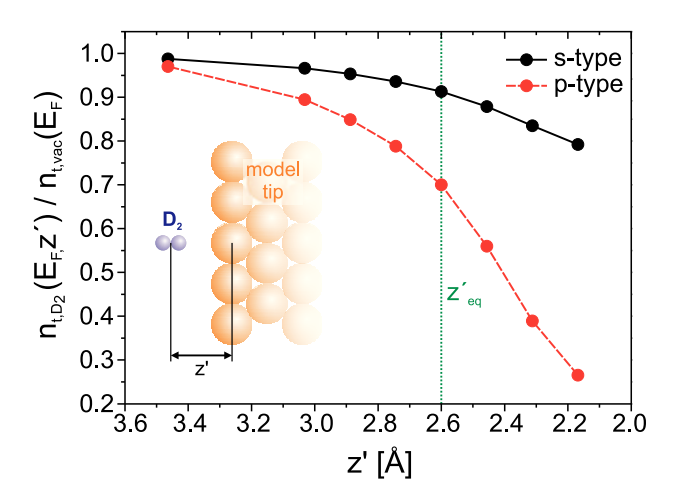


Figure 5.8: DFT-LDA simulated $n_{t,D_2}(E_F, z')/n_{t,vac}(E_F)$ vs. D₂-tip distance z' for s- (black) and p-type (red) orbitals at the Au atom below the deuterium molecule. $n_{t,D_2}(E_F, z')$ is the LDOS of the model tip at the Fermi level at given D₂-tip distance z' and $n_{t,vac}(E_F)$ is the LDOS at the Fermi level of the bare tip electrode. Equilibrium distance z'_{eq} is indicated by the vertical line. Image reproduced from reference [204]

A sketch of the model is shown in the inset of figure 5.8, it contains a single D_2 molecule in front of a Au(111) surface which represents the electrode. In the calculations, the geometry of the model has been optimized in a 3×3 overlayer on a three layer thick Au surface within the local density approximation (LDA). The equilibrium position of the molecule resulting from this geometry is an upright standing D_2 molecule in an on top position above the surface in a distance of z' = 2.6 Å (green dotted line in figure 5.8).

Starting from the equilibrium state, the distance between the molecule and the surface has been varied in steps of 0.15 Å and the LDOS of the surface for each distance has been calculated. To calculate the LDOS the quantum mechanical states are projected on the local orbitals $(s,\,p_z\,\,,\,d_{z^2})$ of the Au atom directly underneath the D₂ molecule while for a better convergence, for the calculation of the LDOS a 11 layer thick Au surface is used.

The calculated LDOS of the Au atom represents the DOS of the model tip at the Fermi level $(n_{t,D_2}(E_F, z'))$, as the Au surface represents the tip electrode in the STHM ex-

5 Formation of the geometric contrast

periments. In accordance with the calculation of the DOS of the tip in the presence of D_2 , one can also calculate the DOS of the bare tip $(n_{t,vac}(E_F, z'))$. Dividing n_{t,D_2} by $n_{t,vac}$ we find that the tip DOS decays substantially with decreasing tip- D_2 distance.

The origin of the decay is the Pauli exclusion principle. As the distance between D_2 and the tip is reduced, the DOS of the metal needs to rearrange locally to minimize the overlap between the closed shell of D_2 and the electronic states in the metal. This rearrangement leads to a depletion of the metal's DOS at the Fermi level [202, 205, 206]. Note, that the energy cost for the rearrangement of the DOS leads to a repulsive force between the D_2 and the metal (Pauli repulsion) which will be further investigated in section 5.5.1.

We can use the depletion of the metal's DOS to estimate the behaviour of the conductance. According to equation 2.27 the conductance of the junction is proportional to the tip-DOS. This means that the conductance G(z) as well as the conductance ratio $R_G(Z)$ should decrease proportional to $n_{t,D_2}(E_F,z')$ when the tip approaches the D₂ molecule. The depletion of the tip-DOS in figure 5.8 indicates that the conductance should decrease with a rate of $0.2 - 1 \text{ Å}^{-1}$. In comparison, the experimental data from fig. 5.6 (b) show rates of 1.1 to 1.5 Å⁻¹.

In order to compare the theoretical and the experimental values one has to take into account that both values are obtained on different z scales. Whereas z' is defined as the distance between D_2 and the tip, the experimental z scale measures the tip-sample separation. Thus we have to take an additional scaling factor $(\frac{dz'}{dz})$ into account. This scaling factor should be in the range between ≈ 0 and 1, where 0 indicates a soft sample (constant D_2 -tip distance) and 1 a hard sample (constant sample- D_2 distance).

The additional scaling factor increases the difference between the experimental and theoretical values, although, taking into account e.g. the effect of the unknown shape of the tip and the effect of the Pauli repulsion on the LDOS of the sample, the correspondence between the two is remarkable. However, considering the neglected effect of the Pauli repulsion on the sample side would amplify the decrease of the conductance, since the conductance is also proportional to the LDOS of the sample (cf. equation 2.27).

The agreement between experimental and theoretical data leads to the conclusion that the decrease of the conductance ratio in regime 2 (cf. fig. 5.6) and thus the origin of the STHM contrast can be explained by the Pauli repulsion between a D_2 molecule and the electrodes of the STM junction.

5.3 Qualitative model: sensor/transducer

Now, we develop a simple qualitative model of the STHM junction and its functionality based on its spectroscopic properties and the results obtained from the DFT calculations. To develop the model step-by-step we repeat again some of the main findings of the previous sections.

The high lateral resolution in STHM images, which is by far higher than the diameter of D_2 , suggests the presence of at most a single D_2 molecule in the active part of the junction during the contrast formation. In addition, the high lateral resolution together with the dependence of the STHM contrast on the tip-sample separation (cf. section 4.2.1) indicates the possibility to restrict our model to one dimension, where the tip-sample distance is the only relevant parameter.

In principle, it could have been possible that the lateral structure of the surface plays a role in the contrast formation, e.g. by dragging D_2 across the surface. However, the spectroscopic characterisation of the junction has shown that the contrast in STHM images is independent of the scanning process. Thus, the mechanism behind the contrast formation does not depend on the lateral structure of the sample across which the tip scans during imaging. Hence, we only need to consider the tip-sample separation in our model and not the lateral position of the tip.

Furthermore, the spectroscopic characterisation indicates that the relevant time scales, on which the processes of the contrast formation take place, are fast on the time scales of the measurement. Therefore we can assume an always in equilibrium bound D_2 molecule between the tip and the sample.

In the above described static geometry, the D_2 molecule will always be located at its equilibrium position between the electrodes. Clearly, the position of D_2 depends on the tip-sample separation and the strength of the interaction with both sides of the junction. As the tip sample distance varies, the distance of D_2 to the tip and the sample changes while D_2 moves to a new equilibrium position. According to the results of the DFT calculations, the changed distance yields variations in the occupation of the electronic states at the Fermi level inside the electrodes due to the Pauli exclusion principle. The variation of the density of states inside the electrodes directly modifies the conductance of the junction, thus produces the STHM contrast.

The information depicted in the previous paragraphs leads to a simple model which explains the contrast formation in STHM images of PTCDA. An operational scheme of the model (STHM junction) in which a single D_2 molecule acts as a combined sensor and

5 Formation of the geometric contrast

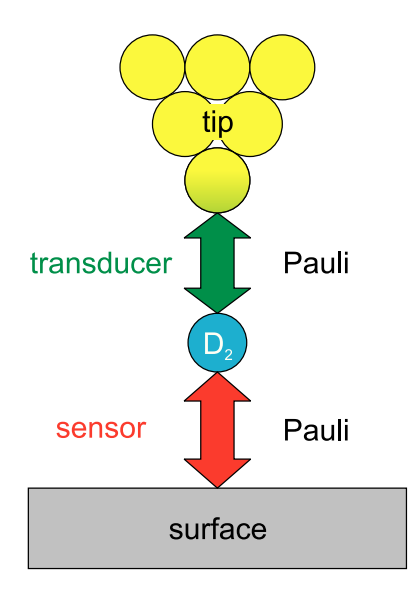


Figure 5.9: Schematic illustration of the sensor/transducer model. The interaction between the single D_2 molecule and the specific part of the junction are indicated by the arrows. In the case of the simple model both arrows indicate the Pauli repulsion between molecule and surface (red) as well as between molecule and tip (green).

signal transducer is shown in figure 5.9. The role of D_2 in the contrast formation is as follows: the sensor part probes the Pauli repulsion from the surface which leads to a certain D_2 -sample distance, whereas the transducer part transforms the tip- D_2 distance into variations of the junction conductance again via Pauli repulsion.

Before we turn to the visualization of the contrast formation with the help of the sensor/transducer model, we will discuss observations and effects which cannot be explained with the simple model:

- The model draws a static picture of the STHM junction, whereas due to the finite temperature ($T_{exp} \approx 5$ K) and the low binding energy of D_2 [200], one could expect that the D_2 is not statically bound to the tip apex. A more realistic picture of the STHM junction would thus have to account for several D_2 molecules which have a limited residence time below the tip. After a certain residence time, the molecule in the junction is displaced and returns or is replaced by an other molecule while the switching from one to the next molecule is much faster than the time of the measurement. An indication for this scenario is the spontaneous switching between the STM and STHM contrast during D_2 deposition.
- The model only deals with a single D_2 molecule confined in the junction and disregards effect originating from the presence of additional D_2 molecules on the surface. However, the presence of other D_2 molecules can be indirectly concluded either from

their influence on the position of the spikes in dI/dV spectra [172] or by their influence on the image contrast at higher coverages of D_2 on the surface (cf. section 3.3).

• In the one dimensional model of the junction the detailed structure of the tip and the surface are not taken into account. This structures leads to different adsorption sites of D₂ at the tip apex and in principle also on the surface. In principle these special adsorption sites should lead to the variability of the contrast achieved with different tips (cf. section 4.2.2) and the STHM contrast of other organic molecules (cf. section 4.1.4) and metal clusters (cf. section 4.4)

In the preceding paragraph we discussed the drawbacks of the model, but before we finally turn to its applications, we would like to note several consequences arising from the model. The described functionality should also work with other closed-shell particles besides hydrogen and deuterium [207]. In addition, the sensor and transducer action is not necessarily restricted to Pauli repulsion. It might also be sensitive to other interactions like van der Waals-, electrostatic-, chemical-interactions which influence the tip- D_2 distance. In fact, the STHM contrast of the intermolecular interactions indicate this ability, since above hydrogen bonds one may expect a higher total electron density (TED) compared to the positions where are no bonds [192], the repulsive force on the D_2 molecule should be larger than above empty spaces. If the contrast of the hydrogen bond would also originate from the Pauli repulsion, the higher TED above the bond would lead to a smaller tip- D_2 distance and therefore to a reduced conductance, thus the bonds should appear dark.

5.3.1 Visualization at Au dimer

The depletion of the density of states, due to the distance-dependent Pauli repulsion, which leads to variations of the conductance in our model, builds the basis for the understanding of the contrast formation in STHM images. To demonstrate the relation between the Pauli repulsion and the conductance of the junction, we will discuss the contrast formation in the STHM image of an inherently simple object, namely a dimer Au adatoms on the Au(111) surface.

The STHM image of the Au dimer together with the estimated trajectory of D_2 during scanning across the dimer as a cut along the xz-plane is shown in figure 5.10. The contrast of the Au dimer (bottom of fig. 5.10) consists of two bright spots corresponding to the two adatoms on the surface. In the center of each of the bright spots a dark area is visible which is usually not observed in conventional STM images.

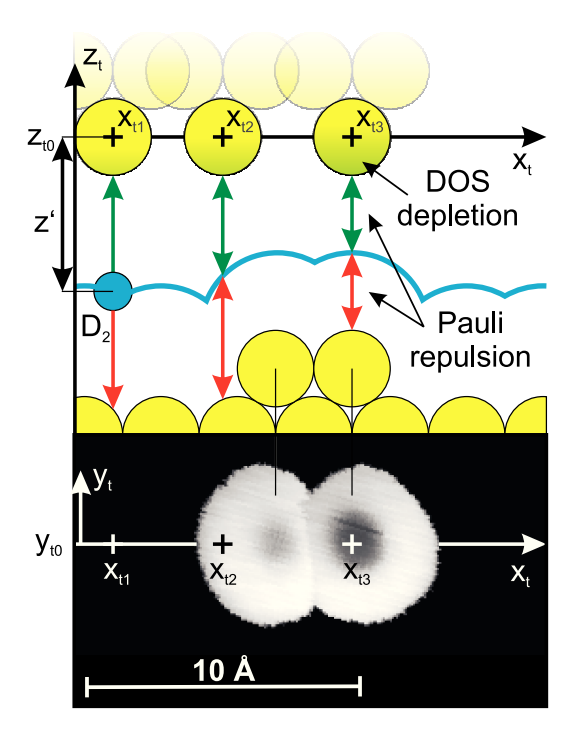


Figure 5.10: Elucidation of the contrast formation in STHM images with the sensor/transducer model. Top: Schematic sketch of the contrast formation as a cut along the xz-plane as the tip scans across the adatom dimer. Three tip positions are marked: x_{t1} next to the dimer, x_{t2} at the onset of the dimer and x_{t3} on top of one of the adatoms. The depletion of the tip-DOS at the different positions is illustrated by the shading in the outermost tip atom whereas sensor and transducer actions are shown as green and red arrows. In addition, the trajectory of the D₂ molecule above the surface is shown (blue line). Bottom: Experimental STHM image of the Au adatom dimer. The image shows two well separated bright spots. The two bright spots corresponds to the two adatoms while in the center of each of the bright spots a darker area is visible indicating the depletion of the DOS. The cut along the xz-plane shown at the top is indicated by the position of the x_t axis. Image parameters: $1.7 \times 1 \text{ nm}^2$, constant height, V = 2 mV

The adatoms appear brighter than the background of the uncovered Au surface due to a reduced effective tip-sample distance when the tip approaches the dimer. The reduced distance leads to an increased sample DOS $(n_s(\vec{r_t}, E_F))$ and therefore to a larger conductance $(G(\vec{r_t}))$ of the junction at tip positions close to the adatoms, e.g. $\vec{r_t} = (x_{t2}, y_{to}, z_{t0})$, compared to positions above the bare surface, e.g. $\vec{r_t} = (x_{t1}, y_{to}, z_{t0})$ (cf. top of fig. 5.10). However, when the tip moves onward, from the onset of the dimer $(\vec{r_t} = (x_{t2}, y_{to}, z_{t0}))$ to a position close to its center, e.g. $\vec{r_t} = (x_{t3}, y_{to}, z_{t0})$, the effective tip-sample distance is further reduced which should lead to an increase of the sample DOS at the position of the tip and therefore to an even higher conductance. The increased conductance above the center of the adatoms suggests that they should appear bright in conventional STM images which is indeed observed [155], whereas in the STHM image (bottom of fig. 5.10) the center of

the adatoms appears darker than their surrounding.

The reason for the difference of the contrast compared to conventional STM lies in the presence of D₂ in the junction. During scanning the D₂ molecule follows the movement of the tip across the dimer as indicated by the trajectory in figure 5.10 (top). The trajectory represents the equilibrium distance z' for each position of the tip $(\vec{r_t} = x_t, y_{t0}, z_{t0})$ above the sample in our static model. Clearly, at the equilibrium distance the force from the surface equals the force from the tip on the D_2 molecule in the junction $(F_{t,D_2} = F_{D_2,s})$. As now the tip moves from $\vec{r_t} = (x_{t2}, y_{to}, z_{t0})$ to $\vec{r_t} = (x_{t3}, y_{to}, z_{t0})$, the force on the D₂ molecule changes as a result of the reduced tip-sample distance, thus D_2 moves to a new equilibrium position. The new equilibrium position is closer to the tip due to the increased Pauli repulsion between D₂ and the sample above the center of the adatom and through this mechanism the D₂ molecule senses the Pauli repulsion from the surface. The stronger repulsion on the sample side, which yields the smaller tip- D_2 separation (z'), is balanced by a higher tip-D₂ force (F_{t,D_2}) , caused by the Pauli repulsion on the side of the tip, where the Pauli repulsion leads to a depletion of the tip DOS (cf. section 5.2). The effect of the DOS depletion on the junctions conductance is so strong that it overcompensates the rise of the conductance due to the smaller tip-sample separation, thus the center of the adatoms appear dark. In this way, the information about the sample DOS is transformed through the Pauli repulsion between the D₂ and the electrodes into variations of the junction's conductance, which can be detected with STM as described by the operational scheme in section 5.3.

5.3.2 Contrast formation above PTCDA

Having analysed the STHM image of the adatom dimer with respect to the sensor/transducer model of the STHM junction, we now turn to the contrast formation above PTCDA. Similar to the case of the dimer, the D_2 molecule follows the tip position during scanning of PTCDA. At each position above PTCDA, D_2 is located at its equilibrium position between the electrodes. This equilibrium position is determined by the balance of the forces at both sides of the junction. As in the case of the dimer, the force between D_2 and the sample will be determined by lateral variations of the Pauli repulsion. If, for example, the tip moves from a position above the center of one of the C_6 rings to a position above a carbon atom, D_2 will have to move to a new equilibrium position closer to the tip due to the increased total electron density (TED) at the position of the atom. According to the DFT results, the smaller tip- D_2 distance leads to a reduction of $n_t(\vec{r_t}, E_F)$ and therefore to a smaller conductance. Thus, in the STHM image (cf. fig. 4.1), positions of the sample

at which the TED is higher (e.g atoms and σ -bonds) appear darker than areas where the TED is lower (inside the ring).

5.4 Testing the model

The developed model of the contrast formation in STHM images, in which a single D_2 molecule acts as a combined sensor and signal transducer, can explain the observed contrast in STHM images of molecular surfaces. To elucidate the generality of the model, in the following we discuss the contrast formation in STHM images showing atomic resolution of a clean metal surface.

5.4.1 Atomic resolution of clean metal surface

The STHM image of the metal cluster in section 4.4 indicates the ability of the STHM mode to resolve metal surfaces with atomic resolution. However, whether the contrast originates from the atomic structure of the cluster or whether the contrast originates from a condensed D_2 layer, comparable to the one observed for PTCDA at high H_2 coverage (cf. fig. 3.3), is not clear from the beginning. In the following, we discuss the origin of the contrast in STHM images of clean Au(111).

Scanning the clean Au(111) surface in STHM mode, a pattern of bright round protrusions appears in the images (cf. fig. 5.11). The distance between adjacent protrusions (g = 2.8 Å) is close to the lattice constant of Au(111) ($\approx 2.85 \text{ Å}$ [94, 168]). The similarity between the lattice constants suggests that the contrast in figure 5.11 is related to the atomic structure of the underlying surface. However, a priori it is not clear whether the contrast in figure 5.11 can be attributed to Au atoms. It is conceivable that the contrast is related to a condensed D₂ layer on the surface. In accordance to the STHM contrast of PTCDA at higher H₂ coverage (cf. fig. 3.3), in reference [172] it is shown that H₂ layers on Cu(111) can be directly imaged with STM.

The image of a H_2 layer in reference [172], which is reproduced in fig. 5.12 of this work, shows a hexagonal arrangement of H_2 molecules similar to the one in figure 5.11. The observed lattice constant in the hexagonal arrangement in figure 5.12 is 3.8 Å. This distance is comparable to the intermolecular distance in solid H_2 and D_2 [173–175]. The considerably higher lattice constant in solid H_2 and D_2 , compared to the value obtained in figure 5.11, makes an H_2 layer unlikely as the origin of the contrast. However, from the different lattice constants alone it is not possible to assign the protrusions in the

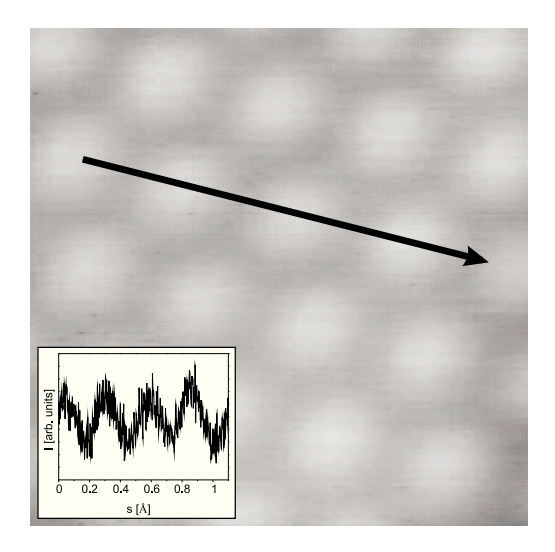


Figure 5.11: Atomic resolution of Au(111) in STHM mode. The single atoms are imaged as bright protrusions. Inset: Line profile indicated by the arrow in the image, used to measure the distance between the atoms ($g = 2.8 \pm 0.1 \text{ Å}$, corrugation = 80 nA). Image parameters: $12 \times 12 \text{ Å}^2$, constant height, V = -3 mV

image to the Au atoms. Due to the high compressibility of solid D_2 [173], with increasing D_2 coverage the D_2 - D_2 distance in the layer may shrink. If this was the case, a strong surface corrugation potential for D_2 on Au(111) would have to be expected which forces the D_2 into a 1 × 1 structure against intermolecular repulsion. However, the D_2 -metal interaction is weak, which leads to a physisorption of D_2 . Additionally, in theoretical and experimental studies almost no difference in binding energy is found between the different adsorption sites (on-top, bridge and hollow) [200, 208–210]. Therefore we conclude that a D_2 layer with 2.8 Å lattice constant is unlikely.

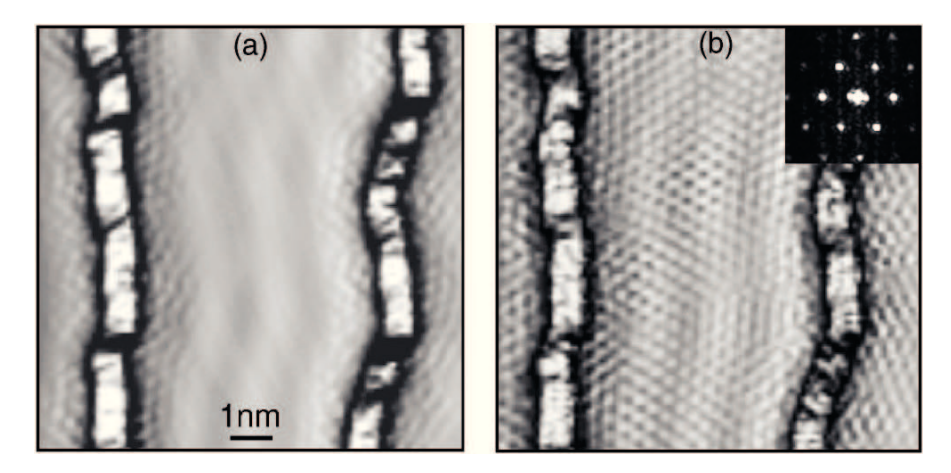


Figure 5.12: STM images of $H_2/Cu(111)$. The image is taken from reference [172]

This conclusion is in agreement with results obtained for another unpolar molecule adsorbed on a closed packed metal surface, namely $N_2/Pt(111)$. It is found that the N_2 molecules arrange in a 3×3 superstructure [211–213]. The density of molecules in this structure is 6.7×10^{14} molecules/cm² [212], which is similar to the density of an uncompressed H_2 -layer(7×10^{14} molecules/cm²) [214], whereas the density of the features in the STHM image is twice larger (13×10^{14} molecules/cm²).

5.4.2 Expectable corrugation without D₂

Assigning the contrast in figure 5.11 to the atomic structure of the surface, we continue with an analysis of the origin of the contrast. Atomic resolution STM images of the Au(111) surface have already been presented before [90, 94, 215, 216]. Thus, the contrast may not be generated by the presence of D_2 in the junction.

One needs to have a closer look at the contrast formation of clean metal surfaces with STM, to determine if the contrast shown in figure 5.11 is caused by the presence of D_2 in the junction. The resolution in STM images is governed by the electronic structure of the tip, i.e. the outermost tip atom. The simplest imaginable tip consists of an s-like orbital at the tip apex. However, an s-wave tip is not sufficient to explain atomic resolution on closed packed metal surfaces, instead a d_z - or p_z -like state close to the Fermi-level is necessary at the outermost tip atom [217]. Due to the preparation procedure of the tip (cf. section 3.2), we expect the tip to be terminated with a cluster of Au atoms. Because of its electron configuration in the ground state ([Xe] .4f¹⁴.5d¹⁰.6s¹ [218, 219]), even the clean tip fulfils the above requirement to achieve atomic resolution in STM images. Thus three different explanations are conceivable to explain the atomic resolution in figure 5.11:

- 1. the Au atom at the tip apex directly produces the contrast,
- 2. at the tip apex an adsorbate atom or molecule was picked up which increases the resolution,
- 3. the contrast is mediated due to the presence of D_2 .

The cleanness of the tip has been tested on PTCDA before imaging Au, therefore we find the second suggestion unlikely to be the reason for the atomic resolution.

To determine whether the contrast originates from a clean tip or not, we compare the corrugation in figure 5.11 with the values presented in references [90, 94, 216]. The corrugation ($\Delta I = I_{max} - I_{min}$) in figure 5.11 is determined from a line profile (cf. inset

in fig. 5.11) as the difference between maximum and minimum current, i.e. the difference in measured currents atop and between the atoms. However, to compare the measured corrugation with the one obtained from constant current STM images, we have to convert the current difference ΔI into a height difference Δz .

For a clean Au terminated tip we assume that the current drops by a factor of 7.6 per Å, as expected for a metallic junction [36]. From the line profile in figure 5.11 we obtain a percentage $K_I = \frac{I_{min}}{I_{max}} * 100 \% = 30 \%$ for the ratio between the currents. Inserting the factor and the current ratio in equation 2.11 yields a height difference of $\Delta z = 0.6$ Å for the clean metal tip.

The calculated height difference Δz for the clean junction is close to the values reported in literature (0.15 Å [216], 0.05 – 0.5 Å [94], 0.1 – 1 Å [90]). Thus, from the corrugation alone, we cannot conclude that the atomic resolution appears due to the presence of D₂ in the junction.

5.4.3 Evidence of D₂ in the junction

To clarify if the atomic resolution is mediated by D_2 in the junction, we turn to the spectroscopic properties of the junction. Figure 5.13 shows two typical dI/dV(V)-spectra recorded above the center of an atom in fig. 5.11. The spectra were measured at two different tip-surface distances after the tip has been approached by 2.7 Å and 3.1 Å from its stabilization point above the surface. In the whole distance range (2.7 Å $< z_{displacement} < 3.1$ Å), we obtain atomic resolution in recorded images.

The spectra in figure 5.13 show the same characteristic features as observed in dI/dV spectra recorded above PTCDA (cf. fig. 5.2), i.e. spikes at $|V_{inel}| \approx 18$ mV and a ZBA appearing as a peak. In addition to the previously observed features an increased noise level is visible between $V_{inel} < |V| < V_{noise}$.

The similarity of the spectra recorded above PTCDA suggests the presence of D_2 in the junction during contrast formation above the Au surface. However, it is not yet clear if the atomic resolution appears due to interactions of D_2 in the junction. To answer this question we look at STHM images recorded at different bias.

To investigate the dependence of the image contrast on the applied bias, we recorded a full dI/dV spectrum at each point of an image. The total series contains $30 \times 30 \ dI/dV(V)$ spectra which allow the reconstruction of images at any bias. Five images reconstructed from the dI/dV(x,y,V)-data are presented in figure 5.14, together with a corresponding spectrum acquired above the center of one of the atoms. In addition, for a comparison

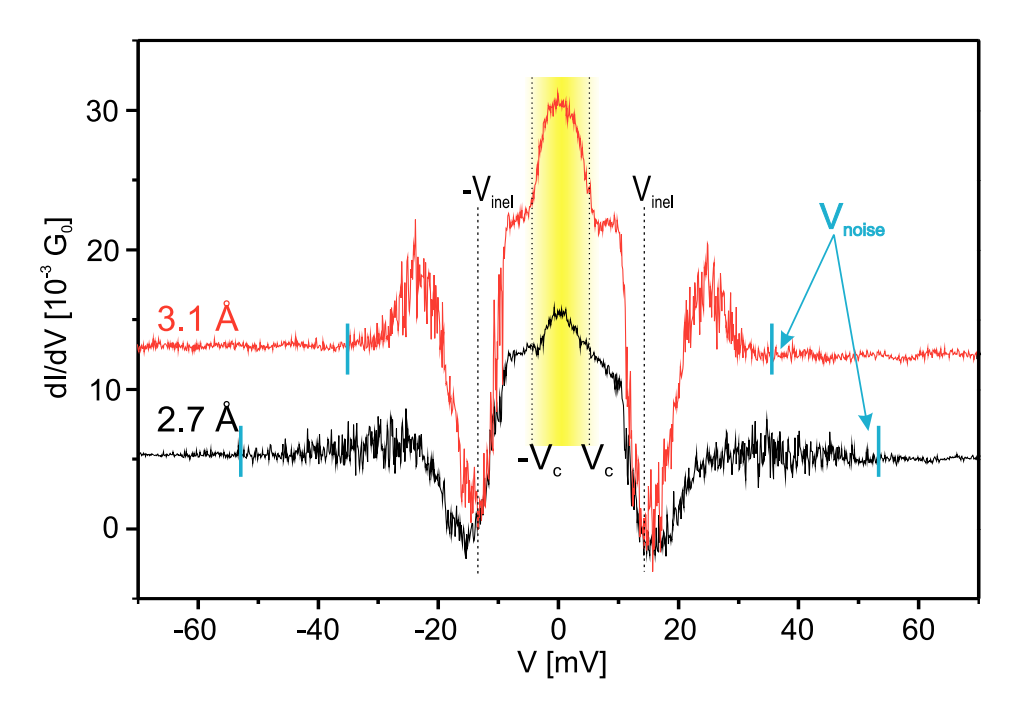


Figure 5.13: dI/dV(V) spectra measured on top of a Au atom. The spectra have been recorded with lock-in detection (amplitude 4 mV, frequency 1 kHz) at absolute tip-sample distance 2.7 Å (red) and 3.1 Å (black). Values of the differential conductance are given in units of the quantum conductance $G_0 = \frac{2e^2}{h} = (12.9 \text{ k}\Omega)^{-1}$.

of the contrast with figure 5.11, image 2 is averaged over a square of 1 Å^2 . The resulting image is displayed as 1 in figure 5.14 (a). In this image the position from which the spectrum was taken is marked (red dot).

The images reconstructed at different voltages reveal that, on the one hand, the contrast in the image reconstructed from the datacube is identical to the one recorded with the scanning tip, while on the other hand the atomic resolution is achieved only in a limited bias range of the ZBA (images 2 & 3), where the contrast shows only minor variations. Beyond the ZBA the contrast quickly disappears and for $|V| > |V_c|$ the images are featureless (images 4-6 in fig. 5.14 (a)).

So far, we saw that the contrast formation does not depend on the scanning of the tip while the atomic resolution only appears in the regime close to zero bias. This behaviour is the same as for the STHM contrast in the case of PTCDA (cf. section 5.1.4). The equal behaviour in both cases suggests the same origin of the contrast, namely the interaction of D_2 with the junction.

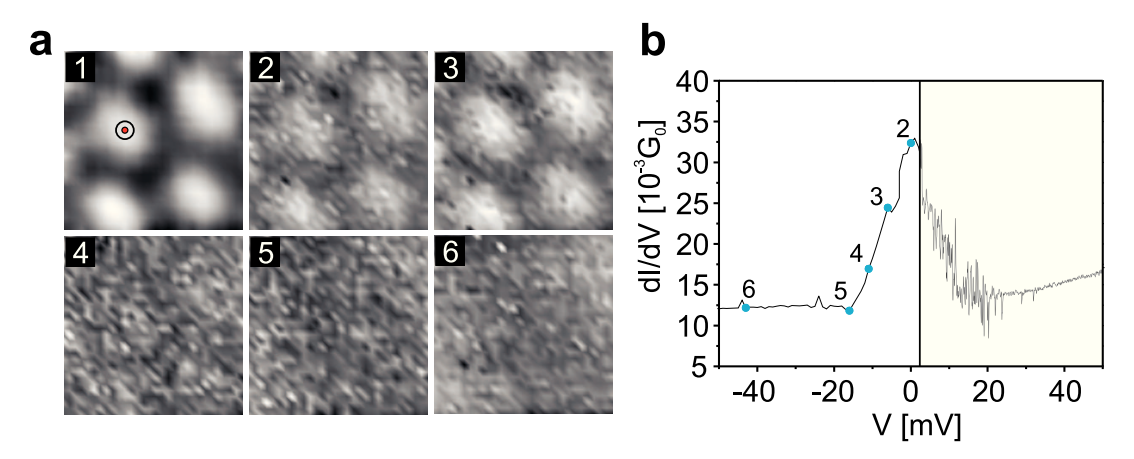


Figure 5.14: Images and spectra reconstructed from a datacube recorded above the clean Au surface. (a) 30×30 pixel, $5.9 \times 5.9 \text{ Å}^2$ dI/dV constant height STHM images extracted from spectroscopic data acquired above Au(111) with D₂. At each pixel of the images one dI/dV(V) spectrum was recorded using lock-in detection (modulation amplitude 4 mV, frequency 4.8 kHz, spectrum acquisition time 1 s). Conductance values in the images rise from black to white. Image 1 is gained from image 2 by smoothing over a square with edge length 1 Å. The conductance values in image 2 vary in the range of $0 < G < 16 \cdot 10^{-3} \text{ G}_0$ while in image 1 the values change only in the range of $0 < G < 6 \cdot 10^{-3} \text{ G}_0$. Besides a background subtraction, to remove a slight contrast change, due to a small vertical drift during scanning, the images 2-6 are displayed as extracted. Bias value for the images: 2: 0 mV, 3: -6 mV, 4: -11 mV, 5: -16 mV, 6: -43 mV. (b) Spectrum recorded at the point marked in image 1 of figure 5.14 (a). The right side is displayed as measured, the left side was averaged over an area with diameter 0.2 Å, indicated by the circle in image 1. In addition the bias voltages at which the images are extracted are marked with blue dots, going from right (image 2) to left (image 6).

5.4.4 Influence of D₂ on the junction conductance

Having assigned the atomic resolution to the presence of D_2 in the junction we can now focus on the origin of the contrast. Since in the case of PTCDA the tip-sample distance during scanning turned out to be a crucial parameter for the contrast formation, in the following we investigate the influence of the tip-sample separation on the conductance of the junction.

To investigate the dependence of the tip-sample distance on the conductance of the junction, we recorded a series of dI/dV-spectra with subsequent reduction of the tip-sample distance by 0.2 Å. The acquired spectra are shown in figure 5.15 for z-displacements ranging from 2.2-4 Å and figure 5.16 for z-displacements of 0-2 Å, where a positive displacement means decreasing of the tip-sample distance from the stabilization point of the tip (V=43 mV, I=54 pA) by the given value.

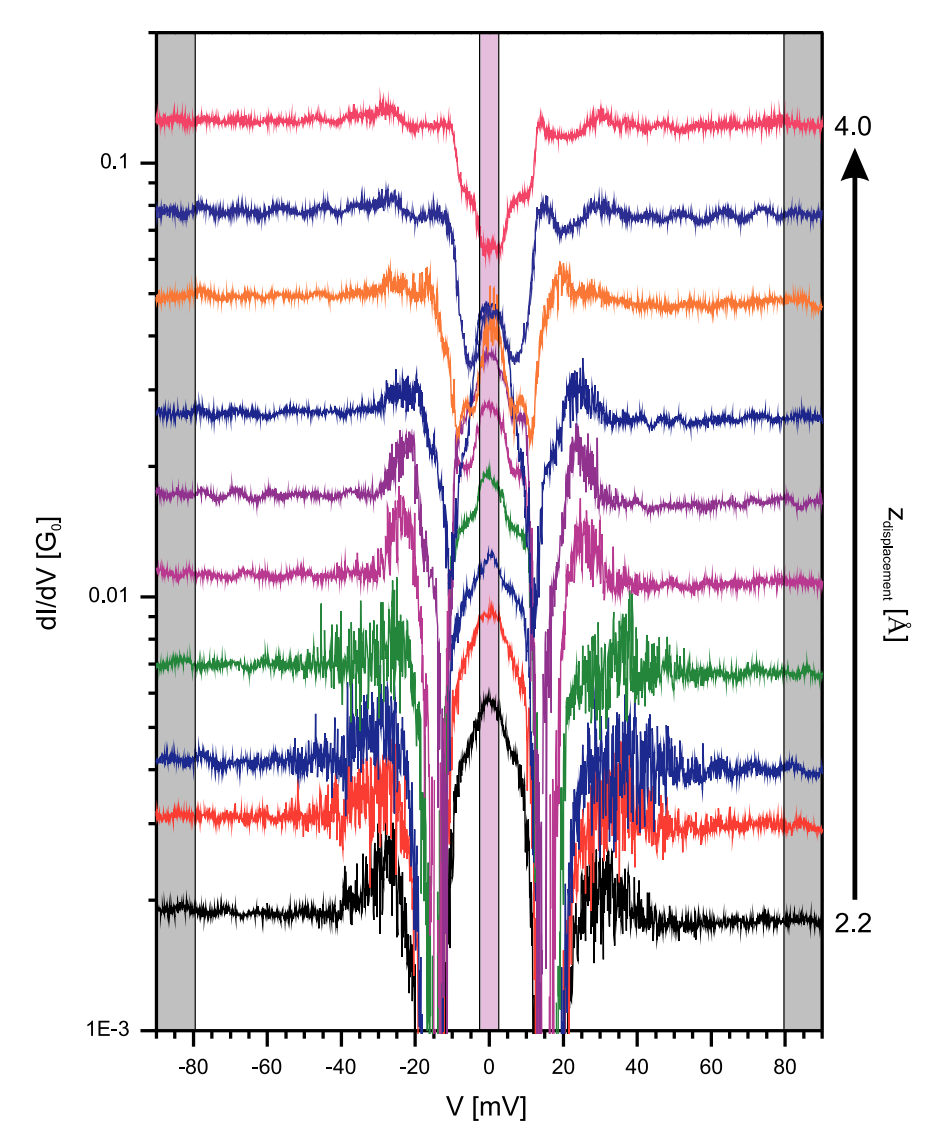


Figure 5.15: dI/dV(V)-spectra recorded with different tip surface distances. The Spectra have been measured with lock-in technique (amplitude = 4 mV, frequency = 1 kHz) on top of a Au surface atom. The spectra cover a range for z-displacement of 2.2-4 Å with a step of only 0.2 Å. Conductance spikes are clearly visible and appear together with a noisy region which outer position changes with the tip-surface distance. For better visualisation spectra are plotted on a logarithmic scale.

For the largest tip-sample separation in the experiment, at the stabilization point of the tip $(z_{displazement} = 0 \text{ Å})$, the conductance of the junction exhibits repeated switching events between two conductance states close to zero bias ($|V| \leq 10 \text{ mV}$). The two conductance states are one with a conventional linear dependence on the applied bias (state 1) in which no D_2 is expected in the junction (cf. fig. 5.2) and a new state with a lower conductance at zero bias (state 2) related to the presence of D_2 in the junction. At smaller tip-sample

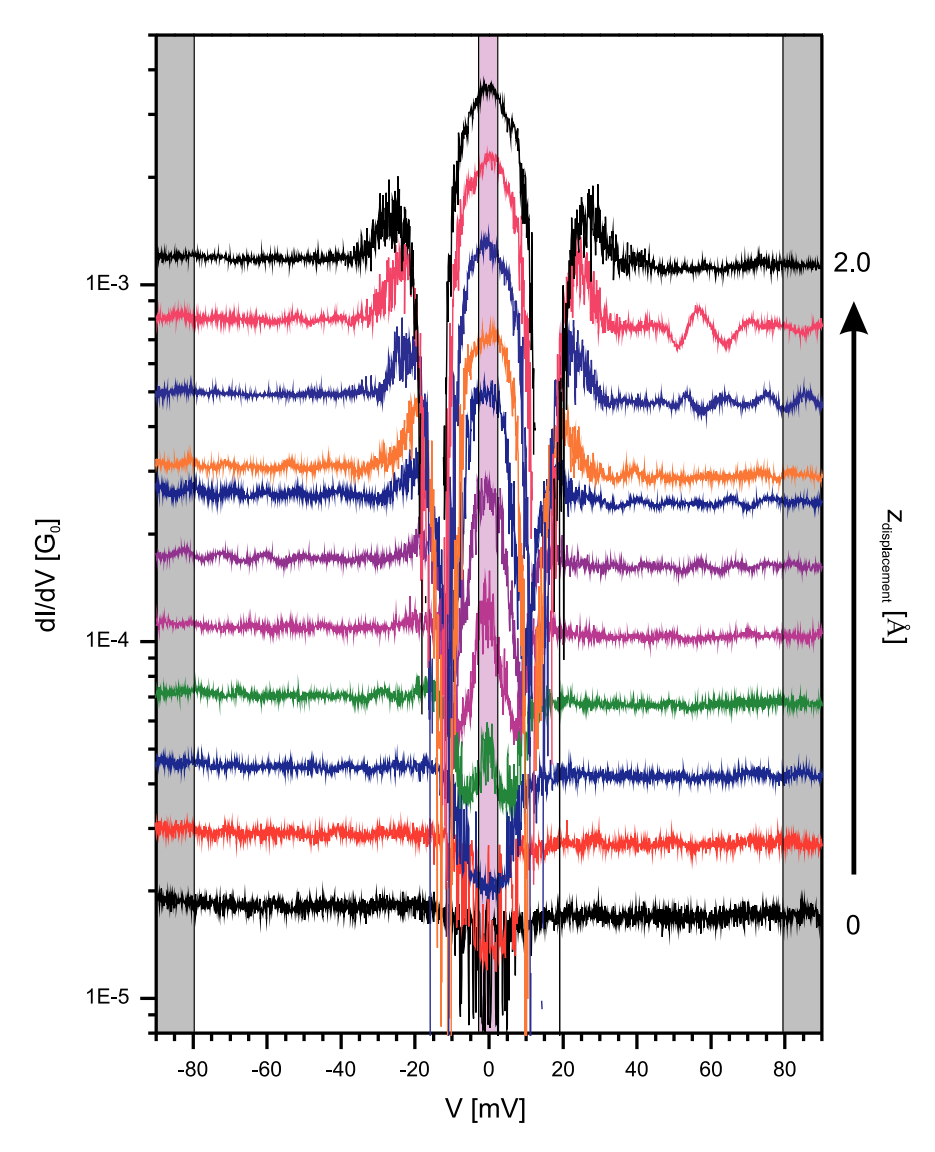


Figure 5.16: Continuing the series from figure 5.15 for smaller displacement (0-2 Å)

separation state 2 stabilizes in the regime close to zero bias (|V| < 20 mV) as indicated by the disappearance of the noise.

The stabilization of state 2 with decreasing tip-sample separation indicates a relation between the tip height and the confinement of D_2 in the junction. Whereas at larger tip-sample separations we observe spontaneous switching between a state in which D_2 is present in the junction (state 2) and the empty junction (state 1), beyond a certain threshold distance, D_2 is not spontaneously displaced from the junction any more. From this finding the following picture of the junction at larger tip-sample separation, compared to the one at which STHM images are recorded, emerges: in absence of the tip, D_2 diffuses

freely on the surface. When the tip approaches to the surface, a potential for D_2 is created between the surface and the tip apex. At larger tip-sample separation, the potential well is not deep enough to confine D_2 and it spontaneously escapes from the junction as indicated by the switching of the conductance to the value of the empty junction. The depth of the potential well created by the tip should increase while the tip approaches, thus at a certain distance the confining potential becomes so deep that D_2 can no longer escape and state 2 stabilizes.

At $z_{displacement} = 0.8$ Å, after state 2 is stabilized, a ZBA-peak appears, while the overall conductance in state 2 first remains lower than the conductance in state 1 (|V| > 20 mV). Decreasing the tip-sample separation further, the ZBA grows with respect to the high bias conductance. At $z_{displacement} = 1$ Å the conductance at zero bias is larger than dI/dV (|V| > 30 mV) while it further increases as the tip-sample separation is reduced. At $z_{displacement} \approx 2.5$ Å the situation reverses and the peak at zero bias starts to shrink with respect to the conductance in state 1 until at ≈ 4 Å it is almost completely vanished. At the same time, as the ZBA conductance rises, the transition from conductance state 1 (junction at elevated bias) to state 2 (junction at zero bias) also exhibits a complex evolution.

Whereas the position of the spikes in the spectra remains constant throughout the whole series ($|V_{inel}| \approx 18 \text{ mV}$), the transition region between the spike and the stabilization of the conductance in state 1 ($|V| = V_{noise}$ cf. fig. 5.13) shows a dependence on the tip-sample separation. While the tip approaches to the surface from $z_{displacement} = 0 \text{ Å}$, the region of increased noise between $V_{inel} < |V| < V_{noise}$ becomes broader until it reaches a maximum width at $z_{displacement} = 2.5 \text{ Å}$. Starting from this distance the width of the noisy region becomes smaller again.

So far, dI/dV spectra recorded above the Au surface in the presence of D_2 show a similar evolution with decreasing tip height as observed before above PTCDA (cf. fig. 5.4). However, above Au we observed an additionally noisy transition region between the two conductance states of the junction. The noisy region shows a similar evolution like the ZBA, i.e. its width first increases while the ZBA grows, while beyond $z_{displacement} = 2.5 \text{ Å}$ both effects disappear, which may indicate a correlation between the two. But since we are particularly interested in the contrast formation, we will concentrate on the evolution of the ZBA.

To compare the evolution of the ZBA with the conductance in state 1, we have extracted dI/dV values from figures 5.15 and 5.16 by averaging the spectra over the two shaded areas and plotted the results against the tip-displacement in the corresponding colour (fig. 5.17). The purple dots (G_{D_2}) show the evolution of the ZBA $(|V| < |V_c|)$ while

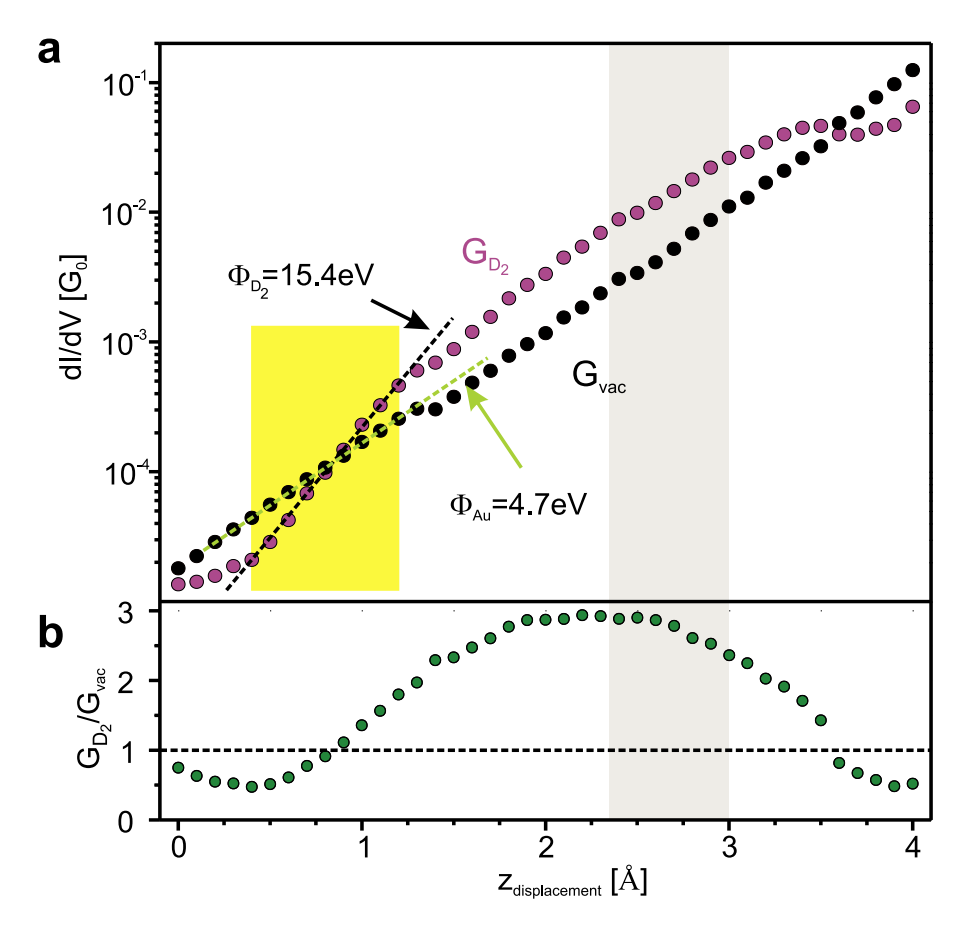


Figure 5.17: Evolution of dI/dV with decreasing tip-sample separation. (a) dI/dV(z) (G(z))-spectra extracted from the spectra in figures 5.15 and 5.16. The colours of the dots correspond to the shaded areas (black = grey, purple = light purple). The area in which the conductance at zero bias shows an exponential dependence on the tip sample separation is highlighted in yellow. From an exponential fit on the data points (green and black dashed lines) in this area we obtain values for the apparent barrier height Φ for the junction with and without D₂. (b) Ratio G_{D_2}/G_{vac} between the spectra in (a). The grey shaded area corresponds to the range of $z_{displacement}$ for which atomic resolution in the STHM images is observed.

the black dots (G_{vac}) show the conductance evolution for the empty junction $(|V| > |V_{inel}|)$.

 G_{vac} shows an exponential increase of the conductance with decreasing tip-sample distance as expected for pure tunnelling. The deviations from the exponential behaviour which appear as small steps at $z_{displacement} = 1.4$ Å, 2.5 Å and 3.6 Å originate from a small offset in the lock-in measurements. In contrast to G_{vac} , G_{D_2} clearly shows a non-exponential increase of the conductance in a wide range of distances.

For the largest tip-sample separations, close to the stabilization point, first the conductance values slowly increase due to the stabilization of state 2. After state 2 is stabilized

and no switching events occur any more, G_{D_2} enters a regime in which it shows an exponential increase with decreasing tip sample distance (0.4 Å $< z_{displacement} < 1.2$ Å). Decreasing the tip-sample separation further, G_{D_2} starts to deviate from the exponential behaviour. In the adjacent regime (1.2 Å $< z_{displacement} < 3.5$ Å), G_{D_2} still increases but the exponent with which the conductance values increases, constantly decreases while the tip approaches, until G_{D_2} and G_{vac} cross each other at $z_{displacement} = 3.5$ Å. Between 3.5 Å and 4 Å, G_{D_2} remains below G_{vac} .

Before we further discuss the relation between the STHM contrast and the evolution of the conductance, we shortly discuss the evolution of the conductance for elevated tip heights in which G_{D_2} exponentially increases. The regime in which we obtain an exponential behaviour of G_2 (yellow shaded area in fig. 5.17 (a)) allows us to further analyse the effect of the presence of D_2 on the junction conductance.

The exponential dependence of the conductance on the tip-sample separation in conventional STM results from the tunnelling probability of the electrons from the tip to the sample and vice versa, which exponentially depends on the length of the barrier and the height of the barrier (cf. section 2.1.2). The exponential evolution of the conductance of G_{D_2} and G_{vac} with decreasing tip-sample separation allows to determine the apparent barrier height Φ in the presence of D_2 and compare it to the one of the empty junction. The apparent barrier height can be extracted from the slope of G_{D_2} and G_{vac} in figure 5.17 (a) as

$$\Phi = \frac{\hbar^2}{2m} \left(2\kappa\right)^2 \tag{5.1}$$

where m is the electron mass and 2κ the slope of the conductance curve (cf. section 2.1.2). Fitting G_{D_2} and G_{vac} and inserting the calculated slopes into equation 5.1, we obtain the apparent barrier height for the empty junction ($\Phi_{vac} = 4.7 \text{ eV}$) and in the presence of D_2 ($\Phi_{D_2} = 15.4 \text{ eV}$).

The main contributions to the apparent barrier height of STM junction are the work functions of tip and sample (cf. section 2.1.4). Since both, tip and sample, in our experiments consists of Au we can compare Φ_{vac} with the work function of Au. The comparison shows, the apparent barrier height of $\Phi_{vac} = 4.7 \text{ eV}$ is close to the work function of the Au(111) surface ($\Phi_{Au(111)} = 5.26 \text{ eV}$ [220]). This means, the obtained value for Φ_{vac} is in the regime in which one could expect the apparent barrier height of a pure metallic Au junction. Thus, the result proves that at elevated bias ($|V| > V_{inel}$) D₂ has no effect on the junctions conductance. However, the situation is different at zero bias.

The presence of D_2 in the junction at zero bias leads to a considerably larger apparent barrier height. The obtained value $\Phi_{D_2} = 15.4 \,\mathrm{eV}$ is ≈ 3 times larger than Φ_{vac} or the work function of the bare surface. How the presence of D_2 affects the properties of the junction so that we obtain a value for the apparent barrier height which is by far larger than the obtained value for the empty junction is not clear. However, if the tip-sample distance is reduced, the conductance of the junction shows deviations from the exponential behaviour and the slope becomes smaller, due to the compression of D_2 in the junction.

Similar to the measurement above PTCDA (cf. fig. 5.6), to quantify the effect of D_2 of the junction conductance while the tip approaches to the surface, we define the ratio $G_{ratio} = G_{D_2}/G_{vac}$. G_{ratio} is plotted in figure 5.17 (b), where in addition the distance range in which atomic resolution is observed is indicated by the grey shaded area.

Now one can compare the evolution of the conductance ratio with the corresponding curve above PTCDA/Au(111) (cf. fig. 5.6). Qualitatively G_{ratio} shows the same behaviour as above PTCDA: from the stabilization point first G_{ratio} rises until it reaches a maximum $(z_{displacement} \approx 2.1 \text{ Å})$. Beyond the maximum G_{ratio} decreases until it drops below 1. In both cases, above PTCDA and Au, beyond the crossing point structural instabilities of the junction occur due to the close vicinity of the tip to the imaged surface. In contrast to the STHM resolution of PTCDA, where the best resolution is observed in a narrow distance range (<0.3 Å) directly before the crossing point of the spectra, here the situation is different. The atomic resolution is observed in a wider distance $(2.3 \text{ Å} < z_{displacement} < 3 \text{ Å})$ which is more than 0.5 Å away from the crossing of the spectra $(z_{displacement} = 3.6 \text{ Å})$. However, the larger distance at which STHM images with atomic resolution are recorded does not automatically mean that the mechanism behind the contrast formation is different.

5.4.5 Contrast formation

In section 5.2 we found that the origin of the non-exponential behaviour of the junctions conductance with decreasing tip-sample separation is the Pauli repulsion acting between D_2 and the electrodes. To assign the atomic resolution of the Au surface in figure 5.11 as a consequence of the Pauli repulsion, one would need to analyse the interaction of D_2 with the surface above different points of the sample. However, such analysis is difficult to perform due to the weak interaction between D_2 and the metal substrate [200, 210]. Instead we analyse the imaging mechanism with respect to the site specific adsorption

properties of another closed shell particle adsorbed on metal surface, namely Xe atoms on Pt(111).

Note that the proposed model of the STHM imaging mechanism (cf. section 5.3) is not restricted to D_2 , but only requires a closed shell particle at the tip apex which follows the movement of the tip. This could be realized e.g. by picking up Xe atoms from the surface with the STM tip [134], the behaviour of Xe should not make a difference compared to D_2 , although the interaction between the noble gas atoms and the metal substrate is much stronger than the D_2 -Au interaction as can be seen e.g. by the static adsorption of Xe on Pt(111) which even allows manipulation of adsorbed atoms with the STM tip [134, 221].

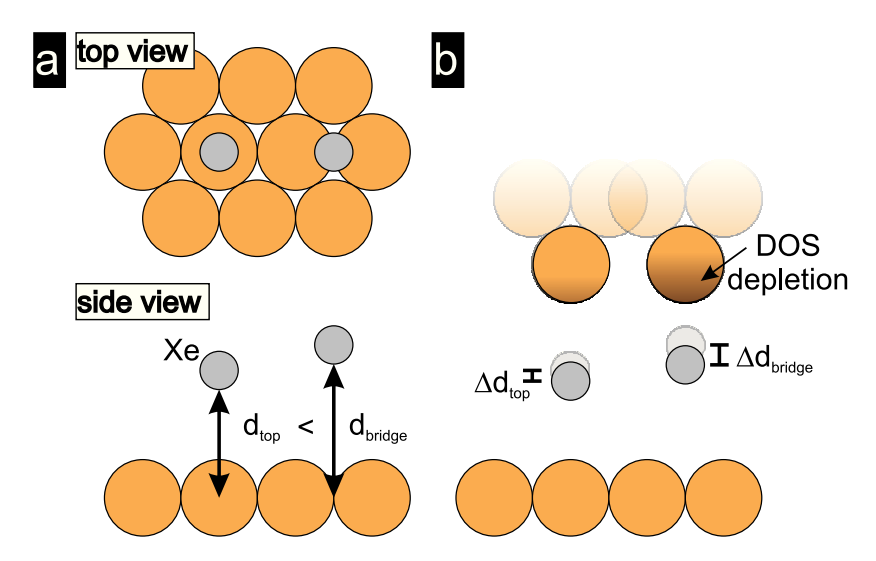


Figure 5.18: Illustration of the imaging mechanism which leads to the atomic resolution on the example of Xe/Pt(111). a) Top (top) and side view (bottom) of the adsorption of Xe/Pt(111) at two different positions above the surface. The interaction with the underlying substrate results in variations of the adsorption height of Xe above different positions of the sample. For example, the adsorption height atop of an atom (d_{top}) is smaller than above the bridge site (d_{bridge}) between two atoms [222] as indicated in the side view. b) Sketch of the displacement of the atoms in the presence of the STM tip. The larger displacement of the Xe atom leads to a stronger depletion of the tip DOS, thus to a smaller conductance of the junction.

The adsorption height of Xe on Pt(111) depends on the position of the atom above the surface [222]. At a position on top of a Pt atom the equilibrium distance between Xe and the surface is expected to be smaller than above the bridge site between two atoms as schematically sketched in figure 5.18 (a). If now the STM tip scans the surface in constant height mode, as usual for STHM images, the Xe atom will have to move to a new equilibrium position closer to the sample (cf. fig. 5.18 (b)). Since the force between the tip and the Xe atom will depend on the distance between the two, the displacement

of the atom out of its former equilibrium position can be expected to be larger above the bridge sites ($\Delta d_{top} < \Delta d_{bridge}$). In turn, the stronger displacement indicates a stronger force resulting from the Pauli repulsion between Xe and the tip. According to our model, the stronger Pauli repulsion yields a stronger depletion of the tip DOS and therefore a lower conductance above the bridge sites of the sample. Thus, the atoms should appear bright in a recorded image.

Note that for the above discussion we only take into account the different adsorption heights of Xe atop and besides the atoms, whereas in reference [222] it is found that one could expect a stronger repulsive force besides the atom than on top of the atom. However, this effect would further amplify the difference between the two adsorption sites.

Applying the results obtained on Xe/Pt(111), we can finally understand the contrast formation in STHM images of Au(111). During scanning a single D_2 is located below the tip apex. The vertical position of D_2 in the junction will depend on its interaction with the electrodes, i.e. tip and sample. When the tip-sample separation during scanning is reduced to a distance $z \leq 2d_{eq}$, where d_{eq} is the equilibrium adsorption height of D_2 above the surface, D_2 will have to move to a new equilibrium position closer to the electrodes. Since the tip-sample distance is kept constant during scanning, the displacement of D₂ will depend on d_{eq} as schematically shown in figure 5.18 (b). Thus, at positions above the surface where d_{eq} is larger, e.g. at bridge sites, we can expect a larger displacement of D_2 out of the former equilibrium position. The larger displacement will result in a stronger repulsive force between D₂ and the sample which is balanced by a repulsive force between the D_2 and the tip. According to our model calculations (cf. section 5.2), the repulsive forces originate from the Pauli repulsion between D₂ and both sides of the junction. At the side of the tip the Pauli repulsion leads to a depletion of the tip-DOS at the Fermi level and therefore to a smaller conductance of the junction. Thus, positions above the sample where the displacement of D_2 is larger (e.g. bridge sites) should appear darker than positions where the displacement is smaller (atop of the atoms). Therefore, the atoms in STHM images (figures 5.11 and 4.21) appear brighter than the positions next to the atoms.

Summarizing the findings above, the origin of the atomic resolution in STHM images is the vertical displacement of D_2 out of its equilibrium adsorption height, as could be shown due to a comparison with the site specific adsorption height of Xe/Pt(111). The contrast formation hereby can be explained by the simple one-dimensional model of the STHM junction, presented in section 5.3 to explain the contrast formation in STHM images of organic molecules, in which a single D_2 molecule acts as a combined sensor and signal trans-

ducer via Pauli repulsion between D_2 and the electrodes.

5.5 Attempt of quantification: calibration of the force sensor

In the previous sections, we developed a qualitative model for the contrast formation in STHM images. According to the sensor/transducer model, presented in section 5.3, the STHM contrast appears due to the repulsive interaction of a confined D_2 molecule with the electrodes of the STM junction. The repulsive interaction leads to a depletion of the DOS of the electrodes at the Fermi level, due to the Pauli exclusion principle, yielding changes in the conductance of the junction depending on the force acting on D_2 . However, the strength of the force which leads to a certain reduction of the junctions conductance has not been addressed up to now.

The force acting on the D_2 molecule is difficult to address by experimental methods. On the contrary, the force acting on the tip can be measured by means of AFM [80, 82, 88, 223, 224]. Especially in dynamic AFM modes small forces between the tip and the sample can be measured with pN resolution [140, 225]. A prominent example of the dynamic modes is frequency modulated AFM (FM-AFM), which allows the reconstruction of the tip-sample force by measurement of the frequency (f) of the oscillating tip [83, 156]. The tip thereby is usually mounted on a cantilever beam. In many cases the change of the oscillation frequency is small compared to the eigenfrequency of the cantilever, thus the frequency shift $df = f - f_0$ is defined, where f is the measured oscillation frequency of the cantilever and f_0 its eigenfrequency.

5.5.1 Force on the tip

To get further insight into the relation between the force on the confined D_2 molecule and the conductance of the STHM junction, we simultaneously recorded dI/dV(V) and df(V) spectra at different tip-sample separations.

Figure 5.19 (a) shows a series of dI/dV(V)-spectra measured above the center of PTCDA on Ag(111) with subsequent decreasing of the tip-sample distance (step = 0.16 Å). The acquired spectra cover a total range of 2.4 Å, approaching from the stabilization point of the tip above the molecule ($z_{displacement} = 0$ Å).

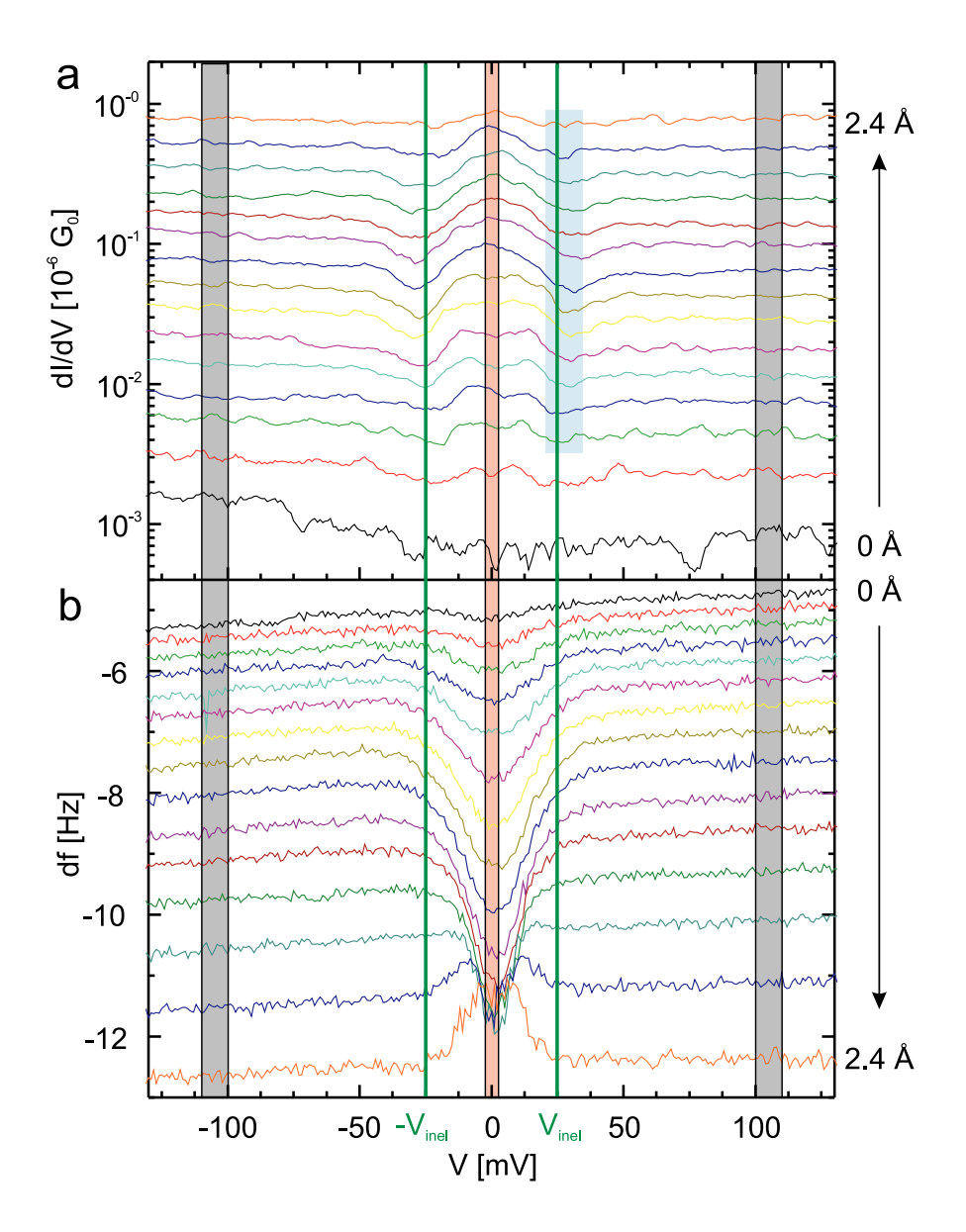


Figure 5.19: Evolution of dI/dV and df spectra with decreasing tip-sample separation. (a) dI/dV-spectra recorded with lock-in detection (modulation amplitude 4 mV, frequency 0.9 kHz), and subsequent reduction of the tip sample separation in steps of 0.16 Å above PTCDA/Ag(111). Light blue shaded area indicates the region of conductance spikes. (b) Simultaneous recorded df-spectra. Spectra corresponding to the same tip-sample distance are plotted with the same colour as in (a). In addition, $-V_{inel}$ and V_{inel} mark the transition between the state where D_2 is present in the junction and the empt junction.

The evolution of the dI/dV(V) spectra shows the same characteristic behaviour as above PTCDA/Au(111) (cf. fig. 5.4), i.e. two structural different states of the junction. One state at $|V| > V_{inel} \approx 25$ mV, in which the junction is empty, and another state at $|V| < V_{inel}$ where D₂ is present in the junction (cf. fig. 5.2). The transitions between the two states appear as spikes in the spectra.

Comparing the obtained spectra with previous experiments one observes the rather low conductance values. The lower conductance may be related to the fact that AFM tips cannot be cleaned so well prior to the experiments. It is conceivable that an oxide layer is present at the tip apex which reduces the conductance of the tip.

df(V) spectra, which have been acquired simultaneously with the dI/dV data, are displayed in figure 5.19 (b) in the same colour-code used in (a) for spectra recorded at the same tip-sample distance. Due to the negative sign of the frequency shift the spectra are displayed from top to bottom with decreasing tip-sample distance, while in figure 5.19 (a) the spectra are shown in opposite order.

Similar to the dI/dV spectra, df curves behave differently in the regime close to zero bias $(|V| < V_{inel})$ than expected without the presence of D_2 . Whereas in conventional AFM experiments the frequency shift shows a parabolic dependence on the applied bias [93, 226], the spectra in figure 5.19 (b) exhibit a non-parabolic evolution. Comparing df- and dI/dV-data, one observes that the bias window in which the non-linearities in the df-spectra appear corresponds to the range between $|V| < V_{inel}$. This finding is not surprising, since at this bias one expects D_2 to be present in the junction. The data shows that the presence of D_2 leads to an increase of the frequency shift $(|df|_{|V| < V_{inel}} > |df|_{|V| > V_{inel}})$ with respect to the empty junction. The rise of |df| depends on the tip-sample separation and increases further with decreasing distance until the situation reverses and a peak appears in the spectra $(z_{displacement} > 2.1 \text{ Å})$.

To get further insight into the evolution of the conductance and the frequency shift with decreasing tip-sample separation for the empty junction and in the state which leads to the STHM contrast, we extract dI/dV and df data at zero bias, where we record STHM images, and at elevated bias $|V| > V_{inel}$, where D_2 is expelled from the junction (cf. fig. 5.2). Plotting the resulting data points against the tip displacement allows the direct comparison between the evolution of the frequency shift in STHM mode with the frequency shift for the empty junction and with the evolution of the conductance ratio (cf. fig. 5.6), which is defined to quantify the effect of D_2 on the conductance of the junction.

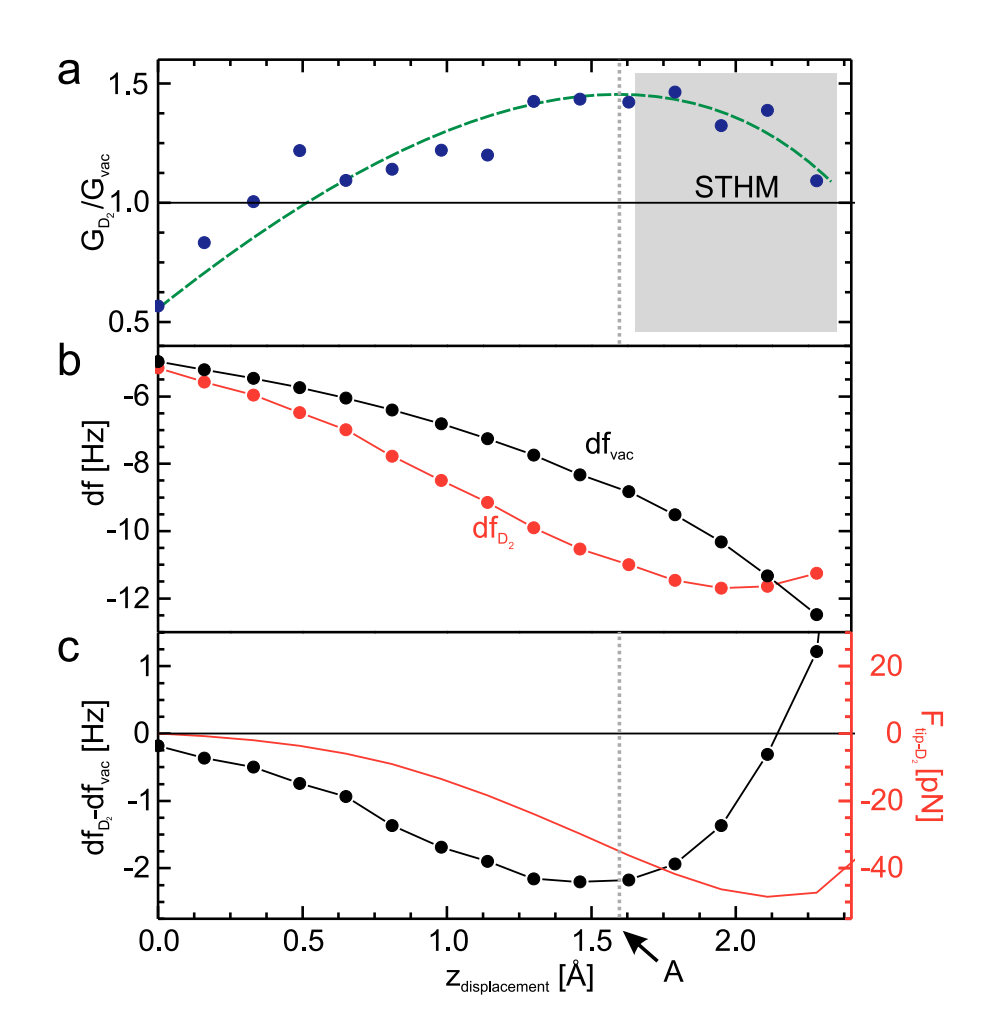


Figure 5.20: Evolution of dI/dV and df values at zero and high bias with decreasing tip-sample distance. Data was extracted from figure 5.19 by averaging over the black (high bias) and red (zero bias) areas. (a) Conductance ratio derived by dividing both spectra. As a guide to the eye the qualitative evolution of the conductance ratio is indicated by the green dashed line. In addition, the distance where the conductance ratio exhibits is maximum is marked as "A" and a dotted line. (b) df(z)-spectra in the correspond colours. (c) Frequency shift with D_2 from (b) after background subtraction (black dots). Integrated frequency shift, which represents the force evolution between D_2 molecule and the tip with decreasing tip height (red line).

Figure 5.20 (a, b) shows the evolution of dI/dV- and df- values at zero bias (df_{D2}) and for $|V| > V_{inel}$ (df_{vac}) with decreasing tip-sample distance. The data points are reconstructed from the spectra in figure 5.19 by averaging over the two shaded areas. The conductance ratio (G_{D_2}/G_{vac}) is shown in figure 5.20 (a) (cf. fig. 5.6) together with a guideline for the

eyes (green dashed line). df_{D_2} is shown in figure 5.20 (b) (red dots) whereas in the same figure the curve for the empty junction (df_{vac}) is shown, which is obtained by taking the mean value of the two data points reconstructed for $V < -V_{inel}$ and $V > V_{inel}$ (black data points in fig. 5.20 (b)).

The conductance ratio shows the same behaviour as observed for PTCDA/Au(111) (cf. fig. 5.6 (b)), i.e. while the tip sample distance is reduced, the conductance ratio first rises, than it reaches a maximum before it drops to values even below one. However, the low conductance values lead to an increased noise in the spectrum, thus the evolution of the conductance can be estimated only qualitatively (green dashed line in fig. 5.20 (a)).

This is different for the evolution of the frequency shift obtained for the two states of the junction, which does not show such a high noise level, thus allows a further analysis. The spectrum recorded at elevated bias (df_{vac}) shows the expected constant increasing of |df|-values with decreasing tip-sample distance due to the increasing attraction between tip and sample [99]. At zero bias, where D_2 is present in the junction, the situation is different. $|df_{D_2}|$ exhibits a maximum at $z_{displacement} \approx 2$ Å, while for shorter distance $|df_{D_2}|$ decreases again.

The maximum and subsequent reduction of |df| indicates an increasing contribution of repulsive forces to the total force acting on the tip with reduced tip-sample distance. However, one can expect that the total force which results in the obtained frequency shift is a superposition of at least two forces. On the one hand, there is the force between the tip and D_2 , which we have identified as the origin of the STHM contrast, and on the other hand there is a contribution to the total force on the tip due to the macroscopic size of tip and sample.

According to equation 2.30, the frequency shift resulting from two force components equals the sum two frequency shifts:

$$df_{tot} = -\frac{f_0}{kA^2} \langle F_{tot} q \rangle \tag{5.2}$$

$$= -\frac{f_0}{kA^2} \left\langle (F_1 + F_2)q \right\rangle \tag{5.3}$$

$$= -\frac{f_0}{kA^2} \langle F_1 q \rangle + \left(-\frac{f_0}{kA^2} \langle F_2 q \rangle \right)$$
 (5.4)

$$= df_1 + df_2, (5.5)$$

where f_0 is the resonance frequency, k is the stiffness, A is the amplitude, q is the deflection of the cantilever and $\langle \rangle$ indicates an average over one oscillation cycle. The

contribution to the total force on the tip originating from the force between the tip and the sample can be estimated by df_{vac} , since it corresponds to the frequency shift resulting from the tip-sample interaction without D₂. Therefore, to remove this background force, which gives an additional attractive component to the total force, we subtract df_{vac} from df_{D_2} .

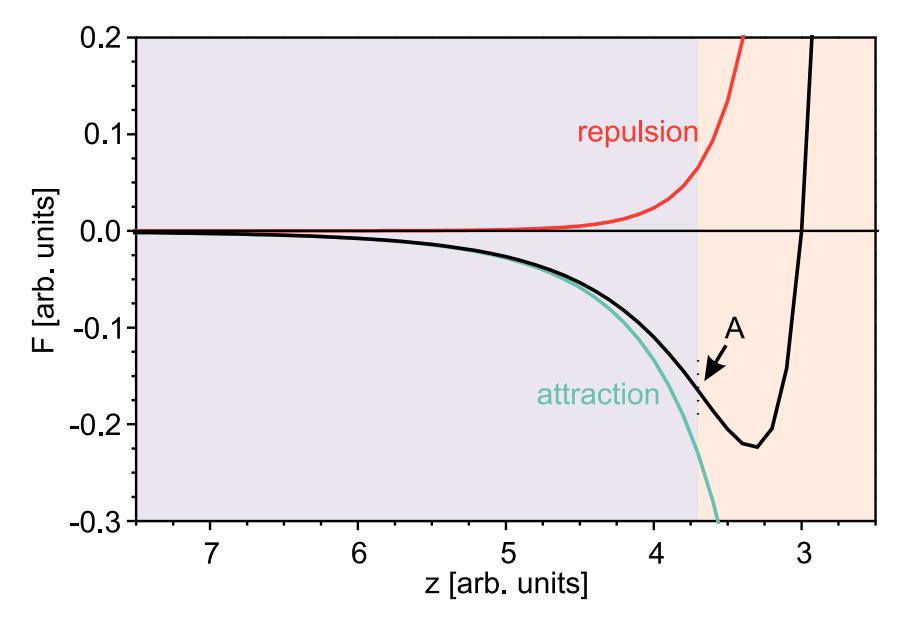


Figure 5.21: Evolution of the contributions to the total force with decreasing tip-sample distance. For the illustration a Lennard-Jones potential consisting of an attractive- (blue curve) and repulsive term (red curve) is chosen. The total force (black curve) is given by the sum of both contributions.

Subtracting the attractive background from the component related to D_2 , the resulting curve (black spectrum in fig. 5.20 (c)) shows the same qualitative behaviour as df_{D_2} before the subtraction. However, the subtraction leads to a shift of the maximum to a larger tip-sample separation ($z_{dispalement} = 1.5 \text{ Å}$), while in addition df values even become positive for $z_{displacement} > 2.1 \text{ Å}$.

From the evolution of the background-subtracted frequency shift, the strength of the tip- D_2 force can be reconstructed. In the limit of small oscillation amplitudes of the cantilever the force can be calculated using equation 2.32. Doing the calculation, the resulting force curve (red curve in fig 5.20 (c)) exhibits a similar behaviour than the df curve, i.e. for larger tip sample separations the force on the tip first increases until it reaches a maximum beyond which the force becomes smaller. Note that in the current context we discuss the evolution for the absolute value of the force whereas its sign only indicates if the force is attractive (-) or repulsive (+). Comparing the resulting force curve with the evolution of the frequency shift, one observes that as long as df values are

negative, the force constantly increases and becomes more and more attractive, while as soon as df values are positive, the attraction is reduced.

The reconstructed force shows that the presence of D_2 in the junction leads to an additional attractive component to the total tip-sample interaction in almost the whole distance range covered in the experiment. The strength of the attractive component depends on the tip-sample distance; the maximum of $|F_{D_2max}| \approx 50 \text{ pN}$ is reached at a distance of $z_{displacement} = 2.1 \text{ Å}$.

After reconstructing the D_2 -related force, we can compare its behaviour with the evolution of the conductance ratio (cf. fig. 5.20 (a)). Comparing both curves one observes that the tip position at which the conductance ratio is maximal coincides with the position where the rate of change of the force changes its sign (distance A in fig. 5.20). Starting from this tip-sample distance, we also obtain atomic resolution of metal surfaces (cf. fig. 5.17). To distinguish what is special about this particular distance, we have to look at the different contributions to the D_2 -related force.

In AFM-experiments measured forces are usually divided into attractive and a repulsive components. To approximate the force on the tip different potentials are used, e.g. Lennard-Jones type, Morse type. However, the speciality of distance A is the same in all of the different potentials. To illustrate the meaning of distance A we look at the attractive and the repulsive contributions to the total force on the example of the Lennard-Jones potential.

Figure 5.21 shows the evolution of total force (black) together with the evolution of its attractive (blue) and repulsive (red) components calculated for a Lennard-Jones potential. The comparison between the curves shows that at the position where the rate of change of the black spectrum changes its sign (distance A in fig. 5.21), the repulsive component starts to overcompensate the attractive part, i.e. the red curve increases faster than the blue one drops. Therefore, we associate point A with the distance at which the tip starts to feel a substantial repulsive interaction. Remarkably, at this distance we start to obtain atomic resolution in STHM images of metallic surfaces (cf. fig. 5.17), while the contrast in STHM images of organic molecules is close to the structure formula of the molecule in question (cf. fig. 5.7), which supports the conclusion that the contrast appears to a repulsive force acting between the tip and D₂.

The best resolution in STHM images of PTCDA is usually achieved when $G_{D_2}/G_{vac} = 1$ (cf. fig. 5.7). At this distance where we expect $G_{D_2}/G_{vac} = 1$, the force on the D_2 molecule is close to zero due to a steep increase of the repulsive interaction at close tip-sample separation (cf. fig. 5.21). The finding that the force on the D_2 molecule at the

distance where we obtain best resolution in STHM images is close to zero is not surprising. In section 5.1.6 we saw that with reducing tip-sample separation the STHM contrast of PTCDA evolves, while the contrast suddenly disappears at tip-sample separations only slightly smaller than the distance at which we obtain the best resolution. Clearly, the resolution depends on the conductance difference between adjacent points in the image. This difference in turn will depend on the difference of the repulsive force on the D_2 molecule and therefore on the slope of the repulsive component which is larger for smaller tip-sample separations. In addition, at the tip-sample distance where the force is zero, it changes from attraction (negative sign) to repulsion (positive sign). The repulsive force than leads to a mechanical squeezing out of D_2 out of the junction which shows up as a sudden loss of the STHM contrast in obtained images at too small tip-sample separation (cf. fig. 5.7 (e,f)).

So far we saw that the obtained force curve for the interaction between D_2 and the tip agrees well with our conclusions from the previous sections. However, a calibration of the conductance curve, i.e. drawing a connection between the conductance behaviour and the force on the D_2 molecule, has not been done yet. Comparing the conductance ratio and the force, we can identify three special points. The first point appears at elevated distances, where the conductance ratio starts to decrease while the tip sample distance is reduced (cf. fig. 5.17). At this distance also the force on the D_2 molecule is close to zero:

$$R(z \to z') \approx 1 \to F(z = z') \approx 0,$$
 (5.6)

where z' is the distance at which the conductance curves with and without D_2 cross each other for larger tip sample separation. The second point is the maximum in the conductance ratio, which is identified as the distance where the radius of curvature of the force changes its sign and D_2 starts to feel the repulsive interaction:

$$\frac{dR}{dz} = 0 \to \frac{d^2F}{dz^2} = 0,\tag{5.7}$$

where R(z) is the conductance ratio and F(z) the force on the tip. Finally, the third point is the distance where the conductance ratio drops below one, at which the force on D_2 is close to zero:

$$R(z) = 1 \to F(z) = 0.$$
 (5.8)

The three distinct points in the evolution of the conductance ratio defined by relations 5.6, 5.7 and 5.8 allow the reconstruction of the force evolution on D_2 from any given evolution of the conductance ratio. However, for a quantitative reconstruction of the force, in addition, the value of the maximum of the force needs to be known, which cannot be

directly obtained from the conductance evolution. However, the maximum attractive force may be expected to be always in the same order of magnitude (here ≈ 40 pN) since it originates from the interaction of the outermost tip atom, a single D₂ molecule and a narrow region of the surface.

So far, we can conclude that the sensor in our model of the STHM junction is sensitive to small forces in the pN regime between the electrodes and D_2 . The obtained conductance ratio in STHM experiments allows in principle the reconstruction of the force evolution and therefore the determination of the force on D_2 from the conductance of the junction. The relation between the force and the conductance leads to a dependence of the image resolution on the tip-sample separation, since STHM images represent lateral variation of the junctions conductance. Consequently, the best resolution in STHM images of organic molecules appear in a regime where the force on D_2 is close to zero, i.e. at the transition from attractive to repulsive force, where the force shows the steepest slope.

6 Outlook: Forthcoming method development

The STHM imaging mode equips the STM with chemical sensitivity by imaging the inner structure of complex organic molecules and the interactions between different adsorbates on metallic surface. To explain the formation of the contrast, we developed a simple one dimensional model in which a single D_2 molecule acts as a combined sensor and signal transducer. In the model we assume that D_2 is statically bound at the tip apex. However, this simplification disregards two properties of the junction which by themselves can give important insight in the sample characteristics, thus they might be used as investigation methods.

One of the disregarded properties is the interaction of D_2 with the electrodes of the junction, which leads to the confinement of D_2 in the junction that shows up as a second conductance state close to zero bias. The confinement depends on a potential well created by the tip and the sample, thus it should depend on the shape [200] and the material [210] of the electrodes. The contribution of the tip to the total potential well does not change at different positions above a sample, therefore, a systematic study of the confinement of D_2 above different positions of the sample gives informations about the local adsorption potential of the sample.

The second property which has been disregarded so far is the dynamics in the junction. Although our spectroscopic investigations have shown that time scales responsible for the contrast formation in STHM images are fast on the time scales of the measurement, we cannot rule out dynamics in the junction. Especially when D_2 is excited out of the junction by application of high bias and the junction returns to the original state after reducing the bias again, it is not clear if the same molecule returns or if it is replaced by another one. In favour of the replacement of the molecule speaks the fact that firstly, D₂ diffuses freely on the surface, so that once the molecule is excited out of the junction it can move in any direction, and secondly that stable imaging in STHM mode is only possible if the D₂ coverage on the surface exceeds a certain threshold value. The second observation indicates that a certain density of D_2 on the surface is necessary to increase the probability that always a D₂ molecule is in close vicinity of the junction when it is operated under STHM conditions, so that it can be confined between the tip and the sample. The movement of D₂ on the surface will depend on the diffusion barriers, the structure of the sample and the coverage of D₂. Thus, the analysis of the dynamic behaviour of the junction may lead to conclusions about all three parameters.

In the following we will discuss preliminary results dealing with the confinement of D_2 in the junction and its dynamic behaviour to illustrate how it may be used in forthcoming methods for surface characterization.

6.1 Lateral maps of the interaction potential

The interaction between D_2 and the electrodes of the STM junction shows up in the complex evolution of the junction conductance depending on the applied bias and the tip-sample separation. Whereas the dependence of the conductance at zero bias on the tip-sample distance leads to the STHM contrast, the dependence on the applied bias has not been addressed so far. In the following we analyse the behaviour of differential conductance spectra at finite bias and fixed distance to elucidate the dependence of the interaction of D_2 with the junction on the structure of the electrodes. The results obtained from such analysis may then be used to extract information about the adsorption potential above the surface in forthcoming investigations.

Differential conductance spectra (dI/dV(V)) reveal the dependence of the conductance on the bias at a fixed tip-sample separation. In the spectra two structural different conductance states have been identified: one state appears in the regime close to zero bias, induced by the presence of D_2 in the junction, and a second state at elevated bias, where D_2 has no effect on the junctions conductance as shown by e.g. the recurrence of the conventional STM contrast (cf. fig. 5.3). The transition between the two states is marked by sharp conductance spikes. These spikes are assigned to excitations of vibrational levels of the junction due to inelastic tunnelling electrons [197, 198].

IETS probes vibrational levels of the STM junction by measuring the differential conductance [42]. The identified levels are usually assigned to vibrational eigenstates of particles adsorbed between the electrodes [50]. Since the levels are assigned to eigenstates of the particle, they usually appear at a specific bias value. However, the spikes in the dI/dV spectra recorded with D₂ in the junction show some variability (25 mV < | V_{inel} | < 60 mV in the center of PTCDA). The variability of the spike position suggests that the excited states are not vibrational levels of D₂, although excitations of H₂ and D₂ layers have been observed at 50 meV (D₂) and 25 meV (H₂) [208]. Thus the excited vibrational levels should originate from a quantity of the junction which changes between different experiments. Possible quantities that change between the experiments are the D₂ coverage and the structure of the electrodes, i.e. the shape of the tip. In reference [172] it is found that with increasing H₂ coverage the position of the spikes shifts to larger

bias ($|V_{inel_{high}}| > |V_{inel_{low}}|$). However, an additional contribution from the shape of the junction cannot be ruled out from the beginning.

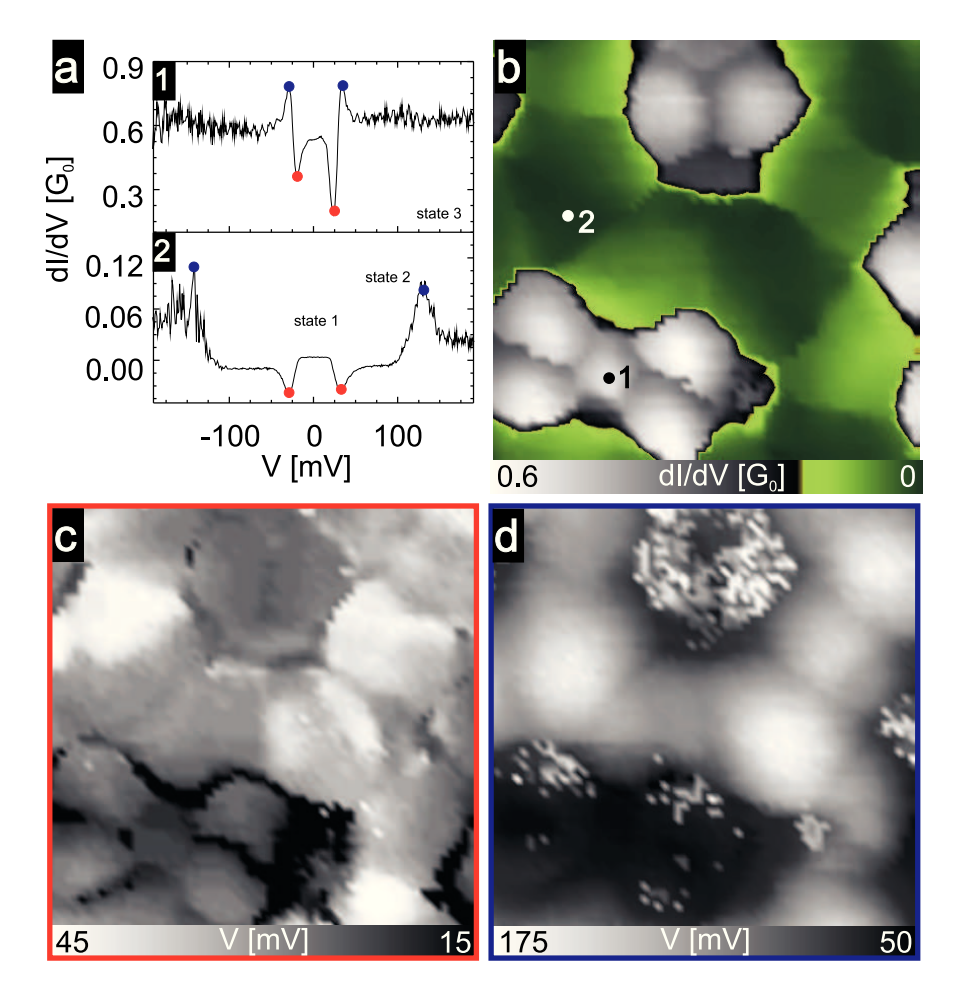


Figure 6.1: Relationship between spike positions in dI/dV spectra and the molecular structure in STHM images at constant height. Data reconstructed from a series of 64×64 dI/dV(x,y,V)-spectra recorded above PTCDA/Au(111) in the presence of D_2 with lock-in detection (modulation amplitude 4 mV, frequency 2.3 kHz). (a) Two examples of the dI/dV-spectra, recorded above the center of PTCDA (a1) and the center of the hollow between the molecules (a2). Positions of inelastic features are marked by red and blue dots (cf. text). (b) STHM image reconstructed from the spectra at V=0 mV. The positions of the spectra in (a) are marked by the black and white dots. (c-d) Lateral maps of the excitation energy at which the inelastic features in (a) appear depending on the tip position. (c) Energy at which the inner (red) features appear. (d) Energymap of the outer spikes at which D_2 is finally expelled from the junction.

To investigate if the structure of the junction effects the bias at which D_2 is excited in the junction, we look at dI/dV spectra recorded at different points of an image. Therefore, we record datacubes consisting of dI/dV spectra at each point of an image while the tip constantly scans the surface. The use of such datacubes out of $dI/dV(x, y, z = z_0, V)$ data

allows the comparison of spectra from different points of the image, while the exact position of the point from which the spectra is taken can be determined with the high lateral resolution of reconstructed STHM images (cf. fig. 5.3).

Figure 6.1 shows results obtained from a datacube recorded above PTCDA/Au(111) which contains 64×64 spectra. Two examples of spectra recorded above the center of PTCDA (1) and above the area between the molecules (2) are shown in figure 6.1 (a). Each of the spectra shows two sets of features, one close to zero bias at $|V| = |V_{red}|$ (red dots) which appears as a dip and one at larger bias at $|V| = |V_{blue}|$ (blue dots) which appears as a peak. The positions where the spectra were recorded are marked in the STHM image reconstructed from the data (fig 6.1 (b)). Figure 6.1 (c-d) show false colour images of the bias at which the dips and peaks appear in the spectra, depending on the lateral position of the tip.

Looking at the spectra one immediately notices that the bias at which the transition between the different states occurs depends on the lateral tip position. The first transition ($|V_{red}|$) happens at a similar bias, while the second transition shifts by $\approx 100 \text{ mV}$ from the position on top to the position between the molecules. Assigning the inelastic features in dI/dV spectra to transitions between structural different states of the junction, we can identify three different states in the spectra in figure 6.1 (a). State 1 close to zero bias $|V| < |V_{red}|$, state 2 for $|V_{red}| < |V| < |V_{blue}|$ and state 3 for $|V| > |V_{blue}|$.

Comparing the reconstructed bias maps of the transitions between the different states (fig. 6.1 (c-d)) with the contrast in the STHM image (fig. 6.1 (b)) reveals that the positions of the bias values is always the same above structural similar positions above the underlying molecular structure. Therefore, like in the STHM image, the bias maps also show the positions of PTCDA molecules and even the position of hydrogen bonds between the molecules with a comparable high lateral resolution. Besides the fact that the bias at which the excitations occur depend on the structure of the junction, this finding indicates that whatever is the origin of the hydrogen bond contrast in STHM images also effects the confinement of D_2 in the junction, so that the bias at which the transition between different states appear in the spectra depends on whether the tip is located above the H-bond or not.

In addition, whereas in figure 6.1 (c) the molecular backbone of the PTCDA molecule in the lower part of the image appears, in figure 6.1 (d) it does not, but instead a flickering appears above the molecules. This flicker appears due to an increased noise in the spectra at bias values larger than $|V_{red}|$ which prohibits an identification of $|V_{blue}|$ at positions where the bright spots appear in figure 6.1 (d). Besides the noise in the image

we obtain an overall higher resolution of the molecules in the bottom part of the images compared to the top part. The improvement of the resolution may originate from a vertical drift of the tip during the measurement. Thus, the improvement may indicate an additional dependence of the bias at which the transitions occur of the tip-sample separation.

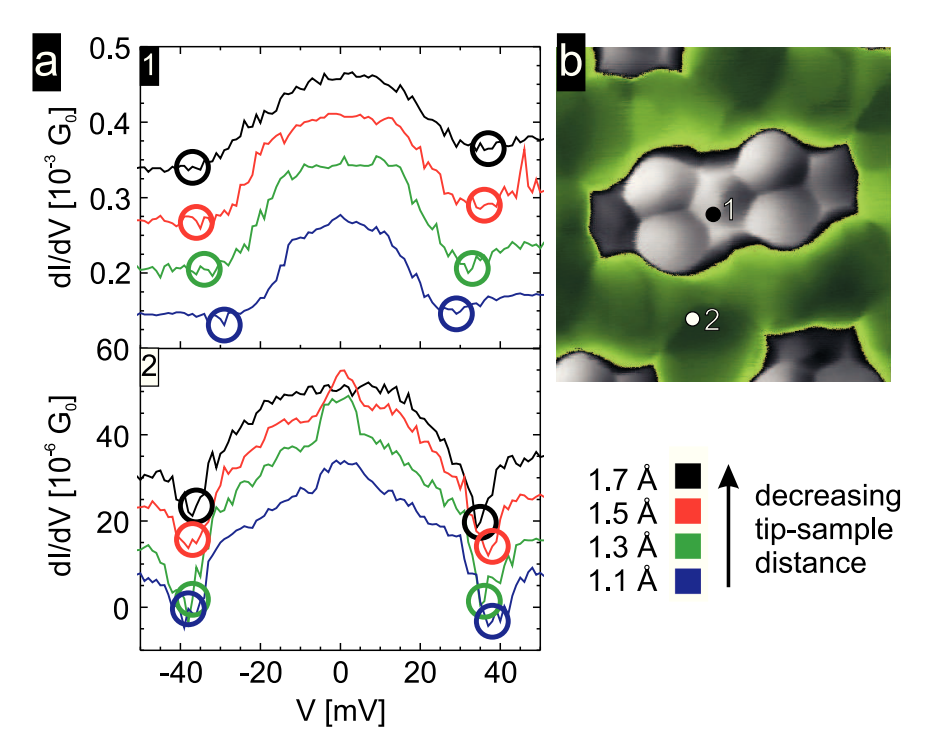


Figure 6.2: Series of dI/dV-spectra recorded above a single PTCDA molecule. The spectra have been measured with lock in detection (modulation amplitude 4 mV, frequency 4.5 kHz) for four different tip-sample separations above the herringbone phase of PTCDA/Au(111) with D₂. (a) Spectra recorded above the center of a PTCDA molecule (1) and in the area between the molecules (2). The positions of inelastic conductance spikes where D₂ is excited out of the junction are marked with circles in the corresponding colour of the spectrum. (b) STHM image of PTCDA/Au(111) where the positions where the spectra in (a) were recorded are marked. The image was recorded after the tip was approached by 1.7 Å from the stabilization point. Bottom panel of (b) shows the colour code and the corresponding tip displacements from the stabilization point. Image parameters: $1.4 \times 1.4 \text{ nm}^2$, constant height, V = -5 mV

To investigate the dependence on the tip-sample separation, we recorded $dI/dV(x,y,z=z_0,V)$ datacubes at different distances z_0 . Figure 6.2 (a) shows dI/dV(V)-spectra recorded above two different points of the image. The spectra in figure 6.2 (a1) have been recorded above the center of PTCDA while the spectra in figure 6.2 (a2) have been recorded between the molecules. The positions from which the spectra were taken are marked in

the corresponding STHM image (fig. 6.2 (b)). At bias values $|V| = |V_{inel}|$ inelastic features appear as dips in the spectra. For the spectra recorded in the center of PTCDA (fig. 6.2 (a1)) the position of the dip moves from |V| = 40 mV to |V| = 30 mV with increasing tip-sample distance. In the spectra recorded between the molecules (fig. 6.2 (a2)) the dip position shows a slight shift in opposite direction

The transition from state 1 ($|V| > |V_{inel}|$) to state 2 ($|V| < |V_{inel}|$) shows up as dip in the spectrum, similar to the behaviour in figure 6.1. In addition in both cases the bias at which the transition occurs ($|V| = V_{inel}$) is very similar between the position above the molecule and the between the molecules. Notably a second transition to a third state like in the above example (cf. fig. 6.1) is not observed for the present tip-sample separation, although images reconstructed at higher bias suggest that such transition should occur.

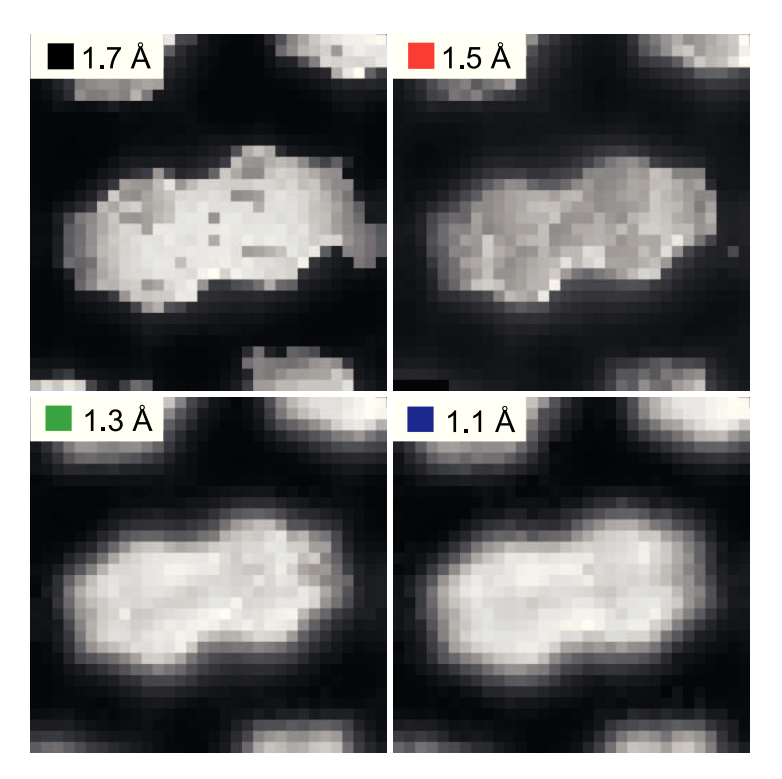


Figure 6.3: Images reconstructed for bias values beyond the spikes (V = 55 mV). The images are reconstructed from all four datacubes recorded at different tip-sample distance (cf. fig. 6.2). All images show deviations from the image contrast usually obtained in STM images of PTCDA/Au(111) where the conductance is homogeneous above the molecule and no submolecular features are expected.

Figure 6.3 shows images reconstructed from all four datacubes at bias (|V| = 55 mV) where the junction is in state 1. All four images reveal deviations from a flat conductance behaviour above the molecule as it is known for the contrast in conventional STM images

(cf. fig. 4.1). This finding leads to the conclusion that at least a second transition should occur at larger bias at which D_2 is finally excited out of the junction. Although the second transition has not been recorded, we can still compare the dependence of V_{inel} on the lateral position of the tip at the different tip-sample distances.

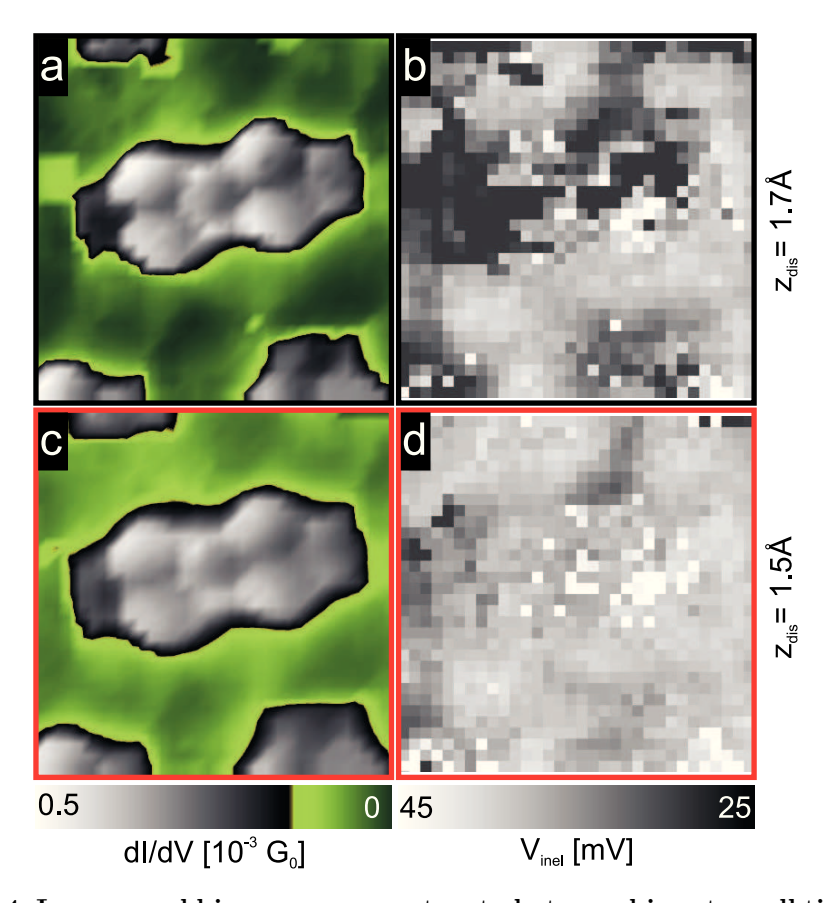


Figure 6.4: Images and bias maps reconstructed at zero bias at small tip-sample separation. (a, c) Images reconstructed from a set of 32×32 dI/dV spectra at zero bias recorded in constant height mode. (b, d) Lateral maps of the bias at which the inelastic conductance spikes occur. The colour of the frames arround the images correspond to the colour code used in figure 6.2.

Figures 6.4 and 6.5 show STHM images reconstructed from the datacubes at zero bias (a, c) together with the corresponding maps of V_{inel} (b, d). The STHM images show an increase in the resolution of PTCDA with decreasing tip-sample distance (cf. fig. 5.7). Whereas the image reconstructed at smallest tip-sample separation shows STHM contrast of PTCDA comparable to the contrast in figure 4.1, the image reconstructed at largest tip-sample distance shows the contrast with the nodal plane along the long axis of the molecule like the contrast in figure 4.5 as expected for increased tip height compared to the one at which we obtain STHM resolution. In addition, the pattern between the molecules which is assigned to the hydrogen bonds between adjacent PTCDA molecules

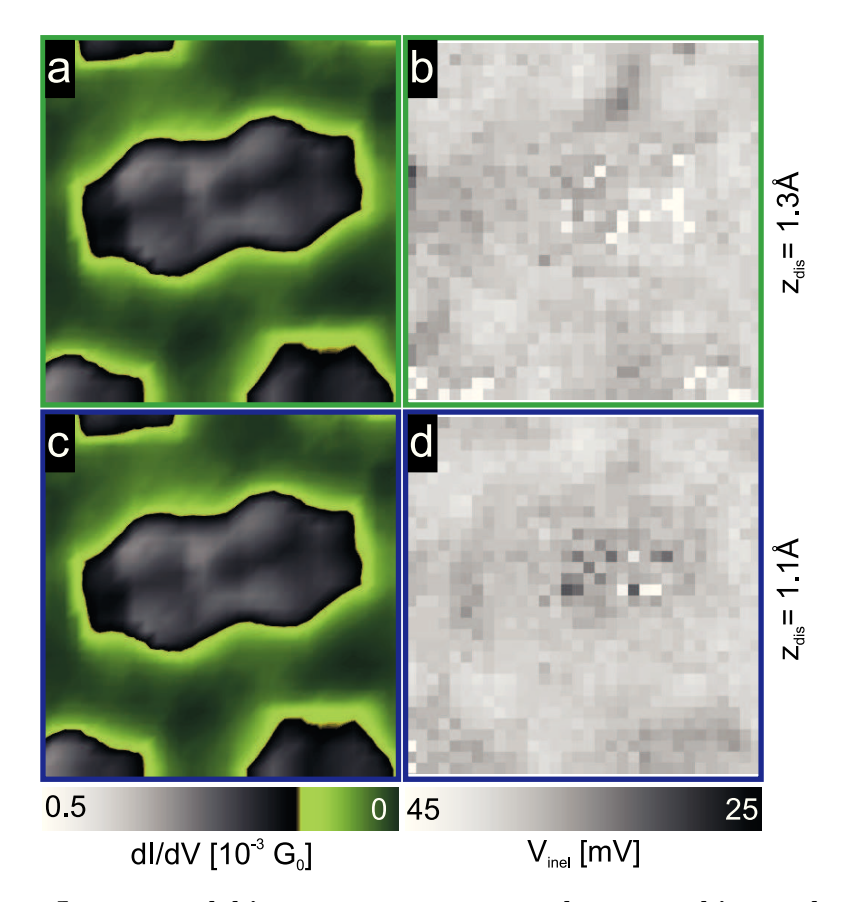


Figure 6.5: Images and bias maps reconstructed at zero bias at larger tip-sample separation. (a, c) Images reconstructed from a set of 32×32 dI/dV spectra at zero bias recorded in constant height mode. (b, c) Lateral maps of the bias at which the inelastic conductance spikes occur. The colour of the frames around the images correspond to the colour code used in figure 6.2. For a better comparison, the images are plotted on the same scale as used in figure 6.5.

shows a similar increasing in the resolution with decreasing tip-sample separation like the contrast of PTCDA, i.e. the pattern is less resolved when the tip-sample distance is increased.

In the bias map reconstructed at smallest tip-sample separation (fig. 6.4 (b)) the shape of PTCDA is vaguely visible, because $|V_{inel}|$ is slightly smaller compared to the rest of the map. With increasing tip-sample distance $|V_{inel}|$ above the molecule shifts to larger values until in figure 6.5 (d) almost no difference between the molecule and its surrounding is visible any more.

The spectra in figure 6.2 (a1) suggest that $|V_{inel}|$ shifts to smaller energies when the tip-sample separation increases, while the energy maps indicate the opposite behaviour. In order to figure out the evolution of V_{inel} at all positions of the map with increasing tip-sample separation, we reconstruct histograms from all maps of V_{inel} . The histograms are

constructed by dividing the bias scale in steps of 2 mV, counting the number of points in the bias map at which V_{inel} has a certain value:

$$\#counts_{2n}(z_i) = \sum_{x,y} \begin{cases} 1, & V_{inel}(x,y,z_i)/[mV] \in \\ 0, & else \end{cases} (6.1)$$

where z_i means the tip-sample separation at which the specific datacube has been recorded and (x, y) denotes the lateral position of a point in the V_{inel} map independent of whether the point is above a PTCDA molecule or not.

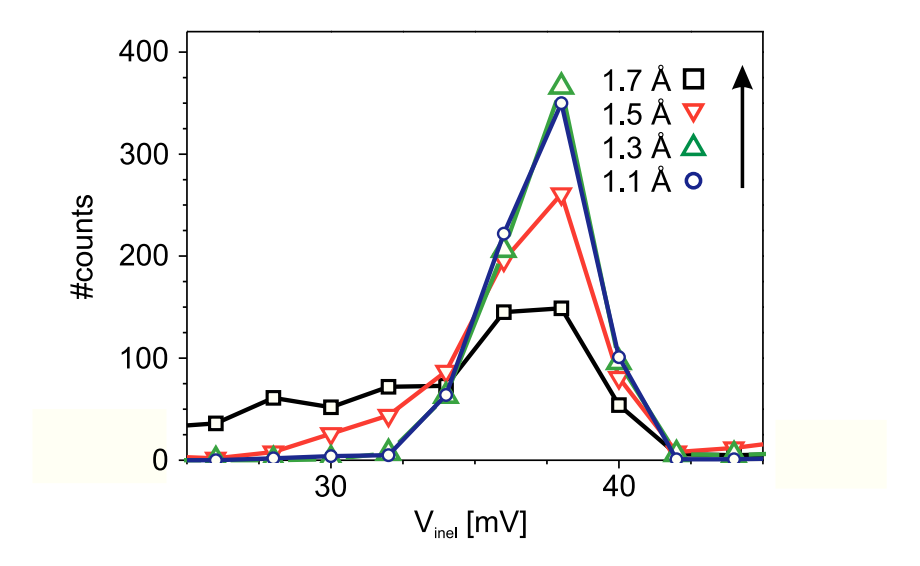


Figure 6.6: Histograms for the four different tip-sample separations reconstructed from the maps of V_{inel} . At smallest distance a tail at smaller energies is visible. With increasing tip distance V_{inel} values accumulate around $E=38~\mathrm{mV}$ while the tail at smaller energies disappears. The applied colour code corresponds to the one used in figure 6.2 (a)

The histograms reconstructed from the four maps of V_{inel} are shown in figure 6.6 in the same energy range as the maps in figures 6.4 and 6.5. For the smallest tip sample separation ($z_{dis} = 1.7 \text{ Å}$, black curve) the V_{inel} increase constantly from $V_{inel} = 25 \text{ meV}$ until a maximum is reached at $V_{inel} \approx 38 \text{ meV}$ before the number of counts quickly drop to zero. Increasing the tip-sample separation, the number of points where V_{inel} is smaller than 38 mV decreases, while the number of points where V_{inel} is larger than 38 mV increases. This behaviour leads to a growing of the peak at $V_{inel} = 38 \text{ mV}$ until for a certain tip-sample separation the situation does not change any more so that the histograms obtained for z displacement of 1.3 Å (green) and 1.1 Å (blue) are identical.

An increase of V_{inel} with decreasing tip-sample distance, as indicated by the spectra in figure 6.2 (a1), is not supported by the histogram. Since most positions above the PTCDA molecules appear darker than the areas between the molecules in the V_{inel} maps recorded at $z_{dis} = 1.7$ Å and $z_{dis} = 1.5$ Å, we can identify these positions with the origin of the tails towards smaller bias (V < 38 Å) in the histograms (black and red curve in fig. 6.6). At larger tip sample separations, the tails towards smaller bias disappear and the V_{inel} values at all tip positions above the sample appear close to V = 38 mV. This finding suggests that in fact the situation is the other way around as indicated by the spectra in figure 6.2 (a1), namely that with increasing tip-sample separation, V_{inel} shifts towards larger values.

In contrast to positions between the molecules where V_{inel} remains constant, the dependence of V_{inel} on the tip-sample separation for tip positions above PTCDA may indicate a lower confinement of D_2 in the junction at tip positions above the molecules. According to this picture the increased contribution of the Pauli repulsion to the total force on the D_2 molecule at tip-sample distances where we obtain STHM resolution (cf. section 5.5.1) yields a weaker binding of D_2 to the electrodes of the junction. Consequently the weaker binding leads to a smaller energy $E = eV_{inel}$ necessary to excite D_2 in the junction, thus V_{inel} shifts to lower values when the tip-sample separation is reduced.

At largest tip-sample separation in the experiment ($z_{dis} = 1.1 \text{ mV}$), V_{inel} values above PTCDA coincide with the values obtained when the tip is located above a position between the molecules as can be seen by the aggregation of V_{inel} around 38 mV (cf. blue spectrum in fig. 6.6). The independence of V_{inel} on the lateral tip position indicates that the energy ($E = eV_{inel}$) necessary to excite D_2 in the junction is independently of the distance between the electrodes. This finding suggests that the interaction of D_2 with the junction, which leads to the position of V_{inel} , is governed by the tip which does not change between the different positions above the sample. The finding of the identity of the histograms at $z_{dis} = 1.1 \text{ Å}$ and $z_{dis} = 1.3 \text{ Å}$ is in favour of this interpretation, since if the interaction is governed by one electrode of the junction at a certain distance, the contribution of the second electrode can be neglected and histograms recorded at even larger separations should not change.

So far, we can conclude that the interaction between D_2 and the electrodes in the present example is mainly governed by the tip while the strength of the interaction shows up by the maximal excitation energy $eV_{inel} \approx 38 \text{ meV}$ around which V_{inel} values aggregate at larger tip-sample separation. The obtained value for the excitation energy is close to the one reported in reference [197] for Pt break junctions containing H_2 (39 meV),

whereas for Pt-D₂-Pt junctions the authors of reference [197] observed a reduction of the excitation energy shifted by the square root of the mass ratio (i.e. $E_{D_2} \approx 27 \text{ meV}$). The comparability between the excitation energies for the Pt junction and our Au tip may indicate a weak dependence of V_{inel} on the material of the tip since due to the larger reactivity of Pt compared to Au [227], one could expect a stronger binding of D₂ to the Pt electrodes.

Now we compare the results obtained from the datacubes at different tip-sample separations with the results obtained from figure 6.1 which has been recorded with a different tip. From the reconstructed bias maps in figure 6.1 (c, d) a determination of the surface structure through the lateral variations of the bias at which D_2 is excited in the junction is in principle possible while from the maps of V_{inel} in figures 6.4 (b, d) and 6.5 (b, d) such characterisation is not possible due to the absence of a contrast between the molecules and the surface. These finding suggest that the bias at which D_2 is excited in the junction strongly depends on interaction between D_2 and the tip. For a strong tip- D_2 interaction the influence of surface is rather weak and no contrast is observed in maps of V_{inel} . Only if the strength of the tip- D_2 interaction is comparable to the D_2 -sample interaction one may expect a contrast in the maps of V_{inel} and therefore a possibility to investigate the interaction between D_2 and the sample surface.

Finally, we would like to note that although the shape of the tip is different in both datasets, as can be seen by the different behaviour of the excitation of D_2 , the different shapes do not limit the imaging capability of the tip in STHM mode as indicated by the identical contrast in reconstructed STHM images. This suggests that in contrast to the STHM contrast, the tip- D_2 interaction, which is responsible for the position of the inelastic features in the spectra, is not only governed by the outermost tip atom which is involved in the imaging process, but a larger part of the tip also contributes to the interaction between D_2 and the tip. Therefore, an analysis of the position of the inelastic features in dI/dV spectra may allow the reconstruction of the tip geometry.

In summary, the inelastic features in dI/dV spectra of the STHM junction do not correspond to eigenstates of D_2 in the junction. The bias at which the transition between different states appear in the spectra rather depend on the interaction of D_2 with the electrodes. The different contrast in reconstructed bias maps, in addition, shows that these interaction depends on the shape of the electrodes, on the side of the tip as well as on the side of the sample. The dependence of the position of the inelastic features could thus be used to reconstruct information about the structure and the interaction potential of the tip and the sample.

6.2 Dynamics in the STHM junction

Up to now all relevant processes of the interaction of D_2 with the electrodes have been fast on the time scale of the measurement so that we could disregard possible dynamic behaviour of D_2 in the junction. However, due to the small binding energy of D_2 on the surface and the finite temperature in our experiments, dynamics should be present. If it would be possible to detect the dynamic behaviour of D_2 with experimental methods, one might gain further insight in the properties of the junction which influence the dynamic behaviour. These properties of the junction could be e.g. the structure of adsorbates on the surface which show up in scattering processes of D_2 .

In the following we discuss experimental observations which go beyond the static model of the STHM junction. The preliminary results clearly show that dynamics are present in the junction while the obtained results lead to suggestions how the effects could be used in systematic analysis to get further insight in sample properties.

6.2.1 Scattering processes

To explain the contrast in STHM images of molecules and metallic surface we developed a static model of the STHM junction in which a single D₂ molecule is statically bound between the electrodes. However, in all the presented images, the imaged samples have been basically flat. If D_2 moves in lateral direction between the electrodes, it is conceivable that the contrast does not appear due to a single D₂ molecule in the junction but rather due to a rapid exchange of D₂ below the tip apex. This exchange would have to be fast on a time scale our measurement, which is basically limited by the equipped pre-amplifier (bandwidth < 1 kHz), so that the movement could not be recognised from the recorded images or spectra. In favour of a movement of D_2 below the tip speaks the observation of spontaneous switching between STHM and STM contrast at low D_2 coverages. According to this picture, if D_2 is present, we obtain STHM contrast while, when the D_2 molecule escapes from the junction and the conventional STM contrast restores, the molecule has escaped. As long as the investigated sample is flat, the movement of D_2 on the sample can be expected to be isotropic but if the sample is inhomogeneous, e.g. due to the presence of adsorbates on the surface, D₂ may be scattered at the border of the adsorbate which result in an anisotropic movement of D_2 on the surface. If now the anisotropic movement of D₂ affects the conductance of the junction, the effect should always be visible when the tip is located close to borders on the surface These borders may be e.g. borders of molecules islands, step edges of the underlying substrate or even single adatoms statically bound to the sample surface. Having a closer look at STHM images of structures which possibly form barriers for the movement of D_2 on the surface, indeed features are visible which do not belong to the imaged structure.

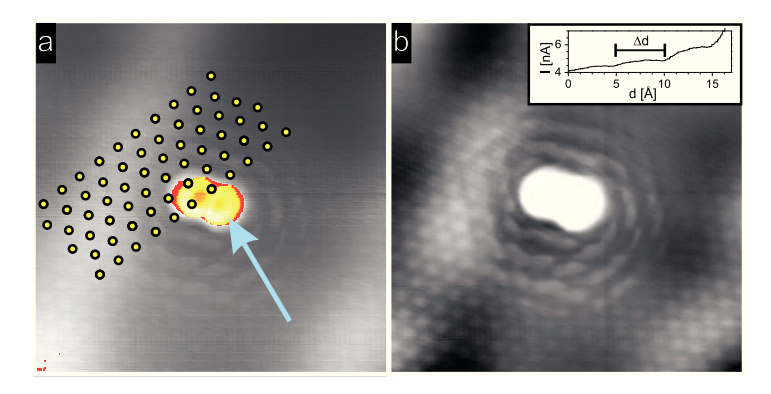


Figure 6.7: STHM image of a dimer of Au-adatoms adsorbed on a Au(111) surface. a) In the upper left part of the image above the adatom dimer the positions of the Au atoms are marked with yellow dots as a guide to the eye. Bright lines from the lower left to the upper right are due to the electronic structure of the surface reconstruction. b) The same image as in (a) but flattened and smoothed to improve the contrast of the atomic structure and the wavy pattern. Inset: Line profile across the wavy pattern. The distance between the minima, determined by the line profile, is $\Delta d = 5 \text{ Å}$. The position at which the line profile is taken is indicated by the blue arrow in (a). Image parameters: $5 \times 5 \text{ nm}^2$, constant height, V = 2 mV

To illustrate the appearance of features which appear close to surface structures in STHM images, we have a closer look at the STHM contrast of the Au adatom dimer on Au(111) presented in section 5.3.1. On the left and right side of the dimer (colour from red to yellow in fig. 6.7 (a)), the typical bright stripes from the herringbone reconstruction of the Au(111) surface are visible [216]. Adjusting the image contrast, one observes that besides the atomic resolution of the adatom dimer, the image contrast reveals atomic resolution of the underlying metal surface (cf. fig. 6.7 (b)). The atoms appear as a regular arrangement of bright spots equally to the STHM contrast of the bare metal substrate (cf. fig. 5.11). In close vicinity of the dimer, the atomic resolution smears out and converts into a wavy pattern of dark and bright areas.

The wavy pattern resembles the outline of the dimer while it also resembles the hexagonal structure of the underlying Au substrate. Therefore, at the first glance one might think that the wavy pattern appears due to a smearing out of the contrast of the atoms. However, the distance between the bright spots of ≈ 5 Å (cf. inset in figure 6.7 (b)) is considerably larger than the lattice constant of Au(111) of 2.85 Å [168]. Thus we can conclude that the underlying atomic structure of the surface is unlikely to be the origin of the wavy pattern around the dimer. But if it is not the atomic structure, one has to

think about another explanation for the contrast.

A conceivable explanation for the appearance of the pattern around the dimer is related to dynamics in the junction. If we assume that D_2 diffuses below the tip apex, the direction of the diffusion can be expected to be isotropic on the surface. The isotropy is broken when a barrier is placed in close vicinity of the tip at which D_2 is reflected. In this case, a standing wave may form between the tip and the reflecting barrier. Such standing wave would change the probability to find D_2 below the tip at each position of the image, thus producing a pattern like the one in figure 6.7.

Assigning the contrast around the dimer to a standing wave pattern, one can also explain the structure of the bright areas and their decreasing intensity with increasing distance between the tip and the dimer. The decreasing intensity of the spots with increasing distance, as shown by the line profile in figure 6.7, may originate from the probability of the reflected D_2 molecule to return to the tip, since the probability should depend on the distance between the scattering centres due to a changed range of angles in which the second scatterer can be found. The shape of the spots, however, may originate from the detailed shape of the centre at which D_2 is scattered. Whereas the adatom dimer exhibits a rather simple shape, the atomic structure of the tip may be complex which results in a dependence of the shape of the standing wave on the angle between the scattering centres, thus producing the different shapes of the areas. Due to the possibility to explain all observed features of the wavy pattern with a standing D_2 wave, we find the standing wave to be a likely explanation for the contrast.

So far, we have observed a wavy pattern around possible D_2 scatterers, e.g. adatoms, steps, molecular islands, in STHM images. The wavy pattern may be identified with a standing D_2 wave between the tip and the scatterer. Clearly the distinct shape of the standing wave pattern will depend on the outline of the scatterer. Therefore, a detailed analysis of the standing wave patterns might be used to reconstruct the shape of the scatterer. Especially, it may be possible to reconstruct the atomic structure of the tip apex, which is usually unknown in STM experiments [36].

7 Summary

The scanning tunnelling hydrogen microscopy (STHM) drives the resolution in STM images to its limits. Images recorded in STHM mode routinely provide atomic scale resolution of metal surface, clusters and organic molecules. The origin of the contrast is a single H_2 (D_2) molecule located below the tip apex which acts as a combined sensor and signal transducer. Therefore, the STHM imaging mode becomes accessible after the condensation of molecular H_2 or D_2 in the junction of a cold STM. The best resolution in STHM images is hereby achieved when the sample is scanned in constant height mode at low bias.

The most striking feature of the STHM mode is the contrast of large plate-like organic molecules. The resolution of the organic molecules closely resembles the chemical structure formula of the molecule in question. The relation between the geometric contrast in STHM images and the structure formula is demonstrated by STHM images of structural different molecules like PTCDA, pentacene, tetracene and SnPc. The direct imaging of the structure of the molecules allows a doubtless identification of the molecules even in complex arrangements. The possibility to distinguish between different molecules directly from the image contrast equips the STM with a chemical sensitivity usually absent in STM experiments. In addition, STHM information contain more in formation.

The STHM mode, for the first time, directly visualizes interactions between different adsorbates on metallic surface. At the same time as the geometric resolution of organic molecules, the interactions appear with remarkable clarity in obtained images. The ability of STHM to directly visualize interactions between different adsorbates is demonstrated on hydrogen bonds in organic layers and polar bonds between organic molecules and metal ions in mixed films. The interactions between the adsorbates are the origin of their self-organisation during adsorption. Thus, the STHM mode allows the investigation of molecular organisation on surfaces from the image contrast, whereas before the presence or absence of molecular interactions could only indirectly be concluded. But STHM not only works on molecules.

Besides the geometric resolution of organic molecules, atomic resolution of metal surface and small metal clusters is easily achieved in STHM images. In STM, structures like metal clusters are usually not imaged with atomic resolution. On the contrary, even small clusters consisting of only two adatoms appear atomically resolved in STHM. Such clusters are used, e.g., as reactive sites in surface catalysis. However, the reactivity depends on

7 Summary

the cluster size. In this context, the contrast in STHM images provides a possibility to determine the size of a cluster by simply counting the atoms.

The above examples indicate the advantages of STHM compared to conventional STM which probes electronic states of the sample close to the Fermi level. These states are often delocalized in the surface plane, thus limits the resolution in obtained images. Due to a smearing out of the contrast across larger surface areas a determination of the atomic structure is usually impossible from conventional STM images. Thus, a determination of the surface structure is only possible for rather simple systems in which the electronic states are localized, e.g. flat atomic surface or weakly interacting molecules. However, information of the surface structure are encoded in energetically lower lying orbitals, since these orbitals are stronger localized at the cores of the atoms. In the case of molecules, imaging these electronic levels would lead to a submolecular resolution in obtained images. The close resemblance between the STHM contrast and the chemical structure of organic molecules suggests that to some extend the STHM mode is sensitive to energetically lower lying electronic levels.

To get further insight in the origin of the mechanism which lies behind the contrast formation in STHM images, we performed a spectroscopic characterisation of the STHM junction. The characterisation has shown that the condensation of H_2 (D_2) is accomplished by the appearance of non-linear conductance spectra. In addition to the conductance spectra, also the dependence of the conductance of the junction on the tip-sample distance shows a unique behaviour. The observed behaviour substantially differs from the conventional exponential dependence of the STM junction.

Looking at STHM images, the obtained contrast also shows a dependence on the tip-sample distance. The contrast in STHM images hereby increases with decreasing tip-sample separation. The dependence of both the image contrast and the conductance on the tip-sample distance suggests a connection between the two, therefore we performed DFT calculations in which the distance between a D_2 molecule and a model tip was systematically varied. Based on the results of the calculations and experimental observation, we developed a model of the STHM junction which explains the contrast formation above the organic molecules.

In the model, a single H_2 (D_2) molecule located below the tip apex acts as a combined sensor and signal transducer. During scanning, the H_2 (D_2) follows the movement of the tip, while the height of the molecule and the surface is determined by the Pauli repulsion between H_2 (D_2) and the sample surface. The Pauli repulsion originates from the overlap of electronic states of the sample with the closed electronic shells of H_2 (D_2). Thus, during scanning H_2 (D_2) follows the contour of the total electron density (TED) of the sample via Pauli repulsion (sensor action). On the side of the tip, the electronic states of the H_2 (D_2) interact with the electronic levels in the tip, where a reduced tip-molecule distance leads to a depletion of the density of states (DOS) in the tip again via Pauli repulsion. The reduced tip DOS, in turn, leads to a lower conductance of the junction (transducer action). Therefore, areas in STHM images where the tip- H_2 (D_2) distance can be expected to be larger appear brighter than areas where the distance is expected to be lower. So far, the described functionality of the sensor/transducer model is not restricted to only H_2 or D_2 . In principle the mechanism should work for any closed shell particle located below the tip apex. In fact a similar resolution for other tip-adsorbate systems has already been presented in reference [228]. However, the achieved resolution depends on the size of the tip termination, thus the contrast may appear blurred, compared to the STHM contrast, if a larger particle is used for imaging.

The Pauli repulsion, identified as the physical process behind the contrast formation, is usually associated with a repulsive interaction. Thus, the H_2 (D_2)-tip combination can be regarded as a nano-scale force sensor which probes the repulsive interaction from the surface. Due to its nanoscopic size the force sensor is intrinsically insensitive to long range forces which usually limit the lateral resolution in AFM experiments. To quantify the force sensor and directly connect the conductance of the STHM junction with the force between D_2 and the tip, we simultaneously recorded the conductance and the frequency shift of a cantilever. As a result of our measurements, we could identify characteristic points in the conductance evolution and the force on the confined H_2 (D_2) molecule. The direct connection between both quantities of the junction indicates that once the sensor is reliably calibrated, it becomes possible to extract quantitative values for the potential above the surface from the conductance evolution of the STHM junction.

Besides the high resolution imaging and the measurement of the force above the surface the STHM mode allows to extract even more information about the sample surface. We present preliminary results which may lead to a further method development on the basis of STHM. The results address the adsorbtion potential of H_2 (D_2) above different positions of the surface and the lateral structure of obstacle walls on the surface. In differential conductance spectra of the STHM junction characteristic spikes mark the energy at which H_2 (D_2) is excited out of the junction. These excitation energies which depend on the structure of the electrodes can be measured with the same lateral resolution as the STHM images themselves. The information about the lateral variation of the excitation energy may provide a possibility to reconstruct the structure of the tip which is usually unknown in STM experiments. Concerning the lateral structure of obstacle wall, we obtained standing wave patterns at the borders of the obstacles. The

7 Summary

standing wave patterns may originate from a resonant scattering of H_2 (D_2) at the obstacle walls, thus containing information of the walls structure and its interaction with H_2 (D_2).

So far, the STHM mode may be considered as a powerful new tool for surface characterisation. Although the STHM mode can be used in any conventional low-temperature STM, due to its close relation to the STM, the STHM inherits some of the limitations of the STM. Thus, the STHM mode can only be applied to conducting samples at low temperatures to allow the condensation of H_2 (D_2). However, we believe that STHM is only one example of a large family of possible tip functionalisations which go beyond conventional STM. In the present example the mechanism behind the contrast formation is the Pauli repulsion between the electrodes and a confined H_2 (D_2), whereas by appropriate functionalisation of the tip other mechanisms may yield image contrasts related to other surface properties (e.g. the polarisability, friction or mechanical stability) which wait to be discovered.

Bibliography

- [1] A. Flammini, D. Marioli, and A. Taroni. A low-cost interface to high-value resistive sensors varying over a wide range. *Instrumentation and Measurement, IEEE Transactions on*, 53(4):1052 1056, aug. 2004.
- [2] F. Balestra, S. Cristoloveanu, M. Benachir, J. Brini, and T. Elewa. Double-gate silicon-on-insulator transistor with volume inversion: A new device with greatly enhanced performance. *Electron Device Letters*, *IEEE*, 8(9):410 412, sep 1987.
- [3] W. Hänsch, Th. Vogelsang, R. Kircher, and M. Orlowski. Carrier transport near the Si/SiO₂ interface of a MOSFET. *Solid-State Electronics*, 32(10):839 849, 1989.
- [4] S. T. Lee, Y. M. Wang, X. Y. Hou, and C. W. Tang. Interfacial electronic structures in an organic light-emitting diode. *Applied Physics Letters*, 74(5):670–672, 1999.
- [5] H. C. Card and E. H. Rhoderick. Studies of tunnel MOS diodes I. interface effects in silicon Schottky diodes. *Journal of Physics D: Applied Physics*, 4(10):1589, 1971.
- [6] H.B. Pacejka and R.S. Sharp. Shear force development by pneumatic tyres in steady state conditions: A review of modelling aspects. *Vehicle System Dynamics*, 20(3-4):121–175, 1991.
- [7] M. Gustafsson, G. Blomqvist, A. Gudmundsson, A. Dahl, E. Swietlicki, M. Bohgard, J. Lindbom, and A. Ljungman. Properties and toxicological effects of particles from the interaction between tyres, road pavement and winter traction material. *Science* of The Total Environment, 393:226 – 240, 2008.
- [8] W. Gruber. Die Genussformel Kulinarische Physik. Ecoein Verlag GmbH, 2008.
- [9] R. Sinha, N. Rothman, C. P. Salmon, M. G. Knize, E. D. Brown, C. A. Swanson, D. Rhodes, S. Rossi, J. S. Felton, and O. A. Levander. Heterocyclic amine content in beef cooked by different methods to varying degrees of doneness and gravy made from meat drippings. Food and Chemical Toxicology, 36(4):279 – 287, 1998.
- [10] H. F. Viljoen, H. L. de Kock, and E. C. Webb. Consumer acceptability of dark, firm and dry (dfd) and normal ph beef steaks. *Meat Science*, 61(2):181 185, 2002.
- [11] H. Ibach, H. Froitzheim, H. Hopster, and S. Lehwald. Electron energy loss spectroscopy for studies of surface vibrations. *Il Nuovo Cimento B* (1971-1996), 39:759–767, 1977.

- [12] T. A. Carlson. Photoelectron spectroscopy. Annual Review of Physical Chemistry, 26(1):211–234, 1975.
- [13] S. Kera, Y. Yabuuchi, H. Yamane, H. Setoyama, K. K. Okudaira, A. Kahn, and N. Ueno. Impact of an interface dipole layer on molecular level alignment at an organic-conductor interface studied by ultraviolet photoemission spectroscopy. *Phys. Rev. B*, 70:085304, Aug 2004.
- [14] M. Wessendorf, C. Wiemann, M. Bauer, M. Aeschlimann, M. A. Schneider, H. Brune, and K. Kern. Electronic surface structure of n ML Ag/Cu(111) and Cs/n ML Ag/Cu(111) as investigated by 2PPE and STS. Applied Physics A: Materials Science & Processing, 78:183–188, 2004.
- [15] M. P. Seah. The quantitative analysis of surfaces by XPS: A review. Surface and Interface Analysis, 2(6):222–239, 1980.
- [16] G. Moretti. X-Ray Photoelectron and Auger Electron Spectroscopy. Wiley-VCH Verlag GmbH & Co. KGaA, 2008.
- [17] Th. Wagner, H. Karacuban, and R. Möller. Analysis of complex thermal desorption spectra: PTCDA on copper. Surface Science, 603(3):482 490, 2009.
- [18] S. K. M. Henze, O. Bauer, T.-L. Lee, M. Sokolowski, and F. S. Tautz. Vertical bonding distances of PTCDA on Au(111) and Ag(111): Relation to the bonding type. Surface Science, 601(6):1566 1573, 2007.
- [19] F. P. Netzer. Determination of structure and orientation of organic molecules on metal surfaces. Vacuum, 41:49 – 53, 1990. International Conference on Solid Surfaces.
- [20] G. Ertl. Untersuchung von Oberflächenreaktionen mittels Beugung langsamer elektronen (LEED): I. Wechselwirkung von O₂ und N₂O mit (110)-, (111)- und (100)- Kupfer-Oberflächen. Surface Science, 6(2):208 232, 1967.
- [21] M. A. Van Hove, W. H. Weinberg, and C. M. Chan. Low-Energy Electron Diffraction. Springer-Verlag, Berlin Heidelberg New York, 1986.
- [22] S. Ino. Some New Techniques in Reflection High Energy Electron Diffraction (RHEED) Application to Surface Structure Studies. *Japanese Journal of Applied Physics*, 16:891, June 1977.
- [23] P. J. Dobson, B. A. Joyce, J. H. Neave, and J. Zhang. Current understanding and applications of the RHEED intensity oscillation techniques. *Journal of Crystal Growth*, 81:1 – 8, 1987.

- [24] W. Coene, G. Janssen, M. Op de Beeck, and D. Van Dyck. Phase retrieval through focus variation for ultra-resolution in field-emission transmission electron microscopy. *Phys. Rev. Lett.*, 69:3743–3746, Dec 1992.
- [25] M. W. Goldberg and T. D. Allen. High resolution scanning electron microscopy of the nuclear envelope: demonstration of a new, regular, fibrous lattice attached to the baskets of the nucleoplasmic face of the nuclear pores. *The Journal of Cell Biology*, 119(6):1429–1440, 1992.
- [26] T. Kizuka. Atomic process of point contact in gold studied by time-resolved high-resolution transmission electron microscopy. *Phys. Rev. Lett.*, 81:4448–4451, Nov 1998.
- [27] D. Cherns. Direct resolution of surface atomic steps by transmission electron microscopy. *Philosophical Magazine*, 30(3):549–556, 1974.
- [28] R. Fink, M. R. Weiss, E. Umbach, D. Preikszas, H. Rose, R. Spehr, P. Hartel, W. Engel, R. Degenhardt, R. Wichtendahl, H. Kuhlenbeck, W. Erlebach, K. Ihmann, R. Schlägl, H.-J. Freund, A. M. Bradshaw, G. Lilienkamp, Th. Schmidt, E. Bauer, and G. Benner. SMART: a planned ultrahigh-resolution spectromicroscope for BESSY II. Journal of Electron Spectroscopy and Related Phenomena, 84:231 250, 1997.
- [29] R. M. Tromp. Low-energy electron microscopy. *IBM Journal of Research and Development*, 44(4):503 –516, july 2000.
- [30] W. Swiech, G. H. Fecher, Ch. Ziethen, O Schmidt, G. Schönhense, K. Grzelakowski, C. M. Schneider, R. Frömter, H. P. Oepen, and J. Kirschner. Recent progress in photoemission microscopy with emphasis on chemical and magnetic sensitivity. *Journal of Electron Spectroscopy and Related Phenomena*, 84:171 – 188, 1997.
- [31] Z. L. Wang. Transmission electron microscopy of shape-controlled nanocrystals and their assemblies. *The Journal of Physical Chemistry B*, 104(6):1153–1175, 2000.
- [32] G. Binnig and H. Rohrer. Scanning tunnelling microscopy. *Helvetica Physica Acta*, 55:726—-735, 1982.
- [33] G. Binnig, H. Rohrer, Ch. Gerber, and E. Weibel. Surface studies by scanning tunneling microscopy. *Phys. Rev. Lett.*, 49:57–61, Jul 1982.
- [34] G. Binnig, H. Rohrer, Ch. Gerber, and E. Weibel. 7×7 Reconstruction on Si(111) Resolved in Real Space. *Phys. Rev. Lett.*, 50:120–123, Jan 1983.

- [35] G. Binnig and H. Rohrer. Scanning tunneling microscopy—from birth to adolescence. *Rev. Mod. Phys.*, 59:615–625, Jul 1987.
- [36] C. J. Chen. Introduction to Scanning Tunneling Microscopy. OXFORD UNIVER-SITY PRESS, 1993.
- [37] W. Clauss, D. J. Bergeron, and A. T. Johnson. Atomic resolution STM imaging of a twisted single-wall carbon nanotube. *Phys. Rev. B*, 58(8):R4266–R4269, Aug 1998.
- [38] M. R. Castell, P. L. Wincott, N. G. Condon, C. Muggelberg, G. Thornton, S. L. Dudarev, A. P. Sutton, and G. A. D. Briggs. Atomic-resolution STM of a system with strongly correlated electrons:NiO(001) surface structure and defect sites. *Phys. Rev. B*, 55(12):7859–7863, Mar 1997.
- [39] M. Makri, C. G. Vayenas, S. Bebelis, K. H. Besocke, and C. Cavalca. Atomic resolution STM imaging of electrochemically controlled reversible promoter dosing of catalysts. Surface Science, 369(1-3):351 – 359, 1996.
- [40] X. Gao, A. Hamelin, and M. J. Weaver. Potential-dependent reconstruction at ordered Au(100)-aqueous interfaces as probed by atomic-resolution scanning tunneling microscopy. *Phys. Rev. Lett.*, 67(5):618–621, Jul 1991.
- [41] J. Wintterlin, J. Wiechers, H. Brune, T. Gritsch, H. Höfer, and R. J. Behm. Atomic-resolution imaging of close-packed metal surfaces by scanning tunneling microscopy. Phys. Rev. Lett., 62(1):59–62, Jan 1989.
- [42] D. M. Lewis, J. E. D. Spencer, and B. O. Field. An introduction to Inelastic Electron Tunneling Spectroscopy (IETS) and its chemical applications. *Spectrochimica Acta* Part A: Molecular Spectroscopy, 44(3):247 – 261, 1988.
- [43] E. Bailo and V. Deckert. Tip-enhanced raman scattering. Chem. Soc. Rev., 37:921–930, 2008.
- [44] R. Berndt, R. Gaisch, J. K. Gimzewski, B. Reihl, R. R. Schlittler, W.-D. Schneider, and M. Tschudy. Photon emission at molecular resolution induced by a scanning tunneling microscope. *Science*, 262(5138):1425–1427, 1993.
- [45] B. C. Stipe, M. A. Rezaei, and W. Ho. Single-molecule vibrational spectroscopy and microscopy. *Science*, 280(5370):1732–1735, 1998.
- [46] L. J. Lauhon and W. Ho. Single-Molecule Chemistry and Vibrational Spectroscopy: Pyridine and Benzene on Cu(001). The Journal of Physical Chemistry A, 104(11):2463–2467, 2000.

- [47] B. Pettinger, B. Ren, G. Picardi, R. Schuster, and G. Ertl. Nanoscale probing of adsorbed species by tip-enhanced raman spectroscopy. *Phys. Rev. Lett.*, 92(9):096101, Mar 2004.
- [48] W. Zhang, B. S. Yeo, T. Schmid, and R. Zenobi. Single molecule tip-enhanced raman spectroscopy with silver tips. The Journal of Physical Chemistry C, 111(4):1733– 1738, 2007.
- [49] X. H. Qiu, G. V. Nazin, and W. Ho. Vibrationally resolved fluorescence excited with submolecular precision. *Science*, 299(5606):542–546, 2003.
- [50] C. Chen, P. Chu, C. A. Bobisch, D. L. Mills, and W. Ho. Viewing the interior of a single molecule: Vibronically resolved photon imaging at submolecular resolution. *Phys. Rev. Lett.*, 105(21):217402, Nov 2010.
- [51] J. Repp, G. Meyer, S. M. Stojković, A. Gourdon, and C. Joachim. Molecules on insulating films: Scanning-tunneling microscopy imaging of individual molecular orbitals. *Phys. Rev. Lett.*, 94(2):026803, Jan 2005.
- [52] K. F. Kelly, D. Sarkar, G. D. Hale, S. J. Oldenburg, and N. J. Halas. Threefold Electron Scattering on Graphite Observed with C₆₀-Adsorbed STM Tips. *Science*, 273(5280):1371–1373, 1996.
- [53] M. Rohlfing, R. Temirov, and F. S. Tautz. Adsorption structure and scanning tunneling data of a prototype organic-inorganic interface: PTCDA on Ag(111). Phys. Rev. B, 76(11):115421, Sep 2007.
- [54] I. K. Song, J. R. Kitchin, and M. A. Barteau. H₃PW₁₂O₄₀-functionalized tip for scanning tunneling microscopy. *Proceedings of the National Academy of Sciences of* the United States of America, 99(Suppl 2):6471–6475, 2002.
- [55] R. Temirov, S. Soubatch, O. Neucheva, A. C. Lassise, and S. Tautz. A novel method achieving ultra-high geometrical resolution in scanning tunnelling microscopy. *New Journal of Physics*, 10(5):053012, 2008.
- [56] L. Gross, F. Mohn, N. Moll, P. Liljeroth, and G. Meyer. The chemical structure of a molecule resolved by atomic force microscopy. *Science*, 325(5944):1110–1114, 2009.
- [57] L. Gross, F. Mohn, N. Moll, G. Meyer, R. Ebel, W. M. Abdel-Mageed, and M. Jaspars. Organic structure determination using atomic-resolution scanning probe microscopy. *Nat Chem*, 2(10):821–825, 2010.

- [58] F. Mohn, J. Repp, L. Gross, G. Meyer, M. S. Dyer, and M. Persson. Reversible bond formation in a gold-atom-organic-molecule complex as a molecular switch. *Phys. Rev. Lett.*, 105(26):266102, Dec 2010.
- [59] G. Binnig, H. Rohrer, Ch. Gerber, and E. Weibel. Tunneling through a controllable vacuum gap. *Applied Physics Letters*, 40(2):178–180, 1982.
- [60] J. A. A. W. Elemans, I. De Cat, H. Xu, and S. De Feyter. Two-dimensional chirality at liquid-solid interfaces. Chem. Soc. Rev., 38:-, 2009.
- [61] J. A. A. W. Elemans. A new look at the chemical reaction. *Materials Today*, 12(7–8):34 38, 2009.
- [62] J. P. Rabe and S. Buchholz. Direct observation of molecular structure and dynamics at the interface between a solid wall and an organic solution by scanning tunneling microscopy. *Phys. Rev. Lett.*, 66:2096–2099, Apr 1991.
- [63] C. T. Herbschleb, S. C. Bobaru, and J. W. M. Frenken. High-pressure STM study of NO reduction by CO on Pt(100). *Catalysis Today*, 154(1–2):61 67, 2010.
- [64] P. Kowalczyk. High temperature STM/STS investigations of resonant image states on Au(111). Applied Surface Science, 253(8):4036 – 4040, 2007.
- [65] L. Piccolo, D. Loffreda, F. J. Cadete Santos Aires, C. Deranlot, Y. Jugnet, P. Sautet, and J. C. Bertolini. The adsorption of CO on Au(111) at elevated pressuresstudied by STM, RAIRS and DFT calculations. Surface Science, 566–568, Part 2(0):995 1000, 2004.
- [66] G. A. Somorjai. New model catalysts (platinum nanoparticles) and new techniques (SFG and STM) for studies of reaction intermediates and surface restructuring at high pressures during catalytic reactions. Applied Surface Science, 121–122(0):1 – 19, 1997.
- [67] L. Bartels, S. Zöphel, G. Meyer, E. Henze, and K.-H. Rieder. Dimer formation and surface alloying: a STM study of lead on Cu(211). Surface Science, 372(1–3):L261 – L265, 1997.
- [68] G. Meyer, L. Bartels, S. Zöphel, and K.-H. Rieder. Possibilities for atom by atom restructuring of surfaces employing native substrate atoms as well as foreign species. Applied Surface Science, 130–132(0):527 – 533, 1998.
- [69] R. Temirov, A. Lassise, F. B. Anders, and F. S. Tautz. Kondo effect by controlled cleavage of a single-molecule contact. *Nanotechnology*, 19(6):065401, 2008.

- [70] B. Voigtländer. Scanning tunneling microscopy studies during semiconductor growth. *Micron*, 30(1):33 39, 1999.
- [71] M. Kugler, Ch. Renner, V. Mikheev, G Batey, and Ø Fischer. A 3He cooled scanning tunneling microscope in UHV and high fields. *Physica B: Condensed Matter*, 280(1–4):551 552, 2000.
- [72] R. H. M. Smit, R. Grande, B. Lasanta, J. J. Riquelme, G. Rubio-Bollinger, and N. Agraït. A low temperature scanning tunneling microscope for electronic and force spectroscopy. *Review of Scientific Instruments*, 78(11):113705, 2007.
- [73] G. Nunes Jr. Scanned probe microscopy at millikelvin temperatures. *Physica B:* Condensed Matter, 280(1–4):546 550, 2000.
- [74] M. Born. Zur Quantenmechanik der Stoßvorgänge. Zeitschrift für Physik A Hadrons and Nuclei, 37:863–867, 1926.
- [75] J. Bardeen. Tunnelling from a many-particle point of view. *Phys. Rev. Lett.*, 6:57–59, Jan 1961.
- [76] J. Tersoff and D. R. Hamann. Theory and application for the scanning tunneling microscope. *Phys. Rev. Lett.*, 50(25):1998–2001, Jun 1983.
- [77] J. Tersoff and D. R. Hamann. Theory of the scanning tunneling microscope. *Phys. Rev. B*, 31(2):805–813, Jan 1985.
- [78] R. M. Feenstra, J. A. Stroscio, and A. P. Fein. Tunneling spectroscopy of the Si(111)2 × 1 surface. Surface Science, 181(1-2):295 306, 1987.
- [79] L. Gross, N. Moll, F. Mohn, A. Curioni, G. Meyer, F. Hanke, and M. Persson. High-Resolution Molecular Orbital Imaging Using a p-Wave STM Tip. Phys. Rev. Lett., 107(8):086101, Aug 2011.
- [80] G. Binnig, C. F. Quate, and Ch. Gerber. Atomic force microscope. *Phys. Rev. Lett.*, 56(9):930–933, Mar 1986.
- [81] E. Meyer, H. J. Hug, and R. Bennewitz. *Scanning Probe Microscopy*. Springer, 2004.
- [82] E. Meyer. Atomic force microscopy. Progress in Surface Science, 41(1):3 49, 1992.
- [83] T. R. Albrecht, P. Grütter, D. Horne, and D. Rugar. Frequency modulation detection using high-q cantilevers for enhanced force microscope sensitivity. *Journal of Applied Physics*, 69(2):668–673, 1991.

- [84] U. Dürig. Relations between interaction force and frequency shift in large-amplitude dynamic force microscopy. *Applied Physics Letters*, 75(3):433–435, 1999.
- [85] S. Molitor. Rasterkraftmikroskopie im UHV: Abbildungsprozesse im Kontaktmodus und im dynamischen Modus am Beispiel der Gold (111) $22(\pm 1) \times \sqrt{3}$ und der Si(111) 7×7 Oberfläche. PhD thesis, Universität Osnabrück, 2001.
- [86] J. E. Sader and S. P. Jarvis. Accurate formulas for interaction force and energy in frequency modulation force spectroscopy. Applied Physics Letters, 84(10):1801– 1803, 2004.
- [87] F. J. Giessibl. High-speed force sensor for force microscopy and profilometry utilizing a quartz tuning fork. *Applied Physics Letters*, 73(26):3956–3958, 1998.
- [88] F. J. Giessibl. Advances in atomic force microscopy. Rev. Mod. Phys., 75(3):949–983, Jul 2003.
- [89] I. Morawski and B. Voigtländer. Simultaneously measured signals in scanning probe microscopy with a needle sensor: Frequency shift and tunneling current. Rev. Sci. Instrum., 81(3):033703, 2010.
- [90] J. V. Barth, H. Brune, G. Ertl, and R. J. Behm. Scanning tunneling microscopy observations on the reconstructed Au(111) surface: Atomic structure, long-range superstructure, rotational domains, and surface defects. *Phys. Rev. B*, 42(15):9307– 9318, Nov 1990.
- [91] R. J. Celotta and J. A. Stroscio. Trapping and moving atoms on surfaces. volume 51 of *Advances In Atomic, Molecular, and Optical Physics*, pages 363 383. Academic Press, 2005.
- [92] F. J. Giessibl, S. Hembacher, H. Bielefeldt, and J. Mannhart. Subatomic features on the silicon (111)-(7 × 7) surface observed by atomic force microscopy. *Science*, 289(5478):422–425, 2000.
- [93] M. Guggisberg, O. Pfeiffer, S. Schär, V. Barwich, M. Bammerlin, C. Loppacher, R. Bennewitz, A. Baratoff, and E. Meyer. Contrast inversion in nc-AFM on Si(111)7 × 7 due to short-range electrostatic interactions. Applied Physics A: Materials Science & Processing, 72:S19–S22, 2001.
- [94] V. M. Hallmark, S. Chiang, J. F. Rabolt, J. D. Swalen, and R. J. Wilson. Observation of Atomic Corrugation on Au(111) by Scanning Tunneling Microscopy. *Phys. Rev. Lett.*, 59(25):2879–2882, Dec 1987.

- [95] S. Hembacher, F. J. Giessibl, and J. Mannhart. Force microscopy with light-atom probes. *Science*, 305(5682):380–383, 2004.
- [96] M. A. Lantz, H. J. Hug, R. Hoffmann, P. J. A. van Schendel, P. Kappenberger, S. Martin, A. Baratoff, and H.-J. Güntherodt. Quantitative measurement of shortrange chemical bonding forces. *Science*, 291(5513):2580–2583, 2001.
- [97] S. Loth, S. Baumann, C. P. Lutz, D. M. Eigler, and A. J. Heinrich. Bistability in atomic-scale antiferromagnets. *Science*, 335(6065):196–199, 2012.
- [98] M. Saint Jean, S. Hudlet, C. Guthmann, and J. Berger. Van der waals and capacitive forces in atomic force microscopies. *Journal of Applied Physics*, 86(9):5245–5248, 1999.
- [99] A. Schirmeisen, G. Cross, A. Stalder, P. Grütter, and U. Dürig. Metallic adhesion forces and tunneling between atomically defined tip and sample. *Applied Surface Science*, 157(4):274 279, 2000.
- [100] M. Ternes, C. González, C. P. Lutz, P. Hapala, F. J. Giessibl, P. Jelínek, and A. J. Heinrich. Interplay of conductance, force, and structural change in metallic point contacts. *Phys. Rev. Lett.*, 106(1):016802, Jan 2011.
- [101] L. Álvarez, S. Peláez, R. Caillard, P. A Serena, J. A Martín-Gago, and J Méndez. Metal-organic extended 2D structures: Fe-PTCDA on Au(111). Nanotechnology, 21(30):305703, 2010.
- [102] A. Abbasi and R. Scholz. Ab Initio Calculation of the Dispersion Interaction between a Polyaromatic Molecule and a Noble Metal Substrate: PTCDA on Ag(110). *The Journal of Physical Chemistry C*, 113(46):19897–19904, 2009.
- [103] J. L. Brédas, J. P. Calbert, D. A. da Silva Filho, and J. Cornil. Organic semiconductors: A theoretical characterization of the basic parameters governing charge transport. *Proceedings of the National Academy of Sciences of the United States of America*, 99(9):5804–5809, 2002.
- [104] Z. Cheng, S. Du, W. Guo, L. Gao, Z. Deng, N. Jiang, H. Guo, H. Tang, and H. Gao. Direct imaging of molecular orbitals of metal phthalocyanines on metal surfaces with an O₂-functionalized tip of a scanning tunneling microscopes. *Nano Research*, 4:523–530, 2011.
- [105] S. Fölsch, P. Hyldgaard, R. Koch, and K. H. Ploog. Quantum Confinement in Monatomic Cu Chains on Cu(111). Phys. Rev. Lett., 92(5):056803, Feb 2004.

- [106] N. Gonzalez-Lakunza, I. Fernández-Torrente, K. J. Franke, N. Lorente, A. Arnau, and J. I. Pascual. Formation of dispersive hybrid bands at an organic-metal interface. *Phys. Rev. Lett.*, 100(15):156805, Apr 2008.
- [107] N. Ueno and S. Kera. Electron spectroscopy of functional organic thin films: Deep insights into valence electronic structure in relation to charge transport property. *Progress in Surface Science*, 83(10-12):490 – 557, 2008.
- [108] S. Wang, W. Wang, and N. Lin. Resolving band-structure evolution and defect-induced states of single conjugated oligomers by scanning tunneling microscopy and tight-binding calculations. *Phys. Rev. Lett.*, 106(20):206803, May 2011.
- [109] M. Alemani, M. V. Peters, S. Hecht, K.-H. Rieder, F. Moresco, and L. Grill. Electric Field-Induced Isomerization of Azobenzene by STM. *Journal of the American Chemical Society*, 128(45):14446-14447, 2006.
- [110] L. Bartels. Tailoring molecular layers at metal surfaces. *Nature Chemistry*, 2(2):87–95, 2010.
- [111] M. Böhringer, M. Morgenstern, W.-D. Schneider, and R. Berndt. Reversed surface corrugation in STM images on Au(111) by field-induced lateral motion of adsorbed molecules. *Surface Science*, 457(1-2):37 50, 2000.
- [112] S. M. Barlow and R. Raval. Complex organic molecules at metal surfaces: bonding, organisation and chirality. *Surface Science Reports*, 50(6-8):201 341, 2003.
- [113] L. Chen, H. Li, and A. T. S. Wee. Delocalized π state between molecules through a surface confined pseudodihydrogen bond. *Phys. Rev. Lett.*, 105(22):226103, Nov 2010.
- [114] I. Chizhov, A. Kahn, and G. Scoles. Initial growth of 3,4,9,10-perylenetetracarboxylic-dianhydride (PTCDA) on Au(111): a scanning tunneling microscopy study. *Journal of Crystal Growth*, 208(1-4):449 458, 2000.
- [115] D. B. Dougherty, W. Jin, W. G. Cullen, J. E. Reutt-Robey, and S. W. Robey. Variable Temperature Scanning Tunneling Microscopy of Pentacene Monolayer and Bilayer Phases on Ag(111). The Journal of Physical Chemistry C, 112(51):20334– 20339, 2008.
- [116] M. Eremtchenko, S. Döring, R. Temirov, and J. A. Schaefer. c_{60} single domain growth on indium phosphide and its reaction with atomic hydrogen. *Phys. Rev. B*, 71(4):045410, Jan 2005.

- [117] S. R. Forrest. Ultrathin organic films grown by organic molecular beam deposition and related techniques. *Chemical Reviews*, 97(6):1793–1896, 1997.
- [118] K. J. Franke, G. Schulze, N. Henningsen, I. Fernández-Torrente, J. I. Pascual, S. Zarwell, K. Rück-Braun, M. Cobian, and N. Lorente. Reducing the Molecule-Substrate Coupling in C₆₀-Based Nanostructures by Molecular Interactions. *Phys. Rev. Lett.*, 100:036807, Jan 2008.
- [119] K. Glöckler, C. Seidel, A. Soukopp, M. Sokolowski, E. Umbach, M. Böhringer, R. Berndt, and W.-D. Schneider. Highly ordered structures and submolecular scanning tunnelling microscopy contrast of PTCDA and DM-PBDCI monolayers on Ag(111) and Ag(110). Surface Science, 405(1):1 – 20, 1998.
- [120] M. Grobis, A. Wachowiak, R. Yamachika, and M. F. Crommie. Tuning negative differential resistance in a molecular film. Applied Physics Letters, 86(20):204102, 2005.
- [121] A. J. Heinrich, C. P. Lutz, J. A. Gupta, and D. M. Eigler. Molecule Cascades. Science, 298(5597):1381–1387, 2002.
- [122] S. Mannsfeld, M. Toerker, T. Schmitz-Hübsch, F. Sellam, T. Fritz, and K Leo. Combined LEED and STM study of PTCDA growth on reconstructed Au(111) and Au(100) single crystals. *Organic Electronics*, 2(3-4):121 134, 2001.
- [123] J. M. Mativetsky, S. A. Burke, R. Hoffmann, Y. Sun, and P. Grütter. Molecular resolution imaging of C₆₀ on Au(111) by non-contact atomic force microscopy. *Nanotechnology*, 15(2):S40, 2004.
- [124] F. Rosei, M. Schunack, Y. Naitoh, P. Jiang, A. Gourdon, E. Laegsgaard, I. Stensgaard, C. Joachim, and F Besenbacher. Properties of large organic molecules on metal surfaces. *Progress in Surface Science*, 71(5-8):95 146, 2003. 2002.
- [125] S. Soubatch, C. Weiss, R. Temirov, and S. Tautz. Site-specific polarization screening in organic thin films. *Phys. Rev. Lett.*, 102(17):177405, May 2009.
- [126] J. A. Theobald, N. S. Oxtoby, M. A. Phillips, N. R. Champness, and P. H. Beton. Controlling molecular deposition and layer structure with supramolecular surface assemblies. *Nature*, 424:1029, 2003.
- [127] M. Toader and M. Hietschold. Tuning the Energy Level Alignment at the $\operatorname{SnPc/Ag}(111)$ Interface Using an STM Tip. The Journal of Physical Chemistry C, 115(7):3099–3105, 2011.

- [128] C. Wagner, D. Kasemann, C. Golnik, R. Forker, M. Esslinger, K. Müllen, and T. Fritz. Repulsion between molecules on a metal: Monolayers and submonolayers of hexa-peri-hexabenzocoronene on Au(111). *Phys. Rev. B*, 81(3):035423, Jan 2010.
- [129] Y. Wang, J. Kröger, R. Berndt, and W. Hofer. Structural and Electronic Properties of Ultrathin Tin-Phthalocyanine Films on Ag(111) at the Single-Molecule Level. Angewandte Chemie, 121(7):1287–1291, 2009.
- [130] L. Schlapbach and A. Zuttel. Hydrogen-storage materials for mobile applications. Nature, 414:353 – 358, 2001.
- [131] Q.-M. Xu, L.-J. Wan, S.-X. Yin, C. Wang, and C.-L. Bai. Effect of Chemically Modified Tips on STM Imaging of 1-Octadecanethiol Molecule. The Journal of Physical Chemistry B, 105(43):10465-10467, 2001.
- [132] P. Liljeroth, J. Repp, and G. Meyer. Current-induced hydrogen tautomerization and conductance switching of naphthalocyanine molecules. *Science*, 317(5842):1203– 1206, 2007.
- [133] J. Repp and G. Meyer. Scanning tunneling microscopy of adsorbates on insulating films. from the imaging of individual molecular orbitals to the manipulation of the charge state. Applied Physics A: Materials Science & Processing, 85(4):399 406, 2006.
- [134] D. M. Eigler and E. K. Schweizer. Positioning single atoms with a scanning tunnelling microscope. *Nature*, 344:524–526, Apr 1990.
- [135] S.-W. Hla. Scanning tunneling microscopy single atom/molecule manipulation and its application to nanoscience and technology. *Journal of Vacuum Science & Technology B: Microelectronics and Nanometer Structures*, 23(4):1351–1360, 2005.
- [136] S.-W. Hla, G. Meyer, and K.-H. Rieder. Inducing Single-Molecule Chemical Reactions with a UHV-STM: A New Dimension for Nano-Science and Technology. *ChemPhysChem*, 2(6):361–366, 2001.
- [137] L. Limot, J. Kröger, R. Berndt, A. Garcia-Lekue, and W. A. Hofer. Atom transfer and single-adatom contacts. *Phys. Rev. Lett.*, 94(12):126102, Apr 2005.
- [138] J. A. Stroscio and R. J. Celotta. Controlling the dynamics of a single atom in lateral atom manipulation. *Science*, 306(5694):242–247, 2004.
- [139] J. A. Stroscio and D. M. Eigler. Atomic and molecular manipulation with the scanning tunneling microscope. *Science*, 254(5036):1319–1326, 1991.

- [140] M. Ternes, C. P. Lutz, C. F. Hirjibehedin, F. J. Giessibl, and A. J. Heinrich. The force needed to move an atom on a surface. *Science*, 319(5866):1066–1069, 2008.
- [141] P. Maksymovych, D. C. Sorescu, and J. T. Yates. Gold-Adatom-Mediated Bonding in Self-Assembled Short-Chain Alkanethiolate Species on the Au(111) Surface. *Phys. Rev. Lett.*, 97(14):146103, Oct 2006.
- [142] A. Kraft, R. Temirov, S. K. M. Henze, S. Soubatch, M. Rohlfing, and F. S. Tautz. Lateral adsorption geometry and site-specific electronic structure of a large organic chemisorbate on a metal surface. *Phys. Rev. B*, 74(4):041402, Jul 2006.
- [143] M. Pivetta, F. Patthey, M. Stengel, A. Baldereschi, and W.-D. Schneider. Local work function Moiré pattern on ultrathin ionic films: NaCl on Ag(100). *Phys. Rev.* B, 72:115404, Sep 2005.
- [144] F. Moresco, G. Meyer, H. Tang, C. Joachim, and K. H. Rieder. Investigation of mechanical and electronic properties of large molecules by low temperature STM. Journal of Electron Spectroscopy and Related Phenomena, 129:149 – 155, 2003.
- [145] F. London and M. Polanyi. Über die atomtheoretische Deutung der Adsorptionskräfte. *Naturwissenschaften*, 18:1099–1100, 1930.
- [146] A. Schirmeisen, D. Weiner, and H. Fuchs. Single-atom contact mechanics: From atomic scale energy barrier to mechanical relaxation hysteresis. *Phys. Rev. Lett.*, 97(13):136101, Sep 2006.
- [147] L. Gross. Recent advances in submolecular resolution with scanning probe microscopy. *Nat Chem*, 3:273–278, Apr 2011.
- [148] N. Moll, L. Gross, F. Mohn, A. Curioni, and G. Meyer. The mechanisms underlying the enhanced resolution of atomic force microscopy with functionalized tips. *New Journal of Physics*, 12(12):125020, 2010.
- [149] Y. Sugimoto, P. Pou, M. Abe, P. Jelinek, R. Perez, S. Morita, and O. Custance. Chemical identification of individual surface atoms by atomic force microscopy. *Nature*, 446:64–67, 2007.
- [150] Y. Sugimoto, P. Pou, O. Custance, P. Jelinek, M. Abe, R. Perez, and S. Morita. Complex Patterning by Vertical Interchange Atom Manipulation Using Atomic Force Microscopy. *Science*, 322:413–417, 2008.
- [151] O. Takeuchi, Y. Ohrai, S. Yoshida, and H. Shigekawa. Kelvin probe force microscopy without bias-voltage feedback. *Japanese Journal of Applied Physics*, 46(8B):5626– 5630, 2007.

- [152] S. A. Burke, J. M. LeDue, Y. Miyahara, J. M. Topple, S. Fostner, and P. Grütter. Determination of the local contact potential difference of PTCDA on NaCl: a comparison of techniques. *Nanotechnology*, 20(26):264012, 2009.
- [153] J. Gaudioso, L. J. Lauhon, and W. Ho. Vibrationally mediated negative differential resistance in a single molecule. *Phys. Rev. Lett.*, 85(9):1918–1921, Aug 2000.
- [154] N. Nicoara, E. Román, J. M. Gómez-Rodríguez, J. A. Martín-Gago, and J. Méndez. Scanning tunneling and photoemission spectroscopies at the PTCDA/Au(111) interface. *Organic Electronics*, 7(5):287 294, 2006.
- [155] M. Ziegler, N. Néel, A. Sperl, J. Kröger, and R. Berndt. Local density of states from constant-current tunneling spectra. *Phys. Rev. B*, 80(12):125402, Sep 2009.
- [156] F. J. Giessibl and H. Bielefeldt. Physical interpretation of frequency-modulation atomic force microscopy. *Phys. Rev. B*, 61(15):9968–9971, Apr 2000.
- [157] J. E. Sader and S. P. Jarvis. Interpretation of frequency modulation atomic force microscopy in terms of fractional calculus. *Phys. Rev. B*, 70:012303, Jul 2004.
- [158] P. M. Hoffmann, S. Jeffery, J. B. Pethica, H. Özgür Özer, and A. Oral. Energy dissipation in atomic force microscopy and atomic loss processes. *Phys. Rev. Lett.*, 87:265502, Dec 2001.
- [159] L. N. Kantorovich and T. Trevethan. General theory of microscopic dynamical response in surface probe microscopy: From imaging to dissipation. *Phys. Rev. Lett.*, 93:236102, Nov 2004.
- [160] S. Hembacher, F. J. Giessibl, J. Mannhart, and C. F. Quate. Local spectroscopy and atomic imaging of tunneling current, forces, and dissipation on graphite. *Phys. Rev. Lett.*, 94:056101, Feb 2005.
- [161] T. Roll, T. Kunstmann, M. Fendrich, R. Möller, and M. Schleberger. Temperature dependence of the energy dissipation in dynamic force microscopy. *Nanotechnology*, 19(4):045703, 2008.
- [162] T. Trevethan, L. Kantorovich, J. Polesel-Maris, and S. Gauthier. Is atomic-scale dissipation in NC-AFM real? Investigation using virtual atomic force microscopy. *Nanotechnology*, 18:084017, 2007.
- [163] M. Fendrich, T. Kunstmann, D. Paulkowski, and R. Möller. Molecular resolution in dynamic force microscopy: topography and dissipation for weakly interacting systems. *Nanotechnology*, 18(8):084004, 2007.

- [164] M. Fendrich, C. Weiss, M. Lange, T. Kunstmann, and R. Möller. Imaging beyond topography. G.I.T. Imaging and Microscopy, 2:25, 2008.
- [165] A. Langner, A. Hauschild, S. Fahrenholz, and M. Sokolowski. Structural properties of tetracene films on Ag(111) investigated by SPA-LEED and TPD. Surface Science, 574(2-3):153 165, 2005.
- [166] S. Duhm, A. Gerlach, I. Salzmann, B. Bröker, R. L. Johnson, F. Schreiber, and N. Koch. PTCDA on Au(111), Ag(111) and Cu(111): Correlation of interface charge transfer to bonding distance. *Organic Electronics*, 9(1):111 118, 2008.
- [167] M. A. Van Hove, R. J. Koestner, P. C. Stair, J. P. Bibérian, L. L. Kesmodel, I. Bartos, and G.A. Somorjai. The surface reconstructions of the (100) crystal faces of iridium, platinum and gold: I. Experimental observations and possible structural models. Surface Science, 103(1):189 217, 1981.
- [168] L. Kilian, E. Umbach, and M. Sokolowski. A refined structural analysis of the PTCDA monolayer on the reconstructed Au(111) surface—"Rigid or distorted carpet?". Surface Science, 600(13):2633 2643, 2006.
- [169] F. S. Tautz. Structure and bonding of large aromatic molecules on noble metal surfaces: The example of PTCDA. *Progress in Surface Science*, 82:479–520, 2007.
- [170] W. A. Hofer, A. J. Fisher, R. A. Wolkow, and P. Grütter. Surface relaxations, current enhancements, and absolute distances in high resolution scanning tunneling microscopy. *Phys. Rev. Lett.*, 87:236104, Nov 2001.
- [171] Y. G. Ptushinskii. Low-temperature adsorption of gases on metal surfaces (review). Low Temperature Physics, 30(1):1–26, 2004.
- [172] J. A. Gupta, C. P. Lutz, A. J. Heinrich, and D. M. Eigler. Strongly coverage-dependent excitations of adsorbed molecular hydrogen. *Phys. Rev. B*, 71(11):115416, Mar 2005.
- [173] I. F. Silvera. The solid molecular hydrogens in the condensed phase: Fundamentals and static properties. *Rev. Mod. Phys.*, 52(2):393–452, Apr 1980.
- [174] M. Nielsen. Phonons in solid hydrogen and deuterium studied by inelastic coherent neutron scattering. *Phys. Rev. B*, 7(4):1626–1635, Feb 1973.
- [175] O. Bostanjoglo and R. Kleinschmidt. Crystal structure of hydrogen isotopes. *The Journal of Chemical Physics*, 46(5):2004–2005, 1967.

- [176] Sz. Csonka, A. Halbritter, and G. Mihály. Pulling gold nanowires with a hydrogen clamp: Strong interactions of hydrogen molecules with gold nanojunctions. *Phys. Rev. B*, 73(7):075405, Feb 2006.
- [177] K. Lonsdale. The Structure of the Benzene Ring in C_6 (CH₃)₆. Proc. R. Soc. Lond. A, 123:494–515, 1929.
- [178] Y. Wang, J. Kröger, R. Berndt, and W. A. Hofer. Pushing and Pulling a Sn Ion through an Adsorbed Phthalocyanine Molecule. *Journal of the American Chemical Society*, 131(10):3639–3643, 2009.
- [179] G. Schull, Y. J. Dappe, C. González, H. Bulou, and R. Berndt. Charge Injection through Single and Double Carbon Bonds. *Nano Letters*, 11(8):3142–3146, 2011.
- [180] G. Schull, T. Frederiksen, A. Arnau, D. Sanchez-Portal, and R. Berndt. Atomic-scale engineering of electrodes for single-molecule contacts. *Nat Nano*, 6:23–27, Jan 2011.
- [181] G. Schull, T. Frederiksen, M. Brandbyge, and R. Berndt. Passing Current through Touching Molecules. *Phys. Rev. Lett.*, 103:206803, Nov 2009.
- [182] T. Ogawa, K. Kuwamoto, S. Isoda, T. Kobayashi, and N. Karl. 3,4:9,10-Perylenetetracarboxylic dianhydride (PTCDA) by electron crystallography. Acta Crystallographica Section B, 55(1):123–130, Feb 1999.
- [183] L. Kilian, A. Hauschild, R. Temirov, S. Soubatch, A. Schöll, A. Bendounan, F. Reinert, T.-L. Lee, F. S. Tautz, M. Sokolowski, and E. Umbach. Role of Intermolecular Interactions on the Electronic and Geometric Structure of a Large π-Conjugated Molecule Adsorbed on a Metal Surface. Phys. Rev. Lett., 100(13):136103, Apr 2008.
- [184] C. Seidel, C. Awater, X. D. Liu, R. Ellerbrake, and H. Fuchs. A combined STM, LEED and molecular modelling study of PTCDA grown on Ag(110). Surface Science, 371(1):123 – 130, 1997.
- [185] J. Kröger, H. Jensen, R. Berndt, R. Rurali, and N. Lorente. Molecular orbital shift of perylenetetracarboxylic-dianhydride on gold. *Chemical Physics Letters*, 438(4-6):249 – 253, 2007.
- [186] M. Mura, X. Sun, F. Silly, H. T. Jonkman, G. A. D. Briggs, M. R. Castell, and L. N. Kantorovich. Experimental and theoretical analysis of H-bonded supramolecular assemblies of PTCDA molecules. *Phys. Rev. B*, 81(19):195412, May 2010.

- [187] T. Komeda, Y. Kim, Y. Fujita, Y. Sainoo, and M. Kawai. Local chemical reaction of benzene on Cu(110) via STM-induced excitation. *The Journal of Chemical Physics*, 120(11):5347–5352, 2004.
- [188] A. Zhao, Q. Li, L. Chen, H. Xiang, W. Wang, S. Pan, B. Wang, X. Xiao, J. Yang, J. G. Hou, and Q. Zhu. Controlling the kondo effect of an adsorbed magnetic ion through its chemical bonding. *Science*, 309(5740):1542–1544, 2005.
- [189] Y. F. Wang, J. Kröger, R. Berndt, H. Vázquez, M. Brandbyge, and M. Paulsson. Atomic-scale control of electron transport through single molecules. *Phys. Rev. Lett.*, 104(17):176802, Apr 2010.
- [190] M. Pfeiffer, T. Fritz, J. Blochwitz, A. Nollau, B. Plönnigs, A. Beyer, and K. Leo. Controlled doping of molecular organic layers: Physics and device prospects. Advances in Solid State Physics, 39:77–90, 1999.
- [191] A. Neumann, S. L. M. Schroeder, and K. Christmann. Adsorption of sodium and potassium on a gold(100) surface: An example of alkali-metal-induced deconstruction. *Phys. Rev. B*, 51(23):17007–17022, Jun 1995.
- [192] T. Steiner. Die Wasserstoffbrücke im Festkörper. Angewandte Chemie, 114(1):50–80, 2002.
- [193] B. P. Hay, J. R. Rustad, and C. J. Hostetler. Quantitative structure-stability relationship for potassium ion complexation by crown ethers. a molecular mechanics and ab initio study. *Journal of the American Chemical Society*, 115(24):11158–11164, 1993.
- [194] C. T. Campbell. The active site in nanoparticle gold catalysis. *Science*, 306(5694):234–235, 2004.
- [195] A. Sperl, J. Kröger, N. Néel, H. Jensen, R. Berndt, A. Franke, and E. Pehlke. Unoccupied states of individual silver clusters and chains on Ag(111). *Phys. Rev.* B, 77(8):085422, Feb 2008.
- [196] J. Kliewer, R. Berndt, J. Minár, and H. Ebert. Scanning tunnelling microscopy and electronic structure of Mn clusters on Ag(111). Applied Physics A: Materials Science & Bamp; Processing, 82:63–66, 2006.
- [197] W. H. A. Thijssen, D. Djukic, A. F. Otte, R. H. Bremmer, and J. M. van Ruitenbeek. Vibrationally induced two-level systems in single-molecule junctions. *Phys. Rev. Lett.*, 97(22):226806, Dec 2006.

- [198] A. Halbritter, P. Makk, Sz. Csonka, and G. Mihály. Huge negative differential conductance in $Au H_2$ molecular nanojunctions. *Phys. Rev. B*, 77(7):075402, Feb 2008.
- [199] M. L. Trouwborst, E. H. Huisman, S. J. van der Molen, and B. J. van Wees. Bistable hysteresis and resistance switching in hydrogen-gold junctions. *Phys. Rev.* B, 80(8):081407, Aug 2009.
- [200] L. Barrio, P. Liu, J. A. Rodríguez, J. M. Campos-Martín, and J. L. G. Fierro. A density functional theory study of the dissociation of H₂ on gold clusters: Importance of fluxionality and ensemble effects. The Journal of Chemical Physics, 125(16):164715, 2006.
- [201] S. Hamel and M. Côté. First-principles study of the rotational transitions of H₂ physisorbed over benzene. The Journal of Chemical Physics, 121(24):12618–12625, 2004.
- [202] R. J. P. Keijsers, J. Voets, O. I. Shklyarevskii, and H. van Kempen. Effect of adsorbed helium on electron tunneling between metal electrodes. *Phys. Rev. Lett.*, 76(7):1138–1141, Feb 1996.
- [203] M. Neumaier, F. Weigend, O. Hampe, and M. M. Kappes. Binding energy and preferred adsorption sites of CO on gold and silver-gold cluster cations: Adsorption kinetics and quantum chemical calculations. Faraday Discuss., 138:393–406, 2008.
- [204] C. Weiss, C. Wagner, C. Kleimann, M. Rohlfing, F. S. Tautz, and R. Temirov. Imaging pauli repulsion in scanning tunneling microscopy. *Phys. Rev. Lett.*, 105(8):086103, Aug 2010.
- [205] N. D. Lang. Interaction between closed-shell systems and metal surfaces. *Phys. Rev. Lett.*, 46(13):842–845, Mar 1981.
- [206] N. D. Lang. Theory of single-atom imaging in the scanning tunneling microscope. *Phys. Rev. Lett.*, 56(11):1164–1167, Mar 1986.
- [207] A. Yazdani, D. M. Eigler, and N. D. Lang. Off-Resonance Conduction Through Atomic Wires. Science, 272(5270):1921–1924, 1996.
- [208] Ph. Avouris, D. Schmeisser, and J. E. Demuth. Observation of Rotational Excitations of H_2 Adsorbed on Ag Surfaces. *Phys. Rev. Lett.*, 48(3):199–202, Jan 1982.
- [209] A. Corma, M. Boronat, S. González, and F. Illas. On the activation of molecular hydrogen by gold: a theoretical approximation to the nature of potential active sites. *Chem. Commun.*, pages 3371–3373, 2007.

- [210] B. Hammer and J. K. Norskov. Why gold is the noblest of all the metals. *Nature*, 376:238-240, 1995.
- [211] L. W. Bruch, R. P. Nabar, and M. Mavrikakis. Weak molecular chemisorption of N₂ /Pt(111). Journal of Physics: Condensed Matter, 21(26):264009, 2009.
- [212] K. Gustafsson, G. S. Karlberg, and S. Andersson. Infrared spectroscopy of physisorbed and chemisorbed N_2 in the $Pt(111)(3 \times 3)N_2$ structures. The Journal of Chemical Physics, 127(19):194708, 2007.
- [213] P. Zeppenfeld, R. David, C. Ramseyer, P. N. M. Hoang, and C. Girardet. Adsorption and structure of N₂ on Pt(111). Surface Science, 444(1-3):163 179, 2000.
- [214] K. Svensson, J. Bellman, A. Hellman, and S. Andersson. Dipole active rotations of physisorbed H_2 and D_2 . Phys. Rev. B, 71(24):245402, Jun 2005.
- [215] S. Chiang, R. J. Wilson, Ch. Gerber, and V. M. Hallmark. An ultrahigh vacuum scanning tunneling microscope with interchangeable samples and tips. *Journal of Vacuum Science & Technology A: Vacuum, Surfaces, and Films*, 6(2):386–389, 1988.
- [216] Ch. Wöll, S. Chiang, R. J. Wilson, and P. H. Lippel. Determination of atom positions at stacking-fault dislocations on Au(111) by scanning tunneling microscopy. *Phys. Rev. B*, 39(11):7988–7991, Apr 1989.
- [217] C. J. Chen. Origin of atomic resolution on metal surfaces in scanning tunneling microscopy. *Phys. Rev. Lett.*, 65(4):448–451, Jul 1990.
- [218] R. C. Weast, D. R. Lide, M. J. Astle, and W. H. Beyer, editors. *Handbook of CHEMISTRY and PHYSICS 70th Edition*. CRC Press, Inc., 1989.
- [219] W. Demtröder. Experimentalphysik 3 Atome, Moleküle und Festkörper. Springer-Verlag Berlin Heidelberg, 2009.
- [220] G. V. Hansson and S. A. Flodström. Photoemission study of the bulk and surface electronic structure of single crystals of gold. *Phys. Rev. B*, 18(4):1572–1585, Aug 1978.
- [221] D. M. Eigler, P. S. Weiss, E. K. Schweizer, and N. D. Lang. Imaging Xe with a low-temperature scanning tunneling microscope. *Phys. Rev. Lett.*, 66(9):1189–1192, Mar 1991.
- [222] J. L. F. da Silva, C. Stampfl, and M. Scheffler. Adsorption of Xe Atoms on Metal Surfaces: New Insights from First-Principles Calculations. *Phys. Rev. Lett.*, 90:066104, Feb 2003.

- [223] R. Proksch. Multifrequency, repulsive-mode amplitude-modulated atomic force microscopy. *Applied Physics Letters*, 89(11):113121, 2006.
- [224] Á. S. Paulo and R. García. Tip-surface forces, amplitude, and energy dissipation in amplitude-modulation (tapping mode) force microscopy. *Phys. Rev. B*, 64(19):193411, Oct 2001.
- [225] H. Hölscher. Quantitative measurement of tip-sample interactions in amplitude modulation atomic force microscopy. *Applied Physics Letters*, 89(12):123109 123109–3, sep 2006.
- [226] X. Q. Chen, H. Yamada, T. Horiuchi, K. Matsushige, S. Watanabe, M. Kawai, and P. S. Weiss. Surface potential of ferroelectric thin films investigated by scanning probe microscopy. *Journal of Vacuum Science & Technology B: Microelectronics and Nanometer Structures*, 17(5):1930–1934, 1999.
- [227] T. Gomez, E. Florez, J. A. Rodriguez, and F. Illas. Reactivity of Transition Metals (Pd, Pt, Cu, Ag, Au) toward Molecular Hydrogen Dissociation: Extended Surfaces versus Particles Supported on TiC(001) or Small Is Not Always Better and Large Is Not Always Bad. The Journal of Physical Chemistry C, 115(23):11666–11672, 2011.
- [228] G. Kichin, C. Weiss, C. Wagner, F. S. Tautz, and R. Temirov. Single molecule and single atom sensors for atomic resolution imaging of chemically complex surfaces. *Journal of the American Chemical Society*, 133(42):16847–16851, 2011.

Acknowledgements

A work like this one would be impossible without the contributions of many people. At this point I would like to take the opportunity to acknowledge them.

First of all, I would like to thank Professor F. Stefan Tautz for giving me the permission to work on my PhD research in the Forschungszentrum Jülich. Secondly, I would like to thank Dr. Ruslan Temirov for being a friend during the last four years and for assisting me with advices and supportive encouragement. My special thanks go to our collaborators in Osnabrück: Professor Michael Rohlfing and Dr. Andreas Greuling for fruitful discussions and supporting our understanding with theoretical calculations.

I owe my deepest gratitude to our other collaborators who contributed with ideas in many discussions. I especially thank our collaborators from Bonn and Dresden.

My special thanks go to Dr. Olga Neucheva and Leonid Kliuienko for their support with technical knowledge about the STM machine, the technical staff in Jülich who supported me with technical advise and solved many of my problems and always had an open ear for my ideas. Additionally, I thank the people from the mechanical and electronic workshops who quickly developed and delivered necessary equipment.

I am grateful for the support of the people from CreaTec and especially Dr. Sven Zöphel who served so many problems with the STM and the STM software.

I need to thank my colleagues and members of PGI-3. Especially, my warm thanks go to Dr. Sergey Soubatch and the groups of Professor Bert Voigtländer and Driv. Doz. Dr. Christian Kumpf who created a warm and friendly atmosphere at work.

I gratefully appreciate the help of Claudia Klamandt and Sonja Lexen for taking care of the paperwork, which is indispensable for research and surviving in Jülich.

Finally my special thanks go to my family, friends and my Girlfriend who supported me through the last years and have always forgiven me when I was busy with work.

I would like to show my gratitude also to people I have forgotten here.

Christian Weiss

List of Acronyms

2PPE - 2 photon photo emission

AFM - Atomic force microscopy

ARUPS - Angular resolved ultraviolet photoelectron spectroscopy

DFT - Density functional theory

DOS - Density of states

DSP - Digital signal processor

EELS - Electron energy loss spectroscopy

FM-AFM - Frequency modulated atomic force microscopy

IETS - Inelastic electron tunnelling spectroscopy

LDA - Local density approximation

LDOS - Local density of states

LEED – Low energy electron diffraction

LEEM – Low energy electron microscopy

NC-AFM – Non-contact atomic force microscopy

PEEM – Photo electron energy microscopy

PTCDA - 3,4,9,10 perylene tetracarboxylic dianhydride

RHEED - Reflection high energy electron diffraction

SEM - Scanning electron microscopy

SnPc - Tin-II-phthalocyanine

STHM - Scanning tunnelling hydrogen microscopy

STM - Scanning tunnelling microscopy

STS - Scanning tunnelling spectroscopy

TED - Total electron density

TEM - Transmission electron microscopy

TPD - Temperature dependent desorption

UHV – Ultra high vacuum

UPS - Ultraviolet photoelectron spectroscopy

XPS - X-ray photoelectron spectroscopy

XSW - X-ray standing wave

ZBA – Zero bias anomaly

List of Figures

1.1	Comparison of images recorded in STM and STHM mode for different organic molecules adsorbed on different metallic substrates	6
2.1	Scheme of the STM feedback loop	8
2.2	Illustration of the image acquiring in constant current mode	9
2.3	Illustration of the difference between the classical- and quantum mechanical description of a particle hitting a potential barrier	10
2.4	Simplified energy diagram of the tunnelling junction	10
2.4	Tip-sample geometry in the Tersoff-Hamann approach	16
3.1	Tip preparation above a clean Au(111) surface to adsorb substrate material at the tip apex	33
3.2	Constant height STM image recorded during the deposition of D_2 on	99
	PTCDA/Au(111)	35
3.3	STHM imaging contrast of PTCDA/Ag(111) recorded with H_2 after too	
	long exposure	36
3.4	Preparation of the tip after condensation of D_2 on the surface $\ \ \ldots \ \ \ldots$	39
4.1	STM and STHM contrast of PTCDA	42
4.2	STM and STHM contrast of pentacene/Ag(111)	44
4.3	STM and STHM contrast of tetracene/Ag(111) $\dots \dots \dots$	45
4.4	STM and STHM contrast of $\operatorname{SnPc}/\operatorname{Ag}(111)$	47
4.5	Differential conductance STHM image contrast at increased tip-sample sep-	
	aration	49
4.6	At to small tip-sample distance the molecular contrast resembles the shape	
	of the gas phase LUMO	50
4.7	Doubling of the STHM contrast	52
4.8	Distorted molecular contrast in STHM mode	53
4.9	$ Differential\ conductance\ STHM\ contrast\ with\ highlighted\ perylene\ backbone$	54
4.10	Typical STHM contrast of PTCDA/Ag(111)	55
4.11	STHM contrast where the four outer rings of the perylene core are imaged	
	more pronounced with respect to the central ring	56
4.12	Faceted STHM contrast	57
4.13	STHM contrast with pronounced shadows inside of the rings $\ldots \ldots$	57
	Interaction in the herringbone phase of PTCDA molecules on $\operatorname{Au}(111)$	60
4.15	Square phase of PTCDA on Au(111)	63

4.16	STHM image of PTCDA in herringbone and square phase	65
4.17	Chemical modified film structure	67
4.18	STM image of the restructured PTCDA/Au(111) after the deposition of K	69
4.19	Comparison of STM contrast between $K/PTCDA/Au(111)$ and the square	
	phase of PTCDA/Au(111)	69
4.20	Imaging molecule-metal bonds in STHM	70
4.21	STHM contrast of metal clusters	73
5.1	Spectroscopic characterisation of the junction after deposition of H_2	77
5.2	dI/dV spectrum measured in the center of PTCDA/Au(111)	78
5.3	Results from a spectroscopic datacube	81
5.4	dI/dV spectra measured in the center of PTCDA/Au(111) with D_2 at	
	different tip-surface distances	84
5.5	Differential conductance with an approaching tip at $-5~\mathrm{mV}$ and $120~\mathrm{mV}$	
	to 130 mV	86
5.6	Direct comparison of the evolution of the conductance with decreasing tip	
	sample distance above different positions of PTCDA	88
5.7	STHM images of PTCDA/Au(111) measured with D_2 at different tip-	
	sample distance	89
5.8	DFT-LDA simulated $n_{t,D_2}(E_F,z')/n_{t,vac}(E_F)$ vs. D ₂ -tip distance z' for s-	
	and p-type orbitals at the Au atom below the deuterium molecule	91
5.9	Schematic illustration of the sensor/transducer model	94
5.10	C	
	$sensor/transducer\ model\ \dots$	96
5.11	Atomic resolution of Au(111) in STHM mode	99
5.12	STM images of $H_2/Cu(111)$	99
5.13	dI/dV(V) spectra measured on top of a Au atom	102
5.14	Images and spectra reconstructed from a datacube recorded above the clean	
	Au surface	103
5.15	$dI/dV(V)\mbox{-spectra}$ recorded with different tip surface distances	104
5.16	Continuing the series from figure 5.15 for smaller displacement	105
5.17	Evolution of dI/dV with decreasing tip-sample separation	107
5.18	Illustration of the imaging mechanism which leads to the atomic resolution	
	on the example of Xe/Pt(111) $\ \ldots \ \ldots \ \ldots \ \ldots \ \ldots$.	110
5.19	Evolution of dI/dV and df spectra with decreasing tip-sample separation .	113
5.20	Evolution of dI/dV and df values at zero and high bias with decreasing	
	tip-sample distance	115

5.21	Evolution of the contributions to the total force with decreasing tip-sample
	distance
6.1	Relationship between spike positions in dI/dV spectra and the molecular
	structure in STHM images at constant height
6.2	Series of dI/dV -spectra recorded above a single PTCDA molecule 125
6.3	Images reconstructed for bias values beyond the spikes ($V=55~\mathrm{mV}$) 126
6.4	Images and bias maps reconstructed at zero bias at small tip-sample sepa-
	ration
6.5	Images and bias maps reconstructed at zero bias at larger tip-sample sep-
	aration
6.6	Histograms for the four different tip-sample separations reconstructed from
	the maps of V_{inel}
6.7	STHM image of a dimer of Au-adatoms adsorbed on a Au(111) surface 133

Lebenslauf:

Persönliche Daten:

Name, Vorname: Weiss, Christian

Geburtstag: 07.04.1980

Geburtsort: Essen

Staatsangehörigkeit: deutsch

 ${\bf Qualifikationen:}$

2000: Abitur

ab 2000 bis 2008: Physik DII, Diplom

ab 2008: Beginn der Promotion

1. Soft Matter

From Synthetic to Biological Materials

Lecture manuscripts of the 39th IFF Spring School March 3 – 14, 2008

Jülich, Germany

edited by J.K.G. Dhont, G. Gompper, G. Nägele, D. Richter, R.G. Winkler (2008),

c. 1000 pages

ISBN: 978-3-89336-517-3

2. Structural analysis of diblock copolymer nanotemplates using grazing incidence scattering

by D. Korolkov (2008), III, 167 pages

ISBN: 978-3-89336-522-7

3. Thermal Nonequilibrium

Thermal forces in fluid mixtures

Lecture Notes of the 8th International Meeting on Thermodiffusion,

9 - 13 June 2008, Bonn, Germany

edited by S. Wiegand, W. Köhler (2008), 300 pages

ISBN: 978-3-89336-523-4

4. Synthesis of CMR manganites and ordering phenomena in complex transition metal oxides

by H. Li (2008), IV, 176 pages ISBN: 978-3-89336-527-2

5. **Neutron Scattering**

Lectures of the JCNS Laboratory Course held at the Forschungszentrum Jülich and the research reactor FRM II of TU Munich

edited by R. Zorn, Th. Brückel, D. Richter (2008), ca. 500 pages

ISBN: 978-3-89336-532-6

6. Ultrafast Magnetization Dynamics

by S. Woodford (2008), 130 pages

ISBN: 978-3-89336-536-4

7. Role of Surface Roughness in Tribology: from Atomic to Macroscopic Scale

by C. Yang (2008), VII, 166 pages

ISBN: 978-3-89336-537-1

8. Strahl- und Spindynamik von Hadronenstrahlen in Mittelenergie-Ringbeschleunigern

von A. Lehrach (2008), II, 171 Seiten

ISBN: 978-3-89336-548-7

9. Phase Behaviour of Proteins and Colloid-Polymer Mixtures

by C. Gögelein (2008), II, 147 pages

ISBN: 978-3-89336-555-5

10. Spintronics – From GMR to Quantum Information

Lecture Notes of the 40th IFF Spring School March 9 – 20, 2009 Jülich, Germany

edited by St. Blügel, D. Bürgler, M. Morgenstern, C. M. Schneider,

R. Waser (2009), c. 1000 pages

ISBN: 978-3-89336-559-3

11. ANKE / PAX Workshop on SPIN Physics

JINR, Dubna, Russia / June 22. - 26, 2009

Org. Committee: A. Kacharava, V. Komarov, A. Kulikov, P. Lenisa, R. Rathmann,

H. Ströher (2009), CD-ROM ISBN: 978-3-89336-586-9

12. Entwicklung einer Nanotechnologie-Plattform für die Herstellung Crossbar-basierter Speicherarchitekturen

von M. Meier (2009), 135 Seiten ISBN: 978-3-89336-598-2

13. Electronic Oxides -

Correlation Phenomena, Exotic Phases and Novel Functionalities

Lecture Notes of the 41st IFF Spring School March 8 – 19, 2010 Jülich. Germany

edited by St. Blügel, T. Brückel, R. Waser, C.M. Schneider (2010), ca. 1000 pages

ISBN: 978-3-89336-609-5

14. 4th Georgian-German School and Workshop in Basic Science

Tbilisi, Georgia / May 3 - 7, 2010

Org. Committee: E. Abrosimova, R. Botchorishvili, A. Kacharava, M. Nioradze,

A. Prangishvili, H. Ströher (2010); CD-ROM

ISBN: 978-3-89336-629-3

15. Neutron Scattering

Lectures of the JCNS Laboratory Course held at Forschungszentrum Jülich and the research reactor FRM II of TU Munich

edited by Th. Brückel, G. Heger, D. Richter, G. Roth and R. Zorn (2010), ca 350 pages

ISBN: 978-3-89336-635-4

16. Ab *initio* investigations of magnetic properties of ultrathin transition-metal films on 4d substrates

by A. Al-Zubi (2010), II, 143 pages

ISBN: 978-3-89336-641-5

17. Investigation of a metal-organic interface realization and understanding of a molecular switch

by O. Neucheva (2010), 134 pages

ISBN: 978-3-89336-650-7

18. Reine Spinströme in lateralen Spinventilen, *in situ* Erzeugung und Nachweis

von J. Mennig (2010), V, 95 Seiten

ISBN: 978-3-89336-684-2

19. Nanoimprint Lithographie als Methode zur chemischen Oberflächenstrukturierung für Anwendungen in der Bioelektronik

von S. Gilles (2010), II, 169 Seiten

ISBN: 978-3-89336-686-6

20. Macromolecular Systems in Soft- and Living-Matter

Lecture Notes of the 42nd IFF Spring School 2011 February 14 – 25, 2011 Jülich, Germany

edited by J. K.G. Dhont, G. Gompper, P. R.Lang, D. Richter, M. Ripoll,

D. Willbold, R. Zorn (2011), ca. 1000 pages

ISBN: 978-3-89336-688-0

21. The spin structure of magnetic nanoparticles and in magnetic nanostructures

by S. Disch (2011), V, 342 pages

ISBN: 978-3-89336-704-7

22. Element-selective and time-resolved magnetic investigations in the extreme ultraviolet range

by P. Grychtol (2011), xii, 144 pages

ISBN: 978-3-89336-706-1

23. Spin-Transfer Torque Induced Dynamics of Magnetic Vortices in Nanopillars

by V. Sluka (2011), 121 pages

ISBN: 978-3-89336-717-7

24. Adsorption von Phthalocyaninen auf Edelmetalloberflächen

von I. Kröger (2011), vi, 206 Seiten

ISBN: 978-3-89336-720-7

25. Time-Resolved Single Molecule FRET Studies on Folding/Unfolding Transitions and on Functional Conformational Changes of Phosphoglycerate Kinase

by T. Rosenkranz (2011), III, 139 pages

ISBN: 978-3-89336-721-4

26. NMR solution structures of the MloK1 cyclic nucleotide-gated ion channel binding domain

by S. Schünke (2011), VI, (getr. pag.)

ISBN: 978-3-89336-722-1

27. Neutron Scattering

Lectures of the JCNS Laboratory Course held at Forschungszentrum Jülich and the research reactor FRM II of TU Munich

edited by Th. Brückel, G. Heger, D. Richter, G. Roth and R. Zorn (2011), ca 350 pages

ISBN: 978-3-89336-725-2

28. Neutron Scattering

Experiment Manuals of the JCNS Laborator Course held at Forschungszentrum Jülich and the research reactorFRM II of TU Munich edited by Th. Brückel, G. Heger, D. Richter, G. Roth and R. Zorn (2011), ca. 180 pages

ISBN: 978-3-89336-726-9

29. Silicon nanowire transistor arrays for biomolecular detection

by X.T.Vu (2011), vii, 174 pages ISBN: 978-3-89336-739-9

30. Interactions between parallel carbon nanotube quantum dots

by K. Goß (2011), viii, 139 pages ISBN: 978-3-89336-740-5

31. Effect of spin-orbit scattering on transport properties of low-dimensional dilute alloys

by S. Heers (2011), viii, 216 pages

ISBN: 978-3-89336-747-4

32. Charged colloids and proteins: Structure, diffusion, and rheology

by M. Heinen (2011), xii, 186 pages

ISBN: 978-3-89336-751-1

33. Scattering Methods for Condensed Matter Research: Towards Novel Applications at Future Sources

Lecture Notes of the 43rd IFF Spring School 2012

March 5 – 16, 2012 Jülich, Germany

edited by M. Angst, T. Brückel, D. Richter, R. Zorn ca. 1000 pages

ISBN: 978-3-89336-759-7

34. Single-Site Green Function of the Dirac Equation for Full-Potential Electron Scattering

by P. Kordt (2012), 138 pages ISBN: 978-3-89336-760-3

35. Time Resolved Single Molecule Fluorescence Spectroscopy on Surface Tethered and Freely Diffusing Proteins

by D. Atta (2012), iv, 126 pages

ISBN: 978-3-89336-763-4

36. Fabrication and Utilization of Mechanically Controllable Break Junction for Bioelectronics

by D. Xiang (2012), 129 pages ISBN: 978-3-89336-769-6

37. Contact Mechanics and Friction of Elastic Solids on Hard and Rough Substrates

by B. Lorenz (2012), iv, 121 pages

ISBN: 978-3-89336-779-5

38. Ab initio Calculations of Spin-Wave Excitation Spectra from Time-Dependent Density-Functional Theory

by M. Niesert (2012), 146 pages ISBN: 978-3-89336-786-3

39. Neutron Scattering

Lectures of the JCNS Laboratory Course held at Forschungszentrum Jülich and the research reactor FRM II of TU Munich

edited by Th. Brückel, G. Heger, D. Richter, G. Roth and R. Zorn (2012),

ca 350 pages

ISBN: 978-3-89336-789-4

40. **Neutron Scattering**

Experiment Manuals of the JCNS Laborator Course held at Forschungszentrum Jülich and the research reactorFRM II of TU Munich

edited by Th. Brückel, G. Heger, D. Richter, G. Roth and R. Zorn (2012),

ca. 175 pages

ISBN: 978-3-89336-790-0

41. Influence of a shear flow on colloidal depletion interaction

by C. July (2012), xviii, 105 pages

ISBN: 978-3-89336-791-7

42. NMR studies on the isolated C39 peptidase-like domain of ABC transporter Haemolysin B from *E. coli*: Investigation of the solution structure and the binding interface with HlyA

by J. Lecher (2012), 126 pages ISBN: 978-3-89336-793-1

43. Spin Correlations and Excitations in Spin-frustrated Molecular and Molecule-based Magnets

by Z. Fu (2012), 208 pages ISBN: 978-3-89336-797-9

44. Crystal and spin structure and their relation to physical properties in some geometrical and spin spiral multiferroics

by N. K. Chogondahalli Muniraju (2012), iii, 190 pages

ISBN: 978-3-89336-802-0

Schriften des Forschungszentrums Jülich Reihe Schlüsseltechnologien / Key Technologies

45. Multiferroicity in oxide thin films and heterostructures

by A. Glavic (2012), xi, 152 pages

ISBN: 978-3-89336-803-7

46. German Neutron Scattering Conference 2012

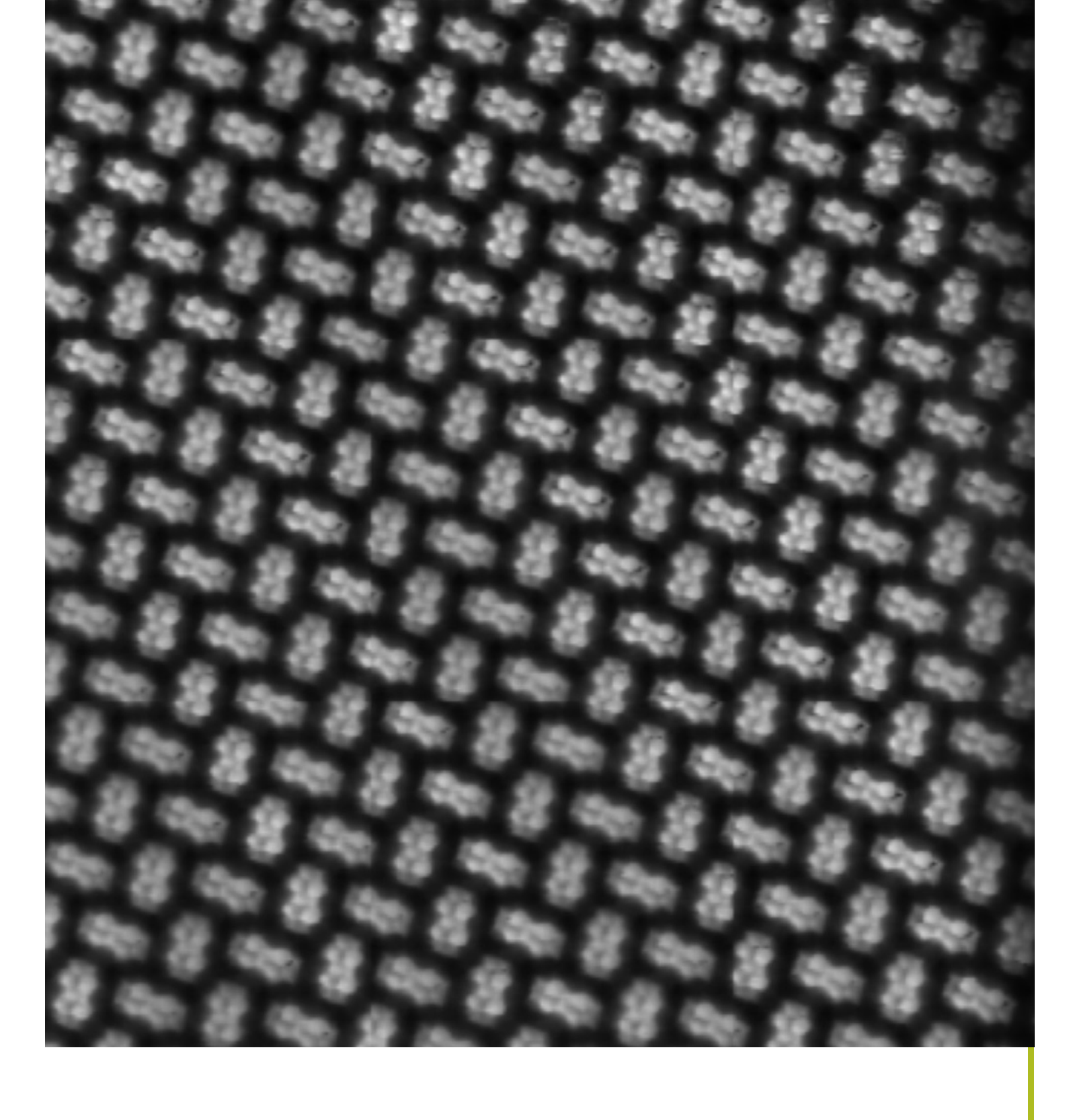
September 24 -26, 2012. Gustav-Stresemann-Institut, Bonn, Germany edited by Th. Brückel (2012)

ISBN: 978-3-89336-807-5

47. STM beyond vacuum tunnelling: Scanning Tunnelling Hydrogen Microscopy as a route to ultra-high resolution

by C. Weiss (2012), II, 165 pages

ISBN: 978-3-89336-813-6



Schlüsseltechnologien / Key Technologies Band / Volume 47 ISBN 978-3-89336-813-6

